

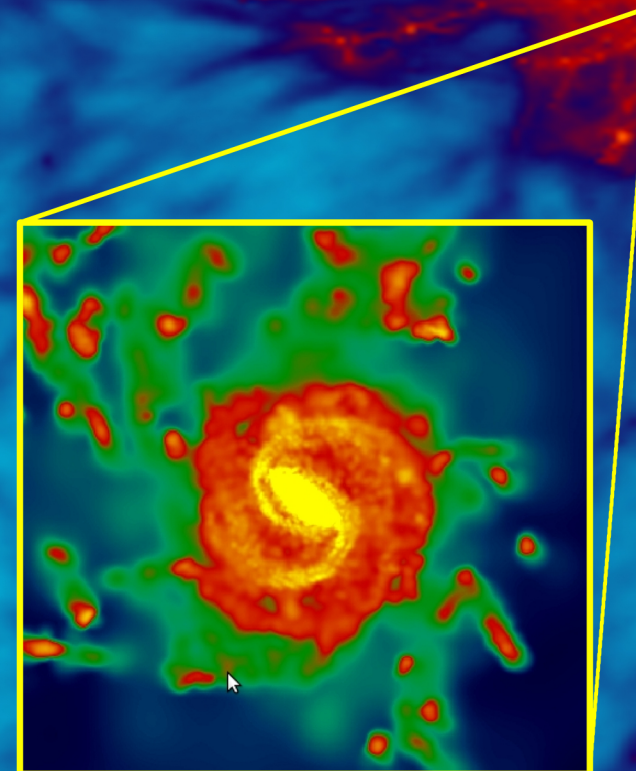
Nature and Nurture in Galaxy Formation Simulations

Nature and Nurture in Galaxy Formation Simulations

Marcel Haas

The evolution of galaxies is one of the most active fields of research in astrophysics these days. Observationally, theoretically as well as numerically many studies are published on a daily basis. In this thesis we take the approach of analyzing a large suite of simulations, drawn from the Overwhelmingly Large Simulations project, from the online available galaxy catalogs build on the Millennium Simulations, as well as some Monte Carlo Simulations, in order to investigate a number of issues regarding the evolution of galaxies over time.

With 'nature and nurture' we generally mean the distinction between internal and external processes, respectively, that affect galaxy evolution. The internal processes are e.g. small-scale phenomena like star formation, supernova explosions and the presence of Active Galactic Nuclei. The density of galaxies in the neighbourhood, the tidal fields of neighbours acting on galaxies and the interaction between galaxies when come near one another are examples of external processes. Both are given attention in this thesis.



Marcel Haas

Stellingen behorende bij het proefschrift

Nature and Nurture in Galaxy Formation Simulations

1. Stervorming in sterrenstelsels wordt gereguleerd door de aanvoer van koud gas en feedback processen, terwijl de efficiëntie van stervorming op kleine schaal slechts van invloed is op de hoeveelheid koud en dicht gas die beschikbaar is voor stervorming. *(Hoofdstuk 2)*
2. Alle populaire omgevingsparameters in de literatuur zijn goede maten voor de massa van de halo van donkere materie waar het sterrenstelsel zich in bevindt. *(Hoofdstuk 3)*
3. Omgevingsparameters die onafhankelijk zijn van de massa van de halo van donkere materie kunnen worden geconstrueerd door gebruik te maken van dimensieloze variabelen, waardoor de massa- en lengteschalen uit het probleem worden weggenomen. *(Hoofdstuk 3)*
4. Wanneer de lichtkrachtverdeling van sterrenstelsels in een simulatie wordt bepaald door er namaakwaarnemingen van te maken en deze verdeling te bepalen zoals waarnemers dat zouden doen, dan komt daar dezelfde verdeling uit als wanneer de helderheden direct uit de simulatie worden gemeten, zonder dat het observationele proces wordt doorlopen. *(Hoofdstuk 4)*
5. De massaverdeling van sterren binnen een sterrenstelsel kan meer lichte ten opzichte van zware sterren bevatten dan de massaverdeling in afzonderlijke stervormingsgebieden, maar dit effect is alleen belangrijk wanneer de massaverdeling van de stervormingsgebieden die van sterclusters volgt tot zeer lage massa's en het is alleen merkbaar in de hoeveelheid OB sterren in en de metaliciteit van het stelsel, en niet in de lichtkracht en kleur. *(Hoofdstuk 5)*
6. De tijd die nu wordt besteed aan het schrijven van waarneem- en computervoorstellen zou in veel gevallen net zo nuttig besteed zijn aan origineel werk met behulp van gearchiveerde data.
7. Hoewel kosmologie zich hiertoe zou kunnen rekenen, is het vakgebied van de vorming en evolutie van sterrenstelsels nog lang geen hoge precisie wetenschap.
8. Statistiek is voor de sterrenkunde veel belangrijker dan het curriculum aan de universiteiten en het gebruik ervan in veel wetenschappelijk publicaties doen vermoeden.
9. De kwaliteit van publicaties van simulatoren zou toenemen door waarnemers te betrekken en vice versa.
10. Popularisatie wordt in de sterrenkunde, maar ook daarbuiten, sterk ondergewaardeerd.
11. Open source software is veelal alleen gratis als je eigen tijd je niks waard is.
12. De kredietcrisis die zich eind 2008 en begin 2009 heeft voltrokken was, behalve een financieel minpuntje, het ultieme bewijs dat economie een sociale en geen exacte wetenschap is.

Stellingen behorende bij het proefschrift

Nature and Nurture in Galaxy Formation Simulations

1. Star formation in galaxies is regulated by the accretion of cold gas and feedback processes, while the efficiency of star formation on the small scales only influences the amount of cold and dense gas available for star formation. *(Chapter 2)*
2. All popular environmental parameters in the literature are good measures for the mass of the dark halo hosting the galaxy. *(Chapter 3)*
3. Environmental parameters that are independent of halo mass can be constructed using dimensionless variables, which remove the mass and length scales imposed on the problem. *(Chapter 3)*
4. If the luminosity function of galaxies in a simulation is measured through the creation of mock images and the analysis of these images with tools observers use, then the same luminosity function is obtained as if the luminosity function would be obtained directly from the simulation, without going through the observational process. *(Chapter 4)*
5. The distribution of stellar masses in a galaxy could contain more massive stars in comparison to low mass stars than the initial mass function in separate star forming regions, but this effect is only important if the mass distribution of star forming regions follows the cluster mass function to very low masses and is only noticeable in the number of OB stars and metallicities of galaxies and not in the luminosities or colours. *(Chapter 5)*
6. The time that is currently invested in writing observing and computing proposals could often be equally well invested in original work using archival data.
7. Although cosmology could be regarded as such, the field of formation and evolution of galaxies is still far from a high precision science.
8. Statistics are much more important for astronomy than the current curricula at universities and the use of it in many scientific publications suggest.
9. The quality of publications by simulators would improve by involving observers, and vice versa.
10. Popularization is strongly undervalued in astronomy and other fields.
11. Open source software is usually only for free if your own time is worth nothing.
12. The credit crisis that occurred in 2008 and 2009 was, besides a financial disadvantage, an ultimate proof that economy is a social, and not an exact science.

If you thought that science was certain -
well, that is just an error on your part.

Richard P. Feynman

NATURE AND NURTURE IN GALAXY FORMATION SIMULATIONS

Proefschrift

ter verkrijging van
de graad van Doctor aan de Universiteit Leiden,
op gezag van de Rector Magnificus prof.mr. P.F. van der Heijden,
volgens besluit van het College voor Promoties
te verdedigen op dinsdag 7 december 2010
klokke 11.15 uur

door

Marcel Richard Haas

geboren te Oosterhout in 1983

Promotiecommissie

Promotor: Prof. dr. Marijn Franx

Co-promotor: Dr. Joop Schaye

Overige leden: Dr. Jarle Brinchmann
Prof. Dr. Koenraad Kuijken
Prof. Dr. Simon Portegies Zwart
Prof. Dr. Huub Röttgering
Prof. Dr. Scott Trager (Rijksuniversiteit Groningen)
Prof. Dr. Frank van den Bosch (Yale University)

Contents

1	Introduction	1
1.1	Galaxy formation	2
1.2	Numerical simulations	7
1.3	The Overwhelmingly Large Simulations	10
1.4	Thesis summary	10
1.5	The (near) future	12
2	Physical properties of simulated galaxies from varying input physics	13
2.1	Introduction	14
2.2	Numerical techniques	16
2.3	Cosmology	28
2.4	Metal-line cooling	30
2.5	Reionization variations	33
2.6	The polytropic equation of state for high density gas	35
2.7	The star formation law	35
2.8	The stellar initial mass function	38
2.9	Supernova feedback	43
2.10	AGN feedback	55
2.11	Conclusions	58
2.A	Numerical convergence tests	62
2.B	The energy and momentum in momentum driven wind models	66
3	Disentangling galaxy environment and host halo mass	69
3.1	Introduction	70
3.2	Popular environmental parameters	72
3.3	Environmental parameters and their relation to halo mass	75
3.4	Environment as a measure of halo mass	84
3.5	Environment independent of halo mass	87
3.6	Conclusions	96
3.A	Obtaining the halo mass from environmental parameters	98
4	The simulated galaxy luminosity function: input physics, dust attenuation and galaxy selection	105
4.1	Introduction	106
4.2	Simulations	108
4.3	Population synthesis	111
4.4	Dust attenuation	116
4.5	Mock images and galaxy selection	120

CONTENTS

4.6	Conclusions	127
4.A	Column densities in SPH simulations	129
5	Variations in Integrated Galactic Initial Mass Functions due to Sampling Method and Cluster Mass Function	141
5.1	Introduction	142
5.2	The underlying mass functions	144
5.3	Sampling techniques	146
5.4	Integrated galactic initial mass functions	150
5.5	The number of O-stars in the Milky Way	158
5.6	Galaxy evolution models	162
5.7	Conclusions	167
6	Nederlandstalige samenvatting	171
	Bibliography	182
	Publications	193
	Curriculum vitae	194
	Nawoord	195

1

Introduction

Since Edwin Hubble showed in the 1930s that the Universe we live in is expanding, our knowledge about the formation of structure has also been expanding. Just like that of the Universe, the expansion of our body of knowledge seems to be accelerating, aided by the ever increasing power of telescopes, detectors, computers and software. This thesis deals with the formation of structure in the Universe, from the viewpoint of computer simulations. As large scale ($>kpc$) processes proceed on timescales many orders of magnitude longer than a human life (or the preparation of a PhD thesis), directly observing this evolution is impossible. Simulations are used to understand how objects evolve, while snapshots of the simulations may be compared to observations, which in essence are nothing more than snapshots of the real Universe.

1.1 Galaxy formation

1.1.1 The growth of structure in the Universe

About 13.7 Gyr ago, the Universe was born in a hot, dense and highly uniform state. The temperature and density of the hot plasma were almost completely uniform. Through the tight coupling between baryonic matter and radiation, the growth of density perturbations in the dark matter was hardly followed by the baryons. At the time of recombination, about 380.000 years later, the Gaussian deviations from the mean density were of order $\delta\rho/\rho \sim 10^{-5}$ and the wavelengths of the perturbations exhibit a spectrum that evolved from an initial power-law spectrum: $P(k) \sim k^{n_s}$, where $P(k)$ is the power at wave number k . The spectral index $n_s \simeq -1$. We know this, because the radiation emitted by the recombination of hydrogen atoms is redshifted by a factor ~ 1100 and observed as the Cosmic Microwave Background by e.g. the COBE and WMAP satellites (for a recent review, see Hu & Dodelson, 2002). The baryons decouple from the radiation and flow into the potential wells already in place (and still growing) in the dark matter.

Because the fluctuations are well within the linear regime, linear theory can be used to calculate the growth of the perturbations, until they get to the non-linear regime, where calculations with pen and paper will generally not suffice. The perturbations grow under gravity, making over-dense regions even denser in the course of time. Meanwhile the Universe expands, lowering the overall density.

The non-linear perturbations decouple from the expansion of the Universe and collapse into gravitationally bound, eventually virialised structures, that are generally named ‘haloes’. Within these haloes galaxies may form. This involves more than just gravity and needs to take full account of hydrodynamics, star formation, feedback effects and other ‘gastrophysical’ phenomena.

1.1.2 The evolution of baryons

The important difference between the formation of dark matter haloes and the formation of galaxies inside them, is the fact that gas is collisional, whereas dark matter is collisionless. Dark matter cannot cool and only acts upon the other (dark) matter through gravity. Gas can cool. Pressure gradients will drive gas flows from high to low pressure and there are many possible ways of injecting heat into gas, both as a result of shocks, where kinetic energy of gas is transformed into internal energy, but also by the absorption of radiation.

At a redshift of about nine (or somewhere between six and fifteen Komatsu et al., 2009, 2010) the first sources of light reionized the Universe. There is a roughly uniform UV background that is the result of young stars and accreting

supermassive black holes (which of the two dominates is redshift dependent) that keeps intergalactic gas above a temperature floor of roughly 10^4 Kelvin (this temperature floor is density dependent, because of the interplay between the ionization by this background and recombination, and redshift dependent due to the adiabatic expansion of the Universe).

Initially, the baryons will just follow the dark matter and decouple from the expansion, to collapse into the dark matter haloes. In the center of these, where the densities are high, radiative cooling will become more efficient (atomic/ionic line cooling scales with the density squared). When gas cools, pressure support is lost and higher densities can be reached.

When galaxies start to form, a large variety of processes come into play that can influence the future evolution of the baryons. In the following two sections we will discuss some internal and external processes that could in principle be important for galaxy evolution. We will hereby focus on processes that are investigated in the remainder of this thesis.

1.1.3 Internal processes in galaxy formation

Gas in haloes is at higher density than gas in the intergalactic medium (IGM). Inside a halo the gas density follows a profile with densities higher in the center than in the outskirts. This density gradient corresponds to a gradient in cooling rate (in the simplest assumption that the temperature and metallicity are initially uniform). Pressure support is lost from the center where the cooling is very efficient, so more gas can fall in and an inward cooling flow establishes. In the center of the halo the gas cools down to roughly 10^4 K and settles in a disk, because the (specific) angular momentum is conserved.

In high density gas, radiative cooling through metal lines can become very efficient and dust column densities can become high enough such that clouds can become self-shielded from photo-dissociating and ionizing radiation. The gas can now become mostly molecular. The rotational and vibrational levels of molecules give rise to many new channels of cooling of the gas. In the gas in the disk, a multi-phase interstellar medium (ISM) establishes, consisting of denser, colder, (partly) molecular clouds, embedded in warmer gas, the spatial distribution of which is fractal.

Eventually, when the gas is cold and dense enough, stars may form. The process of star formation itself is very complicated and many theses could be, and have been written on the formation of stars from a giant molecular cloud. For people who work on scales of galaxies and bigger, this star formation process is often heavily simplified, sweeping all details on scales smaller than $\sim 10^4 M_\odot$ under the carpet. Empirical relations between e.g. gas surface density and star formation

rates are used. Star formation in galaxies is observed to follow a close relation between the gas surface density and the star formation rate surface density, a relation known as the Kennicutt-Schmidt (Kennicutt, 1998a) law: $\dot{\Sigma}_* = A\Sigma_g^n$, with $n \approx 1.4$ and A a normalization factor that depends on the stellar initial mass function (IMF), because star formation rate indicators are only sensitive to stars above some mass, because it is the effect of ionizing radiation that is measured.

After stars have formed, they evolve and eventually die. During their lifetimes, stars of different mass expel different chemical elements at different times, through stellar winds and/or explosions. These chemical yields are added to the interstellar medium (ISM) around the stars. This enrichment results in more efficient cooling, and in the possibility to form dust. The relative yields of different metals depends on the IMF, as different types of stars are the main producers of different elements.

The most massive stars already start exploding as Supernovae (SNe) after a few million years and inject about 10^{51} erg of kinetic energy per explosion into the surrounding gas. Part of the energy will be thermalized in shocks and radiated away. The remainder can stir up the surroundings of the star forming region (increasing the local turbulence), it can blow ‘super bubbles’ around complexes of star forming regions and might even blow large scale galactic winds. It is therefore obvious that SNe have a considerable impact on their host galaxy.

Most, if not all, galaxies that have a spheroidal component (elliptical galaxies, or disk galaxies with a bulge) also host a supermassive black hole (SMBH) in their centres (Kormendy & Richstone, 1995; Ferrarese & Merritt, 2000). These SMBHs accrete gas from an accretion disk, a process in which part of the rest mass energy that is accreted is not added to the mass of the black hole but radiated away. This radiation may heat and push surrounding gas. This AGN feedback comes in two flavours in nature: the relatively quiet accretion mode for low accretion rates (compared to their Eddington limit), which is called ‘radio mode’, as these systems are observed as radio galaxies. AGN with high accretion rates (comparable to the Eddington limit) have strong optical emission lines and the feedback corresponding to this mode is often called ‘quasar mode’. The energy output corresponding to black hole growth depends on the mass and accretion rates of the black hole, and is stronger for more massive black holes, which tend to live in more massive spheroids.

1.1.4 External processes in galaxy formation

Galaxies do not live alone in the Universe. Galaxies do have neighbouring galaxies, either within the same dark matter halo (for sufficiently massive haloes) or in haloes next to them.

One of the main drivers of galaxy evolution is the mass of the galaxy’s host

dark matter halo. This host halo mass sets the gravitational potential well, and therefore affects the central density. Also, more massive haloes are in general older and therefore can start forming stars earlier. Most of the gas in the halo which is not already cold and inside the galaxies, is very tenuous and hot, at about the virial temperature of the halo. In order to form stars this gas needs to cool down, and the cooling time is a strong function of the temperature (the gas has to cool down further from higher temperatures, and the cooling rate is a complicated but in general a decreasing function of temperature in the temperature range $10^5 - 10^7$ K, see e.g. Wiersma et al., 2009a).

The rate at which, and the mode in which, gas accretes onto haloes is also a function of halo mass. Gas can accrete in two main modes: hot and cold (e.g. Kereš et al., 2005; Ocvirk et al., 2008). With hot accretion we indicate gas that flows in and shock heats near the virial radius to about the virial temperature of the halo. When gas accretes cold, streams (and clumps) of high density fall into the center, but the energy gained in the (smaller) shocks are efficiently radiated away and therefore do not add to the temperature. Gas that accretes cold does not have to cool down much before it can participate in star formation, whereas shock heated gas at the virial temperature (at least in massive haloes) has very long cooling times and therefore can delay star formation significantly. The transition from cold to hot accretion is not sharp (in many haloes a fraction of the gas accretes hot and a fraction accretes cold) and lies at around a halo mass of order $10^{12} M_{\odot}$, with more massive haloes accreting more gas in the hot mode (Dekel & Birnboim, 2006; Dekel et al., 2008).

Dark matter haloes are clustered. The amount of clustering is a function of mass, such that more massive haloes cluster more strongly (e.g. Kaiser, 1984; Cole & Kaiser, 1989; Mo & White, 1996). More massive haloes also have more sub-haloes containing galaxies and the fraction of the mass of a DM halo that is in substructure is roughly constant with halo mass (Gao et al., 2004). If there is a minimum (sub-) halo mass for galaxy formation, then a more massive halo hosts more small (satellite) galaxies.

As revealed by the marvelous images of colliding galaxies, interactions between two systems are also of importance in the growth of galaxies. The tidal torques the two galaxies exert on each other drive gas flows inward, thereby fueling a central star burst, and possibly a quasar outburst of the central SMBHs (which eventually may merge too). For a few dynamical times, the galaxies will have an elevated star formation rate, and the end product of a major merger (mass ratio $\geq 1/3$) is often an elliptical galaxy, regardless of the Hubble types going in to the collision. For elliptical galaxies, which have hardly any cold gas to form stars from, the dominant growth mechanism is mergers, and the most massive ellipticals in the known Universe are thought to be the result of a series of major and minor

mergers, deep inside the potential wells of massive DM haloes.

1.1.5 The interplay between internal and external processes in galaxy formation

In the previous paragraphs we listed many processes that are important in galaxy formation. To what extent the different physical processes are important, and how they act together to make up galaxy evolution, is the largest unknown in galaxy formation theory.

Whereas star formation is a necessary ingredient to form (optically) observable galaxies, it is not clear what sets the star formation rate in galaxies. Gas accretion is a necessary ingredient, and so is gas cooling. Feedback processes counteract cooling, and possibly also accretion, by blowing gas out of galaxies. It is expected that star formation in galaxies is to some extent self-regulated. If the cooling and accretion processes are dominant over feedback processes, stars will form while gas pressure support falls. Therefore, more gas will collapse and stars will form until feedback, e.g. in the form of SN explosions, is able to ‘counteract’ star formation. If, on the other hand, feedback is dominant over the cooling and accretion processes, star formation will cease, SN feedback will decrease and cooling and infall will result in more star formation, until the rate of star formation reaches some sort of quasi-equilibrium with the amount of feedback.

In galaxies of very different mass, the equilibrium between feedback and star formation may happen at very different scales. In more massive galaxies, the pressure in the ISM is higher, the amount of mass that need to be swept up by winds blown by SNe is larger, and the potential well from which the wind needs to escape deeper. With only an energy limit to the amount of feedback (the total amount of energy from SNe) it is not clear how this equilibrium settles in different environments. For example, at the same energy a lot of mass can be kicked at low velocity or vice versa. An upper limit for the energy input in winds is not necessarily related to the amount of energy available from SNe, if winds are driven by radiation pressure of the stellar population, rather than by the SN explosions themselves. An equilibrium between feedback and star formation may not always be possible. For example, if SN driven bubbles do not blow out of the galaxy and feedback is very inefficient. If that is the case, other feedback mechanisms like AGN feedback are required to suppress the star formation rate of galaxies.

The interaction between accretion flows bringing in new fuel for star formation and the outflows driven by star formation is a complicated non-linear process and requires accurate, high-resolution numerical simulations. Studies have not yet converged on how this interplay works, how the hot and cold accretion fractions depend on halo mass, redshift and feedback.

The problem of ‘nature versus nurture’ deals with the extent to which internal and external processes influence galaxy properties. A lot of observational work has been done in this field. Star forming properties of galaxies are found to be correlated with the stellar mass of galaxies, with their gas fractions and with surrounding galaxy densities (see references in Table 3.1 in Chapter 3). The colours and magnitudes of galaxies in turn depend largely on their stellar mass and recent star formation histories (e.g. Kauffmann et al., 2003; Blanton et al., 2005), and therefore also correlate with mass and environment. Because we know that the stellar mass (at least for the central galaxies of haloes) correlates with halo mass, and environmental density also correlates with halo mass Lemson & Kauffmann (1999), it is not yet clear what the main driving factor is, and whether there is more than one driving factor in galaxy evolution at all.

1.2 Numerical simulations

Although astronomy has always been, and will probably remain, an observationally driven science, a large part of our understanding of the evolution of structure in the Universe stems from simulations. In simulations, the evolution of a physical system is in principle completely determined by the code and the initial and boundary conditions. In some sense, you will ‘get out what you put in’. In practice it is, however, usually far from trivial to understand the outcome from the physics in the code and the initial and boundary conditions. Non-linear behavior of the system and the interplay between different ingredients of the simulation require a detailed investigation of the results in order to increase our understanding of the simulated objects.

In galaxy formation simulations, a lot of progress has been made over the past decades (for a somewhat dated review see Bertschinger, 1998). Although Eulerian mesh based codes (in which the volume is discretized) have also been used successfully for simulations of galaxies in a cosmological context, I will here focus on Lagrangian simulations, in which the mass in the Universe is discretized in particles, because those kind of simulations form the basis of a large part of this thesis.

1.2.1 Simulations of the dark matter component of the Universe

Until recently, cosmological simulations (simulations of a large, representative volume of the Universe with box sizes much larger than the objects of interest) were mainly N -body simulations in which only gravity is followed in a Universe in which the mass is discretized in point-like particles. These simulations predict the evolution of the dark matter component of the Universe, with the ‘details’ of

the baryonic physics neglected. As following only gravity is relatively easy, our understanding of the large-scale structure of the Universe has rapidly increased due to simulation projects which followed only the dark matter component of the Universe (see e.g. Springel et al., 2005).

Galaxies in N -body simulations

With the evolution of dark matter alone, nothing can be said about the properties of the galaxies in such simulations. Semi-analytic models (SAMs) have been created in order to form a galaxy population on top of the dark matter simulations (Croton et al., 2006; Bower et al., 2006; De Lucia & Blaizot, 2007). These consist of analytic recipes, which depend on the merger history of the halo the galaxies are in. The recipes describe how gas flows into the haloes, cools, form stars, explode as SNe and how SMBHs form, grow and influence the gas in their haloes.

These SAMs generally come with a large number of free parameters (which are mostly motivated by the baryonic physics described in Section 1.1), so it is very well possible to form a galaxy population that is very representative of the galaxy population that is observed. The model parameters are usually tweaked to reproduce a few observables (principally the $z = 0$ galaxy luminosity function), and the model is then used to predict others. Given the large number of free parameters and functions, many of which may be poorly constrained or even unphysical, the predictive powers of these models may be questionable, but at least it is possible to create a galaxy population that matches a variety of observations.

Variations on N -body simulations

Galaxy formation models do not necessarily need N -body simulations in order to predict the behaviour of the dark matter component of the Universe. Several alternatives exist and are often used (they are usually less computationally expensive, but may lack small scale details and are less accurate). In extended Press-Schechter theory, for example, the dark matter halo merger histories can be obtained analytically. Another variation uses halo mass functions obtained from either analytic theory or N -body simulations and link the luminosities of observed galaxies to the dark matter haloes. In halo occupation distribution (HOD) models, the self-similarity of dark matter haloes is used, such that the number of galaxies, and their mass distribution is known as a function of the halo mass (e.g. Berlind & Weinberg, 2002). Using the resulting distributions of galaxies in haloes, galaxy luminosities from an observed galaxy luminosity function can be linked to these galaxies.

1.2.2 Smoothed Particle Hydrodynamics and sub-grid physics

Although the above methods can produce galaxy populations that satisfy observational constraints, they are not always physically well-motivated. Often, the different ingredients do not have a chance to interact, and in many cases the physical prescriptions for ingredients like gas cooling, star formation, feedback etc. are strongly simplified versions of reality. In order to gain physical insight into the interplay between baryonic processes in galaxy formation, one needs to follow the evolution of the baryons more self-consistently using simulations.

One way to do so, and this is the method used for most of this thesis, is to simulate the Universe with both a dark, and a baryonic component in hydrodynamical simulations. Gas particles discretize the mass in the simulated volume, and their hydrodynamical properties (e.g. density and pressure) are obtained by averaging over a kernel containing a fixed number of neighbours. These particles can then exert gravity and pressure on each other and evolve hydrodynamically, rather than just under the act of gravity. Such simulations are much more computationally challenging than the N -body simulations discussed above.

Although we take the smoothed particle hydrodynamics (SPH) approach (Monaghan, 1992) in order to follow the evolution of the gas (and the response of the dark matter to the presence and evolution of baryons), many of the processes shaping galaxies happen on scales below the resolution limit of cosmological simulations. As we will see below, typical particle masses in simulations of representative volumes of the Universe are limited (because the particle number is limited by computer memory and processor speed) to $m_p \gtrsim 10^5 M_\odot$ in the highest resolution simulations available, but more often one or more orders of magnitude higher. Gas cooling is a process on the scale of atoms, stellar evolution happens on scales of about $1 M_\odot$ and the evolution of supernova remnants may require a similar resolution. These are just a few examples, in Chapter 2 we will go into many small-scale processes. Obviously, recipes have to be developed in order to describe the effect of small scale processes below the resolution scale of the simulation. These are called ‘sub-grid models’, and these are the ingredients that make different SPH simulations differ from each other (strongly).

To date, an extensive and fair comparison between the many different sub-grid models has not been made. A systematic comparison of sub-grid models requires a suite of simulations, run with the same code, on the same initial conditions, varying the sub-grid recipes one-by-one. That is exactly what the Overwhelmingly Large Simulations project set out to do.

1.3 The Overwhelmingly Large Simulations

A recent effort in simulating a representative volume of the Universe is conducted at Leiden Observatory, the Netherlands and is called ‘The Overwhelmingly Large Simulations’ (*OWLS*, Schaye et al., 2010), a project catalyzed by the temporary availability of the IBM BlueGene/L supercomputer ‘Stella’ which was built for the LOFAR collaboration in Groningen. The name of the project is not only supposed to tell you that the simulated volumes are large, but also that the number of variations in the sub-grid modeling is unprecedented for cosmological simulation projects. The philosophy of *OWLS* is to keep the simulation ingredients as simple as possible and to vary sub-grid models and/or parameters one by one (away from what we call the ‘reference model’).

By “keeping things simple”, we mean that when we have to introduce a sub-grid model for an unresolved process, we keep this model simple, and do not introduce more parameters than necessary and/or justifiable.

The simulations are extensively described in Schaye et al. (2010) and an extensive summary is given in Chapter 2. Over 50 high resolution simulations have been carried out, totaling many tens of terabytes as a result of millions of CPU-hours of calculation. In this thesis we will focus on the populations of galaxies formed in the different *OWLS* runs. With such an extensive set of simulations, many studies are possible, and this thesis only contains a small subset of what *has been* done, let alone what *could be* done.

1.4 Thesis summary

In **Chapter 2** a summary is given of all *OWLS* runs used in this thesis. The influence of the physics and resolution of the simulation (in terms of mass as well as box size) on the resulting galaxy population at $z = 2$ are discussed. As the variation of sub-grid models is the unique feature of *OWLS*, we discuss the effect of all the sub-grid models in quite some detail. We look at the relation between properties of Friends-of-Friends (FoF) haloes in the high resolution simulations. In particular, the star formation rate (SFR), the build up of stellar mass, and gas, star and baryon mass fractions as a function of halo mass are used to assess the effectiveness of the various feedback models and we compare shortly to observations. Interesting conclusions from this chapter are that the star formation rate of a galaxy is self-regulated by gas accretion (set by halo mass and gas cooling) and feedback and that the star formation recipe regulates the amount of available fuel (i.e. the gas mass fraction) of the haloes, but not the star formation rate.

As the extent to which halo mass and environment sets galaxy properties is not

yet clear, we investigate in **Chapter 3** how to disentangle the influence of halo mass and environment. It is well known that environmental density and halo mass correlate. In the literature, many different definitions of environmental density occur. We make use of the Millennium Simulation and semi-analytic models of galaxy formation in order to investigate the correlation between environmental parameters and halo mass on a galaxy population which matches observational constraints. We show how well popular environmental parameters correlate with halo mass, as a function of the scale on which environment is measured. We will show that if the minimum mass/luminosity of the neighbours used to characterize the environment is fixed relative to the mass/luminosity of the halo in question, and if the distance to these neighbours is scaled to a typical distance for the galaxy in question (e.g. the virial radius of its host halo) that then the measure of environmental density can be made to be independent of halo mass. If one wants to investigate the effects of halo mass (‘internal environment’) and ‘external environment’ separately, it is most useful to use one parameter that correlates very strongly with halo mass (e.g. the number of galaxies within roughly a virial radius) and one that is independent of halo mass.

In order to compare simulations and observations one can go two ways: determine physical properties from observables and compare these to the simulations, or extract observables from the simulation and compare these to observed galaxy properties. In **Chapter 4** we extract luminosity functions from the OWLS simulations and investigate how these depend on input physics, dust attenuation and galaxy selection. The dependence of the LF on input physics is very similar to the dependence of the stellar mass function on input physics, which was already shown in Chapter 2. Dust attenuation is hard to estimate in SPH simulations with particle masses exceeding the mass of absorbing clouds in the ISM of galaxies. We estimate it from the column density of metals, normalized to the extinction as a function of metal column in the solar neighbourhood. As the definition of galaxies used by simulators (gravitationally bound structures of particles) and observers (some region of an image that exceeds the background in intensity) are fundamentally different, we try to assess if the obtained luminosity function in simulations can be expected to be the same as the observed luminosity function of galaxies, under the assumption that the underlying galaxy populations are identical. To that end we project our star particles onto images, smear the images with a point spread function (PSF) and extract the galaxy luminosity function with the tools observers would use. We find that the LFs are in general very similar to the ones directly obtained from the simulations, but that PSFs which are large compared to the galaxies may flatten the faint end of the LF, which would alleviate a major tension between observed and simulated LFs.

Finally, in **Chapter 5** we investigate the stellar content, broadband photom-

etry and metal enrichment of idealized galaxy models in the framework of the so-called ‘integrated galactic initial mass function’ (IGIMF, see Kroupa & Weidner, 2003; Weidner & Kroupa, 2004, 2005, 2006). Star formation occurs mostly in clusters (Lada & Lada, 2003; Piskunov et al., 2008). These clusters follow a mass distribution, that is quite similar in shape to the stellar IMF (e.g. Larsen, 2002; Bastian, 2008). The cluster mass function favours low mass objects, so if the power-law mass function were to extend all the way down to clusters of just a few solar masses, it is clear that the IMF summed up over all clusters must be deficient of high mass stars compared to the underlying IMF. A star can, after all, not be more massive than its host cluster. We will investigate the IGIMF under various assumptions for the method used to sample the stellar masses in the clusters and for different cluster mass functions. We use the IGIMFs as input IMFs for the GALEV population synthesis models (Bicker et al., 2004; Kotulla et al., 2009) to obtain broadband magnitudes and metallicities of closed box galaxy models. We find that the change in broadband colours from IMF to several versions of the IGIMF is smaller than the galaxy-to-galaxy scatter of colours. The O-star content of our Milky Way is significantly altered by the effects of clustered star formation, but the exact number that e.g. GAIA (Perryman et al., 2001) will observe depends on various other uncertain quantities. If the IGIMF indeed significantly deviates from the IMF (which depends on the unknown low mass behaviour of the star cluster mass function), then the metal content of galaxies is the most promising discriminator between (IG)IMFs.

1.5 The (near) future

The studies described in this thesis do answer some open questions in the field of galaxy formation, but are by no means final answers to the large open questions. Many of the simulated properties of galaxies do not correspond to observations and many of the physical processes in the simulations are highly (over-) simplified. In the near future much progress can be made on both the computational and the observational side of this topic. Whereas numerical models will become ever more sophisticated (due to the availability of more computing power and due to an improvement of software), observations with the new and upcoming observational facilities like JWST, ALMA, LOFAR, E-ELT and many others will shed new light on the state of galaxies and larger scale structures in the near and distant Universe.

2

Physical properties of simulated galaxies from varying input physics

Abstract

We investigate the baryonic properties, such as stellar mass, (specific) star formation rate, gas consumption time scale, and gas fraction, of haloes at redshift two using a large set of high-resolution cosmological simulations from the *OWLS* project. We vary the sub-grid models for radiative cooling, reionization, the pressure of the unresolved multiphase ISM, star formation, feedback from massive stars and AGN, as well as the cosmology, box size and numerical resolution. While reionization and metal-line cooling are important for low- and high-mass haloes, respectively, galactic winds driven by feedback from star formation and/or accreting black holes determine the main properties of galaxies. The star formation rate is regulated through the ejection of gas by galactic winds. The gas fraction, and thus the star formation rate, adjusts until the (time averaged) rate at which energy/momentum are injected is sufficient to balance the accretion, which is itself determined by cosmology and cooling. Consequently, the assumed star formation law affects the gas fractions, but not the star formation rates. The predictions are sensitive to variations in the sub-grid implementation of galactic outflows, even if the energy per unit stellar mass is fixed. Feedback becomes inefficient if the initial wind velocity falls below a minimum value that increases with the pressure of the ISM and hence with halo mass. In galaxies from which winds do not escape, the pile up of newly formed metals results in catastrophic cooling and strong star formation. Our results suggests that a wide range of stellar mass functions could be produced by varying the initial wind velocity and mass loading with halo mass. In fact, even without such tuning many of our models predict stellar mass functions that agree with the observations. Reproducing the high values of the observed specific star formation rate appears, however, to be more difficult. In particular, the efficient feedback required to reproduce the mass function results in much lower specific star formation rates than observed.

2.1 Introduction

The formation of structure in the dark component of the Universe is reasonably well established by means of high resolution gravitational N -body simulations (e.g. Springel et al., 2005). The large-scale structure statistics derived from these gravity-only simulations agree very well with observations. The formation and evolution of galaxies is, however, much less well understood. Modeling the baryonic component is much more difficult than simulating the dark matter due to the collisional nature of the gas and the wealth of phenomena that need to be taken into account (cooling, star formation, feedback, etc.).

There are two popular approaches to tackle this challenging task. In semi-analytic models, analytic descriptions of the behaviour of the baryonic component, as a function of the dark matter halo mass, merging history and environment, describe the evolution of gas and stars (e.g. Kauffmann et al., 1999; Somerville & Primack, 1999; Croton et al., 2006; De Lucia et al., 2006; Fontanot et al., 2006, 2007; Monaco et al., 2007; De Lucia & Blaizot, 2007; Somerville et al., 2008; Bower et al., 2008). The freedom to choose functional forms and parameter values combined with the ability to run large numbers of models, ensure that reproducing observations is usually within reach. While this approach has great advantages, such as the ability to make mock galaxy surveys that are sufficiently realistic to reveal observational biases, there are also significant drawbacks. The large number of parameters can make it difficult to identify the key physical processes. More importantly, the ability to reproduce observations with a model that uses unphysical functional forms or unrealistic parameter values to describe physical processes can easily result in erroneous conclusions and misplaced confidence.

The other approach is to follow both the dark matter and the baryonic components by direct simulation. While the dark matter is nearly always simulated using particles, the baryons can either be modeled with Eulerian methods (discretizing the volume in an (adaptive) grid, Ryu et al., 1990; Cen et al., 1990; Cen & Ostriker, 1992; Gnedin, 1995; Bryan & Norman, 1998; Teyssier, 2002; Gottlöber & Yepes, 2007) or using the Lagrangian approach also used for the dark matter (discretizing the mass using particles, e.g. Evrard, 1988; Hernquist & Katz, 1989; Thomas & Couchman, 1992; Steinmetz & Mueller, 1993; Couchman et al., 1995; Serna et al., 1996; Shapiro et al., 1996; Steinmetz, 1996; Katz et al., 1996; Tissera et al., 1997; Dave et al., 1997; Springel & Hernquist, 2003a,b; Oppenheimer & Davé, 2006; Davé & Oppenheimer, 2007; Oppenheimer & Davé, 2008; Schaye et al., 2010). Here, the freedom is limited to the parametrization of unresolved sub-grid processes, principally outflows driven by feedback from star formation. The high computational expense associated with full numerical simulations prevents thorough explorations of parameter space. Together with the reduced level of freedom,

this means that numerical simulations tend to be less successful in reproducing observations of galaxy populations than semi-analytic models. Compared with the semi-analytic method, the advantages of the simulation approach include the much reduced (though still present) risk of getting the right answers for the wrong reasons, the ability to ask more detailed questions due to the tremendous increase in resolution, and the fact that not only galaxies, but also the intergalactic medium is modeled.

As many processes related to the baryons are not (well) resolved by even the highest resolution simulations, they are dealt with in the so-called sub-grid models. Among these are radiative cooling (e.g. Sutherland & Dopita, 1993; Wiersma et al., 2009a), the temperature and pressure of the multiphase gas at high densities (in the rest of the paper loosely called ‘the ISM’) and the formation of stars (e.g. Katz et al., 1996; Springel & Hernquist, 2003a; Schaye & Dalla Vecchia, 2008), the energy and momentum fed back by these stars into the ISM/ICM/IGM (e.g. Springel & Hernquist, 2003a; Dalla Vecchia & Schaye, 2008), stellar mass loss (e.g. Tornatore et al., 2007; Wiersma et al., 2009b) and the growth of supermassive black holes and associated feedback processes (e.g. Sijacki & Springel, 2006; Sijacki et al., 2007; Booth & Schaye, 2009).

In this work, we will use large, cosmological, hydrodynamical simulations to investigate a number of basic baryonic properties of haloes, including the (specific) star formation rate, stellar mass, gas and baryon fraction. In this way we will get a handle on the physical processes that determine the properties of galaxies and on the importance of the freedom that arises from choosing particular sub-grid models. As reproducing observations is not our main goal at this stage, we have not attempted to fine-tune our models or to optimise the sub-grid implementations.

We make use of the large suite of smoothed particle hydrodynamics (SPH) simulations from the *Overwhelmingly Large Simulations* project *OWLS* (Schaye et al., 2010). The large variety of input physics in the different runs, as well as the possibility to study the detailed numerical convergence of the results, enables us to investigate properties of haloes and their relation to the physical and numerical parameters. In the sub-grid models the philosophy is taken to keep it as simple as possible, and where possible the parameters are calibrated by observations. In particular, we will test several implementations of galactic winds, we will investigate the importance of metal-line cooling, and we will vary the treatment of the unresolved, multiphase interstellar medium, the star formation laws, the cosmological parameters, the stellar initial mass function, and the reionisation history. One implementation of AGN feedback will also be compared to the other models (for a comparison of several AGN models in the context of the *OWLS* suite, see Booth & Schaye, 2009).

This work complements that of Schaye et al. (2010), where we introduced the

simulations and compared the cosmic star formation histories predicted by the various models. The global star formation rate can be decomposed into a dark matter halo mass function, which is determined by the cosmology, and the statistical distribution of the star formation rate as a function of halo mass. Here we will study the latter, which is astrophysically more relevant than the global star formation rate as it removes the main effect of cosmology (the mass function) and allows us to investigate how the various baryonic processes vary with mass. Whilst we will add a dimension to the work of Schaye et al. (2010) by investigating the dependence on mass, we will remove another one in order to keep the scope of the study manageable. Thus, we will limit ourselves to $z = 2$ and to the high-resolution series presented in Schaye et al. (2010) (these runs were halted at this redshift). To get further insight, we will study many more properties of galaxies than the star formation rate. We will also study the stellar mass function which, however, does depend on the cosmology.

The structure of this chapter is as follows. In Section 2.2 we will describe the main features of our reference simulation, which serves as the baseline for the comparison between models, we describe how we select galaxies and we give an overview of the results. We elaborate on the physics variations in the subsequent Sections, where we discuss variations of cosmology (Sect. 2.3), metal-line cooling (Sect. 2.4), reionization (Sect. 2.5), the equation of state for high-density gas (Sect. 2.6), the star formation law (Sect. 2.7), the stellar initial mass function (Sect. 2.8), supernova feedback (Sect. 2.9), and AGN feedback (Sect. 2.10). After reading Section 2.2, all the other section can be read or skipped, depending on the readers' interests. Section 2.11 summarizes the conclusions. In Appendix 2.11 we present the tests showing the numerical convergence of our simulations, while Appendix 2.11 shows that the amount of energy and momentum inserted in the winds in the momentum driven wind models of Section 2.9.4, which are themselves taken from Oppenheimer & Davé (2006, 2008), is higher than what is available from either SN explosions or radiation pressure.

2.2 Numerical techniques

For a detailed discussion of the full set of *OWLS* models we refer the reader to Schaye et al. (2010). Here we will briefly summarize the reference simulation, its relevant numerical properties and the we will make some general notes on the physical properties we will show in all subsequent sections, which describe variations of the sub-grid models.

Table 2.1: Overview of the cosmological parameters of WMAP3 (*OWLS* reference) and WMAP1 (as used in the Millennium Simulation). Symbols have their usual meaning.

	WMAP3	WMAP1
Ω_m	0.238	0.25
Ω_b	0.0418	0.045
Ω_Λ	0.762	0.75
σ_8	0.74	0.9
n	0.951	1.0
$h = H_0 / (100 \text{ km s}^{-1} \text{ Mpc}^{-1})$	0.73	0.73

2.2.1 Overwhelmingly Large Simulations

The simulations are performed with an extended version of the N-Body Tree/SPH code `GADGET3` (last described in Springel, 2005) in periodic boxes of 25 and 100 comoving $h^{-1}\text{Mpc}$. There are 512^3 dark matter and equally many baryonic particles (which can be either collisionless ‘stars’ or collisional ‘gas’ particles). The particle mass of the highest resolution simulation under consideration (25 $h^{-1}\text{Mpc}$ box size, 2×512^3 particles) is $8.68 \times 10^6 M_\odot$ for dark matter and $1.85 \times 10^6 M_\odot$ for baryons (initially, the baryonic particle masses change in the course of the simulation due to mass transfer from star particles to gas particles). The gravitational softening length initially is fixed in comoving coordinates at $1/25$ the inter-particle spacing. Below $z = 2.91$ the softening is fixed in proper units, at $0.5 h^{-1}\text{kpc}$.

Initial conditions are generated with `CMBFAST` (Seljak & Zaldarriaga, 1996) and evolved forward in time from an initial glass-like state using the Zel’Dovich (1970) approximation to $z = 127$, where the simulation is started. The cosmology assumed is summarized in Table 2.1 and is deduced from the WMAP 3 year results (Spergel et al., 2007). The results are largely consistent with the more recent WMAP5 results (Komatsu et al., 2009), the most notable difference is in σ_8 , which is 1.6σ lower in WMAP3 than in WMAP5. The primordial helium mass fraction is set to 0.248

As the subgrid model variation is the main power of the *OWLS* suite, we will now describe the parameters and subgrid models used in the reference simulations. The next sections will be devoted to descriptions of the variations of the sub-grid models and how the different input physics affects the resulting galaxy population.

In the simulation radiative cooling and heating are calculated element-by-element by explicitly following the 11 elements H, He, C, N, O, Ne, Mg, Si, S, Ca and Fe in the presence of the Cosmic Microwave Background and the Haardt & Madau (2001) model for the UV/X-ray background radiation from quasars and

galaxies, as described in Wiersma et al. (2009a). Note that the gas is assumed to be optically thin and in photo-ionization equilibrium.

At sufficiently high pressures, deep inside haloes, we expect the gas to be composed of several phases, ranging from hot/warm tenuous gas to cold, dense molecular clouds. This high density, multi-phase interstellar medium (ISM) is not resolved (and our simulations lack the physics to describe it). The formation of a cold phase and instabilities to form stars require a physical hydrogen number density of $n_{\text{H}} > 10^{-1} \text{ cm}^{-3}$ (Schaye, 2004) and particles with such densities are put on a polytropic effective equation of state (EoS). Their pressure $P \propto \rho^{\gamma_{\text{eff}}}$, where γ_{eff} is the polytropic index and ρ is the physical proper mass density of the gas. We use $\gamma_{\text{eff}} = 4/3$, such that both the Jeans mass and the ratio of the Jeans length and the SPH kernel are independent of the density, thus preventing spurious fragmentation due to a lack of numerical resolution (Schaye & Dalla Vecchia, 2008). The normalization of the polytropic equation of state is such that the energy per unit mass corresponds to 10^4 K for atomic gas with primordial abundances at the star formation threshold ($P/k = 1.08 \times 10^3 \text{ K cm}^{-3}$ for $n_{\text{H}} = 10^{-1} \text{ cm}^{-3}$). Star formation is followed stochastically, with a pressure dependent star formation rate, obtained from the observed Kennicutt-Schmidt law (Kennicutt, 1998a) and local hydrostatic equilibrium, as discussed in Schaye & Dalla Vecchia (2008). Gas particles are only allowed to form stars when they are on the EoS, so there is a threshold density for star formation of $n_{\text{H}} > 10^{-1} \text{ cm}^{-3}$.

The mass loss of the gas by AGB stars and by Type Ia and Type II (including Type Ib,c) supernovae is followed explicitly for the 11 elements needed for the cooling, as described in Wiersma et al. (2009b). The star particles are assumed to be simple stellar populations (SSPs) with a Chabrier (2003) initial mass function (IMF). The energy feedback from massive stars and supernovae is implemented kinetically, giving a number of SPH neighbours of newly formed stars a kick with a velocity of 600 km s^{-1} . The number of particles receiving such a kick is set by the dimensionless mass loading factor η , which is the amount of mass kicked in the wind per unit solar mass of stars formed. We use $\eta = 2$, which together with the chosen velocity corresponds to about 40% of the energy available from supernovae of type II (including Ib,c), for our assumed Chabrier (2003) IMF. For details on the kinetic wind implementation, see Dalla Vecchia & Schaye (2008).

2.2.2 Halo identification

Haloes are identified using a Friends-of-Friends (FoF) algorithm, linking together all dark matter particles which are closer to each other than the linking parameter ($b = 0.2$ times the mean inter-particle distance). FoF identifies iso-overdensity contours of $\delta \equiv (\rho - \bar{\rho})/\bar{\rho} \approx 3/(2\pi b^3) \approx 60$ (Lacey & Cole, 1994). Outside these

contours, due to particle noise, some regions will also be selected as haloes. These haloes will be excluded by the particle number cuts we will make further on, as motivated by the convergence tests. Baryonic particles are linked to their nearest dark matter particle and belong to the same group, if any.

Following the convergence tests presented in Appendix 2.11, we only include haloes that contain at least 100 star particles when looking at halo properties as a function of stellar mass. We use a minimum of 2000 dark matter particles when we plot properties against halo mass. These two cuts produce nearly identical halo samples in the reference simulation and ensure that only well resolved haloes are considered.

Whenever we show the correlation between two halo properties, the plot consists of lines that connect the medians of bins, evenly spaced in the quantity plotted along the horizontal axis, if there are at least 30 points in that bin. If not, then the next bin extends to include the first next 30 objects. The last bin may contain between 0 and 30 objects. We bin the data starting from the high mass end. There, the difference in mass for two consecutive haloes is much bigger than at the low mass end, and in this way we are sure that the value of the mass at the high mass end of the plots is always the mean of the mass of the 15th and 16th most massive systems.

2.2.3 Physical properties

In subsequent sections we will study the relations between several physical properties of haloes. Simulations will be compared in sets that vary in only one aspect (e.g. only varying supernova feedback, or only varying the physics related to high density gas and star formation). The reference model (denoted *REF* and described in Sect. 2.2.1) will always be plotted as a black solid line, in order to intercompare the sets. The *REF* model serves as a baseline for our exploration of parameter space, but it should not be regarded as our ‘best model’. For a more detailed description of the physics in the simulations we refer to Paper I. We will keep to the same order of model variations in Paper I for easy comparison. All sections will start with a summary of the models which should be sufficient to understand the discussion, but for more details we refer the reader to Paper I.

A graphical representation of the gas density of a galaxy formed in a representative set of models is shown in Fig. 2.2.2. The galaxy resides in a halo of total mass $\sim 10^{12.5} M_{\odot}$. It was first identified in the ‘*REF*’ simulation, where its position (centre of mass of all particles within 10% of the virial radius) is determined. The line of sight is along the z-axis, which is almost perfectly aligned with the angular momentum vector of the gas within 10% of the virial radius ($\cos(\phi) = 0.994$). For the other simulations the image is centered on the same position, showing the re-

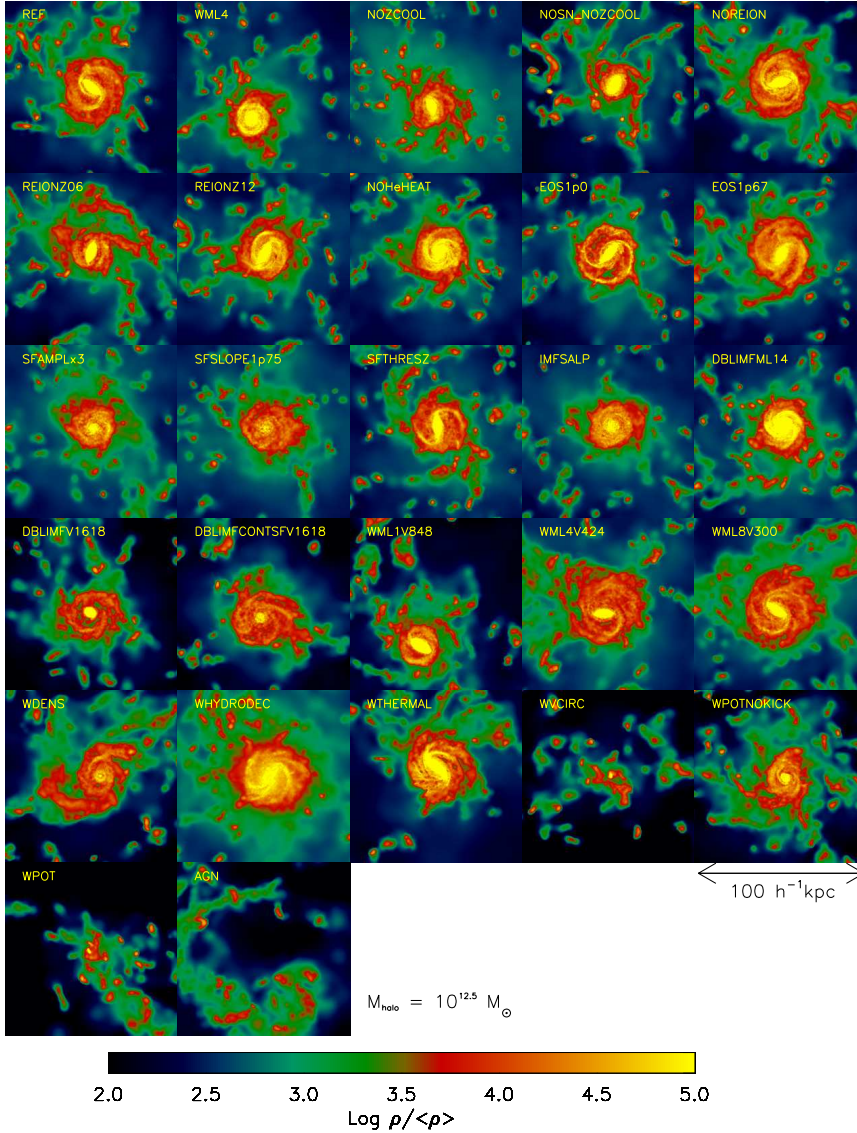


Figure 2.1: A graphical representation of a galaxy in a halo of $10^{12.5} M_{\odot}$ in 20 of our simulations at redshift 2. The colour coding denotes the gas density divided by the mean density of the universe. All frames are 100 comoving kpc/h on a side and are centered on the position of the galaxy in the ‘REF’ simulation. The gas density in a 100 comoving kpc/h box is projected. The orientation of the line of sight is along the z-axis, which is almost perfectly aligned with the angular momentum vector of all material inside 10% of the virial radius of this galaxy in the ‘REF’ simulation.

markable similarity in the positions and orientations of the galaxies. The ‘*MILL*’ simulation, as described below, was run with another cosmology, resulting in a different distribution of galaxies over the volume. This model was therefore left out.

In Fig. 2.2 we include all physics variations and plot 9 combinations of physical properties. The black line is the reference model from which we vary the input physics. In subsequent sections we will discuss sets of simulations which vary the input physics in some specific way. The upper two rows have halo mass on the horizontal axis, while the lower three panels show some properties as a function of stellar mass. Note that the upper six and lower three panels obey different resolution limits, as explained in Appendix 2.11. Fig. 2.2 shows the reference model in black and all other simulations in grey, such as to provide an idea of how much the different relations diverge in the different models. The remainder of this section gives some background on the panels where necessary. For every set of physical properties that will be discussed in the following sections we will use the same panels.

2.2.4 Properties as a function of halo mass

Panel (A) shows the stellar mass as a function of halo mass, which mainly serves as a way to connect the panels that have halo mass on the horizontal axis (A – F), to panels that have stellar mass on the horizontal axis (G – I). Panel (F) shows the stellar mass fraction of haloes as a function of their total mass and contains the same information. Dividing by the halo mass, though, emphasizes the differences between the models, because the stellar mass and total mass are tightly (and almost linearly) correlated.

In panel (B) we show the star formation rate of haloes as a function of their total mass. As we show in Fig. 2.2 the SFRs span slightly more than an order of magnitude at the high halo mass end, and less than an order of magnitude at the low mass end (except for the simulation without feedback and metal-line cooling). At the high mass end, the simulations with weak feedback (as described in Section 2.9) are the ones with the highest SFR, while the simulations showing a low SFR have either very efficient SN feedback, or AGN feedback.

In all panels (C) we plot the baryon fractions of the halo as a function of halo mass. We over-plot the universal baryon fraction (Ω_b/Ω_m), as appropriate for our default cosmology. Without feedback and metal-line cooling (which we will show separately in Fig. 2.4), the baryon fraction is very high, at around the universal value. Effective feedback sets the fractions well below the universal value, by factors up to 6 below it as can be seen in Fig. 2.2.

Most of our simulations show baryon fractions that are lower, and depend more

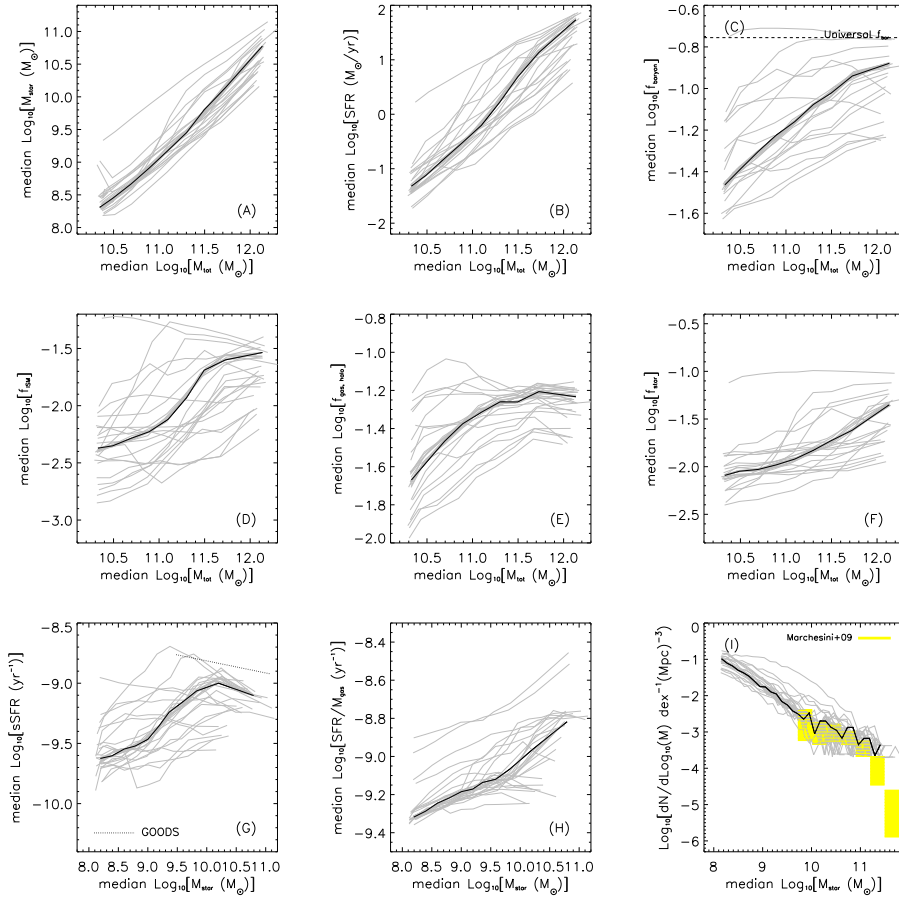


Figure 2.2: Median relations between halo properties in all the simulations described in this work. The reference model is shown in black and all other models are shown in grey. In subsequent sections we will consider sets of simulations in more detail. On the top two rows we show the halo mass as a function of stellar mass (panel A), star formation rate (panel B), baryon mass fraction (panel C), fraction of mass in the ISM (panel D), fraction of mass in other gas in the halo (panel E) and stellar mass fraction (panel F). The last three (second row) and up to the total baryonic mass fraction shown in panel (C). The last row shows stellar mass versus specific star formation rate (panel G), inverse of the gas consumption time scale (panel H) and the number density (the stellar mass function, panel I). We show medians in bins along the horizontal axes as described in the text for all haloes that satisfy the convergence criteria that apply to that specific panel.

strongly on mass, than those found by Crain et al. (2007). Those simulations included no cooling, no star formation and no feedback processes, making the results hard to compare directly. Our simulation without cooling and without feedback has a baryon fraction that goes above the universal value, whereas Crain et al. (2007) always stays below, at roughly 90% (unless the gas is preheated, then they do find a strong evolution with mass, as we do). Note, though, that we *do* include cooling from hydrogen and helium and star formation, whereas Crain et al. (2007) do not.

Panels (D) and (E) show the fraction of the mass that is in gas in the ISM and the rest of the gas in the haloes, respectively. In general, both are increasing functions of the total mass, although again some of the very inefficient feedback models show very high gas mass fractions in low mass haloes.

In the panels (F) we will look into the stellar mass fractions of haloes (the sum of the middle row panels, A through F, gives the upper right panel, C). As it will turn out, the stellar mass fractions tell us how well star formation is suppressed by the feedback model under consideration, whereas the baryon fractions of the haloes show a distinction between feedback models which remove gas from the ISM and models that remove the gas from the halo altogether.

2.2.5 Properties as a function of stellar mass

The integral of the SFR over time until the moment under consideration ($z = 2$ in this case) gives a stellar mass. Relations between SFR and stellar mass are not so well converged as those with halo mass (see Appendix 2.11). In higher resolution simulations the stellar mass that builds up is higher, because the star formation is well resolved already at earlier epochs (under-resolved star formation underestimates the SFR). The relations between stellar mass and SFR are very similar to the relations between halo mass and star formation rates (we do not show them). One notable difference occurs between the simulations without feedback and metal-line cooling. The much higher SFR in the simulation without feedback has resulted in the build-up of galaxies with very high stellar masses.

The specific star formation rate

An often used observational parameter is the specific star formation rate (sSFR), defined as the star formation rate divided by stellar mass. It basically is the inverse of the time needed to form the current stellar population with the current star formation rate. As colours of galaxies mainly measure the relative fraction of old to young stars (due to the different spectral regimes they shine in), the colour of a galaxy usually is a good measure of its sSFR (averaged over the recent past). In many previous studies the sSFR is used to distinguish starbursts from quiescently

star forming galaxies (comparing the sSFR to some other time scale, usually the Hubble time).

A good reason to look at sSFR instead of SFR is the almost linear relationship between stellar mass of haloes and their SFR, as we will show below. Dividing out the stellar mass removes the linear dependence and highlights deviations from this relation. Note that in a plot of sSFR against stellar mass there is no more information than in the plot of SFR against stellar mass.

The observations we will compare to are taken from Daddi et al. (2007), who measured the obscured and unobscured star formation by taking SFRs from the UV and IR together. They did this for *K*-selected *sBzK* galaxies (star forming, see Daddi et al., 2004) in the GOODS fields at $z \sim 2$. The median of the SFR as a function of stellar mass is well fit by $\text{SFR} = 250 \cdot (M_*/10^{11} M_\odot)^{0.9}$, and the scatter is constant at about 0.2 dex. The scatter is not shown in the Figure, but is similar, although a bit smaller (~ 0.1 to 0.15 dex) in the simulations. Both the stellar masses and the star formation rates need to be converted to our cosmology and IMF, as explained in Sect. 2.2.5. The (cosmology and IMF corrected, see below) data from the GOODS fields of Daddi et al. (2007) have been transformed to sSFR instead of SFR. We plot the observed relation only on the mass range that actually is observed: $5 \times 10^9 M_\odot < M_{\text{star}} < 2 \times 10^{11} M_\odot$. Halo mass is much harder to observe than stellar mass and/or SFR (which usually come from SED modeling). Therefore we only show the specific star formation rate as a function of stellar mass.

As can be seen from panel (G) of Fig. 2.2 the medians of the sSFR of haloes span only a limited dynamic range of about an order of magnitude and are all lower than the observed relation, except for a very small range of stellar masses in simulations with inefficient feedback at these masses (see Section 2.9).

The slope in the relation between stellar mass and the specific star formation rate of a galaxy seem only to agree with the observations of Daddi et al. (2007) on mass ranges where the feedback is inefficient (either in simulations without feedback, or in the high mass haloes of simulations with relatively low wind velocities) and in the simulation with thermal supernova feedback. In simulations with ineffective feedback the slope in the sSFR– M_* relation is negative, and even steeper than in the observations, while the simulation without feedback (and without metal-line cooling) shows a very similar slope to observations over a large range of masses (panel (G) of Fig. 2.4). The difference in normalization between the observations and our simulations may be due to the stellar masses in the simulations being too low (as star formation is only resolved at relatively low redshift), by the simulated star formation rates being too low or by the observed SFRs being too high. Besides, there may be systematics in the observations as well.

In the simulations with very strong feedback, either due to high wind veloci-

ties or to the inclusion of AGN, the specific star formation rates tend to become relatively independent of stellar mass. For these strong feedback models, the discrepancy in normalization between the observed and simulated star formation rates at given stellar mass are largest, though.

The agreement between observations and simulations without effective feedback in the slope of the relation is at odds with common tendency to invoke very effective stellar feedback in low mass haloes in semi-analytic models (e.g. Cole et al., 1994; Somerville & Primack, 1999; Cole et al., 2000; De Lucia et al., 2004) and simulations (e.g. Katz et al., 1996; Springel & Hernquist, 2003a) in order to fit the faint end of the luminosity function of galaxies in the local universe .

The gas consumption time scale

As star formation is expected to be more strongly influenced by the amount of available gas than by the amount of stars already formed, we define a second type of specific star formation rate, now normalizing the SFR by the mass in star forming gas. This is the inverse of the time needed to convert the present reservoir of star forming gas (i.e. gas that is on the equation of state) into stars with the present star formation rate, i.e. the inverse of the ‘gas consumption time scale’. We plot the inverse of the gas consumption time scale as a function of stellar mass in panel(H).

Comparing simulations to observations

To correct observationally inferred stellar masses and SFRs from the cosmology assumed in the literature to our cosmology, we multiply them by the square of the ratio of luminosity distances [$d_{L,\text{our cosm}}(z)/d_{L,\text{obs cosm}}(z)$]. The subscripts ‘our cosm’ and ‘obs cosm’ denote our cosmology and the cosmology under which the observations are transformed into masses/SFRs, respectively.

The IMF assumed for the observations of the SFR we will compare our simulations to was the Salpeter (1955) IMF, whereas our stellar masses and SFRs are based on the Chabrier (2003) IMF. We therefore divide the observationally inferred SFRs by a factor 1.65, which is the asymptotic (reached after only 10^8 yr) ratio of the number of ionizing photons predicted by Bruzual & Charlot (2003) for a constant star formation rate. For comparison, the correction factor is ~ 7 for the top-heavy IMFs used in starburst models (see Sect. 2.8.2). This top-heavy IMF is, however, really extreme.

For stellar masses, the IMF conversion factor is more sensitive to the age of the population and the observed rest-frame wavelength. As the light in most wavelength bands is dominated by massive stars and the high mass end of both the Salpeter and Chabrier IMFs are power laws with very similar power law indices,

we use the same factor of 1.65 as we used for the SFRs. For very old populations observed in red wavelength bands (tracing stellar continua, rather than dust emission) the conversion factor should be different. We verified that the K-band mass-to-light ratio is about a factor 1.65 smaller for a Chabrier than for a Salpeter IMF for SSPs and constantly star forming populations, for the full range of ages and metallicities available in the Bruzual & Charlot (2003) population synthesis package. We therefore also divide by a factor of 1.65 to convert stellar masses from the Salpeter to the Chabrier IMF.

In all panels (I) we will look at the number densities of galaxies as a function of their present day stellar mass at redshift 2. We bin the galaxies in 30 equally spaced bins in $\log M_*$, between the lowest resolved halo mass (containing 100 star particles, as the convergence tests allow us, see Appendix 2.11) and the highest available stellar mass in the simulation. The resulting stellar mass functions (MFs) are shown in panels (I). Over-plotted is an observed MF from a combined sample, using the deep near-infrared Multi-wavelength Survey by Yale-Chile, the Faint Infrared Extragalactic Survey and the Great Observatories Origins Deep Survey-Chandra Deep Field South surveys, as presented by Marchesini et al. (2009), also at $z = 2$.

In their paper, Marchesini et al. (2009) do a careful job in investigating all kinds of random and systematic errors. Here, we compare to their $1/V_{max}$ method results, including all uncertainties, but we leave out the bottom-light IMFs that they test. The reason for this is that they dominate the systematic errors and are more extreme assumptions than the variations in the other quantities. Also, for bottom-light IMFs there are only arguments at high redshift (Davé, 2008; van Dokkum, 2008; Wilkins et al., 2008a), and the interpretation of the observations are full of uncertainties themselves. The sources of random errors include poisson errors on the number counts, cosmic variance and the random errors from the use of photometric redshifts. These random errors are added in quadrature. To these random errors we linearly add the maximum of the systematic errors in the same mass bin, as Marchesini et al. (2009) did. The systematic errors include the systematic component in the errors from photometric redshifts, errors arising from different population synthesis packages (they test for Bruzual & Charlot, 2003; Maraston, 2005; Charlot & Bruzual, 2009) varying the metallicities of the stellar populations and the use of different extinction curves (Milky Way from Allen 1976, SMC from Prevot et al. 1984; Bouchet et al. 1985 Calzetti et al. 2000).

The correction factor for the IMF is very small, as the IMF used in the observational study is a diet Kroupa IMF. From Marchesini et al. (2009) we take the correction factor from Salpeter to the diet Kroupa: 1.6. With the factor between Salpeter and Chabrier (our IMF) of 1.65, the correction factor for stellar masses here is $1.65/1.6 = 1.03$ (diet Kroupa being slightly more massive for the same

observed luminosity). As this number is also derived from population synthesis packages, which come along with their own uncertainties we chose not to convert masses for the difference in IMFs. We do correct the masses for the difference in luminosity distances as described earlier. Number densities also need to be converted, as the volume at a given redshift is different for different angular diameter and comoving distances. Therefore, the number density (ϕ_*) is corrected for the ratio of volume elements (at the redshift under consideration, it is a function of the cosmological parameters given in Table 2.1). All numbers are given in natural units, without factors of the Hubble parameter, just as in Marchesini et al. (2009).

The resulting $1/V_{max}$ estimate of the analysis of Marchesini et al. (2009) is shown in the yellow shaded regions in all panels (I). We interpolated their values, as $z = 2$ is exactly on the boundary between two of their redshift bins ($1.3 < z < 2$ and $2 < z < 3$, respectively). We weigh the averaging to the sizes of the redshift intervals (weight 1.2 and 0.8 respectively), which results in parameters very consistent with $z = 2$ results of the Newfirm Medium-Band Survey (Marchesini et al. 2010, in prep.). The mass bins are not exactly the same in both redshift intervals either. The difference is very small. The upper mass limit of the most massive bin is the same and they use bins which are constant in $\log(M)$, of size 0.3 dex (at $1.3 < z < 2$) and 0.29 dex (at $2 < z < 3$), resulting in a difference of bin centre in the lowest mass bin 0.055 dex. We interpolate the mass bins in the same way as the errors, although using just either the low or high redshift mass bins instead would not make a noticeable difference. Note that we plot the logarithm of the number of galaxies per unit $\log M_*$, per unit volume.

As can be seen from panel (I) of Fig. 2.2 our mass functions fall well within the observed range, when all uncertainties are taken into account. This is true for a large sub-set of simulations, except some of the strongest feedback models (like the double IMF models in Fig. 2.9, the high constant wind velocity of Fig. 2.10, some of the momentum-driven wind models in Fig. 2.14 and AGN feedback in Fig. 2.15), which have too few very massive systems. Some very weak feedback models produce too many massive systems. At low masses it needs to be noted that our simulations go steeper than most faint end slopes of derived Schechter function parametrizations, but that this is largely outside the observed range of stellar masses.

Combining the results in panels (B) and (I) shows an interesting behaviour of the simulations: although the SFR is too low by a factor of a few, as compared to observations, we do form enough galaxies of all masses (and possibly too many low mass systems). A similar discrepancy, which may be related to the one highlighted here, is indicated by the works of Hopkins & Beacom (2006); Wilkins et al. (2008b), where they show that there is an internal discrepancy in measurements of the star formation rate density evolution and the build up of stellar mass density.

They conclude that the integral of the star formation rate results in a higher stellar mass than observed nowadays. One of many solutions is a possible overestimate of SFRs by a factor of a few. This would bring the observations and our simulations to much better agreement. See also Schaye et al. (2010) for a discussion on the integrated star formation properties of the simulations presented here.

2.3 Cosmology

Fig. 2.3

In order to investigate the dependence of the galaxy properties on cosmology, and to facilitate comparisons to earlier work, we vary the cosmology from the WMAP 3-year results (Spergel et al., 2007) to the so-called ‘concordance cosmology’ that was used in many previous studies including the Millennium Simulation (Springel et al., 2005). We will refer to this set of cosmological parameters as the ‘Millennium cosmology’ and denote the model assuming this cosmology ‘*MILL*’.

The main differences in the cosmologies is the value of σ_8 , which is 0.74 in our reference cosmology, but 0.9 in the other model, and the universal baryon fraction Ω_b which is 0.0418 in all our simulations, except in the ‘*MILL*’ simulation where it is 0.045. Other parameters are summarized in Table 2.1. In order to roughly match the peak in the observed global integrated star formation history the simulations with Millennium cosmology used a mass loading of $\eta = 4$ for the winds, rather than the $\eta = 2$ used in the reference model (Schaye et al., 2010). To isolate the effect of cosmology, we therefore compare it to a simulation with our default cosmology, but with a mass loading of $\eta = 4$ (‘*WML4*’), which then corresponds to about 80% of the available energy from SNe. In Fig. 2.3 the effect of the cosmology can be addressed by comparing the blue dashed and red dotted line, which correspond to the WMAP3 and WMAP1 (‘Millennium’) cosmological parameters (as indicated in Table 2.1), respectively.

σ_8 basically sets the time scale for structure formation: a higher σ_8 corresponds to earlier structure formation (e.g. Peebles, 1993). As the concentration at a given mass is set by formation time, SFRs could be influenced by the value of σ_8 , through different central densities. The two runs with different cosmologies (the red dotted and blue dashed line) assume the same wind energy per unit stellar mass (twice the energy assumed in the reference model, so 80% of the available supernova energy). The SFR of high mass haloes is slightly higher for the WMAP1 cosmology than for the WMAP3 cosmology, due to the different central densities at given mass, even if the feedback energy is the same. The much larger difference in the integrated star formation rate density of the universe, shown in Paper I is largely the effect of a different halo mass function at the same redshift. The larger number of haloes

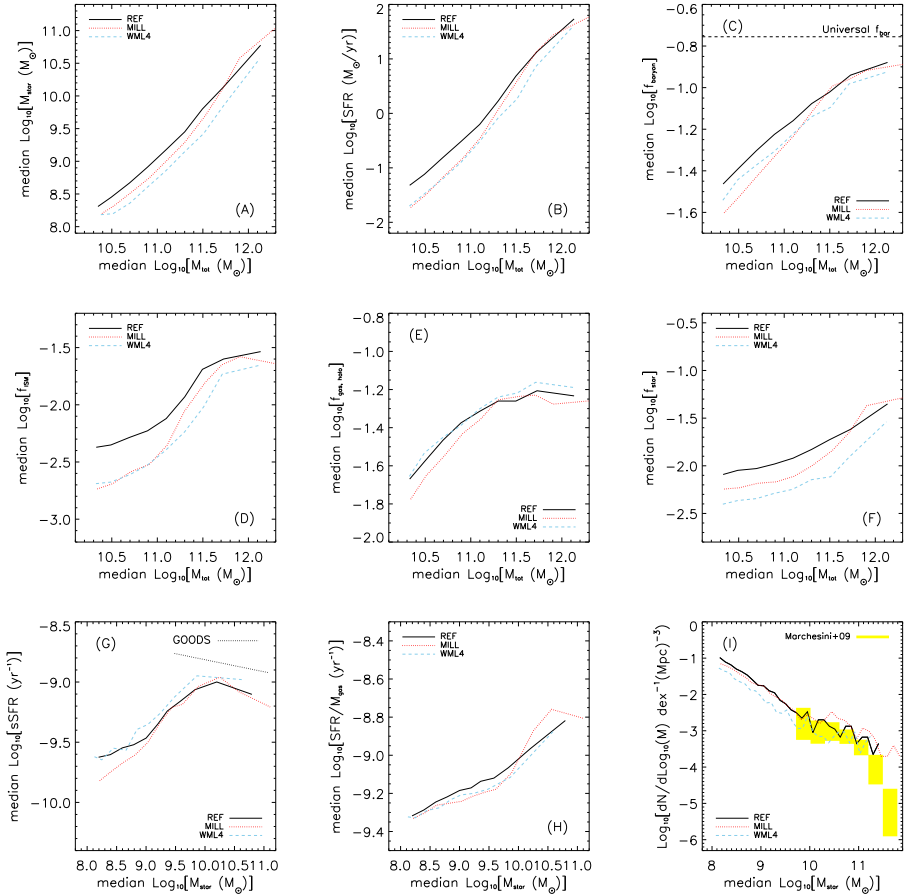


Figure 2.3: Like Fig. 2.2, but now only for a set of simulations in which the cosmology is varied from the WMAP three-year results, as in the reference model (black solid line), to the cosmology from the WMAP first year results (red dotted line), as they are used in the Millennium simulation. In the ‘*MILL*’ simulation the supernova feedback was implemented with a two times higher mass loading in the winds, so two times more energy in the winds. The ‘*WML4*’ (blue dashed line) run has the same cosmology as the reference model, but the same feedback as the ‘*MILL*’ model, so for the effect of the cosmology the red dotted line should be compared to the blue dashed, while a comparison of the black solid and the blue dashed line shows the effect of increasing the wind mass loading with a factor of two.

results in a much higher global SFR density for the model with higher σ_8 .

In the Millennium cosmology, the halo mass function is slightly higher than in our cosmology. This also holds for the stellar mass function, as shown in panel (I) and from panel (F) we learn that the stellar mass fraction as a function of halo mass is also higher (for models with the same feedback).

2.4 Metal-line cooling

Fig. 2.4

In this set of simulations we investigate what the effect is of cooling by metal lines. Simulations without any metal-line cooling are mostly affected in terms of gas cooling from temperatures of $\sim 10^{5-6}$ K, where the line cooling by metals is relatively efficient (e.g. Wiersma et al., 2009a). If gas shock heats to high temperatures while accreting onto galaxies, ignoring metal-line cooling will make it harder to cool down sufficiently to make it onto our artificial equation of state (see Section 2.6), where it is able to form stars. Metal-line cooling was turned off in the ‘*NOZCOOL*’ models. A galaxy formed in these models can be seen in Fig. 2.2.2. Turning off metal-line cooling reduced the extent of the gaseous disk in this massive system, as cooling the gas at high temperatures in the halo is less efficient.

Comparing the red dotted with the black solid curve (the reference model) in panel (B) of Fig. 2.4 shows the effect of metal-line cooling on the star formation rates of galaxies. In general, metal-line cooling increases the SFR, because cooling rates increase with increasing metallicities (e.g. Cox & Tucker, 1969; Sutherland & Dopita, 1993; Wiersma et al., 2009a). This difference increases with halo mass, because the fraction of gas that is accreted hot and the halo virial temperature both increase with mass. The cooling is more and more affected by metals (the cooling rates of heavier elements have a peak at higher temperatures) for haloes of higher mass and higher virial temperature.

The mass fraction in ISM gas, as shown in panel (D) of Fig. 2.4 also shows that the fraction of ‘cold’ ISM gas is drastically lower for high mass haloes without feedback, than with feedback. For the higher halo masses, for which the feedback is inefficient (see Section. 2.9), there is a difference in gas consumption time scales, as can be seen in panel (H): star formation is more efficient in the models with metal-line cooling than in the models without. For low stellar masses, the winds (and thus the newly created metals) easily escape the galaxy, such that the difference in gas consumption time scale vanishes.

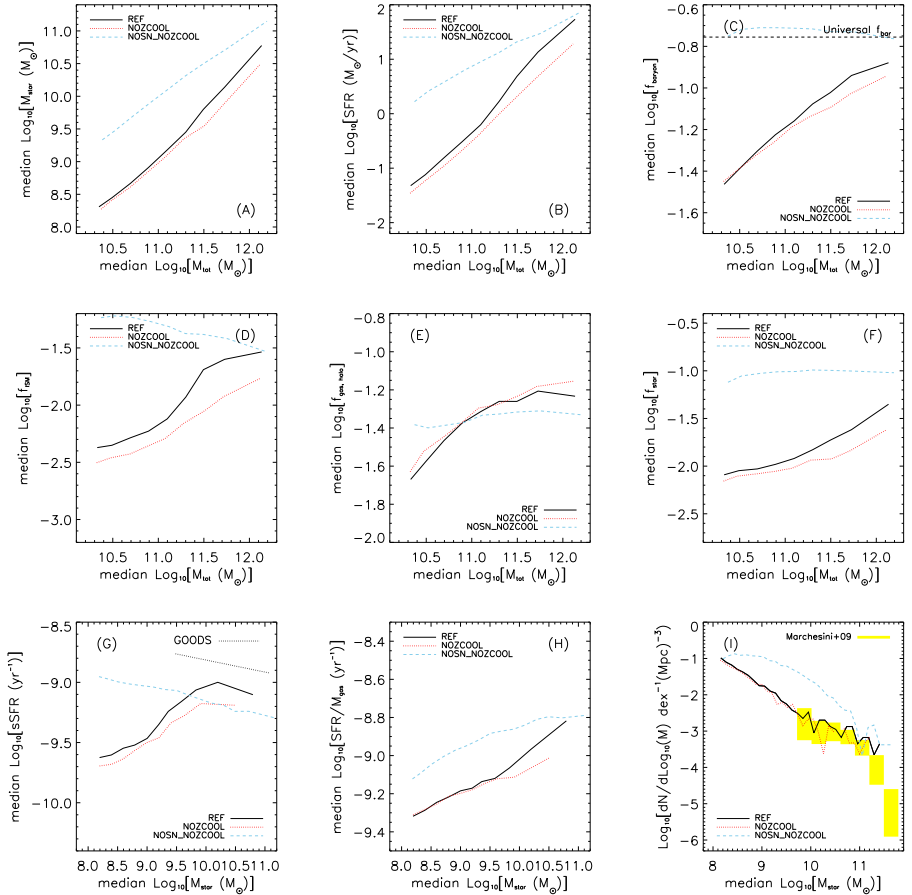


Figure 2.4: Like Fig. 2.2, but now only for a set of simulations in which the metal line cooling an/or the kinetic supernova feedback are turned off. The red dotted line shows the effect of turning of only metal line cooling, compared to the black line which shows the reference model. Turning off metal-line cooling and supernova feedback results in the relations shown by the blue dashed line. The effect of the supernova feedback is thus illustrated by the difference between the blue dashed and red dotted lines.

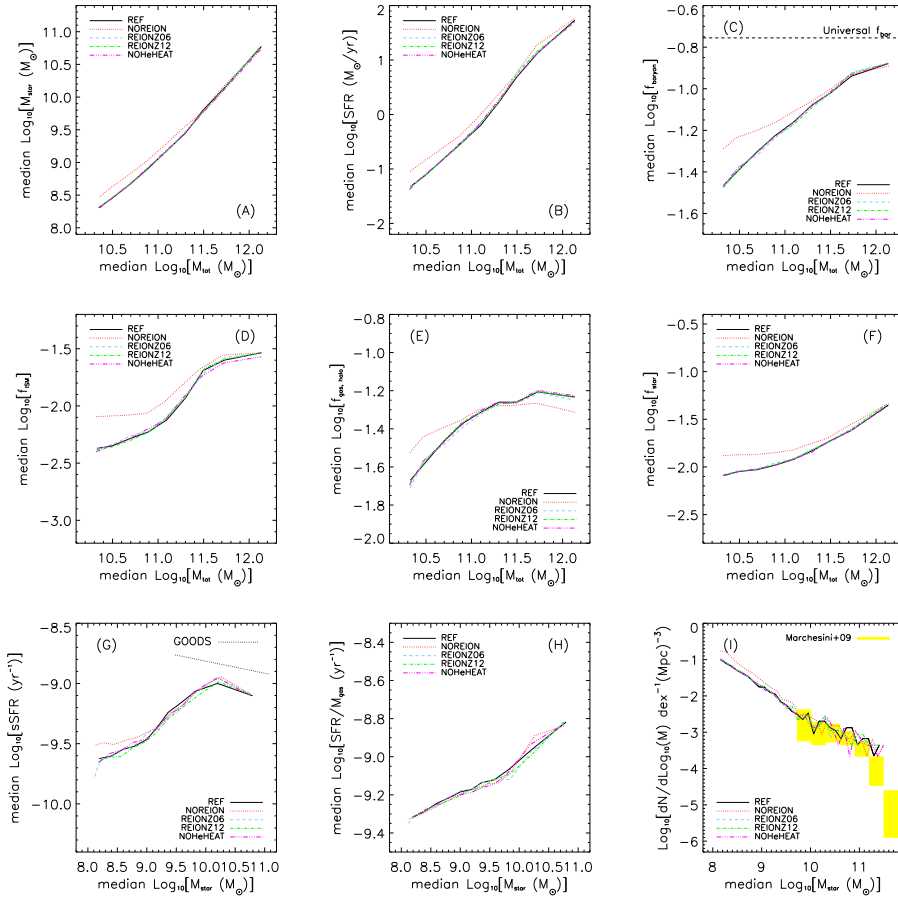


Figure 2.5: Like Fig. 2.2, but now only for a set of simulations in which the reionization implementation is varied. In the reference model (black solid line) the evolving uniform UV background is turned on at $z = 9$. The red dotted line shows a simulation that has no UV background at all, whereas in the blue dashed and the green dot-dashed lines the background is turned on at $z = 6$ and $z = 12$ respectively. The magenta dot-dot-dot-dashed line shows a simulation in which no extra heat input due to helium reionization around $z = 3.5$ is implemented.

2.5 Reionization variations

Fig. 2.5

Reionization is implemented by turning on the model for the UV background from galaxies and quasars of Haardt & Madau (2001). As shown in Wiersma et al. (2009a) the gas is quickly heated to $T \sim 10^4$ K following reionization. Note that we assume the UV background to be uniform and the gas to be optically thin. In our reference model we set the redshift of reionization to $z_r = 9$. To investigate the effects of reionization, we compare to a model without reionization (*'NOREION'*) and to two in which we have varied the redshift at which we turn on the UV background: one at redshift 12 (*'REIONZ12'*) and one at redshift 6 (*'REIONZ06'*). In *'NOHeHEAT'* we do not inject 2 eV per atom at around $z = 3.5$, as we do in our other models. This energy input is needed to match observationally inferred temperatures in very low density IGM gas. As this is only important for gas that mainly cools through adiabatic expansion, this extra input is not important in galaxies, as we will also show below.

The simple picture of the influence of reionization on the properties of haloes, is that gas residing in haloes with a virial temperature lower than $T_{\text{vir}} \sim 10^4$ K will be evaporated. The thermal energy of the gas is in that case higher than the gravitational potential energy of the haloes, so the baryons are not bound to the dark matter. In panel (E) of Fig. 2.5 we compare the gas fractions of haloes in the simulations with the various reionization models. Indeed, in low mass haloes the gas fraction is lower because of reionization. At high masses the gas fraction is slightly lower without reionization than with.

As shown in panel (B) of Fig. 2.5, the effect of reionization is indeed that in low mass haloes the SFR is suppressed (compare the reference model to the model without reionization). The amount of suppression decreases with increasing halo mass. Whether reionization happened at redshift 12, 9 (reference model) or 6, is no longer important at redshift 2.

The extra heat input due to Helium reionization is negligible at gas densities typical of haloes. The unimportance of Helium reionization holds for all properties of the haloes we will investigate in this work. We therefore conclude that the extra heat input to the IGM from helium reionization is only important for the temperature of the IGM and has no effect on the properties of haloes formed in the simulations.

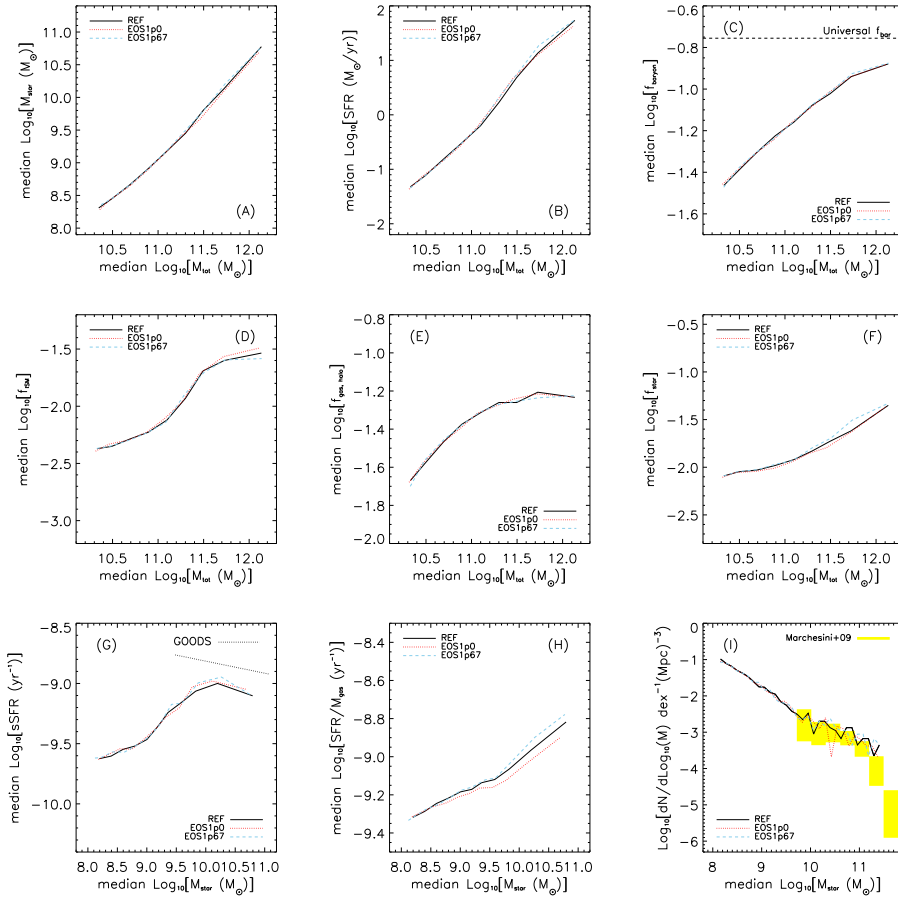


Figure 2.6: Like Fig. 2.2, but now only for a set of simulations in which the equation of state (EoS) for high density gas is varied. In the reference model (black solid line) we use a polytropic EoS with a power law index of $\gamma = 4/3$, because this is numerically convenient. The red dotted line shows the results from a simulation with a shallower (less stiff) EoS, with a power law index of 1 (isothermal). The blue dashed line is the result of a simulation with a stiffer equation of state: $\gamma = 5/3$.

2.6 The polytropic equation of state for high density gas

Fig. 2.6

Our simulations lack both the resolution and the physics to model the multiphase ISM. We therefore impose an effective equation of state (EoS) for all gas particles with densities higher than $n_{\text{H}} = 0.1 \text{ cm}^{-3}$.

As the effectiveness of feedback depends on hydrodynamic effects (mainly drag forces), as we will show later, the equation of state imposed on the high density gas may be important. Although the star formation histories of the isolated disk galaxies of Schaye & Dalla Vecchia (2008) do not strongly depend on the imposed EoS (provided that the star formation law works independently of the equation of state), the structure of the disk (among which the thickness) does.

All imposed EoS are polytropic: $P \propto \rho^{\gamma_{\text{eff}}}$. For the reference case, $\gamma_{\text{eff}} = 4/3$, both the Jeans mass and the ratio of the Jeans length and the kernel of the SPH particles are independent of the density, making it a numerically convenient choice. Two other EoS are implemented in other runs. The first one is an isothermal equation of state, $\gamma_{\text{eff}} = 1$ (*'EOS1p0'*), the other one is adiabatic, $\gamma_{\text{eff}} = 5/3$ (*'EOS1p67'*).

From the gas density distributions shown in Fig. 2.2.2 it is clear that stiffer equations of state pressurize the gas more strongly, resulting in a smoother distribution of gas. In Paper I it was already shown that the polytropic index had little influence on the total cosmic star formation rate density. In panel (B) of Fig. 2.6 we show that the relation between halo mass and SFR is unaffected by the polytropic index. Although the structure of the galaxies may be significantly altered (see Fig. 2.2.2), their integrated star formation properties are insensitive to the stiffness of the equation of state.

More generally, all physical properties of haloes (except for the gas consumption and star formation time scales) are very insensitive to changes in the polytropic index in the range of $1 - 5/3$. This also ensures that more complicated models for the multi-phase ISM will most likely not make haloes behave differently from what is shown in this paper.

2.7 The star formation law

Fig. 2.7

Star formation is implemented using a pressure law. It reproduces the observed star formation rate surface density - gas surface density law, the Kennicutt-Schmidt law (Kennicutt, 1998a): $\dot{\Sigma}_{*} = A(\Sigma_{\text{g}}/1 M_{\odot} \text{ pc}^{-2})^n$, with $n = 1.4$ and $A = 1.151 \times 10^{-4}$

CHAPTER 2. PHYSICAL PROPERTIES OF SIMULATED GALAXIES

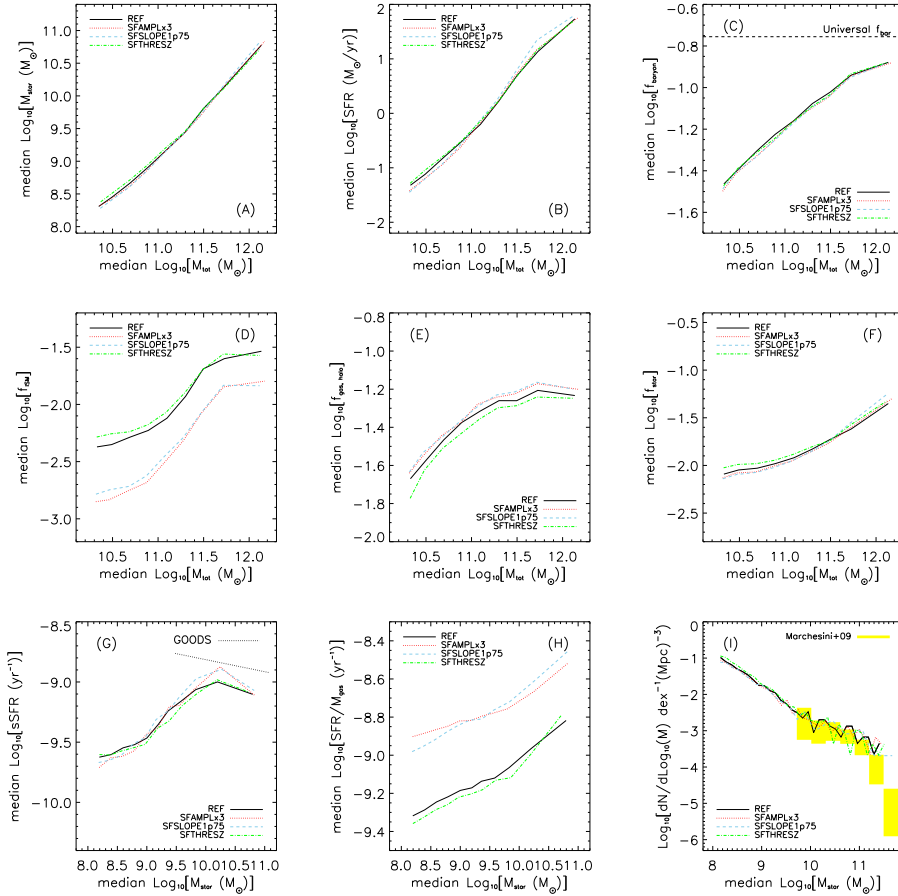


Figure 2.7: Like Fig. 2.2, but now only for a set of simulations in which the only variation is in the implementation of star formation. All simulations reproduce a Kennicutt-Schmidt-like law. The reference model (black solid line) reproduces the KS-law as it is observed, with a slope in the power law relation between gas surface density and star formation rate surface density of 1.4 and the observed normalization. The red dotted line is the result of a simulation which has the same power law slope in the KS law, but has a three times higher amplitude (three times higher star formation rate for given gas density). The model showed with the blue dashed line has steeper dependence of star formation rate on gas density, and at all densities above the star formation threshold, the normalization of the KS-law is higher as well. Both these models therefore have more efficient star formation. The green dot-dashed line shows the results of a simulation in which the star formation threshold is a function of the gas metallicity.

$M_{\odot}\text{yr}^{-1} \text{ kpc}^{-2}$ (Kennicutt, 1998a), although these values remain controversial (e.g. Blanc et al., 2009). The threshold density for star formation and the normalization of the star formation law are obtained from observations. The normalization should be appropriately scaled to the IMF that is used, see Sect. 2.2.5. For details about our implementation of the star formation law, see Schaye & Dalla Vecchia (2008).

Three different star formation models are run to compare with the standard, observed KS-law. One model uses a factor 3 higher normalization, which implies that for a gas particle with the same pressure, the SFR is a factor 3 higher (*'SFAMPLx3'*). In the other run, the power-law slope of the KS-law is increased from $n = 1.4$ to 1.75 (*'SFSLOPE1p75'*). The normalisation of this model is chosen such that the SFR surface density is the same for $\Sigma_{gas} = 1 M_{\odot}/\text{kpc}^2$. As this is below the star formation threshold, this KS-law is more efficient than the reference one at all densities. The third variation on the reference model is a model in which the threshold density for star formation (and therefore also for gas going onto the equation of state) depends on the metallicity of the gas, $\rho_{th} \propto Z^{-0.64}$, such that the threshold density is equal to the reference simulations' if the metallicity is $0.1Z_{\odot}$, (*'SFTHRESHZ'*). This model reproduces the metallicity dependence of the critical surface density for the formation of a cold, molecular phase predicted by Schaye (2004).

As we show in panel (B) of Fig. 2.7 the slope, normalization and threshold density of the Kennicutt-Schmidt law are unimportant for the SFR of a halo. Making star formation at a given density either three times more effective or making the star formation rate a steeper function of the local gas density (and more effective at all densities) does not affect the star formation rate of a halo. Also, making the threshold density for star formation a function of metallicity does not influence the star formation rate of a halo. This indicates strongly that *the global star formation rates of haloes are set by the available fuel and feedback only* and not by the details of how high density gas is treated and how star formation is implemented. In other words: *star formation is self-regulated by the available fuel and feedback*.

If haloes have the same star formation rate, while for a given density gas particles have a higher star formation rate, then the haloes must adapt their reservoir of star forming gas to the higher star formation efficiency. In simulations with more efficient star formation laws, we expect the fraction of gas that is on the EoS to be lower, in order to get the same total SFR and energy injection from feedback into the ISM. In panel (D) of Fig. 2.7 we show that this is indeed the case. While the total gas fractions (not shown) are the same for all implementations of star formation, the amount of gas that is on the EoS, and forming stars, is lower in more efficient star formation models. The more effective star formation laws in these simulations make the gas stay shorter in a star forming phase, as can be seen from panel (H), where we clearly show that the gas consumption time scales are indeed

much shorter, such that the smaller amount of available star forming gas (shown in panel D) forms as many stars in the same halo and releases an equal amount of SN energy back into the ISM. As soon as the density is sufficient the gas is transformed into stars and their feedback prevents other gas from becoming star forming (such that the SFR is unaffected). The feedback accompanied with the more efficient star formation regulates the amount of gas condensing onto the ISM and regulates star formation.

Total baryon fractions and the amount of gas in the halo that is not star forming (panels C and E) are much less sensitive to the efficiency of star formation, as they are largely set by the amount of baryonic accretion and ejective feedback.

2.8 The stellar initial mass function

The stellar initial mass function is under heavy debate in literature. Here, we take the approach of using a popular IMF (Chabrier, 2003) in most simulations. The IMF is important for several aspects of these simulations. First of all, the different ratios of low to high mass stars will result in differences in the integrated colours of stellar populations and in different chemical yields. Also, a different number of SNe per unit stellar mass formed asks for consideration of a change of feedback. In the following two section we will discuss two additional simulations that use different IMFs: Section 2.8.1 shows the simulation results under the assumption of a Salpeter IMF, while Section 2.8.2 discusses a set of simulation with more extreme IMFs in extreme star formation environments.

2.8.1 Salpeter IMF

Fig. 2.8

We also ran a simulation with the Salpeter (1955) IMF, rather than the Chabrier (2003) IMF used in the reference model (*‘IMFSALP’*). Due to the absence of a turnover at the low mass end, the fraction of low-mass stars is higher for the Salpeter IMF. Therefore, for every solar mass of stars formed, there is less energy available from high mass stars, as also described in Sect. 2.2.5. We did rescale the normalization of the star formation law accordingly, but we used the same wind parameters as in the reference model (so $1.65 \times 40\% \approx 66\%$ of the total supernova energy). From Fig. 2.2.2 it can be seen that both IMFs result in galaxy properties that look very similar. Also, in later Sections we will show that the properties of galaxies are not drastically different, although comparisons with observations require rescaling to a consistent IMF to explain differences between models.

In the simulation with the Salpeter IMF (*‘IMFSALP’*) the fraction of mass in the ISM is lower and the gas consumption time (panels D and H of Fig. 2.8) is

2.8. THE STELLAR INITIAL MASS FUNCTION

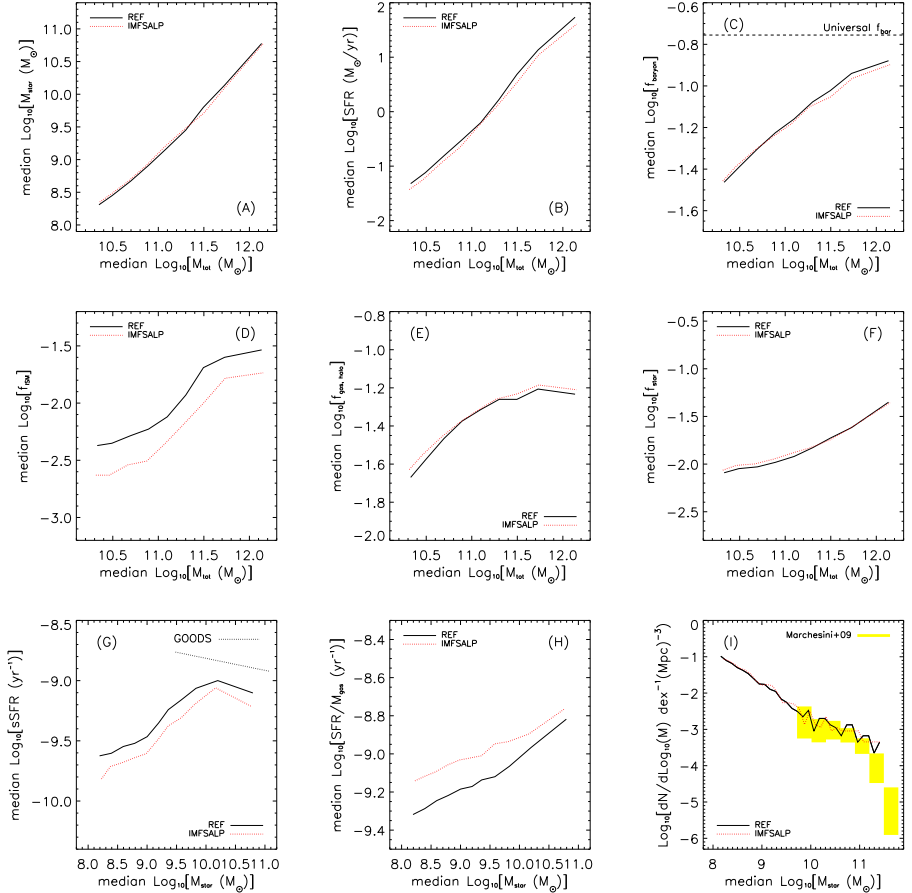


Figure 2.8: Like Fig. 2.2, but now only for two simulations with a different IMF: the reference model (black solid line) uses a Chabrier (2003) IMF, whereas the other simulation (red dotted line) is run assuming a Salpeter (1955) IMF. The main difference between the two is the number of high mass stars formed per unit stellar mass formed, but the high mass slopes are almost identical.

slightly shorter than in the reference model. This is due to the lower amount of gas turned back into the ISM, due to the lower fraction of massive stars per unit stellar mass. The regulation of star formation by SN feedback and the fact that the total energy in the winds are the same for both simulations result in a less massive star forming gas reservoir in the ISM of the galaxies, and very similar stellar content of the haloes (panels A and F).

In panel (H) of Figs. 2.6, 2.7 and 2.8, where the simulations with different EoS indices, KS-laws and stellar IMFs are shown we see the self-regulation of the star formation illustrated once more. The polytropic EoS index is unimportant for the gas consumption time scale. Making the Kennicutt-Schmidt law more effective, though, results in much shorter gas consumption time scales. This is reasonable, as the same gas density/pressure results in a higher star formation rate in both these models, and is explained already in Sect. 2.7. Below, when we discuss different SN feedback implementations we will see that the SN feedback is crucial in setting the star formation properties of haloes. The cooling of gas and the feedback of energy into the ISM work together such as to put back the same amount of SN energy into the ISM (for a given feedback model), regardless of the details of the high density gas or the star formation law.

2.8.2 Simulations with a top-heavy IMF at high pressures

Fig. 2.9

In order to keep SN feedback effective in high mass galaxies, higher wind velocities are needed (as will be shown below). In another set of simulations (*‘DBLIMF’*) stars are assumed to form with a top-heavy IMF (an IMF with power law $dN/dM \propto M^{-1}$) if the gas pressure exceeds $P/k = 2.0 \times 10^6 \text{ cm}^{-3} \text{ K}$ (evaluated at the resolution limit of the simulations). Observationally, there is some evidence that star formation in gas with high pressure (such as starbursts and in the centre of the Galaxy) occurs with an IMF that is flatter than Chabrier (e.g. McCrady et al., 2003; Stolte et al., 2005; Maness et al., 2007).

The total energy from Supernovae Type II per unit stellar mass formed is higher for a top-heavy IMF (a factor of 7, comparing the aforementioned top-heavy IMF with the default Chabrier IMF). This extra energy can be used to increase either the wind mass loading or the wind velocity. We tried both options. To facilitate comparisons with the reference run, in one run the velocity was kept fixed at 600 km s^{-1} , but the mass loading was set to $\eta = 14$ (*‘ML14’*). In the other one, the mass loading was kept fixed at $\eta = 2$ and the wind velocity was increased to $v_w = 1618 \text{ km s}^{-1}$ (*‘V1618’*).

When changing the IMF suddenly at some pressure, it is not immediately clear what to do with the star formation law. The Kennicutt-Schmidt law is inferred

2.8. THE STELLAR INITIAL MASS FUNCTION

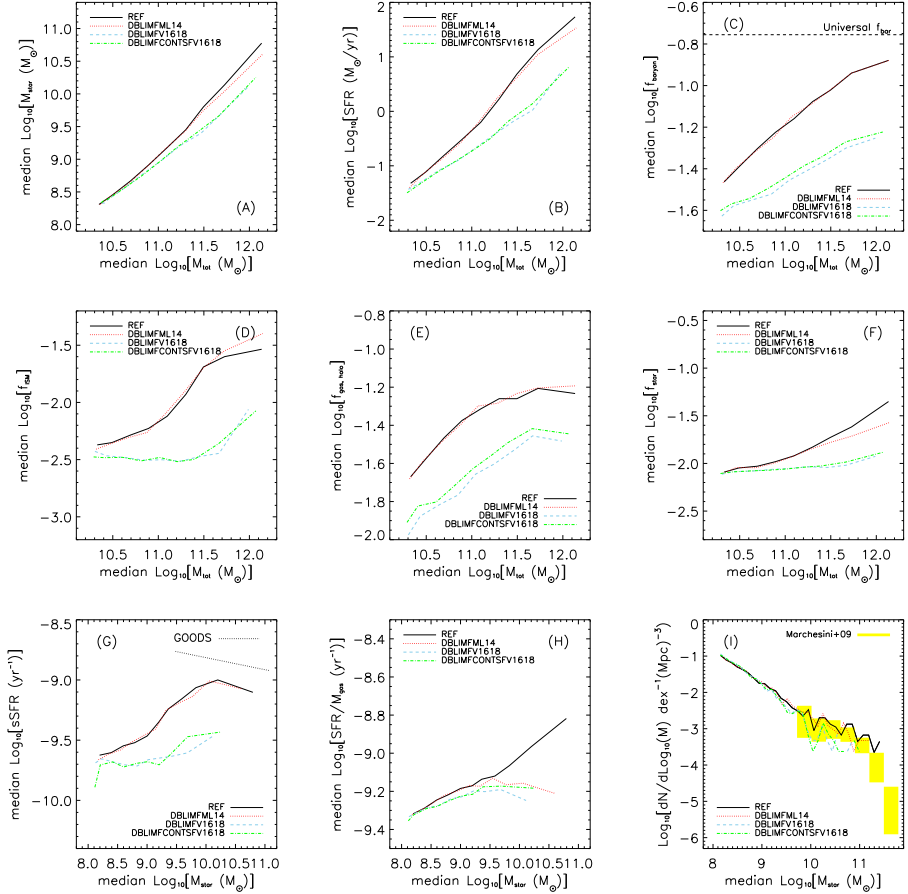


Figure 2.9: Like Fig. 2.2, but now only for a set of simulations in which a top-heavy IMF is used for star formation at high pressure. The reference model (without top-heavy IMF) is shown by the black solid line. The extra available SN energy per unit stellar mass formed can be put in mass loading or velocity of the winds, which is the difference between the red dotted line (mass loading 7 times higher than in the reference model, at the same wind velocity) and the blue dashed line (mass loading as in the reference model, but a wind velocity of 1618 km s^{-1}). With a jump in the IMF at some pressure, one can either let the star formation rate be a continuous function of the density, or let the rate of formation of massive stars (which is what is observed) be continuous with density. This is the difference between the blue dashed (continuous formation of massive stars) line and the green dot-dashed line (continuous star formation rate, so a jump in the formation rate of massive stars at some pressure).

from observations probing massive stars. Therefore, the total SFR depends on how many low-mass stars are formed together with these massive stars. When changing the IMF, the star formation law can be changed in two ways:

1. From observations there is no indication of a discontinuity in the formation rate of massive stars with pressure. Although this is most likely the result of the IMF being a continuous function of SFR or pressure (if there is a relation at all), we nevertheless implemented a model that changes the normalization of the KS-law such that the formation of massive stars is continuous, resulting in a discontinuous SFR as a function of pressure (the KS-law normalization drops at the pressure above which the IMF is top-heavy). These models are indicated by ‘*DBLIMF*’.
2. If the (total) SFR as a function of pressure is continuous, the formation of massive stars must be discontinuous, given that we assumed the IMF to change suddenly above some critical pressure. Models with a continuous SFR include ‘*DBLIMFCNTSF*’ in their ‘name’.

In Sect. 2.7 we showed that the normalization of the KS-law does not influence the mass function or SFR distributions of galaxies. We therefore expect differences with respect to the reference model to be due to the extra energy input from SN feedback and/or the increased rate of production of metals that results from a top-heavy IMF.

When comparing simulations to observations, we do not correct for the stellar mass of simulations with a double IMF. On average, only $\sim 10\%$ of the star particles in the simulation box formed with a top-heavy IMF (this depends slightly on resolution and hardly on whether the rate of formation of massive stars, or rather of all stars together is a continuous function of density). In Schaye et al. (2010) it was shown that at late times, this correction should be made, but at $z = 2$ the integrated SFR of the universe is not different whether or not the SFRs of particles at pressures higher than the threshold pressure for the top-heavy IMF are corrected for another assumed IMF (the SFR inferred under a Chabrier IMF would be higher than the actual SFR).

The extra energy due to the higher fraction of high mass stars, only has an effect when these particles are launched at sufficiently high velocities. Therefore, the simulation that uses the extra energy to increase the mass loading do not show any change with respect to the reference model for massive galaxies, as the winds do not escape the galaxies. If the extra energy is used to increase the wind velocity, then the feedback does become more effective. The extra energy input is more important in high mass haloes, as the fraction of stars formed at a density above the double IMF threshold increases with halo mass (in total $\sim 10\%$ of the stars in

the simulation are formed with a top heavy IMF, at this resolution). Whether we choose to have a total SFR that is continuous with pressure or a continuous rate of formation of massive stars (and therefore a jump in total SFR as a function of pressure) is not important.

The baryon fraction in the ‘*DBLIMFML14*’ is indistinguishable from the reference model (note that the stellar mass fractions are slightly lower in the simulation with a double IMF and the excess energy put in mass loading), indicating that the gas with the extra energy from the excess of high mass stars does perturb the galaxy more and keep the ISM at low pressure, but the baryons do not escape the halo. They do escape the halo in the double IMF simulations with the extra energy put in wind velocity, as shown in panel (C) of Fig. 2.9. From panel (B) of Fig. 2.9 it is clear that putting the extra available energy from supernovae in top-heavy IMF stellar populations in mass loading did not change the SFR of a galaxy. In panel (H) it can be seen that the gas consumption time scale, nevertheless, has increased by the same amount as it did for the double IMF simulations that put the energy in wind velocity. So although, as a function of stellar mass the star formation rates of the reference model and ‘*DBLIMFML14*’ are similar, the gas consumption times are shorter in the reference model. We note that, as shown in panel (F), the stellar mass fraction of this simulation is lower than that of the reference model, and we can see in panel (D) that in this simulation the star forming gas mass fraction as a function of halo mass is *higher* than in the reference model. We can conclude that this form of feedback, which has ~ 7 times more energy, results in a *larger* reservoir of star forming gas, which is used up more slowly, as it is kept kept at lower pressure. The high mass loading in the simulation ‘puffs up’ the galaxy, such that although there is a large reservoir of gas to form stars from, the SFR still is the same as it would be without a fraction of the stars formed with a top heavy IMF.

A tiny difference in the stellar mass fraction in the simulation with a top-heavy IMF for high pressure star formation that puts the excess energy of SNe in mass loading: the extra available energy results in a minor decrease in stellar mass fraction by $z = 2$, whereas the difference in (s)SFR is hardly visible. Only a small fraction of the star particles forms with a top-heavy IMF, but those star particles loose mass quickly. Besides, the stellar mass content is the integral of the SFR over time, so tiny differences in the SFR add up to a noticeable difference in stellar mass.

2.9 Supernova feedback

In order to run simulations without any feedback from supernovae (SNe) all the way to the final redshift, we turned off metal-line cooling. The very high metallic-

ities and, consequently, very high densities reached would otherwise result in very high cooling rates and very short time steps. Therefore, in order to compare simulations with and without SN feedback, we compare the simulation without metal-line cooling and SN feedback (*'NOSN_NOZCOOL'*) with the simulation without metal-line cooling (*'NOZCOOL'*) in Fig. 2.4.

Star formation in haloes will in general be regulated by the amount of available fuel, and therefore the inflow rate of cold gas and by the feedback that accompanies the formation of massive stars, which may prevent or suppress further star formation by removing or heating the available gas. In panel (B) of Fig. 2.4 we compare the SFR as a function of halo mass for simulations without SN feedback (and without metal-line cooling) with the reference model, which does include both SN feedback and metal-line cooling. SN feedback accounts for the difference between the *'NOSN_NOZCOOL'* and *'NOZCOOL'* simulations, shown by the blue dashed and red dotted curves, respectively. The SFR in the simulation without SN feedback is much higher at a given halo mass. The difference declines with increasing halo mass, as the effect of SN feedback becomes less important for more massive systems (e.g. White & Frenk, 1991).

In Fig. 2.9.1 we compare the stellar mass fractions of the two simulations of Fig. 2.3 with the same cosmology, but a factor two difference in wind energy (the energy difference is put in mass loading), but now in a 100 Mpc/h box (using 2×512^3 particles as well) at redshift zero. It can be clearly seen that at some mass the winds become very ineffective and the stellar mass fractions of the halo rise steeply ($10^{-11.2} M_{\odot}$ at redshift 2 and $10^{-12.2} M_{\odot}$ at redshift zero and at 8 times lower resolution). Below this mass, in the regime of effective winds, the difference in stellar mass fraction is exactly the factor two difference in feedback energy. Although it is mainly velocity that sets the effectiveness of the winds, at a given velocity the stellar mass fraction is still a factor two lower for a simulation with a mass loading of the wind that is a factor 2 lower. This shows how well self-regulation of the star formation by supernova feedback works.

2.9.1 Winds with constant energy per unit stellar mass formed

Fig. 2.10

In the set of models shown in Fig. 2.10 we vary the parameters of the winds resulting from massive stars and core collapse supernovae. More specifically, we compare 4 simulations which all use the same feedback energy per unit stellar mass formed. The winds are implemented kinetically and are specified by the mass loading (the amount of mass put in the wind per unit of mass transformed into stars) η (denoted by *'ML'* in the simulation names) and the velocity with which this mass is kicked, v_w . For more detailed information about the wind implementation, see

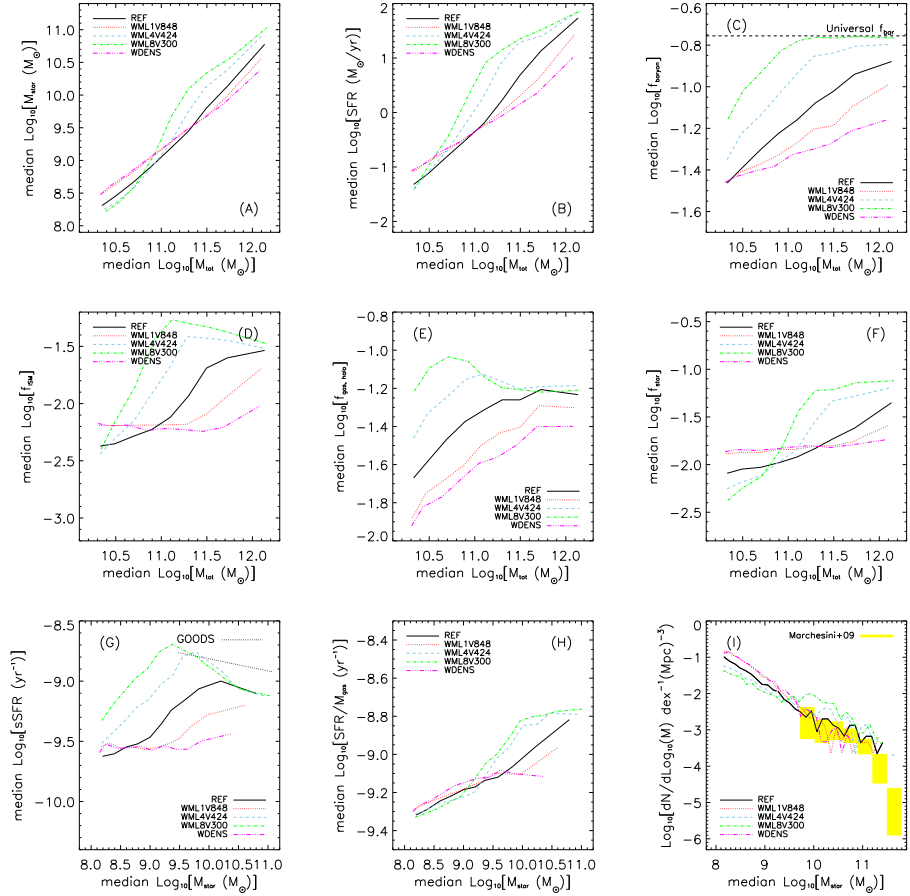


Figure 2.10: Like Fig. 2.2, but now only for a set of simulations in which the wind velocity and mass loading are varied. The reference simulation (black solid line) has a mass loading of $\eta = 2$ and a wind velocity of 600 km s^{-1} . The simulations shown by the red dotted, blue dashed and green dot-dashed lines show variations on this at the same energy, but with the mass loading changing by a factor of 2 (and, therefore, the velocity by a factor $\sqrt{2}$), giving a mass loading of 1 (a velocity of 848 km s^{-1} , red dotted line), 4 (a velocity of 424 km s^{-1} , blue dashed line) and 8 (velocity of 300 km s^{-1} , green dot-dashed line). The magenta dot-dot-dot-dashed line represents a simulation which has a mass loading and velocity dependent on the local density, such that the energy in the wind is still the same and the velocity is proportional to the local sound speed.

Dalla Vecchia & Schaye (2008). The reference simulation assumes a mass loading of 2, and a wind velocity of 600 km s^{-1} , which corresponds to 40 per cent of the energy available from core collapse SNe. The wind kinetic energy scales linearly with mass and quadratically with velocity, a change of factor n in the mass loading requires a factor $n^{-1/2}$ change in the wind velocity. The mass loadings in the four simulations are 1, 2 (reference), 4 and 8, with corresponding velocities of 848, 600, 424 and 300 km/s, respectively. An example of the notation used throughout the paper would be ‘*WMLIV848*’ for $\eta = 1$ and $v_w = 848 \text{ km s}^{-1}$.

We expect that winds with a constant velocity will not be efficient in every halo. Aside from gravity, which sets a gravitational escape velocity, ambient gas has to be swept up and dragged along. This will slow down the wind due to the conservation of momentum and due to ram pressure forces. This gas drag increases with the pressure of the ISM and thus with the mass of the galaxy. Above some halo mass, the winds will be slowed down too much and will not escape the galaxy any longer. Dalla Vecchia & Schaye (2008) showed explicitly that slowing down the winds and making them inefficient above some mass is caused by gas drag rather than gravity (we will show this again below, in Sect. 2.9.2). Because of the dependence of the mass at which the winds become ineffective (as shown below) we have also performed simulations in which the wind velocity scales with local properties. One such simulation, with constant energy in the winds, is called ‘*WDENS*’. In this simulation the distribution of the energy over mass and velocity is determined by the local gas density (i.e. the density of the gas from which the star particle formed) as follows: $v_w \propto \rho^{1/6}$, $\eta \propto \rho^{-1/3}$, which implies $v_w \propto c_s$ for the effective equation of state $P \propto \rho^{4/3}$ that we impose onto the ISM (see Section 2.6), where c_s is the sound speed. The normalization is such that the wind velocity and mass loading are the same as in the reference model if the gas density equals the star formation threshold, i.e. $n_H = 0.1 \text{ cm}^{-3}$. From Fig. 2.2.2 it is clear that this variation in wind velocities does not result in very different appearances for the galaxies, whereas the star formation properties differ strongly.

In Fig. 2.10, the simulations with constant wind energies, but different mass loading factors and wind velocities are compared. At low halo mass, the models are very comparable. At some halo mass the SFR (panel B) suddenly goes up strongly, and the mass at which this happens increases with wind velocity. Comparing the different models in Fig. 2.10 to the ‘*NOSN_NOZCOOL*’ in Fig. 2.4 shows that the relation between SFR and halo mass is, at high stellar masses, similar to the simulation without any feedback (and without metal line cooling), suggesting that the feedback indeed is completely ineffective. High wind velocities are slightly less efficient at low halo mass, because of the lower mass loading in the winds. For the low mass systems, the wind velocity is not important, as the winds escape the halo anyway.

For the ‘*WDENS*’ model, the energy injected in the wind per unit stellar mass is also the same as in the reference model, but the initial wind velocity scales with the local sound speed. The relation between halo mass and SFR is even shallower than it is for the run with $v_w = 848 \text{ km s}^{-1}$, indicating that the feedback is efficient for all haloes. At high masses, this is the most effective wind model with constant energy.

We have seen that for haloes that have ineffective feedback (due to too low velocities), the star formation rate is very high, and the relation between star formation rate and mass has a shallower slope than for simulations with effective SN feedback. One important result that can be seen from the comparison of the reference model with the model without metal-line cooling (Fig. 2.4) is that turning off metal-line cooling reduces the star formation mostly in the highest mass haloes. Although this model has the feedback as in the reference model, the star formation rate apparently is lower. In paper I it was already argued that metals reduce the efficiency of the winds. The low wind velocities will result in more centrally concentrated metal distributions, reducing the efficiency of the winds more strongly in high mass, than in low mass haloes. Comparing the simulations in Fig. 2.10 with the simulation without metal-line cooling in Fig. 2.4 shows that the transition from effective winds to ineffective winds is much more gradual in the absence of metal-line cooling.

As is clear from panel (I) of Fig. 2.10, bringing down the slope of the low mass end of the stellar mass function can be attained by increasing the mass loading factor in constant energy winds. The highest mass loading still gives a low mass end slope that is steeper than power law fits to the low mass end in the observations, although the discrepancy only occurs on masses lower than those observed.

In panel (F) of Fig. 2.10 we show the stellar mass fractions of the simulations of different wind models with the same energy and it can be seen that at the very low mass end, the simulations with a low velocity (and therefore high mass loadings) the stellar mass fractions are lower than for simulations with a lower mass loading. This also reflects in a shallower low mass end slope of the stellar mass function, as illustrated in panel (I). Fig. 2.9.1 shows the stellar mass fractions of two simulations which differ by a factor of 2 in feedback energy (as described in Section 2.3). The difference in energy is used to increase the mass loading at fixed velocity, such that the inefficiency of the winds kicks in at the same halo mass. At the low halo mass end, the difference in stellar mass fractions of the two simulations is a factor of 2. This illustrates how the energy in the feedback directly sets the fraction of the mass that transforms into stars.

The baryon fractions and the fraction of the mass in warm-hot gas in the halo (panels C and E) show that at low halo masses, the amount of gas (or, equivalently, baryons) in the halo is higher for lower wind velocities. These winds, even if they

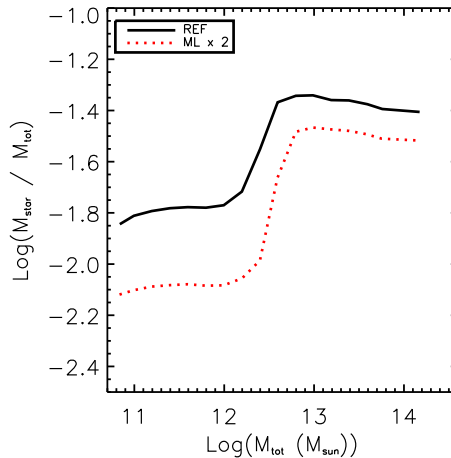


Figure 2.11: The stellar mass fraction as a function of halo mass in $100 h^{-1} \text{Mpc}$ boxes with 512^3 particles at redshift 0. We compare here two models with each other that differ in supernova feedback energy by a factor of two (two times higher mass loading in the wind, same wind velocity) at redshift 0.

do escape the ISM and near vicinity of the galaxy, can not escape their parent halo.

A comparison of (G) and (H) is once again an illustration of the regulation of star formation by SNe. The gas consumption time scales (in the regime where the winds are all efficient) are very similar. Per unit stellar mass formed, the same amount of SN energy is fed back into the ISM and used efficiently to suppress star formation. The sSFR, as displayed in panel (G) are different, because the build-up of stellar mass has been different. The gas consumption time scale is likely the best indicator for at which mass the winds become inefficient.

2.9.2 Hydrodynamically decoupled winds

Fig. 2.12

Most simulations using the code GADGET-2 employ the Springel & Hernquist (2003a) implementation of kinetic SN feedback. In this model the wind particles, once launched, are temporarily decoupled from the hydrodynamics. The coupling is turned on again after a fixed amount of time (50 Myr), or when the density of the wind particle falls below some value (10% of the star formation density threshold, i.e. when $n_{\text{H}} < 10^{-2} \text{ cm}^{-3}$), whichever occurs first. During decoupling a gas particle experiences gravity, but no hydrodynamic drag. Decoupling the winds is expected to result in a different SFR for high mass galaxies, as feedback will

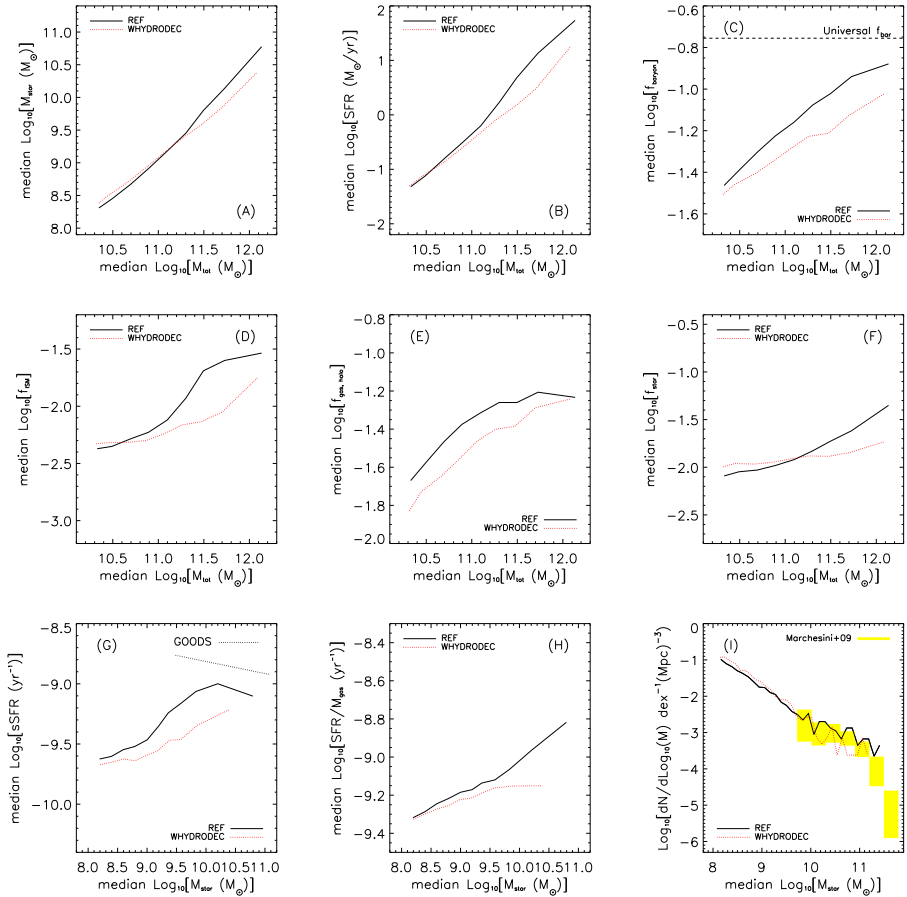


Figure 2.12: Like Fig. 2.2, but comparing only the reference simulation (black solid line) and the simulation in which the wind particles are temporarily decoupled from the hydrodynamics (red dotted line).

remain efficient in the halo mass range where our reference model becomes inefficient due to gas drag in the ISM (see Dalla Vecchia & Schaye, 2008). In practice, decoupling the wind particles means that the wind particles fly out of the galaxy before they couple again, and therefore do not drag any other ISM particles. The winds leave the galaxies at much higher velocities than in the *OWLS* reference model (and all other wind models as well), mimicking simulations that use a much higher wind energy and velocity. For a detailed study of the effect of decoupling for the case of isolated disk galaxy simulations, see Dalla Vecchia & Schaye (2008). For comparison, we have also run a model with the Springel & Hernquist (2003a) decoupling, denoted ‘*WHYDRODEC*’. Note that isolated galaxies formed with decoupled winds look less realistic, particularly at low masses (Dalla Vecchia & Schaye, 2008). From Fig. 2.2.2 we can see that the gas density outside the disc is much higher in this model.

Decoupling the wind hydrodynamically gives effective feedback for all haloes, as the mass of the gas that has to be dragged along is zero, so all particles launched in the wind escape the galaxy. Therefore, the SFR for this simulation is lower at (relatively) high masses than the reference model. For the lowest mass, where the reference model also has very effective feedback, as discussed in Sect. 2.9.1, the difference decreases, as shown in Fig. 2.12. From this large difference between the ‘*WHYDRODEC*’ and the ‘*REF*’ models we can conclude that it is not gravity (which acts on the winds in both simulations), but the hydrodynamic forces which makes the winds less prone to escape in high mass haloes, as was already shown by Dalla Vecchia & Schaye (2008).

Because of the lag of hydrodynamic coupling in the first few tens of Myrs, the gas flows out to large distances. When it couples to the hydrodynamics again, it still has a larger velocity than it would have had at the same location, if the coupling was never broken. Therefore, also at larger distances it is still easier for the gas to flow out. This results in the lower baryon fractions, and fractions of mass in gas in the halo in the model with hydrodynamic decoupling, as is shown in panels (C) and (E) of Fig. 2.12. The fact that the gas does not drag along surrounding gas while it is in the ISM of the galaxy it is launched from results in a larger fraction of the mass in the ISM in the lowest mass haloes (with decoupling, more mass would have been dragged outwards), as shown in panel (D). This also results in a slightly higher stellar mass fraction at low mass, as shown in panel (F).

2.9.3 Thermal SN feedback

Fig. 2.13

Instead of launching the wind by injecting kinetic energy, we also use an implementation of thermal feedback, in which we inject thermal energy into the gas

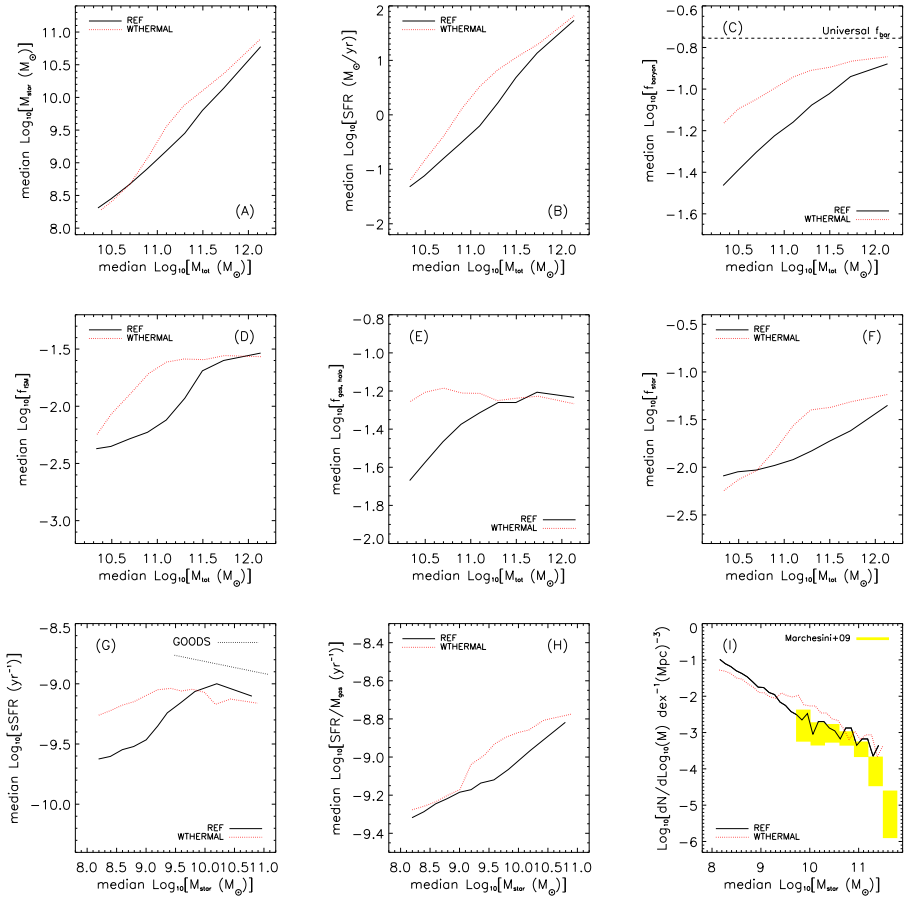


Figure 2.13: Like Fig. 2.2, but comparing only the reference simulation (black solid line) and the simulation in which the supernova feedback is implemented thermally, instead of kinetically (red dotted line).

surrounding the star particle that has exploding SN. If the available energy is distributed amongst all SPH neighbours, the rise in temperature corresponding to the energy input is so low that radiative cooling will be very efficient. In that case, particles will immediately radiate away this energy and feedback will have little effect, unless the cooling is temporarily turned off (Mori et al., 1997; Thacker & Couchman, 2000; Kay et al., 2002; Sommer-Larsen et al., 2003; Brook et al., 2004; Stinson et al., 2006). Therefore, we choose to inject the thermal energy into neighbouring gas particles, ensuring that the temperature of the particle rises to within the radiatively inefficient regime, using a temperature rise of $\Delta T^* = 10^{7.5}$ K. The expectation value for the number of particles to heat is then 1 for 40% of the available SN energy. For details on the thermal feedback implementation we refer to Dalla Vecchia & Schaye (in prep.).

Although injecting 100% of the available SN energy can be justified in the case of thermal feedback (the 40% chosen in the other implementations described above allowed for radiative losses), we choose to use 40% in order to facilitate comparison with the other models.

The thermal implementation of SN feedback is shown in Fig. 2.13. Although the same energy is used per unit stellar mass formed, the thermal implementation is less effective than the kinetic implementation. Note that it is still much more effective than thermal implementations used in literature (e.g. Kay et al., 2003) and that we still use only 40% of the available SN energy, whereas 100% could be justified in these models as well. At low masses, the SFRs are higher than the reference model, and get close to the wind models with low velocities ($v_w = 424$ km s⁻¹). For higher masses, the relation between halo mass and SFR joins the tracks of ineffective feedback for the simulations discussed in the previous section.

The thermal implementation also is more effective at low masses than at high masses, as illustrated by the gas consumption time scale (panel H), the stellar mass fraction (panel F) and the fraction of the mass in the ISM (panel D). Whenever thermal energy is transferred to gas particles, these particles respond by adiabatic expansion due to their suddenly higher temperature. While expanding, they push away other gas particles, and as such a large scale outflow may still arise. Depending on the mass of a galaxy, the cooling time (due to different metallicities and different pressures) and the surrounding ambient pressure (which makes it harder to expand) influence the effectiveness of this form of feedback.

2.9.4 ‘Momentum-driven’ wind models

Fig. 2.14

Galactic winds could be driven by radiation pressure on dust grains in the wind, which drag along the gas (Murray et al., 2005). Here the driving force of the wind

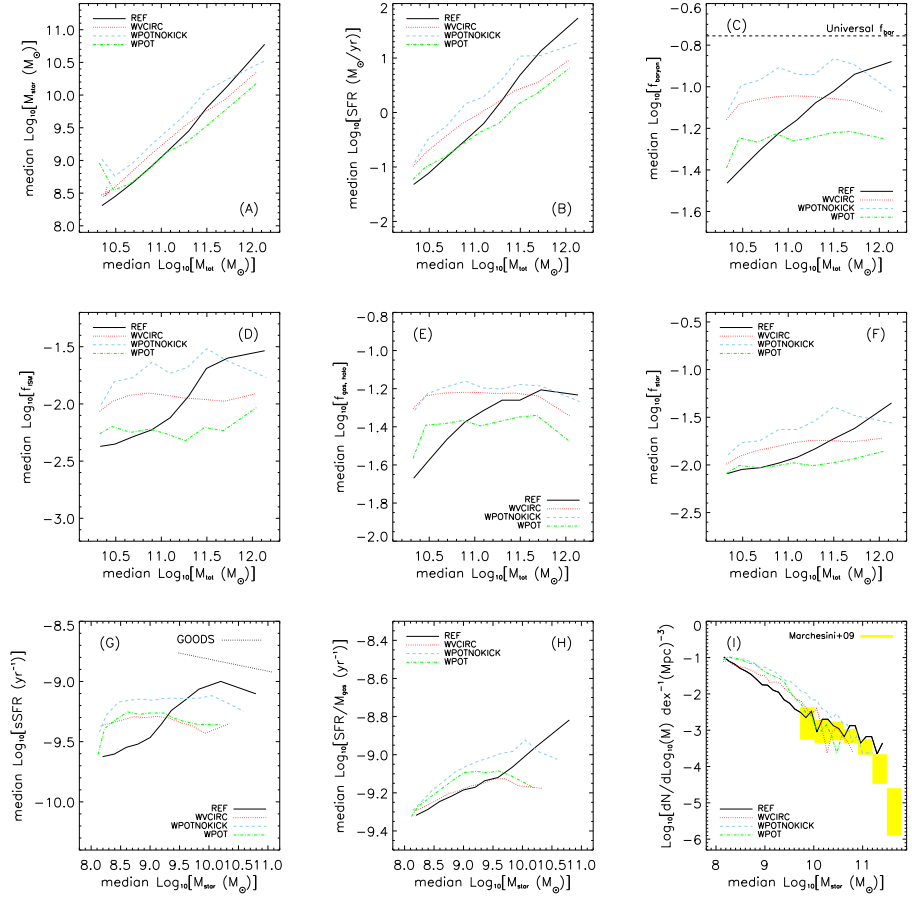


Figure 2.14: Like Fig. 2.2, but comparing a set of simulations with momentum driven winds to the reference simulation (black solid line). In ‘WVCIRC’ (red dotted line), the wind velocity depends on the circular velocity of the halo the wind is launched from, while in ‘WPOTNOKICK’ and ‘WPOT’ it is the local gravitational potential that sets the wind velocity (without and with a kick, shown by the blue dashed and green dot-dashed lines respectively). The energy in these winds is not constant and generally exceeds the energy in the reference simulation.

is the radiation pressure which injects momentum into the outflow and therefore such models live under the common name of ‘momentum driven winds’. As it is the stellar continuum radiation driving the dust grains, the efficiency of such winds increases with galaxy luminosity and, therefore, mass.

We implemented some such models, which are similar to the momentum driven wind models used by Oppenheimer & Davé (2006, 2008). Here, the energy of the wind is not constant, but depends on either the local potential (‘*WPOTNOKICK*’) or the circular velocity, $v_c = \sqrt{GM_{\text{vir}}/R_{\text{vir}}}$ of the halo the wind is launched from (‘*WVCIRC*’). Note that the energy put in the wind per unit stellar mass formed scales with the mass ($E \propto M^{1/3}$) and exceeds the available energy from SNe for the most massive galaxies ($M \gtrsim 10^{12.5} M_\odot$, the exact mass of equality is redshift dependent, due to the redshift dependence of the virial radius). We show in Appendix 2.11 that, compared to the momentum available from radiation pressure, the momentum in the winds in these simulations is overestimated by an order of magnitude or more.

In ‘*WVCIRC*’ the wind velocity and mass loading are given by $v_w = (3 + n)v_c/\sqrt{2}$ and $\eta = \frac{1}{\sqrt{2}} \times (v_c/v_{\text{crit}})^{-1}$, where n and v_{crit} are parameters, set to 2 and 150 km s^{-1} , respectively. From the image in Fig. 2.2.2 it can be seen that the ‘*WVCIRC*’ wind model completely disrupts the disc of the galaxy.

In the ‘*WPOTNOKICK*’ model, the wind velocity is given by $v_w = 3\sigma$, where σ is the velocity dispersion, calculated from the gravitational potential: $\sigma = \sqrt{-\Phi/2}$. In ‘*WPOT*’ we added an extra kick in the velocity of $2 \times \sigma$, as did Oppenheimer & Davé (2006). These models both have velocities that depend on the local gravitational potential. This potential is, however, more closely related to the large-scale structure you are in, than to the mass of the halo. Note that in all models we do couple the wind particles to the hydrodynamics, whereas earlier studies did not.

The effects of the different momentum driven wind models are shown in Fig. 2.14. Scaling the energy with the potential of the star forming particle or with the mass of the halo the wind is launched from results in relatively shallow relations between SFR and halo mass. The relation for ‘*WPOTNOKICK*’ is noisier than the other momentum driven wind models, because the local potential tells you more about the large scale structure the halo is in than about the actual mass of the halo, and therefore the energies at given halo mass scatter more. Giving the wind an extra kick in velocity on top of the kick it would be given in ‘*WPOTNOKICK*’, as done in ‘*WPOT*’, results in even stronger feedback and correspondingly lower SFRs.

For most simulations, there is a very tight correlation between the gas consumption time scale and stellar mass, with not much scatter between the simulations, especially at the low stellar mass end. As long as the feedback is efficient, the

gas consumption time scale is a decreasing function of stellar mass, independent of wind velocity and mass loading. The energy in the winds make some difference as can be seen in panel (H) of Fig. 2.14, where the momentum driven wind models are plotted.

In panel (C) of Fig. 2.14 one can read off the effectiveness of the momentum driven wind models in terms of the baryon fractions of the haloes. These models are successfully used by Oppenheimer & Davé (2006); Davé & Oppenheimer (2007); Finlator et al. (2007); Oppenheimer & Davé (2008) to fit the $z = 6$ luminosity function, the evolution of C IV and to explain the galaxy mass-metallicity relation and $z = 0$ IGM abundances. Here we show that the haloes have roughly constant baryon fractions with halo mass and fairly high compared to most other models, except in the most massive haloes, where the other models overshoot the momentum driven wind models. Tests on the enrichment of the IGM in our simulations are studied in more detail in future studies.

In panel (F) of Fig. 2.4 we show the stellar mass fraction as a function of total halo mass for the simulations described in Sect. 2.9. More efficient feedback (so, high wind velocities in high mass haloes, like in the momentum-driven wind models, the hydrodynamically decoupled winds and the simulations with a double IMF where the excess energy is put in wind velocity) results in flatter stellar mass fractions as a function of mass. For haloes for which the wind velocity is too low for the winds to escape, the stellar mass fraction shoots up. Only for the very most massive haloes, for which some of the SN feedback models in Fig. 2.10 (the constant wind velocity models) are very inefficient, some simulations have a stellar mass fraction approaching the stellar mass fraction of the simulation without SN feedback and without cooling. If the wind velocity is sufficiently high to make the feedback efficient, the mass loading will set the amount of fuel for star formation that is removed from the system. In the momentum driven wind models as discussed here, the mass loading becomes higher for lower mass galaxies, that's why the slope of the stellar mass function (panel I) is getting shallower towards lower masses.

2.10 AGN feedback

Fig. 2.15

Many varieties of AGN feedback have been implemented, see Booth & Schaye (2009), of which we will show only one. Haloes are identified at small time intervals during simulation runtime, with FoF, as described earlier. If a halo has a mass of at least $4 \times 10^{10} M_{\odot}$ and no black hole yet, a seed black hole is placed at the position of the most bound baryonic particle. The mass of the seed black hole is

CHAPTER 2. PHYSICAL PROPERTIES OF SIMULATED GALAXIES

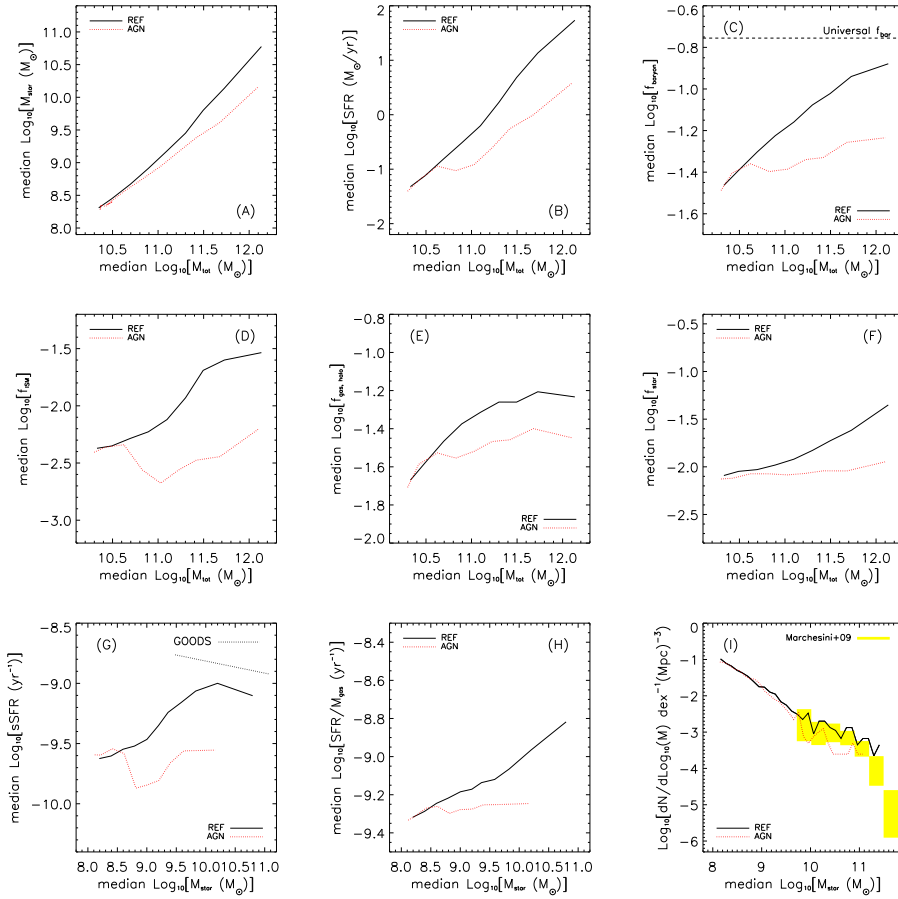


Figure 2.15: Like Fig. 2.2, but only comparing the reference model (black solid line) to a simulation that includes AGN feedback (red dotted line).

15.6 times smaller than the mass of a baryonic particle ($9 \times 10^4 M_{\odot}$). The black hole is then grown by accretion, limited by the Eddington limit, or mergers. This growth is self-regulated, in the sense that the black holes grow very fast (at the Eddington rate) onto the black hole mass - stellar mass relation and then continues to grow along the observed relations. AGN feedback on the surrounding gas is implemented thermally, i.e. the black hole stores its accreted energy until the feedback will heat one neighbour (stochastically) by 10^8 K. The radiative efficiency is assumed to be 10% and 15% of the feedback energy is assumed to couple to the ISM, i.e. the feedback energy $\dot{E}_{feed} = 0.015\dot{m}_{accr}c^2$.

As described by Booth & Schaye (2009), this model reproduces the observed black hole scaling relations, the black hole fundamental plane and the global black hole density of the Universe. Fig. 2.2.2 shows that AGN feedback is the only model as destructive as the momentum driven winds in terms of removing gas from the haloes. This is also visible in panels (C - E) of Fig. 2.15, where it is obvious that the ISM and halo gas content (and thus the baryonic content, which is dominated by gas in the halo) of galaxies is strongly reduced above some halo mass.

AGN feedback has been argued to suppress star formation in high mass haloes (e.g. Di Matteo et al., 2005; Croton et al., 2006; Bower et al., 2008; Booth & Schaye, 2009; McCarthy & Others, 2009). In order to overcome cooling catastrophes in high mass haloes, a continuous source of heating is necessary, shutting off almost all star formation (e.g. Edge & Stewart, 1991; Markevitch, 1998; Khalatyan et al., 2008). In panel (B) of Fig. 2.15 we show the halo SFR as a function of mass for the AGN feedback model. Indeed, the effect of AGN is strongest at high masses, but is already noticeable for masses as low as $10^{-10.6} M_{\odot}$. When seed black holes are inserted into haloes, the AGN quickly grow onto the scaling relations, as shown by Booth & Schaye (2009) and are effective in heating up the gas in the central regions of the galaxy and decreasing the SFR. Panels (B) and (F) of Fig. 2.15 shows that the inclusion of AGN feedback indeed lowers the star formation rate of haloes and, as a result, the stellar mass fractions.

From the panels (D), (E) and (F) it can be seen that AGN are very efficient at removing gas from the ISM and slightly less efficient in removing gas from haloes. AGN lower the stellar mass fraction by a slightly smaller amount than it lowers the fraction of the mass in the ISM by redshift 2, as stellar mass also builds up in lower mass systems in which AGN feedback is less efficient. The stellar mass function, as shown in panel (I) slightly undershoots the observed stellar mass function. The SN feedback in this simulation was tuned to reproduce the total star formation rate density of the Universe fairly well. Including the extra AGN feedback will then under-reproduce the stellar mass content of the Universe.

2.11 Conclusions

We have analysed a large set of high-resolution cosmological simulations from the *OWLS* project (Schaye et al., 2010). We focused on the baryonic properties of (friends-of-friends) haloes at redshift 2, while varying parameters in the sub-grid models for radiative cooling, reionization, the pressure of the unresolved multi-phase ISM, star formation, stellar feedback and AGN feedback, as well as the cosmology, box size and mass resolution.

A central conclusion from this work is that the star formation rate is self-regulated by galactic winds driven by massive stars. The star formation rate adjusts so that the (time averaged) rate at which energy and momentum are injected is sufficient to balance the gas accretion rate. This self-regulation happens through the ejection of gas from the galaxy in large-scale outflows. For a fixed redshift and halo mass, the accretion rate is determined by cosmology and cooling. As the cooling rate is very sensitive to metallicity, chemical feedback is also important.

For low-mass haloes ($M \lesssim 10^{11} M_{\odot}$, $M_* \lesssim 10^9 M_{\odot}$) the reheating associated with reionisation is important, although by $z = 2$ the results are insensitive to the redshift at which reionisation happened, at least as long as it happened no later than $z = 6$, as required by observations. Without reionisation, these haloes would host higher-mass galaxies with higher gas fractions.

For halo masses $M \gtrsim 10^{11} M_{\odot}$ AGN feedback becomes significant and for $M \gtrsim 10^{12} M_{\odot}$ ($M_* \gtrsim 10^{10} M_{\odot}$) it strongly reduces the star formation rates and gas fractions. We note, however, that the mass for which AGN feedback becomes important can be changed by modifying the parameters of the black hole accretion model (Booth & Schaye, 2009). As was shown by Booth & Schaye (2009), AGN feedback self-regulates the growth of supermassive black holes through the ejection of gas from galaxies. As a result, the black hole growth rate adjusts so that the (time-averaged) rate at which energy and momentum are injected balances the rate at which gas accretes onto the galaxy. As the black hole regulates the gas fraction, it also regulates the star formation rate.

Conclusions that support this picture of self-regulated star formation and other conclusions from this work can be summarised as follows:

- The gas fractions of galaxies are sensitive to the assumed star formation law. If star formation is more efficient, the gas fraction is lower. This is a result of self-regulation: the gas fraction increases until the formation rate of massive stars is sufficient to drive galactic winds that can balance the rate at which gas accretes onto the galaxies. As a consequence, the star formation rates and stellar masses are insensitive to the assumed star formation law.
- In order for kinetic feedback to be efficient in suppressing star formation, the

initial wind velocity must exceed a minimum, halo mass dependent, velocity. As was also shown by Dalla Vecchia & Schaye (2008), if the wind speed is too low, the outflow is quenched by hydrodynamic drag in the ISM. As the pressure of the ISM increases with the mass of the galaxy, so does the required wind velocity. If the velocity is sufficiently high, then the mass loading factor sets the amount of mass removed from the system and hence the efficiency of the feedback.

- If winds do not escape the galaxies, the pile-up of newly created metals results in catastrophic cooling. The gas is efficiently converted into stars and gets exhausted. This results in a change in the relation between star formation rate and the mass of a galaxy. The SFR as a function of mass quickly becomes flatter because of the exhaustion of gas.
- The stellar mass, star formation rates, and gas fractions of galaxies are insensitive to the stiffness of the equation of state that we impose on the unresolved, multiphase ISM.
- In a cosmology with a higher σ_8 structure formation happens earlier, and therefore, galaxies in a fixed halo mass at a fixed time have somewhat higher stellar masses. The characteristic densities are also higher, which reflects the higher density of the Universe at the time the halo formed. These higher densities, in turn, cause feedback from star formation to become inefficient at slightly lower masses if σ_8 is higher. The differences in halo properties between different cosmologies are, however, much smaller than the differences between the cosmic star formation histories we found in Schaye et al. (2010). This is because the halo mass function is sensitive to cosmology, which is more important for the star formation history than the relatively small change in the internal properties of the galaxies at a fixed time and halo mass.

We compared our predictions to two different observational results: the specific star formation rate as a function of stellar mass and the stellar mass function. The latter function can be thought of as a convolution between the halo mass function and the stellar mass as a function of halo mass. As we are using the WMAP year-3 cosmology, our mass function is not quite right. In particular, our underestimate of σ_8 will cause us to underestimate the stellar mass function. Under the assumption that the difference in cosmology only affects the halo mass function, which is correct to first order (as our comparison of the WMAP year-1 and year-3 cosmologies confirms), we could correct our stellar mass function. We have not done this here, but plan to do so in future work.

The comparison with observations revealed that:

- In almost all simulations, the stellar mass function is close to the observed number densities of galaxies over much of the observed mass range. The shape is different though, with most models having a steeper low-mass end. None of the simulations predict a clear exponential cut-off at the high-mass end, but this could just be due to our limited box size (we plan to test this soon). The low-mass end is only steeper than extrapolations of Schechter-function fits to the observations. Except for models with inefficient feedback, the number densities agree well within the observed mass range.
- For a fixed wind energy per unit stellar mass, the slope of the low-mass end of the stellar mass function increases with the wind velocity. This is because higher wind velocities keep the feedback efficient up to higher masses. In addition, low wind velocities correspond to high mass loading factors and thus to more efficient feedback provided the wind velocity remains sufficiently high, as will be the case for lower mass galaxies. This suggests that we could reproduce a wide range of stellar mass functions by making the wind velocity a function of the halo mass, even for a fixed amount of energy.
- The predicted specific star formation rates as a function of stellar mass are lower than observed. The discrepancy is worst for models in which the feedback is efficient. The negative slope in the relation between the sSFR and stellar mass is only reproduced by models for which feedback is inefficient in the observed mass range. Models without any efficient feedback still underpredict the sSFRs because their stellar masses are high. The only models that can reproduce the high values of the observed sSFRs are those with very efficient feedback in low-mass galaxies (i.e. models with high mass loading factors) and these models still only match the observations for the stellar masses corresponding to the halo mass at which the feedback is becoming inefficient. For higher stellar masses the sSFRs are again too low and the stellar mass function too high.

Thus, there is tension between the observed stellar mass function and the observed sSFRs. The high observed star formation rates are difficult to match unless feedback suddenly becomes inefficient at the lowest stellar masses for which observations are available ($M_* > 10^{9.5} M_\odot$). It cannot be inefficient in low-mass progenitor haloes though, because otherwise the stellar mass would already be too high, which would reduce the sSFR and would overpredict the stellar mass function. The feedback can also not remain inefficient as the stellar mass increases or else the stellar mass function would again be too high.

Our investigation clearly shows that winds driven by feedback from star formation determine the main properties of galaxies residing in haloes of a given mass.

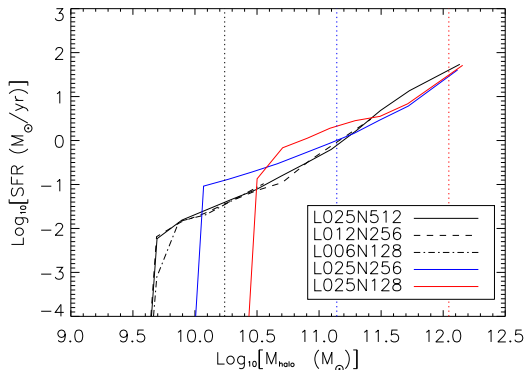


Figure 2.16: Median star formation rate as a function of halo mass at $z = 2$ for 5 simulations with different particle numbers and/or box sizes as indicated in the legend. The vertical dotted lines indicate the mass of 2000 dark matter particles in the simulations shown by the curves in the corresponding colours. At the low mass end, the median SFR falls to zero, as more than half of the haloes in a bin do not have gas particles with a density above the star formation threshold. Above a mass corresponding to 2000 dark matter particles per halo, the SFR as a function of halo mass is reasonably well resolved.

Even for a fixed amount of energy per unit stellar mass, variations in the sub-grid implementation of feedback from star formation provide us with considerable freedom. This freedom can possibly be exploited to match observations spanning a wide range of masses, which would provide the simulations with some of the attractions of semi-analytic models. However, this potential success comes also with the disadvantages of such models: the underlying physics would remain poorly understood. As higher resolution simulations become feasible, the need for subgrid models to generate galactic outflows in cosmological simulations will hopefully be removed.

Further improvement in our understanding of the physics that determines the global properties of galaxies will likely come from theoretical models and observations focusing on galactic winds. The physics of star formation is less crucial as the time-averaged, galaxy-wide star formation rates are regulated by the large-scale outflows.

Acknowledgements

We kindly thank Danilo Marchesini for useful discussions about the observations of the stellar mass function and for providing his results in digital form. We furthermore are grateful to *OWLS* collaboration for useful discussions about and comments on this work. The simulations presented here were run on Stella, the LOFAR BlueGene/L system in Groningen and on the Cosmology Machine at the Institute for Computational Cosmology in Durham as part of the Virgo Consortium research programme.

Appendix A. Numerical convergence tests

In order to investigate the convergence of our results with respect to box size and resolution, the reference model is run in 5 different simulations, together making up complete sets of three simulations with the same box size, but different resolution and another set of three simulations with constant resolution but different box sizes. The simulation that is common to both, is the reference simulation used throughout the paper. We will denote the simulations as ‘*LXXXNYYY*’, where *XXX* is the size of the simulation box in comoving h^{-1} Mpc and *YYY* is the number of particles per spatial dimension (for both dark matter and baryons we use YYY^3 particles). So, the reference simulation here is ‘*L025N512*’.

The two sets are:

- *L025N512*, *L012N256* and *L006N128*, which all have the same numerical resolution, but a different box size, varied in steps of a factor of two. These three runs will be shown in black lines with different line styles (solid, dashed and dot-dashed, respectively).
- *L025N512*, *L025N256* and *L025N128*, which have the same box size, but different resolutions. The mass and spatial resolutions change by a factor of 8 and 2, respectively. These will be shown by black, blue and red solid lines, respectively.

In this Appendix we will show all Friends-of-Friends haloes identified in the simulation that have at least 20 dark matter particles, which, as we will show, is not enough to obtain converged results.

Fig. 2.16 shows that the box size has no influence on the star formation rates, as the lines with different line styles (which corresponds to runs with the same resolution but different box sizes) all overlap. The only effect is in the sampling of the mass function: in a bigger box higher halo masses are sampled. This is as expected: the dense regions of haloes do not care about the size of the universe

one simulates (provided it is large compared with the objects themselves), but rare objects can only be sampled in sufficiently large boxes.

Mass resolution is an issue when simulating star formation, as can be seen by comparing the black, red and blue solid curves in Fig. 2.16. The minimum non-zero SFR a halo can have corresponds to having one star forming particle at the star formation threshold. For simulations with lower particle masses this minimum SFR is lower (the minimum SFR in the highest resolution simulation is $6.2 \times 10^{-4} = 10^{-3.2} M_{\odot} \text{ yr}^{-1}$ and scales linearly with particle mass). For the lowest halo masses for which the median star formation rates are non-zero, the SFR will be slightly overestimated. The overestimate results from the underestimate of the SFR at lower masses, which makes both gas consumption and gas removal through feedback less efficient. Because the lines all get close together at high masses, we conclude that the halo star formation rates converge at the high mass end. The unresolved star formation at early epochs (when a given halo is less massive) accounts for only a small fraction of the stellar mass in massive objects.

In Fig. 2.16 the vertical dotted lines denote 2000 times the dark matter particle mass in the simulations of the same colour. The halo star formation rates are reasonably converged above these halo masses, as can be seen by comparing the blue and black curves (highest versus eight times lower spatial resolution) to the right of the vertical blue dotted line. The halo mass regime where the median star formation rate is zero, because more than half the haloes do not have any gas particles with densities above the star formation threshold, is also removed when demanding a minimum number of 2000 dark matter particles per halo. The haloes are responsible for the sharp drop in the lowest mass bin.

The build-up of stellar mass is influenced by the SFR at all epochs prior to the epoch at which it is measured. As all haloes were initially small and thus poorly resolved, the early build up of stellar mass is underestimated. Indeed, Schaye et al. (2010) have already shown that our higher resolution simulations resolve the cosmic star formation rate at earlier epochs. We therefore expect that the convergence of the (s)SFR as a function of stellar mass is slightly worse than that of the SFR as a function of total halo mass.

Fig. 2.17 shows the same simulations as Fig. 2.16, but now we plot the specific star formation rate against halo stellar mass (SFR/M_{*}). The vertical cut-off at the low mass ends corresponds again to haloes for which the median star formation rate is zero. At slightly higher stellar masses the specific star formation rate decreases with stellar mass, but in this regime the results depend strongly on resolution. The same three regimes as in Fig. 2.16 can be identified, plus one additional effect: as the resolution is decreased, a fixed stellar mass corresponds to a smaller halo mass and hence a lower star formation rate. The mass range over which the sSFR is an increasing function of stellar mass starts at a stellar mass corresponding to

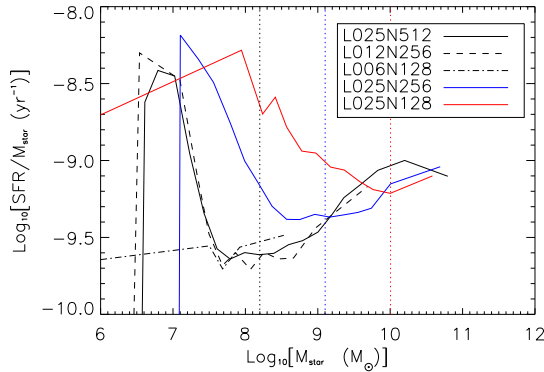


Figure 2.17: The median specific star formation rates of haloes as a function of their stellar mass at $z = 2$ for 5 simulations with different particle numbers and/or box sizes as indicated in the legend. The vertical dotted lines indicate the mass corresponding to 100 star particles in the simulations shown by the curves in the corresponding colours. The sharp cut-off at low masses again stems from the fact that there is a minimum to the (non-zero) SFR. Right of the vertical dotted lines the specific star formation rates are reasonably well converged.

about 100 star particles, as indicated by the vertical dotted lines. This is also the regime for which the results become insensitive to resolution, as can be seen by comparing the solid black and blue lines rightwards of the blue, dotted line and by comparing the solid blue and red curves rightwards of the red, dotted line. We note that, as expected, the same trends are found for $\text{SFR}/M_{\text{gas}}$.

Fig. 2.18 shows the stellar mass fraction as a function of halo mass for the same set of simulations as used in Fig. 2.16. The vertical dotted lines indicate our adopted resolution limit of 2000 dark matter particles. The diagonal dotted lines indicate the stellar mass fraction for haloes consisting of 100 star particles, which is our resolution limit for plots with stellar mass on the horizontal axis. The fact that for a given resolution (i.e. colour), the solid curve intersects the two dotted lines in nearly the same place, implies that the cuts of 100 star particles and 2000 dark matter particles are very comparable for the set of simulations of the reference model at high resolution. Above this resolution limit of 2000 dark matter particles, the stellar mass fractions are nearly converged. At lower resolution, a minimum number of dark matter particles is a more stringent cut than a minimum number of star particles. Throughout the paper we use a minimum number of dark matter particles when we plot quantities as a function of halo mass.

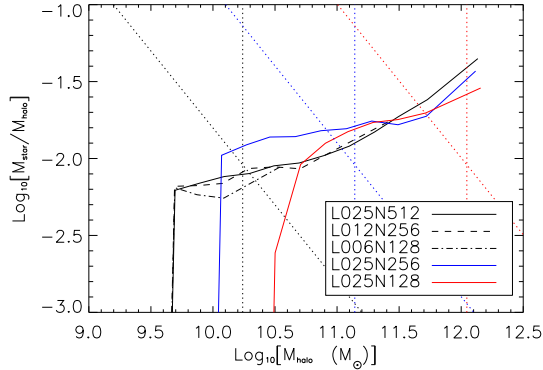


Figure 2.18: Median stellar mass fraction as a function of halo mass at $z = 2$ for 5 simulations with different particle numbers and/or box sizes as indicated in the legend. The vertical dotted lines indicate the mass corresponding to 2000 dark matter particles in the simulations shown by the curves in the corresponding colours. The diagonal black dotted line indicates the relation for haloes with 100 star particles (the cut that is made in the rest of the paper where relations with stellar mass are shown). As can be seen, in the highest resolution simulation, the cuts made throughout this paper in minimum number of dark matter particles and the minimum number of star particles roughly correspond to each other. At lower resolutions, the cut in dark matter particle number is more stringent.

Although we will not show them here, we found that stellar mass functions are already converged with respect to mass resolution for haloes with 10 star particles or more. Cuts in the number of dark matter particles, or in the total particle number, are much more delimiting. One would throw away many more haloes if a total particle number cut is made instead of a star particle number cut (the stellar mass function is only as nicely converged at $z = 2$ for haloes with 500 particles of all types together as it is for a minimum of 10 star particles). To be consistent with the rest of the results show in the paper, we only plot stellar mass functions for haloes with at least 100 star particles.

In general, every relation plotted in this paper demands its own particle number cuts for convergence. We find that 2000 dark matter particles or 100 star particles per halo results in good convergence for most of the quantities. These two cuts are therefore adapted throughout the paper. To avoid biasing the results, we impose a cut of 2000 dark matter particles when looking at relations with total halo mass and of 100 stars particles when investigating correlations with stellar mass.

Appendix B. The energy and momentum in momentum driven wind models

In this Appendix we will look in more detail into the energy and momentum injection in the ‘momentum driven wind models’, such as those used by Oppenheimer & Davé (2006, 2008) and in this work. Inspired by Murray et al. (2005), these models represent galactic winds which are driven by the radiation pressure from the galaxies’ stellar population on the dust grains in the galactic outflows. As such, the amount of energy per unit stellar mass formed is not constant, but scales with galaxy mass as $E_w \propto M^{1/3}$. The total momentum used in the wind models is chosen so that the the total star formation rate density of the universe is fit, and is not restricted by what is actually available from SNe and radiation pressure.

Here, we will compare the momentum that goes into the wind, as compared to the momentum from the SNe themselves, as well as that resulting from the radiation pressure on the dust by the underlying stellar population. As default parameters for the SN ejecta we take that $10 M_\odot$ of material is flowing out at a velocity of 3000 km s^{-1} (Murray et al., 2005). This sets both a kinetic energy and a momentum for this outflow.

For the radiation pressure, which results in an available momentum for the outflow, we will use the spectral synthesis models of Bruzual & Charlot (2003, (BC03)). We make the following assumptions:

1. Radiation is not scattered back and forth. In principle, from back-scattering a large gain in momentum can be obtained. We are talking here about stellar continuum radiation, which after the absorption by dust grains will be re-emitted at very long wavelengths, for which the optical depth is very low. The cross-section for this radiation to be back-scattered and be absorbed by another dust grain is very small. Only for extremely high physical densities, the shell that is driven will become optically thick for the thermal radiation of the dust grains. In that case, the diffusion of the photons outward may boost the momentum. This is a situation which can only be realized at the very early stages of driving the wind inside the molecular cloud, not at scales at which winds in the simulations are driven ($\sim \text{kpc}$).
2. All the radiation is used to drive an outflow. This, together with the previous point means that all the momentum in radiation is transferred to out flowing gas. Note that this is a very strong assumption, which makes the estimated outflow momentum from the radiation pressure an *upper limit*.
3. The driving radiation source is a simple stellar population of solar metallicity with a Chabrier (2003) IMF, the spectrum of which is well described by the

2.B. Energy and momentum in momentum driven winds

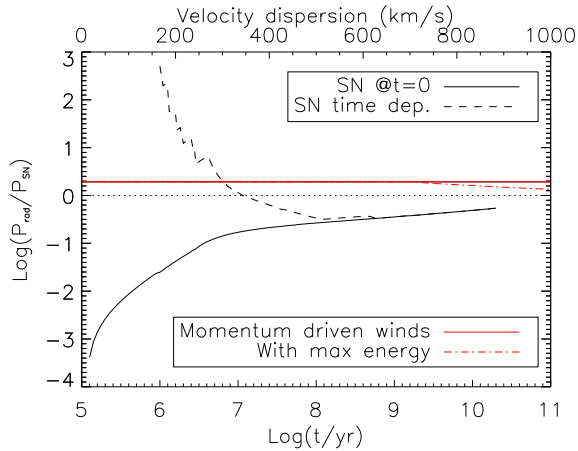


Figure 2.19: In black we show the ratio between the momentum available from radiation pressure and the momentum available from the supernova explosions themselves (assuming that $10 M_{\odot}$ is ejected at 3000 km s^{-1} per supernova event). The solid black line assumes that all SNe go off at $t = 0$, so it is the integral of the radiation pressure as a function of SSP age, normalized by the total momentum in SNe. The dashed line instead has the momentum from radiation normalized to the total momentum from SNe up to that age. In red we show the amount of momentum that is put into the winds in the momentum driven wind simulations. The ratio between the red line solid line and the black dashed line (about an order of magnitude at $t = 10^7 \text{ yr}$) is therefore the factor by which the momentum is boosted in the simulations compared to what comes from radiation. The top horizontal axis refers to the red dot-dashed line, which shows the momentum in winds in the model of Oppenheimer & Davé (2008), where the energy in the winds is limited to 2 times the energy available from SNe. This only becomes a small correction at velocity dispersions greater than 700 km s^{-1} . As the momentum from radiation is an upper limit, it is clear that the amount of momentum in the winds in the momentum driven wind simulations is unrealistically high.

high resolution spectra of the BC03 set of spectra for all ages.

In a time interval Δt , during which the source has luminosity L , the energy and momentum that the radiation can transfer to the gas are $E_{rad} = L \cdot \Delta t$ and $p_{rad} = L \cdot \Delta t/c$, respectively, where c is the speed of light.

In Fig.2.19 we show, as a function of age of the SSP, the total momentum the radiation can have transferred to the out flowing gas, up to that age. This value is normalized by the total amount of SN momentum, assuming the mass and velocity given above. The solid black line is under the assumption that all SNe go off at $t = 0$ (so normalized to the total available momentum from supernovae that result from the SSP), while the dashed black line follows the timed SN explosions (for all of which the same momentum is taken). This timed release is estimated from the number of neutron stars and black holes present in the sample according to the BC03 package. This adds up to the same number of SNe at the age where the lines meet ($t \sim 10^8$ yr). The red lines in the plot show the amount of momentum that is used in the simulations described in the paper. The solid horizontal line shows the momentum that is used in all momentum-driven wind models described in this paper. The model used in Oppenheimer & Davé (2008) limits the energy in the winds to be two times the energy available from SNe, which results in the red dot-dashed line, in haloes with velocity dispersions as shown on the top horizontal axis. This maximum to the energy makes little difference, and no difference in haloes of velocity dispersion lower than 700 km s^{-1} .

From Fig.2.19 we learn that the amount of momentum available from radiation is, even after the entire 20 Gyr lifetime of the SSP still falls short by a factor of a few, compared to the total momentum in the SN ejecta. Remember that the momentum from radiation is an upper limit. At the time all SNe just went off, there is a factor 7 difference between the two.

3

Disentangling galaxy environment and host halo mass

Abstract

The properties of observed galaxies and dark matter haloes in simulations depend on their environment. The term “environment” has, however, been used to describe a wide variety of measures that may or may not correlate with each other. Useful measures of environment include, for example, the distance to the N^{th} nearest neighbour, the number density of objects within some distance, or, for the case of galaxies, the mass of the host dark matter halo. Here we use results from the Millennium simulation and a semi-analytic model for galaxy formation to quantify the relation between different measures of environment and halo mass. We show that most of the environmental parameters used in the observational literature are in effect measures of halo mass. The strongest correlation between environmental density and halo mass arises when the number of objects is counted out to a distance of 1.5 – 2 times the virial radius of the host halo and when the galaxies/haloes are required to be relatively bright/massive. For observational studies this virial radius is not easily determined, but the number of neighbours out to $1 - 2 h^{-1} \text{Mpc}$ gives a similarly strong correlation with halo mass. For the distance to the N^{th} nearest neighbour the (anti-)correlation with halo mass is nearly as strong provided $N \geq 2$. We demonstrate that this environmental parameter can be made insensitive to halo mass if it is constructed from dimensionless quantities. This can be achieved by scaling both the minimum luminosity/mass of neighbours as well as the distance to the nearest galaxy/halo to the properties of the object that the environment is determined for. We show how such a halo mass independent environmental parameter can be defined for both observational and numerical studies. The results presented here will help future studies to disentangle the effects of halo mass and external environment on the properties of galaxies and dark matter haloes.

3.1 Introduction

The formation and evolution of galaxies depends on both internal and external processes ('nature vs. nurture'). Among the internal processes are radiative cooling and the formation of a multi-phase medium, formation and feedback from stars and accretion of gas onto and feedback from super-massive black holes. It is generally assumed that halo mass is the fundamental parameter that drives the internal processes for isolated galaxies. External processes are important because galaxies do not live alone in the Universe. Galaxy interaction can induce gravitational torques that can significantly alter the angular momentum structure of the matter in galaxies. This can for example lead to a starburst or to more rapid accretion onto the central black hole, which may trigger a quasar phase. Smaller galaxies may accrete onto the halo of a more massive galaxy. As a galaxy moves through the gaseous halo of a more massive galaxy it may lose gas due to ram pressure forces. Winds and radiation from nearby neighbours may also affect the evolution of a galaxy. To what extent the properties of galaxies are determined by internal and external processes is still an open question.

Even if halo mass were the only driver of galaxy evolution, galaxy properties would still be correlated with environment. Because peaks in the initial Gaussian density field cluster together, more massive galaxies will live close to each other ('galaxy bias'). A correlation between surrounding galaxy density and internal galaxy properties therefore does not necessarily imply a causal relation between the two.

Early, analytic models predicted that the clustering of haloes depends only on their mass (Kaiser, 1984; Cole & Kaiser, 1989; Mo & White, 1996), while later papers have shown that clustering also depends on properties like formation time (Gao et al., 2005), concentration, substructure content, spin and shape, even for fixed mass (e.g. Harker et al., 2006; Wechsler et al., 2006; Bett et al., 2007; Gao & White, 2007; Jing et al., 2007; Macciò et al., 2007; Wetzel et al., 2007; Angulo et al., 2008; Faltenbacher & White, 2010). All dependencies other than the one with halo mass are, however, second-order effects. Lemson & Kauffmann (1999) already showed that the only property of a dark matter halo that correlates with the (projected) number density of surrounding galaxies is its host halo mass. Other properties like spin parameter, formation time and concentration do *not* depend on the surrounding dark matter density. The formation time and the halo merger rate are found to depend on environment (Gottlöber et al., 2001; Sheth & Tormen, 2004; Fakhouri & Ma, 2009; Hahn et al., 2009).

Both observations and simulations have difficulty disentangling halo mass from the external environment. The two are correlated (higher mass haloes live, on average, in denser environments) and finding an environmental parameter that does

not correlate with halo mass is non-trivial. Of course, the mass of the dark matter halo hosting a galaxy is important for the evolution of that galaxy, so halo mass is as good an environmental parameter as any other. One would, however, like to be able to distinguish halo mass (the “internal environment”) from the environment on large scales (the “external environment”). It is not a priori clear whether the environmental parameters used in literature measure halo mass, and if so, whether they measure *only* halo mass, or whether they are also, or predominantly, sensitive to the external environment.

Observationally, halo mass is hard to determine. Group catalogues, abundance (or stellar mass - halo mass) matching, and weak gravitational lensing all provide statistical measures of halo mass. Strong gravitational lensing is another way of measuring the total mass of a massive lens system. Nonetheless, most observational data sets will have to do without dark matter halo mass and define environmental parameters based on the distribution of visible matter (usually stellar luminosity) only.

Many observational studies have, nevertheless, investigated the effect of the environment on the physical properties of galaxies. In general, galaxies form their stars earlier and faster in higher density environments (e.g. Lewis et al., 2002; Baldry et al., 2004; Balogh et al., 2004a,b; Kauffmann et al., 2004; Thomas et al., 2005; Smith et al., 2006) and their galaxy morphologies become more (pressure support dominated) early type, as opposed to (rotation dominated) late type (e.g. Dressler, 1980; Dressler et al., 1997; Wilman et al., 2009). From observations alone it is very hard to judge whether these trends are driven mostly by halo mass or whether other halo properties and/or large-scale environment play an important role. Crain et al. (2009) find, using the *GIMIC* simulations that halo mass is the only driver of the star forming properties of galaxies. As in observations environment is usually contrasted with stellar mass (rather than halo mass), an observationally based distinction between mass and environment may tell us more about the stellar mass – halo mass relation than about the difference between external environment and halo mass.

In simulations, halo mass (and other halo parameters) are readily available. From simulations much ‘cleaner’ definitions of environment can be obtained, as the distance to other objects is very well known in three dimensions, contrary to observations which can only provide a precise distance perpendicular to the line of sight. Radial velocity differences give an indication of the distance along the line of sight, but peculiar velocities complicate a precise radial distance measure.

Many different measures of environment have been used in the literature. Some are closely related by construction, while the relation between others is more obscure. In this paper we compare several popular indicators of environments. The aim is to investigate which indicators correlate strongly with each other and with

halo mass and which ones do not. We measure environmental parameters using a semi-analytic model for galaxy formation constructed on the merger tree of dark matter haloes formed in the Millennium Simulation (Springel et al., 2005), so that we also have halo masses available. We will present environmental parameters that measure halo mass, but are insensitive to external environment, along with environmental parameters that are insensitive to halo mass. These can be used for studies that aim to separate the effect of halo mass and external environment. We will show that most of the environmental indicators used in literature measure predominantly halo mass. In the remainder of the paper we will use the term ‘environment’ whenever we mean to quantify distances to nearby galaxies, surrounding galaxy densities etc., but never when referring to halo mass, in order to clearly distinguish the two.

This paper is organized as follows. Section 3.2 gives a short overview of the literature on environmental parameters, both from observations and simulations. In Section 3.3 we determine some of the often used environmental parameters and investigate their correlation with host halo mass. The strength of the correlation with halo mass depends on the distance scale used in the environmental parameters, as we will show in Section 3.4. In Section 3.5 we discuss how to construct an environmental parameter that is independent of halo mass. Finally, we conclude in Section 3.6.

3.2 Popular environmental parameters

The study of the effect of the environment on the evolution of galaxies has undergone considerable progress through large galaxy surveys, like the Sloan Digital Sky Survey (SDSS; Stoughton et al., 2002) and (z)COSMOS (Scoville et al., 2007; Lilly et al., 2007). Many different definitions of environmental density exist. Observationally, the density around galaxies must usually be based on the distribution of the galaxies themselves, as the full distribution of mass is very hard to measure reliably. In observational studies two slightly different flavours are very often used: one in which the number density of galaxies within a fixed distance are counted, and one in which the distance to the N^{th} nearest neighbour is measured. Table 3.1 contains a short summary of the literature on the environmental dependence of galaxy properties, both from observations and from simulations. We will expand on these in this section and will study some of these in more detail using the galaxy catalogues in the Millennium database in the next section.

For the environmental parameters it is important, as we will show below, whether the masses of the other galaxies used to measure the environmental have a fixed physical lower limit (or luminosity), or whether the minimum mass is a fixed

3.2. POPULAR ENVIRONMENTAL PARAMETERS

fraction of the mass of the galaxy one wants to know the environment of. It also matters whether the distance out to which the environment is measured is fixed in absolute terms or whether it is fixed relative to some length scale related to the galaxy in question (e.g. the virial radius of its host halo). In Table 3.1 we indicate for environmental parameter listed (described in the first column) out to what distance (or a distance equivalent parameter) the environment is measured (second column), and whether the minimum mass/luminosity of the galaxies used for the environmental estimate is fixed in absolute terms or whether it is a fixed fraction of the mass/luminosity of the galaxy in question (if applicable, third column). The final column lists references to papers employing the parameter. From Table 3.1 it is clear that only very few papers take minimum masses of neighbours and/or distances relative to properties of the galaxy's host halo.

Two main classes of observational parameters can be identified: those which measure the number of galaxies out to a given distance, and those which measure the distance out to a given N^{th} neighbour. Note that using the number of galaxies out to a given distance is equivalent to using the number density of that same sample of galaxies (and the same holds for the distance to N^{th} nearest neighbour and the density of galaxies in the volume out to the N^{th} nearest neighbour). These two broad classes of methods are not identical, but the difference is subtle. In high density regions the N^{th} neighbour is, on average, closer by and the scale on which the environment is measured is therefore smaller, while the other class of methods measures the density on a fixed scale.

The environmental parameters used in simulation studies are sometimes similar to the ones used for observations, but can also be very different. Using a similar definition allows one to directly compare models and observations. However, with the full (dark matter and baryonic) density field available, simulators can also determine parameters like the total amount of mass in spheres around the galaxy in question. Such quantities might influence the evolution of a galaxy, but are difficult or impossible to obtain observationally.

It is well known that high mass galaxies preferentially live in higher density environments. A correlation between halo mass and environmental density is therefore expected. For example, Kauffmann et al. (2004) use a semi-analytic model of galaxy formation to show how their measure of environmental density (number of galaxies within $2 h^{-1}\text{Mpc}$ projected, and a redshift difference less than 1000 km s^{-1}) correlates with halo mass. It is, however, unlikely that halo mass is the only characteristic of the environment that matters. With that in mind, Fakhouri & Ma (2009) have tried to construct an environmental parameters that does not scale with halo mass. They found that the mean over-density in a sphere of 7 Mpc, excluding the mass of the halo, gives the most mass-independent parameter of the three parameters they studied. They did not quantify the degree of correlation, but their

CHAPTER 3. DISENTANGLING ENVIRONMENT AND HALO MASS

Table 3.1: Overview of environmental parameters that are frequently used in literature. They are grouped by the different ways of determining out to which distance the environment is measured either in observational or simulation studies. The first column specifies the environmental parameter, and the second and third column indicate out to what distance the environment is measured and whether the minimum mass/luminosity is fixed or scales with the galaxy in question. The fourth column specifies the references for the papers: 1: Dressler (1980), 2: Postman & Geller (1984), 3: Gómez et al. (2003), 4: Goto et al. (2003), 5: Whitmore & Gilmore (1991), 6: Whitmore et al. (1993), 7: Weinmann et al. (2006), 8: Cooper et al. (2005), 9: Cooper et al. (2006), 10: Cooper et al. (2008), 11: Balogh et al. (2004a), 12: Balogh et al. (2004b), 13: Baldry et al. (2006), 14: Bamford et al. (2009), 15: Cassata et al. (2007), 16: Pimblet et al. (2002), 17: Lewis et al. (2002), 18: Blanton et al. (2003b), 19: Blanton et al. (2003a), 20: Hogg et al. (2003), 21: Hogg et al. (2004), 22: Blanton et al. (2005), 23: Kauffmann et al. (2004), 24: Blanton & Berlind (2007), 25: Kovač et al. (2010), 26: Fakhouri & Ma (2009), 27: Espino-Briones et al. (2007), 28: Ishiyama et al. (2008), 29: Lemson & Kauffmann (1999), 30: Harker et al. (2006), 31: Hahn et al. (2009), 32: Faltenbacher (2009), 33: Ellison et al. (2010), 34: Wilman et al. (2010), 35: Macciò et al. (2007), 36: Crain et al. (2009), 37: Hester & Tasitsiomi (2010), 38: Abbas & Sheth (2005), 39: Maulbetsch et al. (2007), 40: Wang et al. (2007)

Parameter	Distance related parameter value	Minimum mass/luminosity	References
<i>From observations</i>			
(Projected) galaxy number density	Average of nearest 10 galaxies	$m_V < -16.5$ $M_V < -20.4$ $M_B < -17.5$	1, 5, 6 6 2
Cluster/Group-centric radius	-	$M_r < -20.5$	3, 4
	-	$m_V < -16.5$ $M_V < -20.4$	5 6
	Scaled to the virial radius	$r < 17.77$	7
Projected galaxy number density out to the N^{th} nearest neighbour with a maximum radial velocity difference Δv	$N = 3, \Delta v = 1000 \text{ km s}^{-1}$	$R < 24.1$	8, 9, 10
	$N = 4.5$	$M_R < -20$	11 - 15, 33
	$N = 5, \Delta v = 1000 \text{ km s}^{-1}$	$M_r < -20.6$	11
	$N = 5, \Delta v = 1000 \text{ km s}^{-1}$	$M_r < -20$	12
	$N = 4.5, \Delta v = 1000 \text{ km s}^{-1}$	$M_r < -20$	13, 14
	$N = 10$	$I < -24$	15
	$N = 4.5, \Delta v = 1000 \text{ km s}^{-1}$	$M_r < -20.6$	33
	$N = 10$	$M_V < -20$	16
Galaxy number density in sphere of proper radius r	$r = 8 h^{-1} \text{ Mpc}, \Delta v \leq 800 \text{ km s}^{-1}$	$r < 17.77$	18 - 20
	$r \approx 1 h^{-1} \text{ Mpc}$	$r < 17.77$	22
Number of neighbours in cylinders with projected radius r	$r = 2 h^{-1} \text{ Mpc}, \Delta v = 1000 \text{ km s}^{-1}$	$r < 17.77$	23
	$r = 1 h^{-1} \text{ Mpc}, \Delta v$ corresponding to 8 Mpc	$r < 17.77$	21
	$r = 0.1 - 10 h^{-1} \text{ Mpc}, \Delta v = 1000 \text{ km s}^{-1}$	$M_{0.1r} - 5 \text{Log}_{10} h < -19$	24
	$r = 1 - 10 h^{-1} \text{ Mpc}, \Delta v = 1000 \text{ km s}^{-1}$	$I_{AB} < 25$	25
	$r = 0.5, 1, 2 h^{-1} \text{ Mpc}, \Delta v = 1000 \text{ km s}^{-1}$	$M_r < -20$	34
Projected galaxy number density in annuli	$1 < R/(h^{-1} \text{ Mpc}) < 3$	$r < 17.77$	23
	$\{0.5, 1, 2\} < R/(h^{-1} \text{ Mpc}) < \{1, 2, 3\}$	$M_r < -20$	34
<i>From simulations</i>			
Halo mass	-	$M > 2.35 \times 10^{10} M_{\odot}$	26
Number of neighbours in spheres of radius R	$R = 2 h^{-1} \text{ Mpc}$	$V_{\text{max}} > 120 \text{ km s}^{-1}$	37
Mass or density in spheres of radius R	$R = 5 h^{-1} \text{ Mpc}$	-	27, 28
	$R = 5, 8 h^{-1} \text{ Mpc}$	-	38
	$R = 7 h^{-1} \text{ Mpc}$	-	26
	$R = 1, 2, 4, 8 h^{-1} \text{ Mpc}$	-	35, 39
	$R = 18, 25 h^{-1} \text{ Mpc}$	-	36
Matter density in spherical shells	$2 < R/(h^{-1} \text{ Mpc}) < 5$	-	29, 30, 31
	$2 < R/(h^{-1} \text{ Mpc}) < 7$	-	26
	$R_{\text{FOF}} < R < 2 h^{-1} \text{ Mpc}$	-	26
	$R_{\text{vir}} < R < 3R_{\text{vir}}$	-	40
Average mass density of surrounding halos	$N = 7$	$200 < V_{\text{max}}/\text{km s}^{-1} < 300$	32
Distance to nearest halo with minimum mass	-	$M_2/M_1 > 3$	28

3.3. ENVIRONMENTAL PARAMETERS AND THEIR RELATION TO HALO MASS

plots indicate a weak, but non-negligible correlation with host halo mass. Observationally, this quantity cannot be determined. As far as we are aware no study to date has found a measure of environment that is independent of halo mass.

3.3 Environmental parameters and their relation to halo mass

In this section we will investigate the relation between several environmental parameters and the host halo mass. First we will briefly summarize the main characteristics of the synthetic galaxy populations used. For the environmental parameters discussed, we will distinguish between the ‘ideal case’ in which the three dimensional locations and the masses of all galaxies are known (as in simulations), and the case in which only projected distances and velocity differences can be measured and only luminosities are available, as is the case for observations.

3.3.1 Simulations

We will compare different environmental parameters using the galaxy catalogue constructed using the semi-analytic model of De Lucia & Blaizot (2007, see also Croton et al. 2006), run on the dark matter-only Millennium Simulation (Springel et al., 2005). The Millennium Simulation follows the evolution of the dark matter distribution using 2160^3 particles in a periodic volume of $500 h^{-1}\text{Mpc}$ from very high redshift down to redshift 0. The model of De Lucia & Blaizot (2007) uses recipes for the evolution of the baryons inside dark matter haloes and is based on the halo merger trees constructed using the halo catalogues of the Millennium Simulation. The model predicts the galaxies’ locations, physical properties such as their stellar masses and star formation histories and observables like colours and luminosities. The model is calibrated to reproduce the redshift zero luminosity function in the K - and b_J -bands. De Lucia & Blaizot (2007), De Lucia et al. (2007) and Kitzbichler & White (2007) showed that this model reproduces many other observed properties of the galaxy population in the local Universe (e.g. the luminosity function at higher redshift, the colour distributions, the stellar mass function and the clustering properties). We will only use the $z = 0$ results.

We take into account all galaxies with stellar masses in excess of $10^{10} M_{\odot}$. This is roughly the same lower mass limit as Fakhouri & Ma (2009) use (they use $1.2 \times 10^{12} M_{\odot}$ total mass). The reason for this choice is an estimate of the resolution limit of these simulations. Boylan-Kolchin et al. (2009) show that the subhalo abundance of haloes in the Millennium Simulation is converged for subhaloes more massive than about $10^{11} M_{\odot}$, roughly independent of parent halo mass (as long as

the parent mass is larger than $10^{12}M_{\odot}$). Guo et al. (2010) also investigate the subhalo abundance convergence of the Millennium Simulation. They compare the dark matter halo mass functions for main- and subhaloes together and conclude that halo and subhalo abundance is converged for $M > 10^{12.1}M_{\odot}$. These halo masses were matched by Guo et al. (2010) to the stellar mass function from the seventh data release of SDSS from Li & White (2009), from which they conclude that the observed galaxies with stellar mass $M_* \gtrsim 10^{10.2}M_{\odot}$ reside in converged haloes. The exact number of neighbours counted in some volume depends on the lower stellar mass limit for galaxies in the sample (or, correspondingly, the flux limit of the survey), but as we will show, the scalings and correlations are usually not sensitive to this lower limit.

3.3.2 The ideal case: using 3-dimensional distances and masses

We will use the simplest version of both classes of observationally determined parameters: the number of galaxies, N_R , within some volume with radius R and the distance to the N^{th} nearest neighbour, R_N . Parameters derived from these numbers (such as the number density of galaxies within that volume, etc.) will obey the same qualitative conclusions.

In Fig. 3.1 we show the correlations between host (Friends-of-Friends) halo mass and three definitions of environment: the number of galaxies within 1.5 virial radii of the galaxies' host haloes, the number of galaxies within $1 h^{-1}\text{Mpc}$, and the distance to the fourth nearest neighbour (left to right). While $N_{1\text{Mpc}/h}$ and particularly $N_{1.5R_{\text{vir}}}$ are strongly correlated with halo mass over the full mass range, halo mass only varies with R_4 for $R_4 \lesssim 2h^{-1}\text{Mpc}$ (corresponding to $M < 10^{13.5}M_{\odot}$).

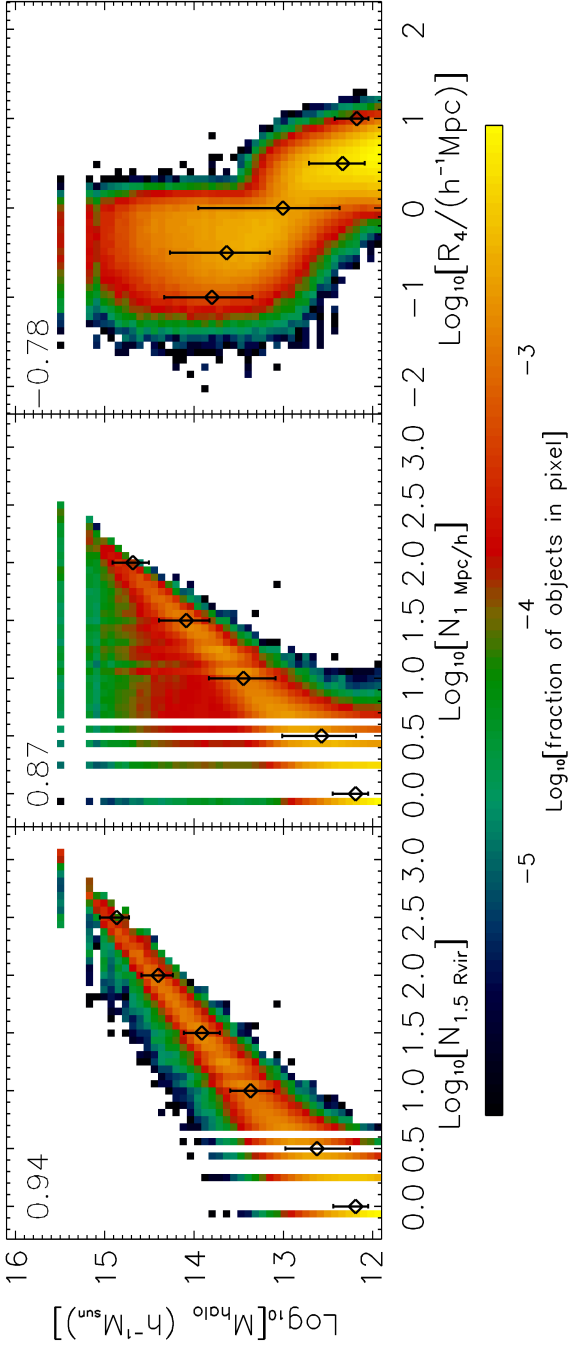


Figure 3.1: The correlations between halo mass and three environmental parameters: the number of galaxies within $1.5 R_{\text{vir}}$ (left panel), the number of galaxies within $1 h^{-1} \text{Mpc}$ (middle panel) and the distance to the fourth nearest neighbour (right panel) for all galaxies with $M_* > 10^{10} M_{\odot}$. The numbers printed in the top-left of each panel indicate the Spearman rank correlation coefficient and the diamond symbols and error bars show the binned medians and the 16th and 84th percentiles (for Gaussian distributions this would be $\pm 1\sigma$) of the distribution. All three parameters are a measure of halo mass. From left to right the correlations with halo mass decrease in strength.

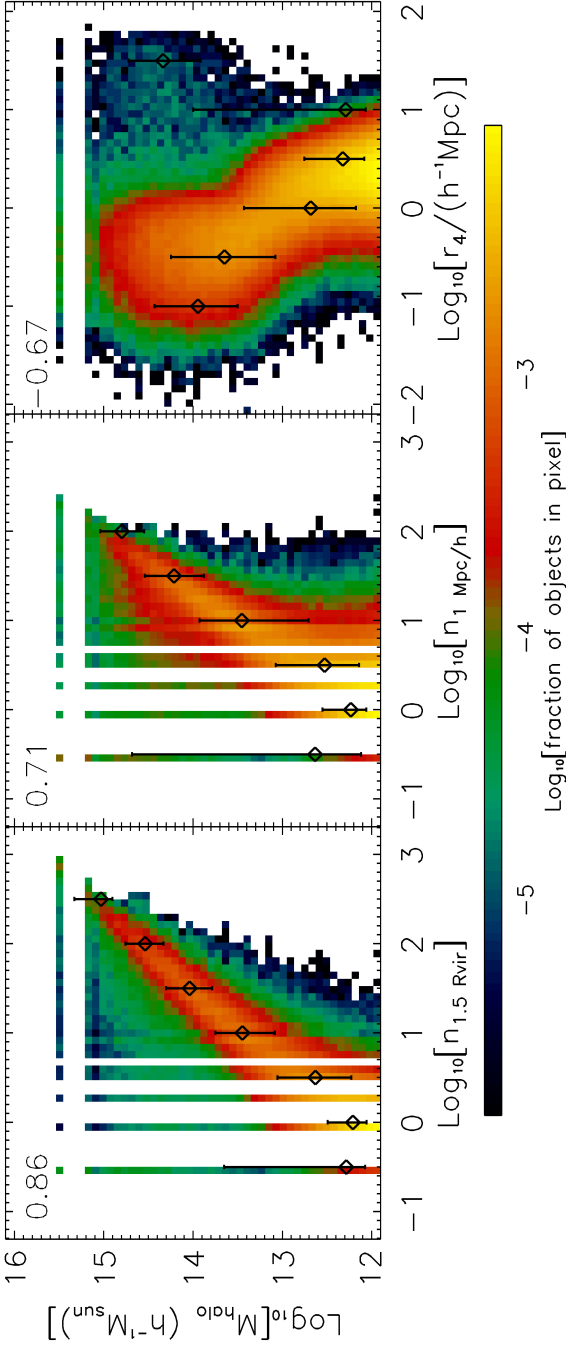


Figure 3.2: As Fig. 3.1, but now for observable versions of the environmental parameters: K -band luminosities rather than stellar masses, projected distances and a cut in redshift difference rather than 3-D separations for all galaxies with $K < -23$. For the left panel, the virial radii of the host haloes still need to be known. The galaxies with $n < 1$ are placed at $\text{Log}_{10} n = -0.5$ for illustrative purpose. The correlations are slightly weaker than the ones found for the ideal case (Fig. 3.1), mainly due to projection effects, which make galaxies populate the regions in the plots which were unoccupied in Fig. 3.1. The correlations are, however, still strong.

3.3. ENVIRONMENTAL PARAMETERS AND THEIR RELATION TO HALO MASS

Number of galaxies within a given distance

If the distance out to which galaxies are counted is scaled to the virial radius of the halo that the galaxy resides in, then the correlation between halo mass and environment is very strong, as is shown in the left panel of Fig. 3.1. Because the region within which galaxies are counted grows with halo mass, a more or less constant fraction of the satellites is counted. A fixed fraction of all satellites is a number of satellites that grows roughly linearly with halo mass, resulting in a very tight correlation. This can be understood in terms of the results found by Gao et al. (2004): the fraction of the mass in subhaloes, the distribution of subhaloes and the shape of the subhalo mass function are independent of host halo mass, while the normalization (so the total number of and total mass in subhaloes) scales (to first order) linearly with halo mass. The number of subhaloes (and thus satellite galaxies) within a radius that is fixed relative to the virial radius therefore grows roughly linearly with halo mass. This makes the parameter $N_{1 \text{ Rvir}}$ a very strong measure of halo mass.

A slightly weaker correlation exists between halo mass and the number of galaxies within a fixed physical distance, as shown in the middle panel of Fig. 3.1 (for a distance of $1 h^{-1} \text{Mpc}$). The upper envelope is populated by the central galaxies in the sample, while the satellites form the less tightly correlated cloud below the relation of the centrals. At the high mass end there are more galaxies with $M_* > 10^{10} M_\odot$ per halo, causing the correlation between $N_{1 \text{Mpc}/h}$ and M_{halo} to weaken.

Distance to the N^{th} nearest neighbour

In the right panel of Fig. 3.1 we show the correlation between the host halo mass and the distance to the fourth nearest neighbour, R_4 (which is very often used observationally, see Table 3.1). The distance R_4 decreases with halo mass, because more massive haloes are on average found in denser environments.

For halo masses $M > 10^{13.5} M_\odot$ the correlation between R_4 and M becomes much weaker. This behaviour arises from the fact that for low halo masses the 4th nearest neighbour (with $M_* > 10^{10} M_\odot$) resides in another halo, whereas at high masses we are counting galaxies within the same halo. The transition between the two regimes depends on the rank n : for higher ranks, the jump occurs at higher halo mass.

The three parameters displayed in Fig. 3.1 all depend on three-dimensional distances. We will now proceed to investigate parameters that are observationally more feasible.

3.3.3 The realistic case: using projected distances and luminosities

Observationally we have no access to the three-dimensional separations between galaxies. Instead, one measures distances projected on the sky and differences in redshift. Moreover, while luminosities are readily available, stellar mass determinations depend on SED modelling, which comes with considerable uncertainty. We will now investigate to what extent the use of observables weakens the correlations compared with the ‘ideal cases’ discussed in Section 3.3.2. As is done in many observational studies (see Table 3.1) we will only make use of galaxies with redshifts that are within 1000 km s^{-1} of the redshift of the galaxy for which the environment is determined. We include both the Hubble flow and peculiar velocities in our calculation of the redshifts. For reference, a velocity difference of 1000 km s^{-1} corresponds to a distance of $10 h^{-1} \text{ Mpc}$ if the peculiar velocity difference is zero. We will denote the parameters using the same symbols as we used for the 3-D distance variants, but with lower case letters. For example, r_4 denotes the projected distance to the fourth nearest neighbour (using only galaxies within the redshift difference cut). We only include galaxies with an absolute K -band magnitude smaller than -23 , which corresponds to $M_* \approx 10^{10.2} M_\odot$. This results in a slightly smaller sample than the one used before. For the sample of galaxies with $M_* > 10^{10} M_\odot$, the luminosity function shows signs of incompleteness at magnitudes fainter than $K = -23$.

In Fig. 3.2 we show the dependence of the parameters similar to those used in Fig. 3.1, but using projected distances and luminosities rather than 3-D distances and stellar masses. Note that the left panel still requires knowledge of the virial radius of the host halo of the galaxy and is therefore hard to determine observationally (we left it in for completeness). The virial radius can be estimated if one has a group catalogue available, like the one by Yang et al. (2007) who grouped galaxies using a friends-of-friends like algorithm. The total luminosities of the groups are then ranked and matched to a ranked list of halo masses, drawn from a halo mass function sampled in a volume equal to that of the survey. This procedure results in the assignment of a host halo mass to all galaxies in the sample. However, if such a catalogue is available, then the halo mass is of course just as well known as the virial radius, so using this environmental indicator as a measure of halo mass is not very useful.

In the middle panel of Fig. 3.2 we show the halo mass as a function of the number of galaxies with a projected distance less than $1 h^{-1} \text{ Mpc}$, with a redshift difference less than $\pm 1000 \text{ km s}^{-1}$ and with $K < -23$. Compared with the 3-D version, there are now more low mass galaxies with a high number of neighbours. This is due to projection effects. We note that the correlation coefficient is still very high (≈ 0.71), so we can conclude that this environmental indicator is a strong

3.3. ENVIRONMENTAL PARAMETERS AND THEIR RELATION TO HALO MASS

indicator of host halo mass. The horizontal scatter (in environmental parameter for fixed halo mass) at low halo masses (roughly 0.3 dex upwards and downwards in number of neighbours) is dominated by the projection effects, while at high masses the scatter (0.2 dex upwards, 0.5 dex downwards in number of neighbours within the projected distance) is mainly caused by satellites in the outskirts of the halo. The scatter in the environmental indicator is smallest for halo masses of about $10^{14} M_{\odot}$, where it is roughly 0.2 dex both upwards and downwards. For a given n_1 Mpc/h the spread in halo masses is small for low and high values of the environmental indicator (roughly 0.3 dex) and highest for values of about 10 neighbours within this distance ($\gtrsim 0.5$ dex in halo mass) and is roughly symmetrical.

In the right panel of Fig. 3.2 we show the projected distance to the fourth nearest neighbour with $K < -23$. Because of projection effects the bi-modal behaviour visible in the right panel of Fig. 3.1 has been smeared out. The correlation with host halo mass is therefore slightly weaker. Because of the discontinuity in the distribution, the correlation coefficient is a function of the masses (both galaxy stellar mass and host halo mass) of the objects that are taken into account.

3.3.4 A multi-scale approach

Wilman et al. (2010) recently measured the number density of galaxies in concentric rings in order to investigate trends in the $u - r$ colour distribution of galaxies with environment at several distance scales (for given small-scale density, if desired). They included all galaxies from the fifth data release of SDSS with magnitude brighter than 17.77 in the r -band and with a mean surface brightness within the half-light radius of $\mu_r \leq 23.0$ mag arcsec $^{-2}$. The number density of galaxies was determined in rings with radii fixed in physical coordinates. In this approach neither the mass nor the distance out to which the environment is determined scales with the properties of the galaxy in question. We therefore expect that these measures of environment vary strongly with halo mass.

The correlation coefficient for the density in annuli with halo mass is roughly 0.5, and depends on both the width and the radius of the annulus, such that smaller radii (within ~ 0.5 Mpc) have larger correlation coefficients and wider annuli mostly show weaker correlations. The power of the method of Wilman et al. (2010) lies in the ability to measure residual trends of galaxy properties with large-scale (annular) environment, while controlling for the environment on some smaller scale (i.e. the projected number density in the inner circle, using the same definitions as our n parameter above). The samples are constructed by taking all galaxies for which the number density of galaxies within the inner radius of the annulus fall within some bin, and are therefore comparable to horizontal slices through the middle panel of Fig. 3.2. From this figure we can see that in such a slice, a very large

range of halo masses (comparable to the full range of halo masses in the catalogue) is still present.

As an example, we show in Fig. 3.3 the correlation between halo mass and the number of galaxies in annuli with an inner and outer radius of 1 and 2 Mpc, respectively, for three narrow bins of the number of galaxies within 1 Mpc (projected distance, within a redshift difference of 1000 km s^{-1}). Each bin contains 1/8 of all the galaxies, where the lowest bin shown (the second panel from the left) corresponds to the lowest 1/8 of the total galaxy population, the middle panel shows the middle 1/8 and the right-hand panel shows the 1/8 galaxies with highest numbers of galaxies within 1 Mpc. From the colour scale it can clearly be seen that the different bins in central number density of galaxies favour different halo masses, as expected from Fig. 3.2.

The correlation coefficients are low, for the second and third panel from the left, which seems to make these parameters nearly halo mass independent. Looking more closely at the Figure, we see, however, a positive correlation between median $n_{1-2 \text{ Mpc}/h}$ and M_h , especially at high mass. The relation with halo mass of this measure of large-scale environment, at fixed small-scale environment depends strongly on the (fixed) scales at which the environment is measured. This, together with varying flux limits in observational surveys makes it a fuzzy measure of halo mass, which is hard to interpret physically.

The trends seen in Fig. 3.3 are a typical example of the ‘multi-scale’ approach of Wilman et al. (2010). Changing the radii of the inner and outer edges of the annuli and/or the width of the bins in central galaxy number density does not affect the qualitative conclusions drawn from Fig. 3.3. The correlation of the number of galaxies in annuli with halo mass becomes weaker if very large distances from the galaxy in question are taken (5-10 Mpc), but it seems likely that that is merely a result of the fact that galaxies at such distances do not have much to do with the galaxy in question anyway.

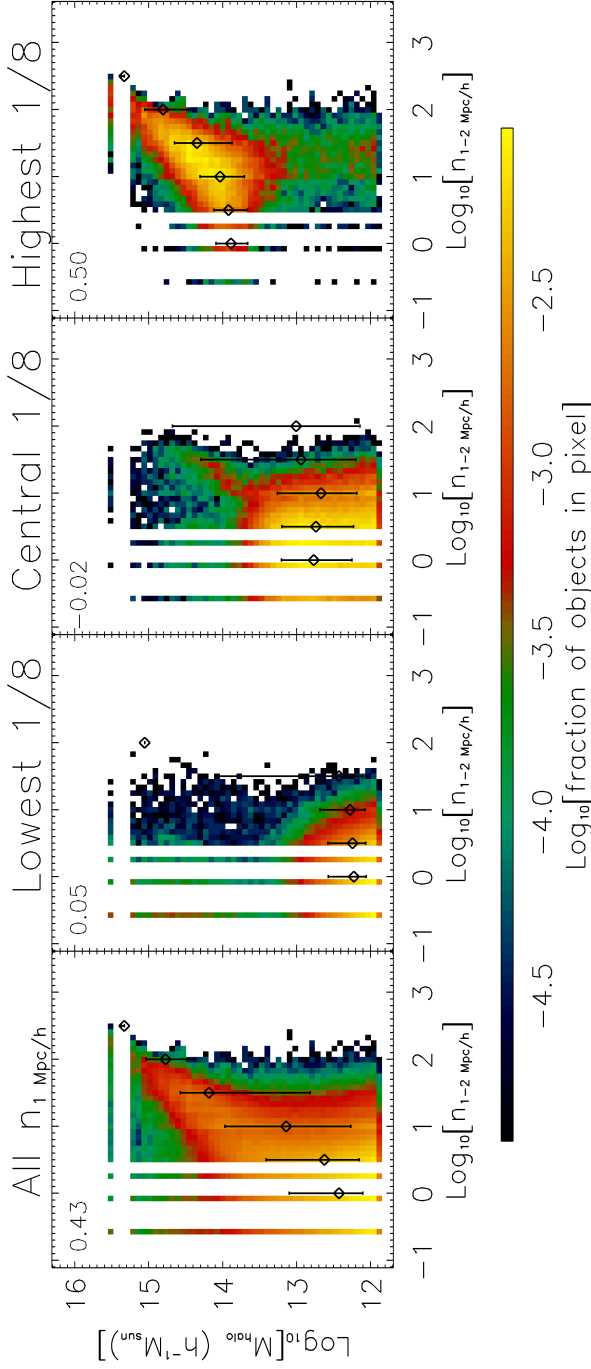


Figure 3.3: Halo mass as a function of the number of galaxies in annuli with an inner and outer radius of 1 and 2 Mpc, respectively. The first panel shows the full sample, while the other three panels correspond to three bins in number of galaxies within 1 Mpc, showing the lower, middle and upper one eighth of the total distribution from left to right. The galaxies with $n < 1$ are placed at $\text{Log}_{10} n = -0.5$ for illustrative purpose. Although the range of halo masses in each bin is large, the typical halo mass is higher for the bins corresponding to higher values of $n_{1 \text{ Mpc}/h}$. The median $\log(M/M_{\odot})$ are 12.3, 12.7 and 14.2, for the three bins respectively. Within each narrow bin of ‘small-scale environment’ there is, at the high halo mass end, still a correlation left between $n_{1-2 \text{ Mpc}/h}$ and halo mass. The low Spearman rank correlation coefficients are dominated by the low halo masses which are much more abundant in every bin of small scale environment.

3.4 Environment as a measure of halo mass

In this section we will study the strength of the correlation between several environmental indicators and halo mass.

We expect the correlation between the number of neighbours and halo mass to be strongest at some given distance. Taking the distance very small will bias against massive galaxies (and results in strong discreteness effects if the number of neighbours is very small, as they can only be integer). Taking the distance too large, on the other hand, will result in a sample of galaxies that does not have much to do with the halo the galaxy resides in.

In Fig. 3.4 we show, for two different environmental parameters, the value of the Spearman rank correlation coefficient with halo mass, as a function of the distance related parameter used to measure the environmental density. In the left panel we show the correlation coefficient between halo mass and the environmental density indicator n_r (the number of galaxies within a fixed physical distance r projected on the sky and within $\Delta v = \pm 1000 \text{ km s}^{-1}$) as a function of r . One example of this type of parameter was shown in the middle panel of Fig. 3.2. Fig. 3.4 shows that the correlation first strengthens with distance, reaches a maximum at a scale of roughly $1 h^{-1} \text{ Mpc}$, and declines slowly thereafter. The vertical arrows indicate the median virial radii for the haloes of all galaxies in the sample of the corresponding, and show that the peak of the correlation strength occurs at distances roughly corresponding to the median virial radius.

In the right panel of Fig. 3.4 we plot the Spearman rank correlation coefficient between halo mass and environment, now parametrized by r_N , the distance towards the N^{th} neighbour (as in the right panel of Fig. 3.2), as a function of the rank N . The correlation coefficients are now mostly negative, as a higher density (corresponding to a higher halo mass) will result in a smaller distance towards the N^{th} neighbour. However, for very massive haloes the distance to the first neighbour is an increasing function of mass, as the neighbour needs to be outside the galaxy itself, and more massive galaxies are larger. Taking more neighbours gives an anti-correlation that becomes stronger for larger numbers of neighbours for high mass galaxies. Lower mass galaxies show the strongest correlation when the distance to the N^{th} nearest neighbour is taken, with $N \gtrsim 3$, but the correlation does not weaken much for larger values. For a sample consisting of very high luminosity galaxies, slightly more neighbours need to be included to get the best measure of halo mass. The median number of neighbours within the virial radius, above the same luminosity cut is indicated with the arrows.

The vertical arrows in Fig. 3.4 indicate the median virial radius of the samples in the corresponding colour (left panel) and the median number of neighbours above the same luminosity limit within the virial radius (right panel). We conclude

3.4. ENVIRONMENT AS A MEASURE OF HALO MASS

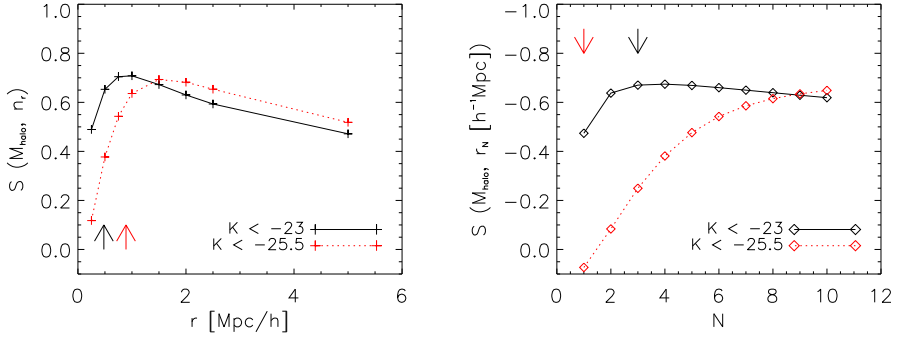


Figure 3.4: The strength of the correlations between halo mass and two of the environmental indicators used straightforwardly in observations, for two samples, with lower luminosity limits as indicated. In the left panel we plot the Spearman rank correlation coefficient between halo mass and the number of galaxies within a given projected physical distance r (and with a cut in redshift difference, as described in the text) as a function of r . The arrows show the value of the median virial radius of the haloes of all galaxies in the sample with the corresponding colour. The right panel shows the Spearman rank correlation coefficient between halo mass and the projected distance to the N^{th} nearest neighbour as a function of the rank N . The correlation coefficient is negative, because more massive galaxies have their N^{th} nearest neighbour closer by. The arrows indicate the median number of neighbours within the virial radius of the haloes above the indicated flux limit. If the environmental parameter is supposed to be a measure of halo mass, galaxies out to a distance of ~ 1 Mpc is a good choice, or the distance to the N^{th} neighbour, with $N = 1$ or 2. This second parameter is a worse measure of halo mass than the first, though the difference is small.

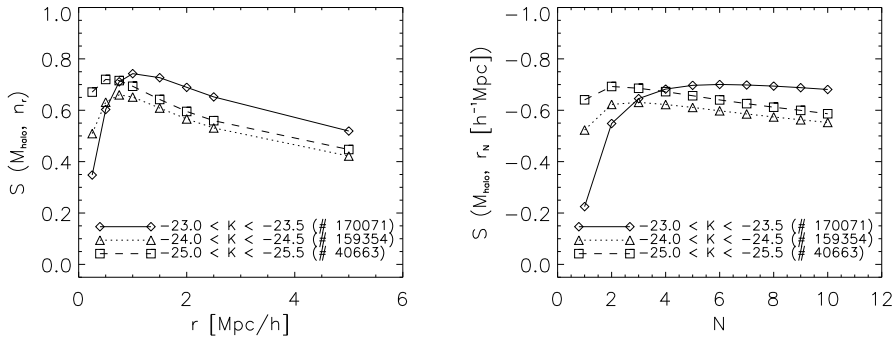


Figure 3.5: The same as Fig. 3.4, but now for three bins in absolute magnitude. We show the correlation coefficients between halo mass and the observationally feasible environmental parameters. For the neighbour search all galaxies with $K < -23$ are taken into account. The shape of the relation between correlation coefficient and the distance related parameters are relatively insensitive of mass, but the correlations are stringer for samples with higher luminosity galaxies. The numbers in between the brackets indicate the number of galaxies in the sample.

that n_r and r_N are both good measures of host halo mass, provided that n_r is measured at $r \geq r_{\text{vir}}$ and/or that the rank of neighbours taken into account is small. If the host halo mass, and thus the virial radius, are not known a priori, it is better to take r larger, as the correlation rapidly weakens towards smaller distances and declines only slowly with increasing distance.

In Fig. 3.5 we break up the samples of Fig. 3.4 in bins of K -band magnitude. In the neighbour search we include all galaxies with $K < -23$, but we plot the Spearman rank correlation coefficient between the environmental parameters and host halo mass for bins of $\Delta K = 0.5$. The correlations are in general weaker than for the whole sample, although the maxima are very comparable. K -band luminosity correlates with stellar mass (although at low masses the mass to light ratios vary stronger), so together with the correlation between stellar and halo mass (which is very strong for central galaxies, which make up roughly half the sample averaged over all stellar masses, and a larger fraction for higher stellar mass or K -band luminosity) one expects to weaken the correlation with halo mass if a narrow range of K -band luminosities is taken. Brighter samples of galaxies are more dominated by central galaxies, for which the correlations between halo mass and environmental indicator are stronger.

As we will show below, using K -band luminosity as a proxy for (virial) mass works well. Guided by the left panel of Fig. 3.2 one might expect that we can im-

3.5. ENVIRONMENT INDEPENDENT OF HALO MASS

prove on n_r as a measure of halo mass if r scales with $L_K^{1/3}$. We have tried this, but the correlation between halo mass and environment does not get stronger (or it gets slightly weaker, with correlation coefficients of 0.65 – 0.7). In the range of halo masses for which we could test it (any range between 10^{12} and $10^{15.5} M_\odot$) the correlation is stronger if a projected distance of 1 Mpc is used than if $r \propto L_K^{1/3}$ is used. Specifically, we tried $r = 1 h^{-1} \text{Mpc} \cdot (L_K/L_0)^{1/3}$, with $L_0 = 10^{\{10.5, 11.0, 11.5, 12.0\}} L_\odot$. We therefore conclude that using a fixed physical projected distance is safe, and easier in practice than a distance scaling with luminosity. We thus advise to use n_r with r of the order of $r \gtrsim R_{\text{vir}}$, if a measure of halo mass is desired. For most observed samples of galaxies $r \sim 1$ Mpc will do, but by iteration better values can be obtained: use $r = 1 h^{-1} \text{Mpc}$, calculate the halo virial radii from the environmental indicator (using the parametrization given in Appendix 3.6) and then iterate if the virial radii strongly deviate from 1 Mpc.

In Appendix 3.6 we provide polynomial fits for the halo mass as a function of several environmental parameters for several lower flux limits, which can be used to obtain halo masses from observed samples of galaxies with measured environmental indicators.

3.5 Environment independent of halo mass

3.5.1 Mass independent parameters for simulations

All the parameters we have looked at so far correlate with halo mass. The lower mass/luminosity limit of galaxies included as possible neighbours was set equal to the resolution limit of simulations, or the flux limit of a survey. As we saw in the left panels of Figs. 3.1 and 3.2, the correlation is strongest and almost linear with halo mass, if the scale out to which galaxies are counted scales with the virial radius of the host halo of the galaxy in question. Per unit halo mass, this galaxy number density (either projected or in a spherical region) is therefore roughly constant. This also holds for dark matter subhaloes in high resolution simulations, as shown by Gao et al. (2004).

In order to obtain an environmental indicator that is independent of halo mass we have to scale out both the mass/luminosity of the galaxy and the length scale in question. We define $D_{N,f}$ to be the three-dimensional distance to the N 'th nearest neighbour with at least f times the virial mass of the halo under consideration, divided by the virial radius of the halo under consideration:

$$D_{N,f} = \frac{r_{N(M_{\text{vir}} \geq f \cdot M_{\text{halo}})}}{R_{\text{vir, ngb}}} \quad (3.1)$$

where the subscripts ‘ngb’ and ‘halo’ indicate the neighbour of the halo under con-

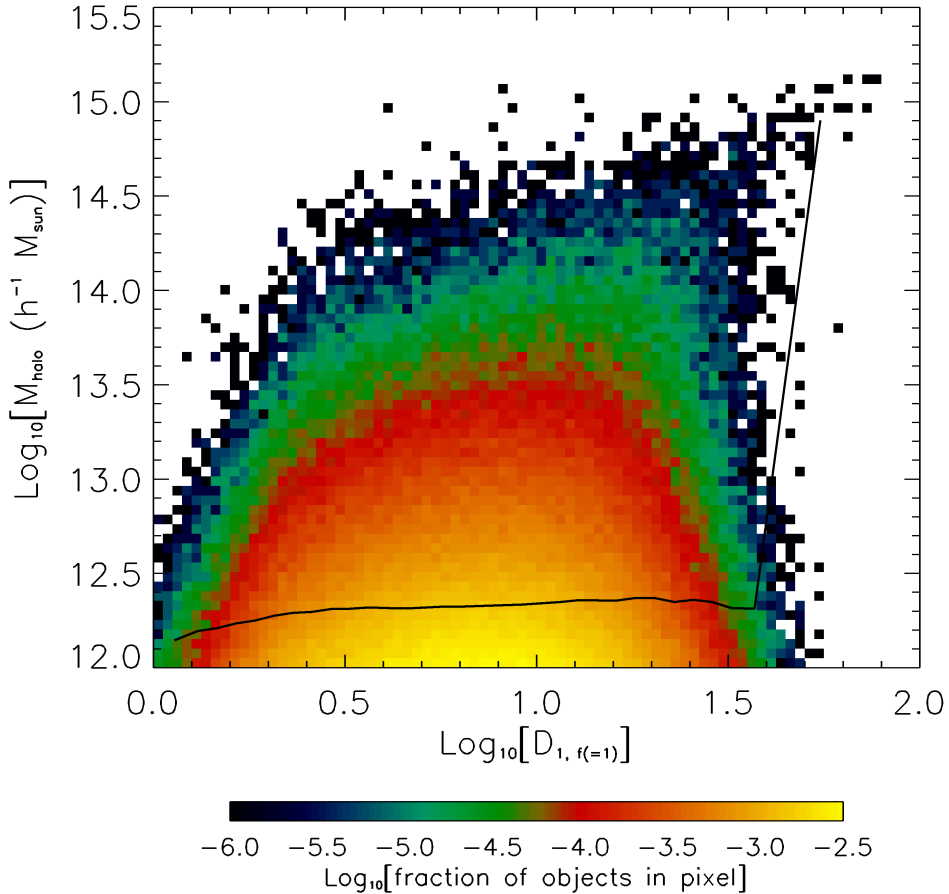


Figure 3.6: Halo mass as a function of the parameter $D_{1,1}$. The colour scale gives the distribution for all central galaxies in the sample, while the solid line is the median halo mass in bins of $D_{1,1}$. The median relation is very flat. The correlation coefficient of this parameter with halo mass is 0.07 (for correlation coefficients as a function of rank, see Fig. 3.7). We can therefore conclude that this measure of environment is highly insensitive to halo mass. At the high $D_{1,1}$ end, where the median halo mass is very high, there is a residual correlation visible because these haloes are on the exponential tail of the mass function.

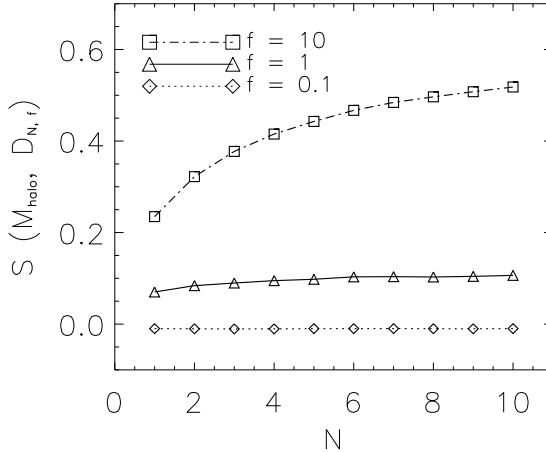


Figure 3.7: The Spearman rank correlation coefficient between halo mass and the environmental indicator $D_{N,f}$ (see Eq. 3.1) as a function of the rank N , for $f = \{1/10, 1, 10\}$. Higher values for f and N result in a stronger correlation in the range of ranks N and halo masses we tried. As $f = 1$ still gives a very small rank correlation coefficient, and because the environmental parameter can only be determined for the whole sample of galaxies for $f \gtrsim 1$, we conclude that using $f = 1$ and a low rank (e.g. $N = 1$) is a good choice if an environmental parameter that is insensitive to halo mass is desired. If haloes can be reliably identified for mass lower than the lowest mass one wants to know the environment for, then a value for f as low as possible should be used.

sideration and the halo itself, respectively. As we are dealing with halo properties, we only take central galaxies (i.e. only Friends-of-Friends haloes) into consideration. The use of the factor f to set the minimum mass of haloes taken into account in the neighbour search and the scaling to the virial radius are the two ingredients that we expect to make the environmental parameter insensitive to mass. $D_{N,f}$ only depends on the dimensionless parameters N and f for a given halo, and is also itself dimensionless.

Because the tidal field of the N 'th nearest neighbour scales with the mass of and distance to this neighbour as M/R^3 and the mass scales with R_{vir}^3 , the parameter $D_{N,f}$ scales with the tidal field to the power $-1/3$. This makes $D_{N,f}$ a very natural environmental parameter for which the physical interpretation is clear.

The colour scale of Fig. 3.6 shows the distribution of haloes at $z = 0$ in the

$D_{1,1} - M_{\text{halo}}$ plane. The curve shows the median $D_{1,1}$ in bins of halo mass. The median halo mass found is always the same for all D , irrespective of the factor f . The median $D_{1,f}$ in the sample is different for different f , though.

The weak correlation that starts to appear at very high values for $D_{1,f}$, especially for large f , is caused by the fact that these are probing the most massive haloes that are on the exponential tail of the Schechter-like halo mass function. Large scale structure is no longer self-similar in that regime, causing a slight positive correlation between $D_{N,f}$ and halo mass. We have verified (by inverting the axes) that for masses $M \ll M_*$ (where M_* is the mass at which the Schechter-like halo mass function transits from a power law into an exponential fall-off), where the mass function is a power law (and therefore scale free) the correlation is very weak. For higher masses, there is a mass scale imposed by the exponential cut-off of the Schechter-like halo mass function. For values roughly above $f^{-1}M_*$, the insensitivity to mass breaks down and a weak positive correlation between halo mass and $D_{N,f}$ appears.

In Fig. 3.7 we show the correlation coefficients between halo mass and $D_{N,f}$ as a function of the rank N for three different values of the mass ratios of galaxies counted as neighbours $f = \{1/10, 1, 10\}$. For all f the correlation between the rank N and host halo mass increases for with the rank. If an environmental indicator is desired that is insensitive to halo mass, $N = 1$ is therefore a good choice. The correlation is weaker for lower values of the ratio between host halo mass and the masses of possible galaxies that are included in the neighbour search. For a value lower than $f = 1$ the environmental indicator cannot be determined for the full resolved sample of haloes (as halo masses need to be at least $M > f^{-1}M_{\text{res}}$, with M_{res} the resolution limit, in order to resolve all possible neighbours). We therefore advise to take $f = 1$, as then the parameter can be defined for all galaxies in the sample and it gives only a very weak correlation with halo mass. If in a sample of haloes some of the studied properties demand a much more stringent resolution limit (e.g. if detailed halo profiles need to be fitted), and if haloes of much lower mass are resolved in terms of their virial mass and position, then one should use values of $f < 1$, e.g. 0.1, as the correlation between halo mass and environment vanishes.

If in the definition of $D_{N,f}$ the virial radius of the neighbour would be replaced by the virial radius of the halo under consideration (thereby losing the connection to the tidal force of the neighbour), the correlation between halo mass and environment gets even slightly weaker (e.g. a Spearman rank correlation coefficient of 0.04 instead of 0.07 between halo mass and $D_{1,1}$). As using the virial radius of the neighbour gives a more intuitive external environmental parameter, we still advice to use the virial radius of the neighbour.

We can conclude that the parameter $D_{N,f}$, with $N = 1$ and $f \leq 1$ results in

an intuitive environmental parameter that is very insensitive to halo mass. We do note, however, that in order to calculate this halo mass independent environmental indicator, one needs a measure of the virial mass of the host halo. From simulations these can be obtained trivially. For observed samples of galaxies this can be estimated using the environmental indicators that do correlate with halo mass strongly, as described in the previous section and detailed in Appendix 3.6. In the next section we will present an environmental indicator that can be obtained from observations that is also insensitive to halo mass.

3.5.2 Halo mass independent parameters for observed samples of galaxies

In some cases it is possible to obtain virial masses and radii for the host haloes of observed galaxies. Using techniques like halo-matching, in which the total luminosity of all galaxies in a group or cluster are added and the ranked luminosities matched to a ranked list of halo masses (from either an analytic halo mass function or a simulation), it is possible to get a reliable estimate for the host halo virial mass of the observed galaxies, see e.g. Yang et al. (2003); van den Bosch et al. (2003); Yang et al. (2007). This requires, however, that a group catalogue is available for the observed sample of galaxies. As such catalogues are only available for a limited number of observational samples, it is something which is often not easily done.

Hence, observationally neither the halo mass independent environmental indicator $D_{N,f}$ nor the virial mass or radius of a halo can be easily determined. We therefore set out here to formulate a variable that can be very easily determined by observers and that is as independent of halo mass as possible. We let the definition of $D_{N,f}$ guide us. We know that we have to scale the minimum masses/luminosities of the galaxies that are taken into consideration in the search for neighbours to be a fixed fraction of the mass/luminosity of the galaxy under consideration and that we have to scale the distance to the neighbours to some typical distance of the neighbour.

We use an observable, the K -band luminosity, instead of stellar mass. Luminosity is easier to measure and does not require the modelling of the spectral energy distribution of the galaxy. We use the K -band because in the very red optical bands and in the near-IR the correlation between luminosity and stellar mass is strongest (aside from the uncertainties arising from the treatment of thermally pulsing asymptotic giant branch, TP-AGB, stars, see e.g. Maraston, 2005; Tonini et al., 2010). We will also have to normalize in distance. As a reference we use typical values for central galaxies in a halo with a virial mass of $10^{13} M_{\odot}$, and therefore a virial radius equal to $0.58 h^{-1} \text{Mpc}$.

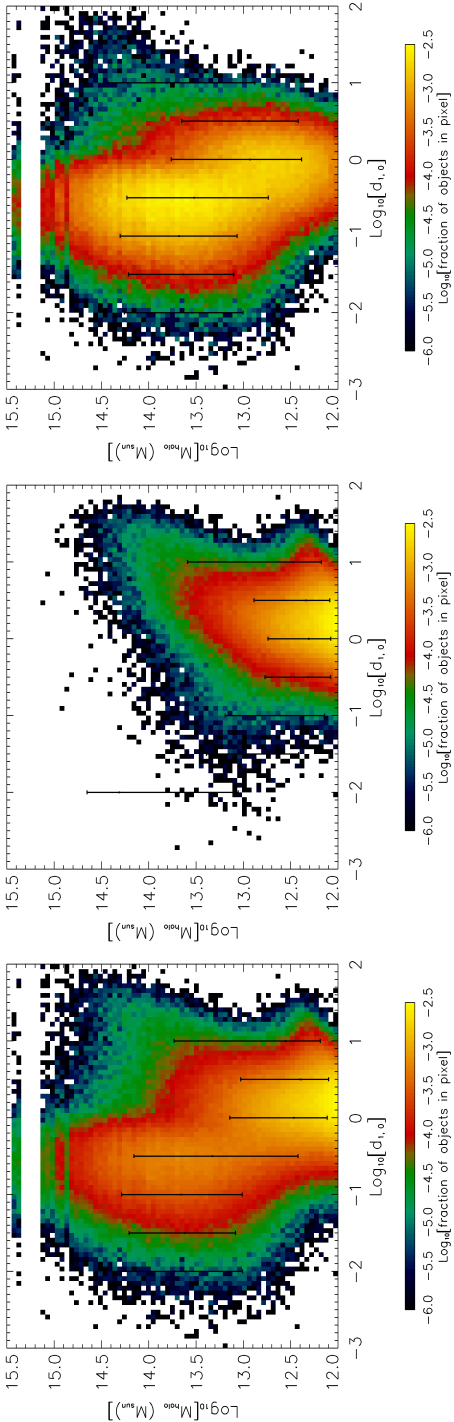


Figure 3.8: The host halo masses of galaxies versus the dimensionless environmental parameter $d_{1,0}$ (see Eq. 3.2), which is easy to measure for observers. In the left panel we show all galaxies in the sample, for which the Spearman rank correlation coefficient is -0.28. The middle and right panel show the relation for the central galaxies and the satellites, respectively. For these subsamples the Spearman rank correlation coefficients are 0.09 and -0.35, respectively, showing that the relation is very weak for central galaxies, as expected, but not so weak for satellite galaxies.

3.5. ENVIRONMENT INDEPENDENT OF HALO MASS

For all central galaxies in a bin of halo mass extending from $10^{12.9}$ to $10^{13.1} M_{\odot}$ we have determined the median K -band luminosity to be $1.4 \times 10^{11} L_{\odot}$. The virial radius, which is used in the definition of $D_{N,f}$, scales with halo mass as $R_{\text{vir}} \propto M_{\text{halo}}^{1/3}$, so we scale the distance used to normalize the environment as $r \propto L_K^{1/3}$ (see below for the neighbour search strategy). As projected distances are more easily measured than three dimensional distances, we use the projected distances (and test both with and without a cut in velocity difference). Our environmental indicator $d_{N,m}$ then becomes

$$d_{N,m} = \frac{r_{N(K \leq K_{\text{gal}} - m)}}{0.58 h^{-1} \text{Mpc}} \cdot \left(\frac{L_{K,\text{ngb}}}{1.4 \times 10^{11} L_{\odot}} \right)^{-1/3} \quad (3.2)$$

where the subscript ‘ngb’ again denotes the neighbour of the galaxy in question, m is the difference in magnitudes (corresponding to a ratio in luminosity/mass, a positive m means that the neighbours must be brighter) between the galaxy in question and the galaxies counted as possible neighbours (we will show $m = 0$ below, and therefore look only for neighbours that are at least as bright as the galaxy under consideration), K is the absolute K -band magnitude and L_K the luminosity in the K -band. $R_{\text{vir},13} = 0.58 h^{-1} \text{Mpc}$ is the virial radius of the ‘reference mass’ of $10^{13} M_{\odot}$.

If $R_{\text{vir},13} (L_K / 1.4 \times 10^{11} L_{\odot})^{1/3}$ would be the virial radius (i.e. if the halo mass to K -band light ratio would be constant), then the external environmental indicator $d_{N,m}$ could be described as distance to the N^{th} nearest neighbour which is at least m magnitudes brighter than the galaxy we are measuring the environment of, normalized to the galaxy’s virial radius.

The colour scale in the left panel of Fig. 3.8 shows the distribution of galaxies in the $M_{\text{halo}} - d_{1,0}$ plane. We include all galaxies in the catalogue with $K < -23$. The sample of galaxies with $M_* > 10^{10} M_{\odot}$ shows signs of incompleteness at magnitudes fainter than $K = -23$. Fig. 3.8 shows that halo mass indeed is weakly sensitive to the parameter $d_{1,0}$. The Spearman rank correlation coefficient is -0.28 , which indicates a weak anti-correlation.

The parameter shown in Fig. 3.8 includes only galaxies within a radial velocity difference of 1000 km s^{-1} . Without this cut in redshift difference the correlation becomes stronger. Taking into account only galaxies within a redshift window is important, but the width of the redshift window is less important as long as it is $\lesssim 10^3 \text{ km s}^{-1}$.

The dependence of the correlation between host halo mass and $d_{N,m}$ on the rank N is shown in Fig. 3.9, for three different values of m . We have chosen to show $m = \{-2.5, 0, 2.5\}$ magnitudes, because a magnitude difference of 2.5 corresponds to a luminosity ratio of 10, similar to the mass ratio of 10 used above. Whenever

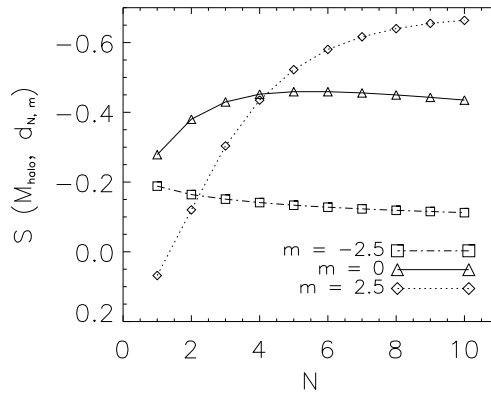


Figure 3.9: The Spearman rank correlation coefficient between halo mass and $d_{N,m}$ as a function of the rank N , for $m = \{-2.5, 0, 2.5\}$ magnitudes. 2.5 magnitudes corresponds to a factor 10 in luminosity. For the sample for $m = 2.5$ magnitudes there are fewer possible neighbours and the nearest neighbour will usually be found in another halo (often even a more massive halo), causing a weak correlation with halo mass. In the sample for $m = -2.5$ magnitudes, the parameter is only defined for a small sample, because neighbours, which have a luminosity 10 times lower than the galaxy in question, need to be resolved as well. If the neighbours are not required to be much more luminous ($m = 0$) they can be either in the same or in another halo, causing a correlation with halo mass that rises for low rank and decrease for higher ranks.

possible neighbours are supposed to be a factor 10 less luminous ($m = -2.5$), the sample for which this parameter can be determined is much smaller (because all possible, lower mass neighbours need to be resolved as well) and the typical haloes the galaxies are in are more massive. This results in the very weak correlation with halo mass for all ranks N , as shown in Fig. 3.9. If neighbours are required to be more than a factor 10 brighter, the most likely neighbours will reside in other (more massive) haloes. If the minimum brightness of possible neighbours is the same as that of the galaxy in question, or higher, the correlation between host halo mass and $d_{N,0}$ first increases with the rank N and goes down after some maximum (because for large rank N the neighbours are more likely to reside in other haloes). This maximum and the rank at which the maximum occurs depend on the lower luminosity limit of the sample and on the difference in magnitudes m . The lowest possible rank $N = 1$ gives a very weak correlation and for the same reason as before

we advice to use a luminosity ratio of 1 ($m = 0$) between the galaxy in question and its possible neighbours. Again, if neighbours within a redshift window can be identified below the flux limit used for the analysis, it is wise to use a value for m as low as possible.

3.5.3 Splitting the sample in centrals and satellites

The middle and right panel of Fig. 3.8 show the distribution of central galaxies and satellites, respectively, in the $M_{\text{halo}} - d_{1,0}$ plane. For these subsamples the Spearman rank correlation coefficient between $d_{1,0}$ and halo mass are 0.09 and -0.35, respectively. The samples combined give the correlation as shown in the left panel. Central galaxies find brighter neighbours that are (often central) galaxies in neighbouring haloes, while for the satellites mostly their own central galaxy is found as neighbour. We expect that the correlation between halo mass and environment is predominantly caused by galaxies finding satellites in their own halo as possible neighbours. Excluding these satellites should result in a much weaker correlation. We postpone such an analysis for future work.

We have verified that for a sample in which the neighbours of galaxies are defined as the nearest brighter galaxy that itself has no brighter neighbour at smaller distance (so it is not itself a satellite of that other galaxy) results in a very low correlation coefficient between halo mass and $d_{N,m}$ for the satellites too. In this case, a satellite galaxy usually finds its own central as a neighbour (unless there is another satellite that is brighter and closer to that the galaxy you are looking at than to its central) and central galaxies find the nearest brighter other central galaxy. A combined sample of all centrals and satellites then still shows a correlation coefficient of ~ -0.4 , as the centrals and satellites show the same bimodal behaviour as shown in the middle and right panels of Fig. 3.8.

Splitting the sample first in a sample of satellites and centrals and excluding the central galaxy of the galaxy's own host halo would probably result in a weaker correlation for the sample as a whole. This could be done by defining a virial radius for each galaxy (based, for example, on its K -band luminosity) and identify satellites by searching for galaxies that fall within the virial radius of another, more luminous, galaxy. These can then be flagged as satellites. A neighbour search for the satellites should then exclude a region as large as the virial radius of their central, in order to be sure that the central galaxy in a neighbouring halo is selected as neighbour. This would significantly complicate the neighbour search and we will postpone this for future work.

3.6 Conclusions

The properties of observed galaxies and dark matter haloes in simulations depend on their environment. The term “environment” has, however, been used to describe a wide variety of measures that may or may not correlate with each other. Useful measures of environment include, for example, the distance to the N^{th} nearest neighbour, the number density of objects within some distance, or, for the case of galaxies, the mass of the host dark matter halo. In this paper we carried out a detailed investigation of several environmental parameters which are popular in the (observational) literature, focusing in particular on their relationship with halo mass.

We measured the environmental indicators from the synthetic galaxy catalogues produced using the semi-analytic models by De Lucia & Blaizot (2007), built on the Millennium Simulation (Springel et al., 2005). This model reproduces the number density and clustering properties of observed galaxies in the low-redshift Universe.

We showed that it is of crucial importance to realise that the degree to which environmental parameters measure host dark matter halo mass is determined by (1) whether the scale out to which the environment is measured scales with some typical scale (e.g. the virial radius) of the galaxy in question and (2) whether or not the minimum mass/luminosity that the neighbours are required to have is fixed in absolute terms or relative to the mass/luminosity of the galaxy in question. Specifically, we found that

1. All frequently used environmental indicators (i.e. some function of the distance to the N^{th} nearest neighbour or the number of galaxies within some given distance, either using three dimensional distances or using projected distances for all galaxies within some radial velocity difference) correlate strongly with halo mass.
2. For the number of galaxies within a given distance, n_r , the correlation with halo mass peaks for distances of 1.5–2 virial radii. The virial radius is for observers in general a difficult quantity to measure, but the correlation with halo mass is nearly as strong for galaxy counts within ~ 1 Mpc.
3. The strength of the anti-correlation between the distance to the N^{th} nearest neighbour, r_N , and halo mass is nearly constant for $N \geq 2$ and only slightly weaker for $N = 1$. The relation between r_N and halo mass is slightly weaker than for n_r if r is taken to be similar to the virial radius.
4. Both n_r and r_N correlate more strongly with halo mass if the neighbours are required to be more luminous or massive.

We have shown that it is possible to construct environmental parameters that are insensitive to halo mass by using only dimensionless quantities. For the case of dark matter haloes in numerical simulations this can for example be achieved by scaling the distance out to which environment is measured to the virial radius of the halo for which the environment is determined and by scaling the minimum required mass to that of the halo in question. The correlation with halo mass becomes smaller if the minimum mass required for neighbours is lower. If the neighbours are more massive than the halo for which the environment is measured, then scaling the distance to the neighbour's virial radius gives more intuitive results and lead to only a slight increase in the strength of the correlation with halo mass. These environmental parameters are, however, only insensitive to halo mass for haloes that are not on the exponential tail of the mass function.

For observers, usually only a position on the sky, some rough indication of the distance along the line of sight and the flux or luminosity in some waveband are available. We showed that analogous environmental measures that are highly insensitive to halo mass can also be constructed using only the K -band luminosities, projected distances on the sky, and a maximum radial velocity difference for neighbours. Specifically, the parameter $d_{1,0}$, defined as the projected distance to the nearest brighter galaxy within a radial velocity difference of 1000 km s^{-1} (that itself does not have a brighter neighbour closer by and therefore probably is a central galaxy of a halo) divided by the K -band luminosity of the neighbour to the power one third, correlates only very weakly with host halo mass.

In summary, when measuring environments for (virtual) observations, we advise to make use of both a halo mass independent measure and a measure that is highly sensitive to halo mass. For purely theoretical studies the halo mass is already known and we therefore advise to use an environmental parameter that is insensitive of halo mass. The following parameters are good choices:

- *Insensitive to halo mass; for simulations:* The distance to the nearest (main) halo that is at least f times more massive than the halo in question, divided by the virial radius of that neighbour. The choice $f = 1$ works well, but if resolution permits it, smaller values yield even weaker correlations with halo mass. Dividing instead by the virial radius of the halo itself gives a slightly weaker correlation with halo mass, at the expense of losing the intuitive definition in which the environment relates to the tidal field due to the neighbour.
- *Sensitive to halo mass; for observations:* The number of brighter galaxies within a projected distance of $\sim 1 h^{-1} \text{ Mpc}$, within a redshift window corresponding to $\Delta v \lesssim 1000 \text{ km s}^{-1} (n_{1 \text{ Mpc}/h})$. Even better would be to subsequently iterate the following two steps until the procedure converges: (i)

check what the corresponding halo masses are using the relations between n_r and halo mass given in Appendix 3.6; (ii) adapt the maximum projected distance to 1.5 times the typical virial radius of the haloes in the sample.

- *Insensitive to halo mass; for observations:* The parameter $d_{1,0}$, as given by Eq. 3.2. The correlation with halo mass is weaker if satellites of the galaxy in question are excluded. This may be possible by requiring neighbours to be further away than some minimum distance. It may even be possible to vary this distance with the virial radius of the neighbour, which can be determined using the measure that is very sensitive to halo mass. This is work in progress.

Many studies have measured galaxy properties as a function of both stellar mass and environment. The environmental indicators used by most authors are effectively measures of halo mass. While halo mass is a perfectly valid measure of environment, and may be particularly relevant for satellites, we note that because stellar mass is also expected to correlate strongly with halo mass, these studies may not have separated “internal” and “external” influences as well as one might naively think. The work presented here will enable future observational and theoretical studies to disentangle the effects of halo mass (internal environment) from those of the external environment. This may eventually tell us whether halo mass is the only important driver of the physics governing galaxy evolution.

Appendix A. Obtaining the halo mass from environmental parameters

In this Appendix we provide fitting functions in order to obtain the halo mass from different environmental indicators, for several lower limits on the galaxy luminosity. This luminosity limit holds for both the galaxies the environment is determined for and for the galaxies included in the neighbour search. We will use the projected quantities, as described in Section 3.3.3, with a maximum radial velocity difference of 1000 km s^{-1} (the fits are not sensitive to this choice) at redshift 0. We show figures corresponding to Fig. 3.2, but without the colour scale and including a polynomial fit that can facilitate future studies that will use the environmental indicators to measure halo mass.

Environmental indicators that are directly obtained from observations

Here we will use environmental parameters that can be obtained directly from observations. In the next section we will describe how a better estimate of halo mass

3.A. Obtaining halo mass from environmental parameters

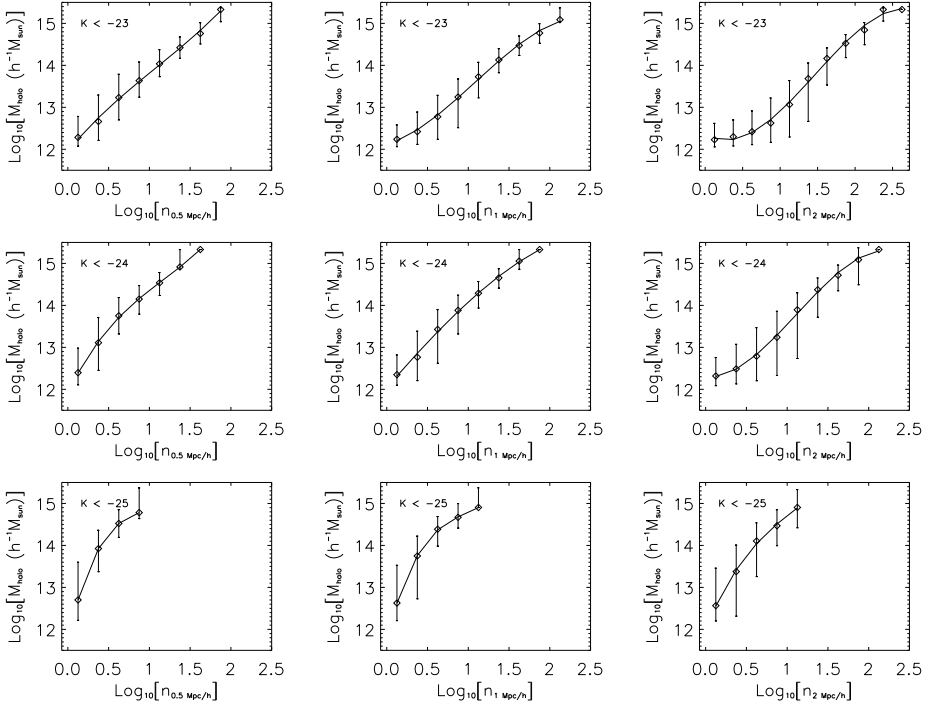


Figure 3.10: Halo mass as a function of three different environmental indicators (corresponding to the columns, $n_{0.5 \text{ Mpc/h}}$, $n_{1 \text{ Mpc/h}}$ and $n_{2 \text{ Mpc/h}}$), for three different lower luminosity limits (corresponding to the rows, $K < \{-23, -24, -25\}$). The symbols are the medians of the data, while the errors represent the 1σ spread (as defined in the text). The solid line is the best fit third order polynomial with coefficients given in Table 3.2.

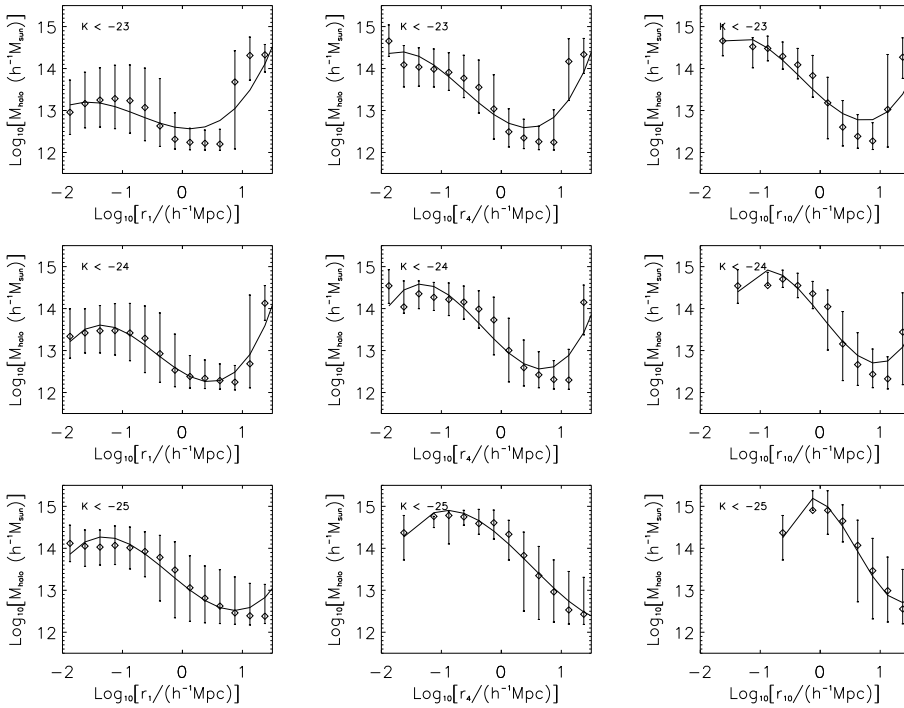


Figure 3.11: Halo mass as a function of three different environmental indicators (corresponding to the columns, r_1 , r_4 and r_{10}), for three different lower luminosity limits (corresponding to the rows, $K < \{-23, -24, -25\}$). The symbols are the medians of the data, while the errors represent the 1σ spread (as defined in the text). The solid line is the best fit third order polynomial with coefficients given in Table 3.2.

3.A. Obtaining halo mass from environmental parameters

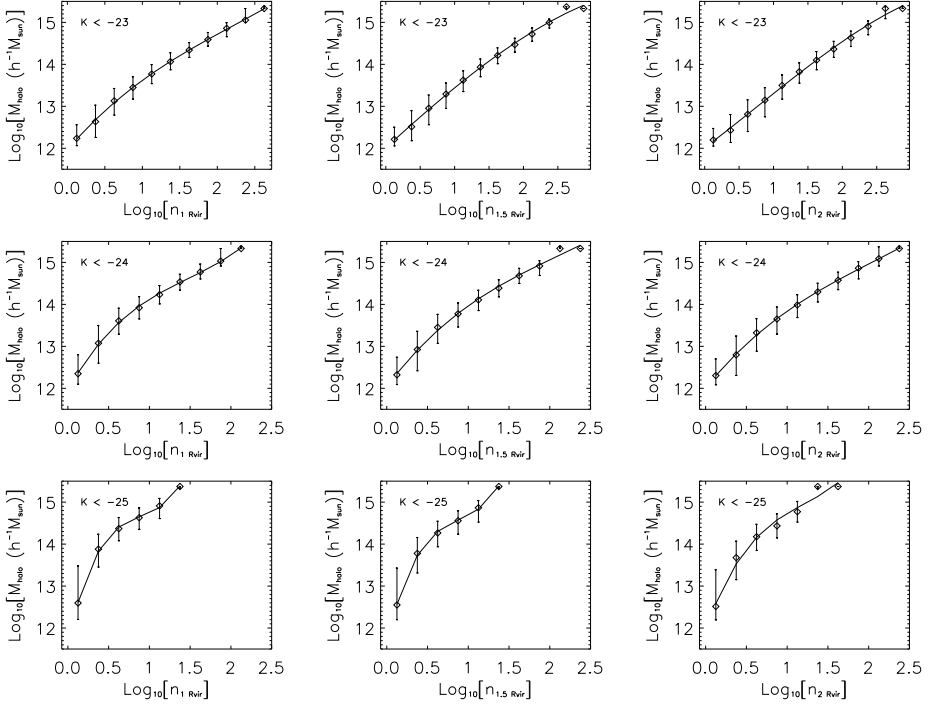


Figure 3.12: Halo mass as a function of three different environmental indicators (corresponding to the columns, $n_1 R_{\text{vir}}$, $n_{1.5 R_{\text{vir}}}$ and $n_{2 R_{\text{vir}}}$), for three different lower luminosity limits (corresponding to the rows, $K < \{-23, -24, -25\}$). The symbols are the medians of the data, while the errors represent the 1σ spread (as defined in the text). The solid line is the best fit third order polynomial with coefficients given in Table 3.2.

can be obtained iteratively. We provide the parameters corresponding to third order polynomial fits for the halo mass as function of the environmental indicators. We fit a function of the form

$$\log M_{\text{halo}} = (\log M_{\text{halo}})_0 + AP + BP^2 + CP^3 \quad (3.3)$$

Where P indicates the logarithm of the environmental parameter in question. We fit on the medians in bins separated by $\Delta P = 0.25$ for all indicators.

The fitted values for the normalization $\log(M_{\text{halo}})_0$ and the three other polynomial coefficients are (A, B, C) are given in Table 3.2 for six different environmental parameters ($n_{0.5 \text{ Mpc}/h}$, $n_{1 \text{ Mpc}/h}$, $n_{2 \text{ Mpc}/h}$, r_1 , r_4 and r_{10}) and for six different upper magnitude limits ($K = \{-23, -23.5, -24, -24.5, -25, -25.5\}$). Similarly, we fit the

(1σ) spread in halo mass at fixed environment:

$$\sigma(\log M_{\text{halo}}) = \sigma(\log M_{\text{halo}})_0 + \alpha P + \beta P^2 + \gamma P^3 \quad (3.4)$$

Note that the distribution is not perfectly Gaussian, nor symmetric, so as a 1σ error we use $\sigma = (p_{84} - p_{16})/2$, where $p_{84,16}$ are the 84'th and 16'th percentile of the distribution. The fit parameters are also given in Table 3.2. The halo mass for a given environment can then be estimated from observational data sets using Eq. 3.3, with the uncertainty given by Eq. 3.4. For completeness, the final column of Table 3.2 indicates the Spearman rank correlation coefficient between the halo mass and the environmental indicator in question for the sample in question.

Similar fits can be requested at the author for different filters used for the selection, different redshifts, different environmental parameters and/or different flux limits.

In Fig. 3.10 we show some of the relations between environment, parametrized by n_r , and halo mass for three different values of r and for three different samples with different lower luminosity limits. The symbols are the medians used in the fits, and the error bars are the 1σ spreads of the data. The solid line is the best fit third order polynomial for which the coefficients are given in Table 3.2.

Fig. 3.11 shows the same, but now for the environment parametrized by r_N for three values of the rank N . Note that these distributions are bimodal as shown in Fig. 3.2, so the correlation with halo mass is in general slightly weaker.

For the samples with a very high flux limit the fits are based on a limited number of galaxies and bins, and are therefore more uncertain. We do not expect that the brightest flux limits quoted here are used for low redshift studies.

A better halo mass estimator

As we have shown in Section 3.3.2 the strongest correlation between halo mass and environment is obtained whenever galaxies are counted within a distance that scales with the virial radius of the halo. In order to do so, an estimate of the halo mass is necessary. Using the relations described earlier in this Appendix, from the observable environmental indicators an estimate of the halo mass can be made. Using

$$R_{\text{vir}} = 0.27 h^{-1} \text{Mpc} \left(\frac{M_{\text{halo}}}{10^{12} M_{\odot}} \right)^{1/3} \frac{1}{1+z}, \quad (3.5)$$

which is the same relation as used in the rest of the paper to obtain virial radii, an estimate for the virial radius can be obtained. z is the redshift, which is zero throughout this paper.

3.A. Obtaining halo mass from environmental parameters

Table 3.2: The coefficients of third order polynomial fits to the halo mass as a function of six different environmental indicators which can be obtained directly from observations above a flux limit (indicated in the first column, fit coefficients in columns 2-5), as well as coefficients of third order polynomial fits to the spread of the data (columns 6-9) and the Spearman rank correlation coefficient between halo mass and the environmental indicator (final column). The symbols are as defined in Eqs. 3.3 and 3.4.

$P = \text{Log}_{10}[n_{0.5} \text{ Mpc}]$									
Maximum K	$(\log M_{\text{halo}})_0$	A	B	C	$\sigma(\log M_{\text{halo}})_0$	α	β	γ	$S(M_{\text{halo}}, P)$
-23	12.0	2.34	-0.70	0.21	0.52	2.17	-2.66	0.78	0.65
-23.5	12.0	2.83	-1.00	0.26	0.52	2.70	-3.84	1.33	0.61
-24	11.9	3.97	-2.15	0.61	0.86	0.98	-1.57	0.41	0.54
-24.5	11.9	5.60	-3.77	0.97	0.92	2.31	-5.53	2.79	0.44
-25	11.8	8.48	-8.40	3.02	1.51	-0.63	-3.33	3.47	0.32
-25.5	12.0	128.00	128.00	0.00	2.38	-6.00	4.00	8.00	0.20
$P = \text{Log}_{10}[n_1 \text{ Mpc}]$									
Maximum K	$(\log M_{\text{halo}})_0$	A	B	C	$\sigma(\log M_{\text{halo}})_0$	α	β	γ	$S(M_{\text{halo}}, P)$
-23	12.1	0.53	1.15	-0.35	0.16	2.84	-2.71	0.67	0.71
-23.5	12.1	1.30	0.56	-0.21	0.32	2.60	-2.52	0.59	0.65
-24	12.0	2.25	-0.14	-0.06	0.50	2.63	-3.05	0.82	0.58
-24.5	11.8	5.06	-3.99	1.56	0.61	4.12	-6.91	2.76	0.49
-25	11.8	7.45	-6.78	2.32	1.02	3.78	-9.57	5.16	0.38
-25.5	12.0	64.00	128.00	0.00	2.62	-4.00	0.00	12.00	0.25
$P = \text{Log}_{10}[n_2 \text{ Mpc}]$									
Maximum K	$(\log M_{\text{halo}})_0$	A	B	C	$\sigma(\log M_{\text{halo}})_0$	α	β	γ	$S(M_{\text{halo}}, P)$
-23	12.4	-1.04	2.06	-0.47	0.20	1.88	-1.05	0.11	0.63
-23.5	12.3	-0.77	2.11	-0.53	0.16	2.45	-1.53	0.20	0.58
-24	12.3	-0.20	2.05	-0.61	0.30	2.69	-1.86	0.26	0.52
-24.5	12.2	1.47	0.78	-0.31	0.41	4.09	-4.13	0.91	0.45
-25	12.0	4.71	-2.86	0.84	0.56	7.28	-14.15	7.07	0.38
-25.5	12.7	6.72	-9.81	5.63	2.00	-2.41	-2.15	4.63	0.28
$P = \text{Log}_{10}[r_1 (h^{-1} \text{ Mpc})]$									
Maximum K	$(\log M_{\text{halo}})_0$	A	B	C	$\sigma(\log M_{\text{halo}})_0$	α	β	γ	$S(M_{\text{halo}}, P)$
-23	12.6	-0.15	0.57	0.26	1.17	-0.35	-0.02	0.06	-0.47
-23.5	12.5	-0.50	0.63	0.37	1.13	-0.41	-0.02	0.10	-0.56
-24	12.5	-0.85	0.59	0.45	1.00	-0.49	0.25	0.29	-0.56
-24.5	12.7	-1.07	0.51	0.46	1.12	-0.32	0.10	0.19	-0.50
-25	13.1	-1.16	0.21	0.33	1.38	0.08	-0.18	-0.01	-0.43
-25.5	14.1	-0.70	-0.30	0.08	1.23	1.04	-0.06	-0.37	-0.29
$P = \text{Log}_{10}[r_4 (h^{-1} \text{ Mpc})]$									
Maximum K	$(\log M_{\text{halo}})_0$	A	B	C	$\sigma(\log M_{\text{halo}})_0$	α	β	γ	$S(M_{\text{halo}}, P)$
-23	12.8	-0.84	0.70	0.37	1.04	-0.07	-0.07	0.02	-0.67
-23.5	12.9	-1.03	0.64	0.41	1.10	0.17	-0.12	-0.06	-0.61
-24	13.1	-1.35	0.48	0.49	1.05	0.18	-0.12	-0.07	-0.52
-24.5	13.5	-1.48	0.20	0.43	1.05	0.54	-0.05	-0.13	-0.42
-25	14.3	-1.24	-0.37	0.24	1.01	0.95	-0.01	-0.37	-0.35
-25.5	14.9	0.26	-2.42	1.02	0.58	0.26	2.36	-1.35	-0.20
$P = \text{Log}_{10}[r_{10} (h^{-1} \text{ Mpc})]$									
Maximum K	$(\log M_{\text{halo}})_0$	A	B	C	$\sigma(\log M_{\text{halo}})_0$	α	β	γ	$S(M_{\text{halo}}, P)$
-23	13.3	-1.30	0.39	0.42	0.99	0.47	-0.06	-0.16	-0.62
-23.5	13.6	-1.63	0.21	0.56	0.93	0.48	-0.10	-0.14	-0.53
-24	13.9	-1.80	-0.06	0.70	0.89	0.71	0.06	-0.25	-0.43
-24.5	14.6	-1.89	-1.27	1.22	1.01	0.52	0.09	-0.19	-0.34
-25	15.1	-0.83	-2.67	1.45	0.97	0.42	0.31	-0.15	-0.28
-25.5	10.6	10.40	-9.15	2.34	2.79	-4.01	4.05	-1.20	-0.13

CHAPTER 3. DISENTANGLING ENVIRONMENT AND HALO MASS

Table 3.3: The coefficients of third order polynomial fits to the halo mass as a function of three different environmental indicators for which a good estimate of the virial radius is needed, above a flux limit (indicated in the first column, fit coefficients in columns 2-5), as well as coefficients of third order polynomial fits to the spread of the data (columns 6-9) and the Spearman rank correlation coefficient between halo mass and the environmental indicator (final column). The symbols are as defined in Eqs. 3.3 and 3.4.

$P = \text{Log}_{10}[n_1 \text{ Rvir}]$									
Maximum K	$(\log M_{\text{halo}})_0$	A	B	C	$\sigma(\log M_{\text{halo}})_0$	α	β	γ	$S(M_{\text{halo}}, P)$
-23	12.0	2.07	-0.50	0.08	0.61	0.04	-0.14	0.02	0.85
-23.5	12.0	2.68	-1.00	0.20	0.65	0.15	-0.32	0.07	0.81
-24	12.0	3.52	-1.75	0.40	0.85	-0.43	0.17	-0.06	0.74
-24.5	12.0	4.38	-2.42	0.56	1.15	-1.32	1.03	-0.34	0.63
-25	11.7	8.66	-8.91	3.33	1.76	-4.44	5.51	-2.31	0.49
-25.5	12.5	8.96	-14.37	8.92	3.06	-14.13	26.25	-15.34	0.31
$P = \text{Log}_{10}[n_{1.5} \text{ Rvir}]$									
Maximum K	$(\log M_{\text{halo}})_0$	A	B	C	$\sigma(\log M_{\text{halo}})_0$	α	β	γ	$S(M_{\text{halo}}, P)$
-23	12.0	1.50	-0.05	-0.02	0.50	0.42	-0.40	0.07	0.86
-23.5	12.0	1.94	-0.34	0.03	0.58	0.35	-0.41	0.07	0.82
-24	12.0	2.59	-0.79	0.13	0.75	0.10	-0.31	0.06	0.75
-24.5	11.9	4.46	-2.74	0.72	1.13	-1.30	1.15	-0.39	0.66
-25	11.7	8.20	-8.34	3.16	1.64	-3.72	4.65	-2.02	0.53
-25.5	12.9	4.59	-3.71	1.40	2.84	-11.68	19.69	-10.26	0.34
$P = \text{Log}_{10}[n_2 \text{ Rvir}]$									
Maximum K	$(\log M_{\text{halo}})_0$	A	B	C	$\sigma(\log M_{\text{halo}})_0$	α	β	γ	$S(M_{\text{halo}}, P)$
-23	12.0	1.24	0.09	-0.04	0.44	0.59	-0.48	0.08	0.86
-23.5	12.0	1.71	-0.20	0.01	0.53	0.56	-0.53	0.10	0.81
-24	12.0	2.39	-0.68	0.11	0.73	0.15	-0.27	0.05	0.75
-24.5	12.1	3.15	-1.18	0.21	0.94	-0.11	-0.25	0.04	0.67
-25	12.0	5.38	-3.62	1.01	1.36	-1.51	0.93	-0.33	0.56
-25.5	12.7	6.42	-7.77	3.74	2.79	-11.36	19.20	-10.01	0.37

A better estimate of the halo mass can then be found by measuring the projected number of neighbours within a given multiple of the virial radius (with the same cut in radial velocity difference), as shown in Section 3.3.3. In Table 3.3 we provide the same third order polynomial fits as in Table 3.2, but for the relation between halo mass and $n_1 \text{ Rvir}$, $n_{1.5} \text{ Rvir}$ and $n_2 \text{ Rvir}$, as well as the corresponding (higher) Spearman rank correlation coefficients. Fig. 3.12 shows the relations for a selection of the fits.

This procedure of obtaining a better estimate for the halo mass can then be used to iterate towards a reliable estimate for the halo mass, including the spread in halo masses at fixed environment (note that this spread is very small for high mass haloes if the neighbours are counted within a multiple of the virial radius of order one.)

We note that these halo masses are measured in the Millennium Simulation, which uses the WMAP first year results for the cosmology, which has (among other differences) a larger amplitude of fluctuations (σ_8). This means that for a given galaxy luminosity, the haloes will be slightly too massive. How this affects the relations between environment and halo mass is not clear.

4

The simulated galaxy luminosity function: input physics, dust attenuation and galaxy selection

Abstract

We investigate the luminosity function (LF) resulting from cosmological hydrodynamical simulations with varying input physics, with and without an estimate for dust attenuation. We find that in simulations in which the supernova (SN) feedback is inefficient in massive galaxies, due to too low a wind velocity, a ‘bump’ in the luminosity function appears due to the overproduction of luminous galaxies. Invoking efficient feedback in these massive galaxies (either through the use of a momentum-driven wind prescription in which the energy in the winds increases with galaxy mass, a top-heavy IMF for star formation at high pressure or AGN feedback) results in a monotonically decreasing LF. Dust attenuation, implemented by assuming that the optical depth scales with the metallicity-weighted column density, is more efficient in galaxies with less efficient feedback, as there is more (high metallicity) gas available in such galaxies. With efficient feedback, little gas is left in the galaxies, reducing the effect of attenuation to close to zero. In low luminosity galaxies the column densities and optical depth are in general lower. From virtual observations we find that the LF as obtained using techniques used for observations results in LFs very similar to those obtained directly from halo catalogues. Nevertheless, for large PSFs (corresponding to typical ground-based seeing conditions) very deep observations may result in shallower faint-end slopes of the LF, due to the preferential removal of low-surface brightness galaxies.

4.1 Introduction

The luminosity function (LF) has proven to be a very powerful tool in studies of galaxy formation and evolution. Observationally, the luminosities of galaxies in some wavelength band are relatively straightforward to obtain provided reasonable estimates of the galaxies' distances can be made (usually from spectroscopic or photometric redshifts) and ignoring dust attenuation. Galaxy formation models, combined with stellar population synthesis models, can predict the luminosities of galaxies. Here, several uncertainties come in to play. For example, the star formation histories and metallicities of model galaxies may not be representative of real galaxies. Population synthesis models also do not come without uncertainty, because the contribution of exotic kinds of stars (e.g. thermally pulsing asymptotic giant branch stars, TP-AGBs) may dominate the spectral energy distribution (SED) of a simple stellar population (in this example, the near-infrared emission) and the inclusion of these exotic stars is non-trivial (e.g. Maraston, 2005; Tonini et al., 2010). The initial mass function of stars is also crucial to determine the SED of galaxies and is not very well constrained, especially not at high redshift. Further issues, specific to simulations are how to model dust extinction without the presence of a multi-phase interstellar medium (ISM) and the (spatial and mass) resolution of the simulations used (see e.g. Jonsson, 2006; Wuyts et al., 2009).

Going the other way, i.e. converting the observed luminosities of galaxies into physical properties through SED modelling, comes at least with the same uncertainties. Added to those are the fact that many different combinations of physical properties are degenerate in their contributions to the SED of a galaxy. As an example, a population may become redder due to ageing, having more metals and/or more dust extinction. In order to break the degeneracies between models a very large range of wavelengths is generally necessary, ideally ranging all the way from the ultraviolet to the far-infrared (or even sub-millimetre). Even then, some problems still exist. Noise in the data can allow different solutions to the results of the SED modelling. Extinction will probably not be uniform across a galaxies, whereas most SED modelling attempts take one single value for the attenuation of a galaxy. For a recent review of SED modelling techniques, see Walcher et al. (2010). Very strong extinction will even result in the removal of a galaxy from the sample, an effect for which correction is nearly impossible.

Semi-analytic recipes for the evolution of the baryonic component of galaxies on top of some underlying dark matter halo merger history, are usually tuned to reproduce the redshift zero LF in one or more broadband filters (e.g. Cole et al., 2000; Croton et al., 2006; De Lucia & Blaizot, 2007; Monaco et al., 2007; Bower et al., 2008). Predictions for higher redshift LFs, or other (physical or observable) properties of the galaxy population, can then be made and tested in order to vali-

date the models. Hydrodynamical cosmological simulations, on the other hand, are usually not tuned to reproduce any LF. The LF is therefore a prediction of the models, but often already ruled out by observations. It is, nevertheless, still interesting to investigate the LF from hydrodynamical cosmological simulations. Especially when varying input physics of the simulations, as is done in this paper, as this makes it possible to investigate what physical ingredients shape the LF of a galaxy population. Previous studies have already focused on the photometric properties of simulated galaxies in various wavelength bands. For example, Nagamine (2002); Nagamine et al. (2004); Night et al. (2006) focus on the photometry of Lyman Break Galaxies at various redshifts and find that many simulations predict a LF with a steeper faint end slope than observed, for moderate assumptions about the extinction. Using their package ‘SUNRISE’, Jonsson et al. (2010) investigate the photometric properties of simulated mergers and from mock light cones constructed from the Millennium Simulation (Springel et al., 2005) with semi-analytic models, Kitzbichler & White (2007) and Stringer et al. (2009) compare the observed optical properties of a large range of galaxies at $0 < z < 5$.

In cosmological simulations, much of the physics that is very important for galaxy formation is not resolved, i.e. important processes take place on (mass, length and time) scales below the resolution limit of the simulations. For this reason, these simulations rely on sub-grid models that describe the effects of the small scale processes on the scale of their resolution (currently typically $\sim 10^6 M_{\odot}$ and/or ~ 1 kpc). There is considerable freedom in the implementation of these sub-grid models and in the values of their parameters. Many possible choices are well motivated, but result in substantially different galaxy populations.

In the current paper we use a small sub-set of the Overwhelmingly Large Simulations (Schaye et al., 2010), in order to investigate the LFs of simulated galaxies. Many of the physical parameters, including the stellar mass function, have already been discussed in Chapter 2. Here we implement the population synthesis models of Bruzual & Charlot (2003) in order to estimate the luminosities of the galaxies in several filters. As already alluded to, the LFs cannot be expected to give as good a match to observations as achieved by semi-analytic models. A major draw-back is also the cosmology used in these simulations, which match the WMAP 3-year results (Spergel et al., 2007), and have a lower amplitude of fluctuations than the currently favoured WMAP-7 year results (Komatsu et al., 2010). A more fundamental prediction of the simulations than the LF is the distribution of luminosities of galaxies as a function halo mass. This relation can then be convolved with a halo mass function from the favoured cosmology in order to predict the LF. We postpone such an analysis to future work and will focus on the LF as directly obtained from the simulations’ halo catalogues.

For these reasons, the goal of this paper is not to match the observed galaxy LF

as well as we can, but rather to

1. investigate how the input physics of the *OWLS* simulations affects the shape of the LF.
2. investigate how we can model dust attenuation in simulations with a resolution typical of current hydrodynamical cosmological simulations.
3. compare the LFs constructed from virtual observations with those from (sub-) halo catalogues.

Observers identify galaxies by selecting regions of pixels, whose surface brightness exceeds the background by some specified threshold. Simulators, on the other hand, usually identify gravitationally bound groups of particles, and call the centres of these structures (containing the stars and cold gas) galaxies. These methods are so fundamentally different, that it is not at all guaranteed that they would yield the same LF, even if they would both have the exact same population of galaxies. We will therefore project our star particles onto images, convolve them with a reasonable point spread function, add noise, and consequently measure the LF with the tools observers would use for this (in this Chapter we use SExtractor, Bertin & Arnouts, 1996). We will show that these two methods yield very similar LFs, which is encouraging for studies comparing modelled and observed galaxies.

The structure of this chapter is laid out as follows. In Section 4.2 we describe the simulations used in this chapter and the physics therein. Section 4.3 describes how we deal with the population synthesis and we show the convergence and evolution of the LFs, followed by a description of how different input physics influence the shape of the LF. Dust attenuation and its effect on the LF are discussed in Section 4.4. The creation of virtual observations and the LFs resulting from the procedure observers would follow are described in Section 4.5 and we conclude in Section 4.6.

4.2 Simulations

For a detailed discussion of the full set of *OWLS* runs we refer the reader to Schaye et al. (2010). Here we will briefly summarize the set of simulations, their relevant numerical properties and the sub-grid models under consideration.

4.2.1 Overwhelmingly Large Simulations

The simulations are performed with an extended version of the N-Body Tree/smooth particle hydrodynamics (SPH) code GADGET3 (an improved version

of GADGET2, last described in Springel, 2005) in periodic boxes of 25 and 100 comoving Mpc h^{-1} . There are 512^3 dark matter and equally many baryonic particles (which can be either collisionless ‘stars’ or collisional ‘gas’ particles). The particle mass of the highest resolution simulation under consideration (25 h^{-1} Mpc box size, 2×512^3 particles) is $8.68 \times 10^6 M_{\odot}$ for dark matter and initially $1.85 \times 10^6 M_{\odot}$ for baryons (the baryonic particle masses change during the course of the simulation due to mass transfer from star to gas particles).

Initial conditions are generated with CMBFAST (Seljak & Zaldarriaga, 1996) and evolved forward in time from an initial glass-like state using the Zel’Dovich (1970) approximation to $z = 127$, where the simulation is started. The cosmology assumed is specified by $\Omega_m = 0.238$, $\Omega_b = 0.0418$, $\Omega_{\Lambda} = 0.762$, $\sigma_8 = 0.74$, $n = 0.951$ and $h = H_0 / (100 \text{ km s}^{-1}/\text{Mpc}) = 0.73$. These values were deduced from the WMAP 3-year results (Spergel et al., 2007) and are largely consistent with the more recent WMAP7 results (Komatsu et al., 2010). The most significant discrepancy is in σ_8 , which is 8% lower in WMAP3 than in WMAP7 (resulting in slightly delayed structure formation in the WMAP3 cosmology).

The names of the simulations are as follows: ‘*NAME*_*LxxxNyyy*’, in which ‘*NAME*’ is a very short description about which parameters are changed (always specified in the text), ‘*Lxxx*’ is the box size, in which $L = \{100, 050, 025\}$, corresponding to 100, 50 and 25 comoving h^{-1} Mpc and ‘*N*’ denotes the number of particles, such that $N = \{512, 256, 128\}$ corresponds to 2 times 512^3 , 256^3 and 128^3 particles, respectively. As an example, the reference model in a 25 h^{-1} Mpc box with 2 times 512^3 particles will be denoted by ‘*REF_L025N512*’.

4.2.2 Subgrid physics in the reference model

Radiative cooling and heating are treated by explicitly following 11 elements in photo-ionization equilibrium with the CMB and a Haardt & Madau (2001) model for the UV/X-ray background radiation from quasars and galaxies, as described in Wiersma et al. (2009a). At some density, deep inside haloes, we know that the gas is composed of several phases, ranging from hot/warm tenuous gas to cold, dense molecular clouds. This high density, multi-phase ISM is not resolved and particles with proper physical hydrogen number densities $n_H > 10^{-1} \text{ cm}^{-3}$ and temperatures $T < 10^5 \text{ K}$ are put on a polytropic effective equation of state (EoS), in which the pressure $P \propto \rho^{\gamma_{\text{eff}}}$, where $\gamma_{\text{eff}} = 4/3$ is the polytropic index (this value is chosen, such that both the Jeans mass and the ratio of the Jeans length and the SPH kernel are independent of the density, thus preventing spurious fragmentation due to a lack of numerical resolution, see Schaye & Dalla Vecchia 2008), and ρ is the mass density of the gas. The normalization of the polytropic equation of state is such that the energy per unit mass corresponds to 10^4 K at a mean molecular

weight of 1.2. Star formation is followed stochastically, with a pressure dependent star formation rate, obtained from the observed Kennicutt-Schmidt law (Kennicutt, 1998a) and local hydrostatic equilibrium, as discussed in Schaye & Dalla Vecchia (2008). Gas particles are only allowed to form stars when they are on the EoS, so there is a threshold density for star formation of $n_{\text{H}} > 10^{-1} \text{ cm}^{-3}$.

The star particles are assumed to be simple stellar populations (SSPs) with a Chabrier (2003) IMF. Stellar feedback from massive stars and supernovae is implemented kinetically, which means that we launch a wind with wind velocity $v_w = 600 \text{ km s}^{-1}$, in which the mass loading is such that the energy in the wind corresponds to about 40% of the energy available from supernovae of type II (including Ib,c), which for our IMF means that the mass loading in the wind $\eta = 2 \times \text{SFR}$. For details on the kinetic wind implementation, see Dalla Vecchia & Schaye (2008). The enrichment of the gas by AGB stars, Type Ia and Type II (including Type Ib,c) supernovae is followed explicitly for the 11 elements needed for the cooling as described in Wiersma et al. (2009b).

4.2.3 Variation of subgrid models

In this chapter, we will make use of three variations to the reference model described above. One, which we will call ‘No SN/No Z cooling’ includes neither supernova feedback nor metal-line cooling. By comparing this model to the reference simulation we can investigate the influence of SN feedback on the LF, with and without dust attenuation. We turned off metal-line cooling because the metallicity of dense gas becomes unrealistically high in the absence of SN feedback. Note that there is still gas cooling through hydrogen and helium. The OWLS name of the simulation is ‘NOSN_NOZCOOL’.

The SN feedback as implemented in the reference model becomes inefficient for high-mass galaxies (Chapter 2), because the pressure in these galaxies is sufficiently high to prevent the wind from escaping. The newly enriched gas surrounding young stellar particles stays where it is and the high metal content and high densities result in effective cooling and star formation. In order to have a simulation with effective feedback from star formation for a wider range of galaxy masses, we implement a model that has a top-heavy IMF if the star particle forms at a pressure $P/k > 2.0 \times 10^6 \text{ cm}^{-3} \text{ K}$ (evaluated at the resolution limit of the simulation). The IMF used is a top heavy IMF with $dN/dM \propto M^{-1}$ (in these units, Salpeter would have an index of -2.35). The excess energy corresponding to the higher fraction of high mass stars per unit stellar mass formed is used to increase the initial wind velocity from 600 km s^{-1} to 1618 km s^{-1} . This model is called ‘Top-heavy IMF’, while its OWLS name is ‘DBLIMFCONTSFV1618’.

In order to investigate the effect of a varying wind mass loading (and to get a

higher mass loading in low mass galaxies) we use a wind model in which the mass loading and the wind velocity depend on the circular velocity ($v_c = \sqrt{GM_{\text{vir}}/R_{\text{vir}}}$) of the halo (determined using an on-the-fly group finder during the simulation) they were launched from, as follows: $v_w = 5v_c/\sqrt{2}$ and $\eta = \frac{1}{\sqrt{2}} \times (v_c/150\text{km s}^{-1})^{-1}$. Note that the energy in these wind models is not constant and increases with galaxy mass (and exceed the total available energy from SNe for the most massive galaxies). In low mass galaxies the mass loading is higher than in high mass galaxies, but the velocity is lower. These models are motivated by a wind driving mechanism in which the winds are accelerated by radiation pressure from the stellar population on dust grains (Murray et al., 2005). We will here call this model 'Momentum driven winds' and its OWLS name is 'WVCIRC'. This model is very similar to the model of Oppenheimer & Davé (2006, 2008)

The last simulation we will discuss here includes AGN feedback. The prescription for the growth of the black holes and the corresponding feedback are described in Booth & Schaye (2009). It is the OWLS simulation 'AGN'. This model produces black holes that follow the observed scaling relations (Booth & Schaye, 2009) and effectively suppress star formation in massive haloes (Chapter 2).

4.2.4 Halo identification

Haloes are identified using a Friends-of-Friends (FoF) algorithm, linking together all dark matter particles which are closer to each other than the linking parameter ($b = 0.2$ times the mean inter particle distance). Baryonic particles are linked to their nearest dark matter particle and belong to the same group, if any. FoF identifies iso-overdensity contours of $\delta \simeq 3/(2\pi b^3) \simeq 60$ (Lacey & Cole, 1994).

Within these haloes, gravitationally bound substructures are identified using the SubFind algorithm (Springel et al., 2001). SubFind starts with the output of FoF and removes any unbound particles. Bound substructures are separated from the main halo and classified as subhaloes. The separation of the subhalo and the main halo occurs at saddle points in the density distribution. All particles inside the subhalo are removed from the main halo, so the mass of the main halo decreases whenever a subhalo is identified. Each subhalo (above some resolution limit, see Sect. 4.3.1) is considered to be a galaxy.

4.3 Population synthesis

We obtain observables (such as magnitudes and colours) for our galaxies using the technique commonly known as population synthesis. The idea behind this technique is to obtain a spectrum of the galaxy by summing up all the spectra of its

CHAPTER 4. SIMULATED GALAXY LUMINOSITY FUNCTIONS

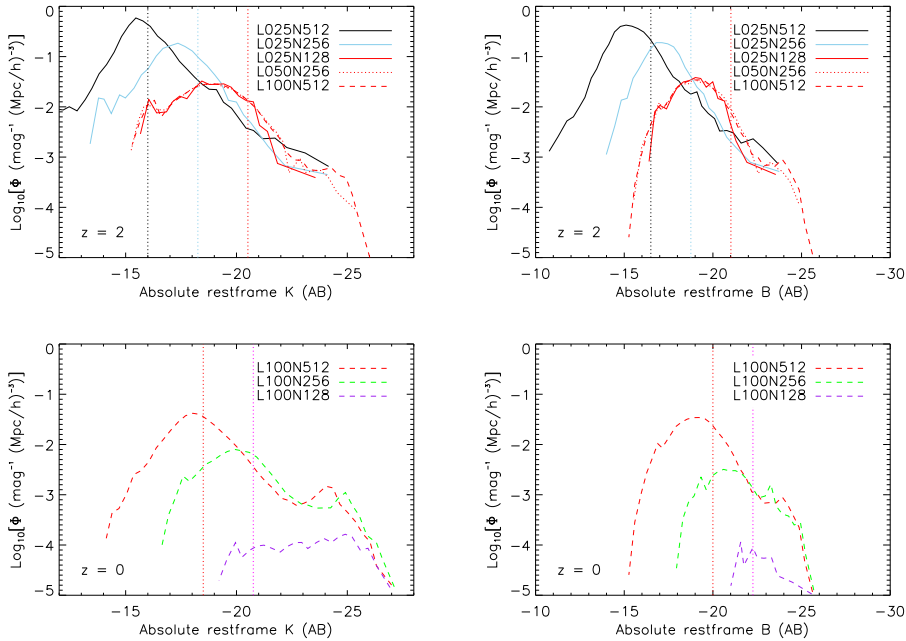


Figure 4.1: In the left-hand panels we show the rest-frame K -band LF of all subhaloes in the reference *OWLS* runs at redshift 2 (upper panel) and 0 (lower panel). Lines with the same line style have the same box size (and different resolutions), while lines with the same colour, but different style have different box sizes at the same resolution. In the right-hand panels we show the same, but now for the B -band. The vertical dotted lines show the adopted resolution limits in the simulations with the resolution corresponding to the same colour. We conclude that the LF is well converged with respect to resolution and that the box size is only important for sampling the high luminosity end of the LF.

stars. To this end, we assume every star particle to be an SSP, i.e. a stellar population with a single age and composition. The spectrum of this SSP then depends on its age, metallicity, mass and the IMF. The spectrum is convolved with a filter profile to obtain (broad-band) magnitude in any waveband desired. As input SSP spectra we use the package of Bruzual & Charlot (2003, BC03 from now on), with a Chabrier (2003) IMF, consistent with the IMF used in the simulations. The mass and metallicity are simply the initial mass and metallicity of the star particle (inherited from its parent gas particle) and the age the time since its creation.

We interpolated the BC03 spectra to a regular grid of 1000 ages and 20 metallicities, bracketed by the lowest and highest age and metallicity available in the BC03 package (so extrapolation was necessary). This step makes the assignment of spectra to star particles computationally more efficient. For every wavelength bin we used a 2-dimensional cubic spline interpolation to interpolate in $\log_{10}(\text{age})$ and $\log_{10}(Z)$, where Z is the metallicity. To obtain magnitudes we use the BC03 filter integration algorithms. This procedure gives a very smooth interpolation between the SSP magnitudes given by the standard BC03 software.

We assign to every star particle a magnitude (or spectrum) from this 20×1000 table by taking the nearest age and metallicity combination available scaling it to the appropriate mass (the initial mass of the star particle). We do not use any other spectra than SSP spectra, as the formation of a star particle is an event that is a delta function in time. In marginally resolved galaxies this means that, because of the stochastic nature of the star formation in these simulations, the age distribution of the stellar content is very spiky. In higher mass galaxies, where there are thousands ($M_{\text{star}} \sim 10^9 M_{\odot}$) to millions of star particles this stochasticity is washed out.

We will here first show LFs without correcting for attenuation. We will focus on rest-frame K -band absolute luminosities, because attenuation should be relatively unimportant in the K -band.

4.3.1 Convergence of the LF

The upper left panel of Fig. 4.1 shows the LF at redshift two in the K -band for 5 different simulations, all with the same physics, but using different box sizes (at fixed resolution, all red lines) and different resolutions (at fixed box size, all solid lines). By comparing the solid lines to one another one can see that with respect to numerical resolution, our LFs are reasonably well converged over a large range of luminosities. The size of the box is only important for the high-luminosity end: we sample the LF to higher luminosities in larger boxes, as expected. At the low-luminosity end there is a down-turn of the LF, which is expected to be due to a lack of resolution in the lowest mass systems. The vertical dotted lines show the resolution limits we adopt for simulations with a resolution of the corresponding colour.

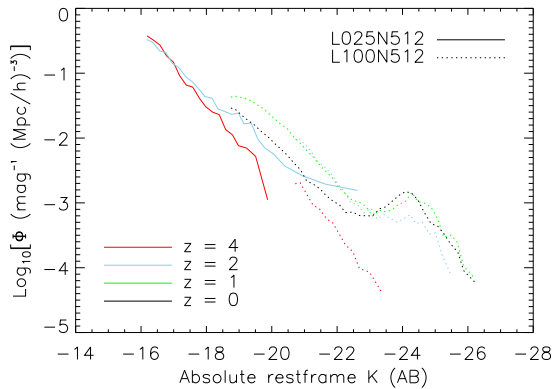


Figure 4.2: The evolution of the LF as a function of redshift for high resolution (solid lines, the *L025N512* simulation) and lower resolution (dotted lines, *L100N512* simulation, which has 64 times lower mass resolution). Different colours indicate different redshifts. The LFs are only shown for the magnitude range we consider converged.

The difference between the vertical lines is $\Delta K = -2.5 \log_{10} 8$, as expected if the resolution limit in luminosity equals the ratio in mass resolution of the simulations. The adopted resolution limit for simulations in a $25 h^{-1} \text{Mpc}$ box with 2×512^3 is $K = -16$.

For simulations with different input physics we verified that the same resolution limit holds at all redshifts we present in this paper. In the upper right panel we show the same, but for the *B*-band. In the *B*-band the adopted resolution limit is $B = -16.5$ for the same resolution simulations.

At redshift zero the resolution can be slightly relaxed (i.e. at the same resolution, the LF is converged down to fainter luminosities), as shown in the lower panels of Fig. 4.1. The adopted resolution limits in the at $z = 0$ are $K = -18.5$ and $B = -20$, respectively, for the $100 h^{-1} \text{Mpc}$ boxes with 2×512^3 particles. The very lowest resolution shown is not well converged at any luminosity. From now on we will only show LFs on the converged luminosity range.

4.3.2 Evolution of the luminosity function

For the reference simulation we show in Fig. 4.2 the evolution of the LF from $z = 4 - 0$, for both the low and the high resolution simulations (the high resolution only for $z = 4 - 2$ as the simulation stops at $z = 2$).

The number densities of galaxies of all *K*-band luminosities grow with time,

and the growth is stronger for higher luminosities. At redshifts lower than two we observe some peculiar behaviour in the low-resolution simulation. Towards $z = 0$ a bump appears in the LF. This feature has also been observed by Oppenheimer et al. (2010) in the stellar mass function at comparable resolution for constant wind models like the simulations presented in Fig. 4.2.

The appearance of the bump is closely related to the feedback prescription used. As discussed in Chapter 2, winds may or may not escape the galaxy and/or host halo depending on the prescription used and the mass of the halo. The winds need to be launched with a sufficiently high velocity in order for the gas to overcome hydrodynamical drag forces in the ISM. The required velocity increases with the pressure of the ISM and thus with the mass of the galaxy (see Dalla Vecchia & Schaye, 2008). If the wind velocities are too low, metal-enriched gas piles up, the star formation rate increases and too many stars are formed. This is visible in Fig. 4.3 as a relatively sharp upturn in the number density of galaxies For $K < -23$.

4.3.3 The effect of feedback from star formation and AGN

Simulations that use wind prescriptions which are efficient in removing gas at all masses do not predict a bump in the LF, as shown in Fig. 4.3. The bump is absent in both the model with a top-heavy IMF for starbursts and for the model that includes AGN feedback, which confirms that it was indeed the result of inefficient feedback in massive galaxies. AGN feedback is most efficient in suppressing star formation in massive galaxies, as was also shown in Chapter 2. At the low-luminosity end the LFs predicted by the the models that include SN feedback, but not the momentum driven winds, converge. This is because in lower mass galaxies the pressure in the ISM is low enough to form the majority of the stars with the default IMF, such that the SN feedback in all these simulations is the same, and because AGN are not active. The momentum driven winds result in a considerably shallower faint-end of the LF. Because the galaxies are of low mass, all wind velocities used are sufficient for the winds to escape the galaxies. In the lower mass galaxies, the wind mass loadings are higher, removing a larger part of the ISM in these galaxies.

So far, we have only looked at the stellar luminosities, which can be compared to attenuation insensitive bands, like the K -band, or to extinction corrected data. Because extinction corrections come with large uncertainties, and does not help for galaxies that were removed from the sample by extinction, it is also useful to try and go the other way around: estimate the extinction that would arise from the distribution of gas (and especially metals) in the simulation and compare directly to observed LFs. We will do this in the next section.

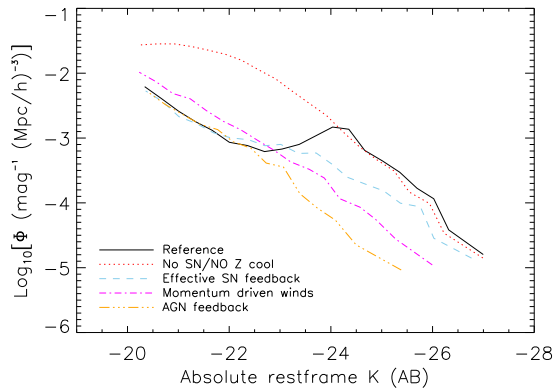


Figure 4.3: The K-band luminosity function at redshift zero for the reference (black solid line), no SN feedback and no metal-line cooling, top-heavy IMF for starbursts (red dotted line), momentum driven wind (magenta dot-dashed line) and AGN feedback (blue dashed line) models. The bump, which is very obvious in the reference simulation, is hardly present in the effective feedback models and absent in the AGN feedback run.

4.4 Dust attenuation

On its way outward through the ISM of a galaxy, star light encounters gas and dust which can absorb or scatter photons. Dependent on the wavelength under consideration, an estimate for the amount of dust attenuation is crucial to get the luminosity (or colour, as dust changes the colour by the wavelength dependency of the scattering and absorption) of a galaxy is crucial.

The clouds in the ISM in the solar neighbourhood that are responsible for the bulk of the attenuation are not resolved by our simulations. We will therefore have to rely on some parametrization (or sub-grid model) for the dust attenuation. Our approach is to model the dust attenuation on a star particle by star particle basis. This allows for gradients of attenuation throughout a galaxy, due to varying gas densities and metallicities. In Appendix 4.6 we explain the procedure of obtaining column densities from the simulations and we show the correlation between hydrogen column densities and several properties of the haloes. The hydrogen column densities towards star particles correlate strongly with the total mass, stellar mass and star formation rate of their host haloes. Correcting for these correlations leaves the spread of about two orders of magnitude in the column densities (for given halo mass, stellar mass or star formation rate) in tact, but there is no correlation left with

either of the other parameters we tried.

Here we will use the metal column densities from star particles integrated outward along a line of sight (L.O.S.) for 100 kpc. We tested the distance up to which the L.O.S. integration should be carried out in the following way. Increasing the distance up to which gas particles are still counted increases the column density up to a few to several tens of kpc, after which it remains constant (there is no EoS gas in between haloes). We therefore chose to use 100 proper h^{-1} kpc for the maximum distance at which particles can still contribute to the L.O.S. towards a star particle. Absorption by the intervening intergalactic medium can be taken into account separately, but we will not consider it here.

4.4.1 Method

In Appendix 4.6 we explained how we compute hydrogen column densities to individual star particles. Because the optical depth due to dust extinction is expected to scale with the metal column rather than the hydrogen column density (dust after all is made up of metals), we estimate dust attenuation for an individual star particle from the metallicity-weighted hydrogen column density in front of the particle and the observed relation between the gas column density and the optical depth in some band for solar metallicity. We then use an extinction law in order to get optical depths for any desired effective wavelength.

The observed relation is based on observations in the solar neighbourhood (at solar metallicity) and relates the optical depth in the B -band to the hydrogen column density: $\tau_B = 5.3 \times 10^{-22} N_H$ as derived by Xu et al. (1997), which is consistent with the results of Larson et al. (2000). With a solar metallicity of 0.012 and the assumption that the optical depth in the B -band due to dust attenuation scales linearly with metallicity, we become

$$\tau_B = 5.3 \times 10^{-22} \int n_H \left(\frac{Z}{Z_\odot} \right) dL \quad (4.1)$$

where n_H is the hydrogen number density and Z is the metallicity. In order to get the attenuation in other wavebands an extinction law can be used. Because the present approach is already full of uncertainties itself, we decide to use a simple power law approximation of the extinction law, given by

$$\frac{\tau_\lambda}{\tau_B} = \left(\frac{\lambda_{\text{eff}}}{\lambda_{B, \text{eff}}} \right)^{-n} \quad (4.2)$$

in which τ_λ is the optical depth at the effective wavelength λ_{eff} , τ_B the optical depth in B from Eq. 4.1 and $\lambda_{B, \text{eff}} = 4391 \text{ \AA}$. The value for the extinction law index n varies among different authors, ranging from 0.7 in the model of Charlot & Fall

CHAPTER 4. SIMULATED GALAXY LUMINOSITY FUNCTIONS

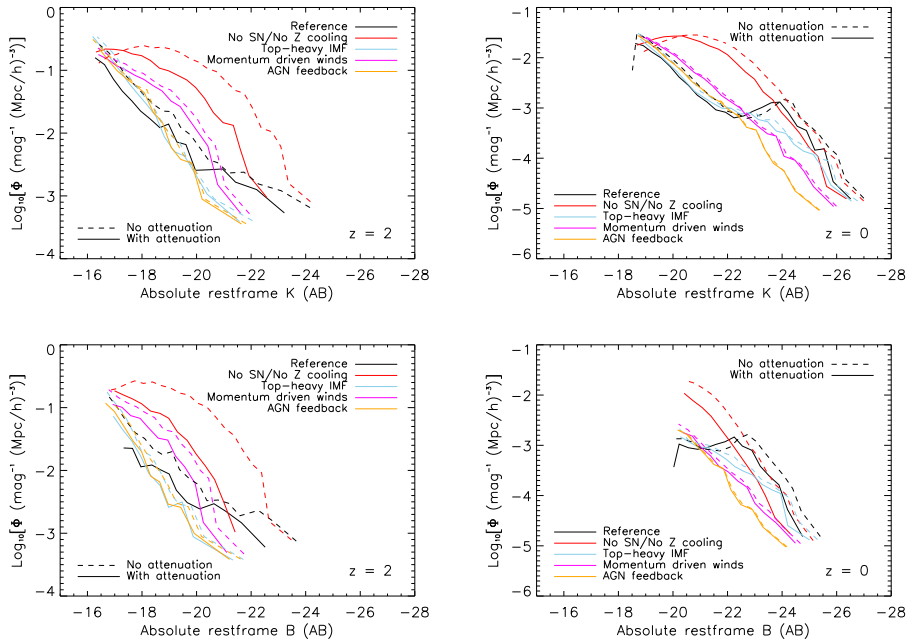


Figure 4.4: The LFs in K (upper panels) and B (lower panels) at redshift 2 (left panels) and 0 (right panels), both including dust attenuation (solid lines) and excluding attenuation (dotted curves, which are also shown in Fig. 4.3). The K -band LF is less influenced by dust attenuation than the B -band LF. Strong SN feedback and AGN feedback lower the high density gas content of galaxies and therefore result in a smaller difference between the attenuated and unattenuated LF.

(2000) to 1.5 for the SMC (Weingartner & Draine, 2001). We use 0.96, after Shao et al. (2007). Some studies use extinction laws which are not pure power-laws, but have features, like the often used Calzetti et al. (1994, 2000) extinction law.

4.4.2 Luminosity functions with dust extinction

The inclusion of dust extinction can potentially change the sign of the effect of feedback on the LF. In simulations with more effective feedback, haloes contain less gas and form less stars. However, the dust attenuation may be much lower in such simulations due to the much lower gas densities.

In Fig. 4.4 we show the rest-frame B - and K -band LFs with and without dust for the same simulations and redshifts as in Fig. 4.3. The effective wavelength of the K -band is almost 5 times longer than that of the B -band, so the optical depth

in K is roughly 5 times smaller than that in B , which corresponds to about 1.7 magnitudes. The difference between the LFs (compare adjacent panels) seems, however, to be somewhat smaller. This arises because the star particles which are visible are the ones with a low extinction, whereas the ones that are heavily obscured are invisible in both filters (even in the K -band the optical depth is high for the highest column densities).

Fig. 4.4 shows clearly that attenuation is less important in simulations with more effective feedback: the simulation with AGN feedback hardly shows any attenuation at all, even in the B -band, because of the efficient removal of ISM gas, especially in the high mass galaxies.

4.4.3 The shortcomings of dust attenuation estimates in cosmological SPH simulations

The ideal situation for simulators would be to rely on dust attenuation estimates observers obtain from their data, and compare their attenuation-corrected luminosities directly to the unattenuated luminosities of simulated galaxies. Unfortunately, the observationally inferred extinction corrections are highly uncertain and are only available for galaxies in which the attenuation was sufficiently modest for the galaxy to be detectable. Moreover, there is not one single number for attenuation of a galaxy. Different stellar populations are covered by different dust clouds, but the only quantity that can usually be inferred from the observations is the effective attenuation of the integrated light of the galaxy. Although these issues make the inclusion of dust attenuation in simulations worthwhile, this procedure is also highly uncertain.

We have only showed one particular estimate of the dust attenuation, while much more are possible. Some authors have used even simpler methods than the one presented here, and others have used much more complicated, (approximate) radiative transfer schemes in order to estimate the simulated galaxy SEDs (e.g. Jonsson, 2006). In real galaxies, small, cold and dense clouds are responsible for the strongest extinctions, but cosmological simulations such as ours do not yet include this cold, interstellar gas phase.

If more ‘realistic’ scenarios for extinction are desired, knowledge about the number, covering factor and column densities of absorbing clouds is required and would thus necessitate some ad hoc assumptions. Even if we were to use a multi-phase model for the gas on the equation of state (e.g. Jonsson et al., 2010; Scannapieco et al., 2010) we would still need to assume some distribution of cloud numbers and sizes. As all this information is not predicted by the simulation itself, the model for the extinction would become disconnected from the simulation. This is the main reason why we instead chose to use an observed relation between metal

column density and the optical depth, which itself is the average of a sample of sight lines that pass through some number of absorbing clouds.

Another method for estimating the attenuation, based on an inversion of the Kennicutt-Schmidt law (in which the column density of gas is estimated from the star formation rate of a galaxy), tends to strongly overestimate the attenuation, because the total attenuation of a galaxy is weighted by the visible luminosity of star particles, and therefore biased towards the least attenuated parts of a galaxy.

4.5 Mock images and galaxy selection

Observers identify galaxies on an image by grouping regions of pixels that have a certain minimum surface brightness. Using packages like SExtractor (Bertin & Arnouts, 1996) this process can be automated in a clear and reproducible way. The methods for galaxy identification used for simulations and observations are therefore very different. We have used SubFind to identify gravitationally self-bound structures, in the centres of which there usually are stars. A galaxy's luminosity is then just the sum of the luminosities of the bound star particles. It is therefore not at all clear that the observers' way of identifying galaxies will give the same brightness for the galaxies as the methods commonly applied to simulations, even if the underlying distributions of galaxies are identical. For example, there might be projection effects in which smaller (satellite) galaxies cannot be separated from the bright galaxy in front or behind them and extended haloes of stellar light may dissolve into the background.

By creating virtual observations, we can perform a galaxy selection procedure very similar to the one used by observers. In this section we will first describe the creation of the images, followed by a description of the SExtractor settings we use to identify galaxies in the images. We will investigate the influence that SExtractor parameters and the parameters for the creation of the mock images (e.g. the size of the point spread function (PSF), the noise properties and the pixel size) have on the obtained LFs. We will use parameter values that are roughly equal to those in a selected set of observations. We will only use the reference simulation at redshift 2, in a $25 h^{-1}\text{Mpc}$ volume, with 2×512^3 particles, except in the resolution study, where we vary the particle number. We will not use the $z = 0$ resolution, because our simulations that go down to $z = 0$ do not have sufficient resolution to match observed data sets.

4.5.1 Creating mock images

We will make images with properties that roughly match those of real observations. We focus on three different surveys. For the *Hubble* Ultra Deep Field (UDF,

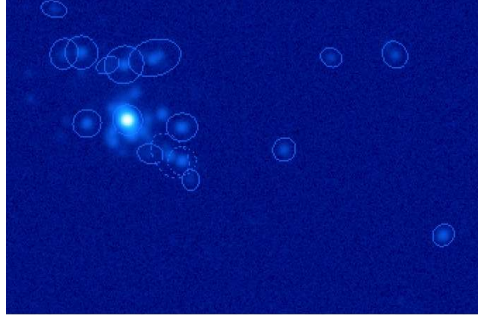


Figure 4.5: An example of the images produced by the described procedure. These come from the reference simulation at redshift two, in the observed MEGACAM i-band. The image shows 340×230 pixels, which corresponds to 17×11.5 arcsec and 580×390 comoving kpc. The parameters are those used to mimic the Hubble UDF, so the PSF is a Gaussian with a FWHM of 0.12 arcsec and the noise is Gaussian with a FWHM of $28 \text{ mag arcsec}^{-2}$. The overdrawn apertures are the apertures defined by SExtractor (check image type ‘APERTURES’) on which the photometry is performed.

Beckwith et al., 2006) the pixel size is 0.05 arcsec, the point spread function can be approximated by a Gaussian with a full width at half maximum (FWHM) of 0.12 arcsec, and the noise on the image (after subtracting the mean) is well approximated by a Gaussian with a standard deviation of $28 \text{ mag arcsec}^{-2}$. For the VIMOS VLT Deep Survey (VVDS, Le Fèvre et al., 2004) the pixel size and PSF (Gaussian FWHM) are 0.205 arcsec and 0.8 arcsec, respectively. The background was different for different nights. For simplicity we assume the noise level to be the same as the one for the UDF: $28 \text{ mag arcsec}^{-2}$ (which is unrealistic, but as we will show below does not influence the results). The last survey we investigate is the Canada France Hawaii Telescope Legacy Survey (CFHTLS, Cabanac et al., 2007). In order to compare to the ‘wide’ survey of CFHTLS, we assume typical exposure times of one hour, which with their standard read-out noise and (AB) magnitude zero-points results in a background subtracted noise described by a Gaussian with FWHM $26.9 \text{ mag arcsec}^{-2}$ on pixels of 0.186 arcsec with a PSF (average seeing conditions) of 0.7 arcsec.

The observational surveys used slightly different filter sets, but in order to facilitate direct comparisons we always use the i-band filter of MEGACAM, as used in the CFHTLS. This is their reddest filter with a reasonable depth. It has an effective wavelength of 770 nm, which at redshift 2 corresponds to an effective rest-frame wavelength of 257 nm. The noise levels for the other data sets are taken from

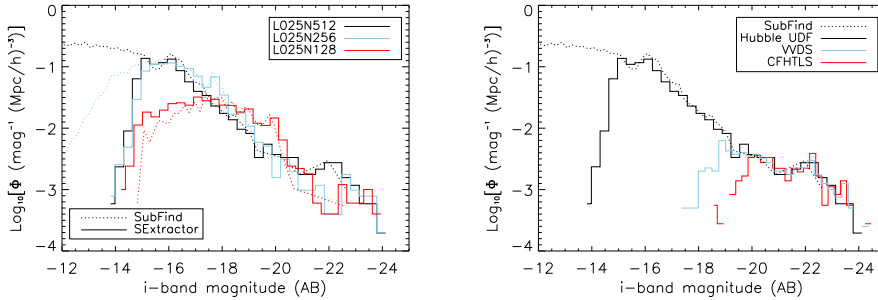


Figure 4.6: *Left panel:* the LF from both SubFind (dotted lines) and SExtractor (solid lines), for three simulations with different numerical resolution, all with the same parameters for the creation of the images and for the detection of galaxies. The differences between the LFs obtained by SExtractor for the different resolutions are entirely due to the underlying distribution of sources and the creation of images and measuring the luminosity functions using SExtractor are insensitive to numerical resolution. *Right panel:* The LF as obtained from SubFind, i.e. directly from the simulations (dotted line), compared to the luminosity function obtained using mock images, mimicking three different observational data sets: Hubble UDF, VVDS and CFHTLS, respectively. The parameters of those data sets can be found in the text.

nearby filters ($F814$ and I for UDF and VVDS, respectively).

For computational efficiency we cut the simulation box in 10×10 regions (of $2.5 \times 2.5 \times 25$ comoving $h^{-1}\text{Mpc}$) and project the stars along the long axis onto pixels of the desired size.

In Fig. 4.5 we show an example of (part of) an image created from the reference simulation at redshift two, with the SExtractor apertures overdrawn. The image shows 340×230 pixels, which corresponds to 17×11.5 arcsec and 580×390 comoving kpc. The parameters are those used to mimic the Hubble UDF, so the PSF is a Gaussian with a FWHM of 0.12 arcsec and the noise is Gaussian with a FWHM of $28 \text{ mag arcsec}^{-2}$. In low density regions it is clear that most if not all sources are well defined. In higher density regions, like the area left of the centre of the image, some emission can be missed. We will use the ‘mag_auto’ magnitudes of SExtractor in the remainder of this chapter.

4.5.2 Comparing the LFs from halo catalogues and mock observations

Fig. 4.6 compares the LFs obtained from virtual observations with those obtained from halo catalogues. The mock observations used parameters for the images and for SExtractor as described above for the Hubble UDF). The left panel compares three simulations with different numerical resolution. In each case the LFs from the mock observations (solid histograms) match those from the halo catalogues (dotted lines) well down to about $i = -15$ ($i = -17$ for the lowest resolution shown). The difference in the LFs from SExtractor for different resolutions are therefore the result of the different star formation histories of the haloes in the simulations, and not of the mock image procedure.

In the right panel of Fig. 4.6 we show the LF from SubFind together with three LFs from mock images, all for the reference simulation at the highest resolution at $z = 2$. These three closely mimic the UDF, the VVDS and the CFHTLS. Down to the luminosities that define the depths of the surveys all three observational data sets follow the LF obtained directly from halo catalogues very well. Thus, if our simulated galaxy sample would be observed by either of the three telescope/instrument combinations described, then the LF obtained would be nearly exactly the same as the true LF of the galaxies in the simulation, down to some limiting magnitude. It is, nevertheless, not straightforward to compare the three LFs, as they differ simultaneously in terms of the background noise level, pixel size and PSF size (the SExtractor settings for the three LFs are, however, identical). In the following sections we will look at the effect of varying the parameters for the mock image creation and for the detection and photometry of the galaxies. We will vary the parameters one-by-one using the parameter values corresponding to the HUDF as our baseline.

4.5.3 Mock image parameters

In this section we will investigate the dependence of the galaxy selection technique using mock images and SExtractor on the parameters used for creating the virtual observations. Specifically, we will vary the noise level, the size of the pixels and the size of the Gaussian PSF. These are all varied away from the HUDF values by factors of 5 and 10, roughly bracketing the other observational data sets.

Increasing the noise level by factors of 5 or 10 results in the LFs shown in the upper left panel of Fig. 4.7. As expected, the minimum observed galaxy luminosity increases with the noise level. The LF is already complete for galaxies that are only 1 magnitude brighter than the faintest detected objects at a given noise level (the underlying galaxy population is the same for the three LFs and shown by the dotted

CHAPTER 4. SIMULATED GALAXY LUMINOSITY FUNCTIONS

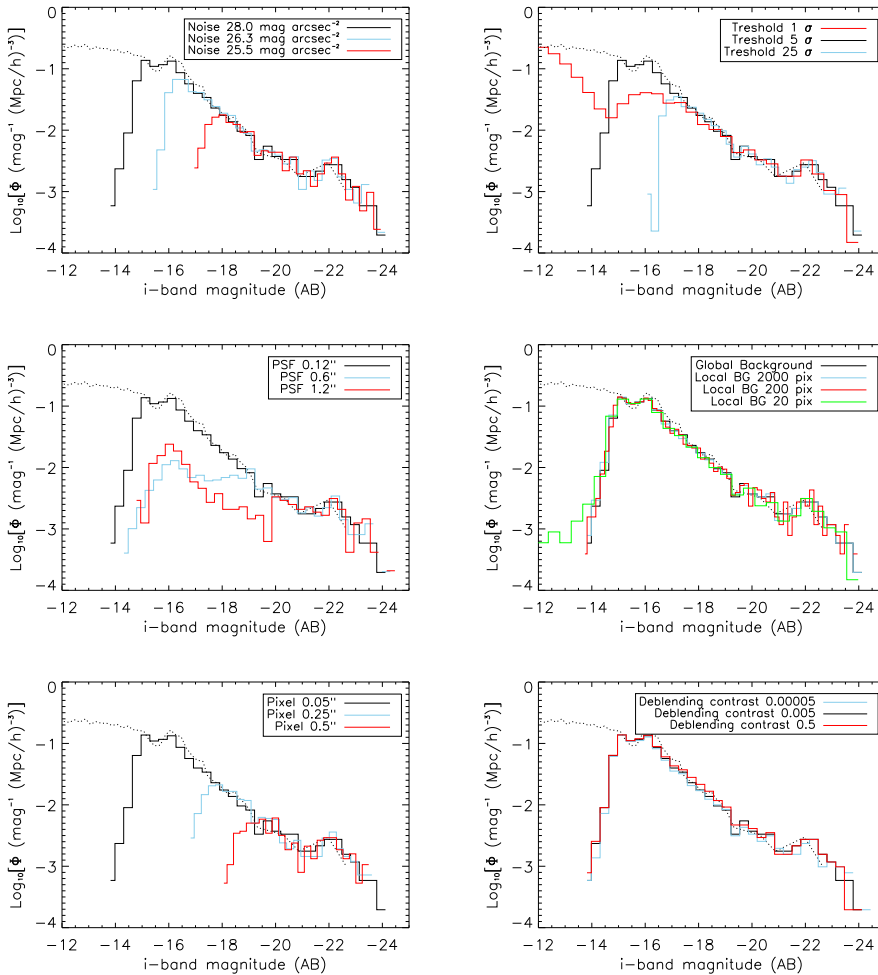


Figure 4.7: The influence of several image creation and SExtractor parameters on the obtained LF. In the *left column* we vary the parameters used when creating the image, from top to bottom: the size of pixels (and thus the resolution) of the images, the size of the PSF (varied over a factor 5 and 10) and the amount of noise (the HUDF value and that increased by a factor of 5 and 10). In the *right column* we vary three important SExtractor parameters, from top to bottom: the minimum deviation of the pixels above the background, the deblending contrast and the background (global as used in the other plots versus a local background determined on a small and on a large area). The solid black line is the default model and is the same in every panel. The dotted black line is the LF of the underlying galaxy population directly from the simulations.

line).

Changing the size of the PSF (from the default, a Gaussian with a standard deviation of $0.12''$) strongly affects the recovered galaxy population. If we increase the PSF (at fixed pixel size) by a factor of 5 or 10, so to a Gaussian with standard deviations of $0.6''$ and $1.2''$, we detect less galaxies as we smear the galaxies out more and we start to lose the low surface brightness objects. Increasing the PSF therefore results in a much flatter LF over a large range of galaxy luminosities, as shown in the middle left panel of Fig. 4.7. Only the very brightest galaxies follow the same LF as the one obtained from images with a smaller PSF. While the SExtractor LF agrees with the intrinsic (i.e. SubFind) LF for $i < -15$ for a $0.12''$ PSF, the two only agree for $i < -19$ and $i < -20$ for PSFs of $0.6''$ and $1.2''$, respectively. Note that a PSF with a standard deviation of $1.2''$ is not extremely large. This may indicate that at high redshift the LF, if observed with spatial resolutions typical for ground based surveys, may be strongly flattened due to the selection technique used to identify the galaxies. Hence, if the ground based surveys shown in Fig. 4.6 had integrated longer and therefore produced observations with a higher signal-to-noise ratio, then the low luminosity end of the measured LF would most likely be shallower than that of the underlying population of galaxies.

The size of the pixels (for a fixed PSF size) is also important for the selection of galaxies, as shown in the lower left panel of Fig. 4.7. Increasing the pixel size results in a higher minimum detected luminosity. Note, however, that in the images with larger pixel sizes, the FWHM of PSF is smaller than a pixel, which is unrealistic.

4.5.4 SExtractor configuration file parameters

The detection of galaxies with SExtractor depends on many parameters, some of which are more crucial than others. In this section we will compare the LFs obtained after changing some of the parameters in the configuration file within acceptable bounds.

The first parameter we vary is the detection threshold. On the image, the software determines a background (for variations of the background estimate, see below) and specifies it by a mean and a standard deviation σ . Sources are then defined to be objects if at least some number of adjacent pixels (5, here) stand out above the background by at least some number of standard deviations. By default, we have set this threshold to 5σ . Decreasing this parameter from 5 to 1σ results in the detection of fainter sources (i.e. sources with a lower surface brightness) as we can see in the upper right panel of Fig. 4.7. A deviation of only 1σ is not rare, so sometimes a collection of noise pixels will be mistaken for a low brightness galaxy. The blending of sources will be more important in highly populated regions, as it

CHAPTER 4. SIMULATED GALAXY LUMINOSITY FUNCTIONS

is easier to connect blobs of emission with pixels exceeding the background by 1σ than with pixels exceeding the background by 5σ . The threshold does not influence the shape of the LF at higher luminosities, as the few pixels with noise-like surface brightness do not add significantly to the luminosity of a bright galaxy. Increasing this threshold by a factor of 5 (i.e. demanding a source to stand out 25σ above the background) results in much less faint galaxies, but high luminosity end is again unaffected.

The estimate of the background on the image is also subject to a few SExtractor settings. In the first place, one can choose between a global or a local background. Global means that it is the same over the whole image, while local refers to a locally determined background. We have so far chosen to use a global background, because that is what our mock images contain. Here we investigate whether or not using a local background influences the selection of galaxies (we leave the background the same when creating the images). For example, in highly populated regions of the universe the local background might be higher, blending low luminosity objects. In the middle right panel of Fig. 4.7, we compare the results of using a global background to results using a local background, for which we set the area used to determine the background to three different (and extreme) values: 2000 pixels (almost as big as the image), 200 pixels and 20 pixels (only slightly larger than the objects themselves). Although the last choice extends the LF to slightly fainter levels, the differences are marginal. We conclude that for our method of adding noise, the selection of galaxies with SExtractor is insensitive to the details of the background estimation (but this would probably change if we were to make the background change gradually across the image).

The last parameter we will investigate is the minimum contrast for deblending. Whenever there is a saddle point in the surface brightness distribution, SExtractor has to decide whether there are two slightly overlapping sources, or whether it is one, with substructure. The parameter that influences this decision is the minimum deblending contrast, which is the ratio between the integrated intensity of both sub-peaks. A very high minimum contrast means that fluctuating fields are more likely to be regarded as one source. For more details we refer to Bertin & Arnouts (1996). The number of levels in surface brightness is left at the default setting, 32. In the lower right panel of Fig. 4.7 we compare several minimum deblending contrasts. Varying the parameter over 4 orders of magnitude (from 0.5 to 5×10^{-5}) does not make an appreciable difference for the recovered LF. We therefore conclude that this parameter is not crucial for our purposes. Another conclusion is that blending of sources is not an important effect for the mock images. If it were, a very low minimum contrast would have been able to detect satellite galaxies as seen in projection before or behind a more luminous galaxy. Note, however, that we may underestimate the number of superpositions of physically unrelated objects

due to the small size of our volume. The spatial resolution of the simulations and images (of order 1 kpc) is also large enough to ensure that all galaxies have fairly smooth surface brightness profiles.

We want to note here that at lower redshift (e.g. $z = 0.1$, the median redshift of SDSS) the differences between the LFs from halo catalogues and from virtual observations could well be larger. At low redshift, the massive haloes contain a large halo of ‘intra-cluster light’, stars that are far away from the central galaxy in a large diffuse halo (up to $\sim 30\%$ of the luminosity of what would be called the central galaxy). It is well possible that such haloes are not picked up by SExtractor as being part of the galaxy. The spatial resolution of the simulations that go down to redshift zero are comparable to the SDSS angular resolution, so resolution issues are likely to play a big role, and for this reason we postpone such an analysis to future work.

4.6 Conclusions

We have investigated the LF of galaxies in several simulations, differing in the input physics. We focused on $z = 2$ and $z = 0$ and investigated an implementation of dust attenuation and its effect on the luminosity function in both the K - and the B -band. Finally, we created virtual observations and obtained the LF using the tools observers would use for the same purpose.

Whenever LFs are obtained from observations with inefficient SN feedback (and no AGN feedback) in high mass galaxies, an over-abundance of high luminosity galaxies appears. This shows as a ‘bump’ in the LF. The high luminosity ends of such simulations correspond to the high luminosity end of the LF of a simulation without any SN feedback, indicating that the feedback in these high luminosity galaxies is indeed very inefficient. In simulations with a top-heavy IMF for star formation at high pressures, for momentum-driven wind models (which have more energy in the winds than available from SN, especially in high mass galaxies) and for simulations with AGN feedback (which are mainly effective in shutting off star formation in high mass haloes) the ‘bump’ disappears and the LF goes steeply down. The low mass end slope of the luminosity function mainly depends on the mass loading in the winds: higher mass loading results in a flatter slope.

The inclusion of dust attenuation can potentially change the sign of the effect of feedback on shape of the LF, because besides lowering the star formation in massive galaxies it also lowers the gas content and possibly the dust content. We estimated the dust attenuation from the metallicity-weighted gas column density towards individual star particles. By doing so, we make sure that the dust atten-

CHAPTER 4. SIMULATED GALAXY LUMINOSITY FUNCTIONS

uation may vary with location in the galaxy and that the attenuation scales with the metallicity and gas column towards star particles. The effect of dust attenuation implemented as such is that the attenuation is strongest in the most luminous galaxies and stronger for simulations with weaker feedback (at given intrinsic luminosity). The difference in attenuation in the K and B -bands is less than the factor of 5 difference in the optical depth for given column density for these two effective wavelengths, because the total apparent luminosity is dominated by the least attenuated stellar emission.

It needs to be noted, that due to the low spatial (and mass) resolution of cosmological simulations, dust attenuation estimated may not be very reliable. As the bulk of the attenuation in the solar neighbourhood happens due to small high opacity clouds (and there is no reason to suspect this is different in other galaxies), dust extinction happens on scales much smaller than the resolution limit of current simulations.

We made mock observations, mimicking three different observational data sets (the Hubble Ultra Deep Field, the VIMOS VLT Deep Survey and the CFHT Legacy Survey) at redshift 2 in a rest-frame UV band. We conclude that down to the flux limits of the surveys the LFs obtained from the virtual observations agree very well with those obtained directly from the halo catalogues. Interestingly though, the size of the point spread function may become very important for very deep, ground-based surveys. For large PSFs (~ 1 arcsec), but deep images and low noise levels, objects of low surface brightness are preferentially removed from the sample. As the fraction of low surface brightness galaxies is higher for lower luminosities, this may substantially flatten the low-luminosity end of the observed LF, compared to the underlying intrinsic LF.

LFs should not be used as discriminators between different cosmological hydrodynamical simulations (as is often done for semi-analytic models of galaxy formation). Even if LFs are obtained by convolving halo mass functions (obtained with the favoured cosmology) with the galaxy luminosity as a function of halo mass, plenty of difficulties still remain. The star formation histories of galaxies in models invoking different sub-grid physics vary strongly and a distinction solely based on the shape of the LF will probably prove degenerate. Also, especially for blue rest-frame wavelengths, dust attenuation will be important, and how to estimate dust attenuation for a galaxy is far from trivial.

Acknowledgements

It is a pleasure to thank Hendrik Hildebrandt and Daniel Szomoru for discussions about the observational sides of this study. The simulations presented here were

run on Stella, the LOFAR BlueGene/L system in Groningen and on the Cosmology Machine at the Institute for Computational Cosmology in Durham as part of the Virgo Consortium research programme.

Appendix A. Column densities in SPH simulations

In order to obtain galaxy magnitudes which include the effect of dust attenuation, we calculate column densities through the simulation box. First, we will summarize how densities are defined in SPH and how we calculate column densities along lines of sight through the simulation box. We will then show how hydrogen column densities depend on galaxy properties. Finally, we will use the column densities of metals in order to estimate the attenuation of stellar light on a star particle by star particle basis.

SPH interpolation and densities

In SPH simulations the density field is discretized by a set of particles whose smoothing kernels determine their contribution to a given physical quantity at a given point in space. Although in principle a kernel can have a plethora of shapes, they are usually chosen to be similar to Gaussians, although they go to zero at small distance from the particle. The most commonly used kernel is the one originally proposed by Monaghan (1992), which consist of two parts, both described by a polynomial. This form goes to zero for a value equal to two times the kernel length. Springel (2005) introduced a kernel, which we use, whose shape is exactly the same, but goes to zero at one kernel length and changes prescription half-way:

$$W(r, h) = \frac{8}{\pi h^3} \begin{cases} 1 - 6\left(\frac{r}{h}\right)^2 + 6\left(\frac{r}{h}\right)^3 & 0 \leq \frac{r}{h} \leq 0.5 \\ 2\left(1 - \frac{r}{h}\right)^3 & 0.5 < \frac{r}{h} \leq 1 \\ 0 & \frac{r}{h} > 1 \end{cases} \quad (4.3)$$

Both transitions from one to the other prescription are continuous up to the second derivative. The value of the smoothing length h is chosen such that for every density there are about N_{SPH} particles within one kernel (in our simulation $N_{\text{SPH}} = 48$). The value of a given physical quantity at the location of particle i (ρ_i), in this example the density, is now given by a summation of all gas particles that fall within the kernel of point p , weighted by that kernel:

$$\rho_i = \sum_{j=1}^N m_j W(|\mathbf{r}_{ij}|, h_i), \quad (4.4)$$

where $\mathbf{r}_{ij} = \mathbf{r}_i - \mathbf{r}_j$. The value of the kernel in the point of interest is determined by increasing a sphere until it contains a constant mass, and therefore about $N_{\text{SPH}} \simeq 48$ particles. Note that the value of the kernel depends on the kernel at the location the density is desired of, but not on the kernels of the other particles. This is called the ‘gather approach’, contrary to the ‘scatter approach’, which we will describe below.

Column densities

Surface mass densities are obtained by integrating the density along a line of sight (L.O.S.):

$$\Sigma = \int_{\text{LOS}} \rho(\mathbf{x}) dL \quad (4.5)$$

where L is a spatial coordinate along the L.O.S.. At every point in space, the physical density is determined by a kernel-weighted sum of all particles (of which ~ 48 should contribute). The method we use to obtain column densities changes the order of the summation over the particles and the integration along the L.O.S.. For every particle we obtain its contribution to the L.O.S. integral, as a function of its impact parameter b . We tabulate the column densities as a function of b in a look-up table. We distinguish between particles whose kernels are crossed completely (from one edge to the other) and particles for which the L.O.S. either starts or ends within its kernel.

For computational efficiency we use the kernel of the particle under consideration, rather than the kernels of all points along the L.O.S.. This is slightly inconsistent with the actual SPH formulation used in `GADGET`, as explained in Section 4.6 (we use the ‘scatter’ rather than the ‘gather’ approach). However, within one kernel length the density will not vary much, leaving the kernels very similar and the errors introduced by this procedure are minor ($\lesssim 1\%$).

For particles with kernels that are completely crossed by the L.O.S. the look-up table is one dimensional, having the impact parameter as the only parameter. We tabulate a value for the column density, normalized to mass (‘column density per unit mass’) and we use spatial coordinates normalized to the kernel (i.e. b/h). The integral is evaluated numerically using Romberg integration. The impact parameter is taken to be between 0 and 1 in 10.000 steps. This reduces the relative error in the kernels of the particles along the L.O.S. to be $O(10^{-4})$.

For particles whose kernel overlaps with the start or the end of the L.O.S., the estimate described above would be too high. For these particles we use a two-dimensional table of (mass- and kernel-normalized) column densities, with the impact parameter and a ‘distance parameter’ (the distance through the kernel, perpendicular to the impact parameter). Due to memory issues we use a lower precision

4.A. Column densities in SPH simulations

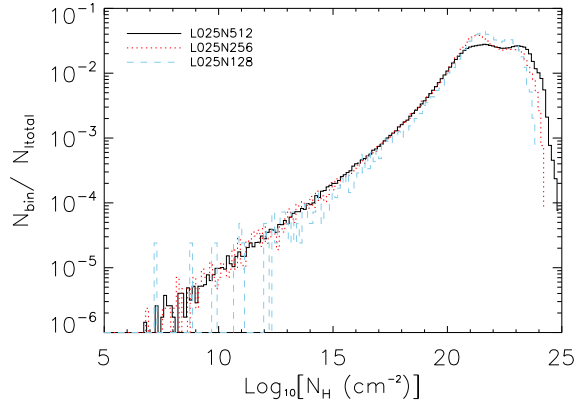


Figure 4.8: The distribution function of column densities in the ‘REF’ simulation at three different resolutions: 512^3 , 256^3 and 128^3 particles. The number of lines of sight in a bin is divided by the total number in the box. Each L.O.S. targets a different star particle.

for this table than for the one-dimensional one. As this table will only be used for a small fraction of the particles (for L.O.S. much longer than a typical particle kernel), the number of steps for both parameters between one and zero is chosen to be 1000. This is a minor limitation, as there are many more particles crossed completely than partially, for L.O.S. longer than a typical particle kernel (\sim kpc). In this work we will mostly consider L.O.S. of 100 kpc, whereas the kernels deep inside the haloes are \sim 1 kpc in the high-resolution simulations.

Column densities towards star particles in cosmological SPH simulations

Selection of gas

In this paper we are interested in the attenuation towards star particles by the gas in a galaxy. Because we are interested in the gas of a galaxy that resembles the ISM, we will only take gas into account that has a density exceeding the star formation threshold. This gas is expected to be responsible for the biggest part of the attenuation and is probably closely related to the gas measured in 21 cm observations and the gas probed by molecular indicators (although this would be a fraction of all EoS gas (in volume even a small fraction), the other part of the EoS gas being the warm and ionized ISM). The L.O.S. are taken along the main axes of the simulation box, and therefore the galaxies are oriented randomly relative to the L.O.S..

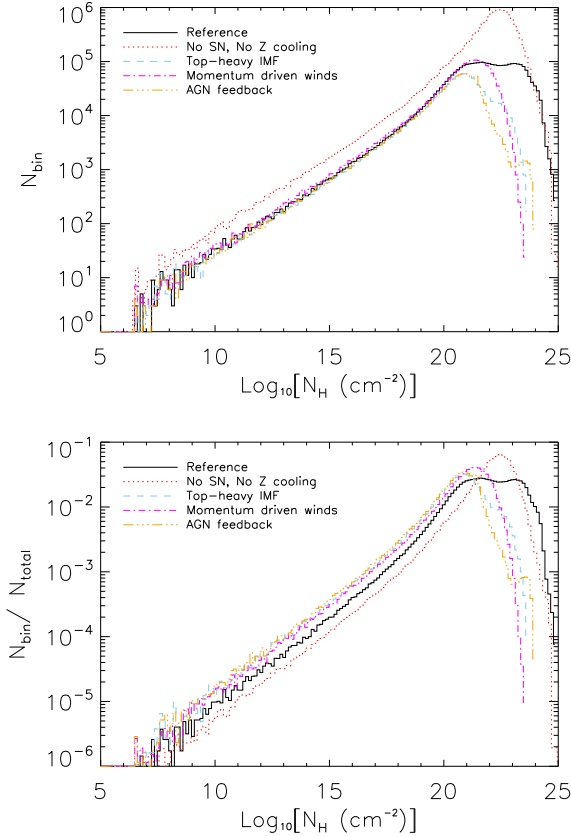


Figure 4.9: The distribution functions of column densities towards star particles in the reference simulation, the simulation without metal-line cooling and SN feedback the simulation in which star formation at high densities occurs with a top-heavy IMF (and the extra available energy is used to increase the wind velocity), the simulation with momentum-driven winds and the simulation including AGN feedback. The low column density ends of the distribution are exactly the same for the simulations with SN feedback. The second, higher peak in the reference simulation is absent in the simulation with effective feedback in high mass haloes.

4.A. Column densities in SPH simulations

We tested the distance up to which the L.O.S. integration should be carried out in the following way. Increasing the distance up to which gas particles are still counted increases the column density up to a few to several tens of kpc, after which it remains constant (there is no EoS gas in between haloes). We therefore chose to use 100 proper kpc/h for the maximum distance at which particles can still contribute to the L.O.S. towards a star particle. When obtaining observables, absorption by the IGM could be added separately, but we will not do so here.

Convergence of the L.O.S. column densities

To be sure that the column densities obtained are not strongly dependent on the numerical resolution, we plot the normalized distributions in Figure 4.8 for three different particle numbers in the ‘REF’ simulation in a 25 Mpc box. The value of every bin is the number of lines of sight in that bin divided by the total number of lines of sight in the box (i.e. the number of star particles in the box). The high column density end of the distribution is slightly dependent on resolution. This was expected as the effectiveness of feedback is also somewhat resolution dependent (Chapter 2). Below $N_H = 10^{21} \text{ cm}^{-2}$ the distribution functions are, however, very similar. The high column density cut-off is higher for higher resolution simulations, because the highest volume density that can be reached depends on the resolution (it scales roughly with the particle mass divided by the softening length squared, and softening and particle mass depend on resolution). In the next section we will show that the differences between different physical models are far larger than the resolution effects.

Distributions of hydrogen column densities for different input physics

The distribution of hydrogen column densities ($N_H = X_H \Sigma / m_H$) towards all star particles in a box of $(25 \text{ Mpc/h})^3$, with the reference parameter set and the three different simulations used in this paper are shown in Figure 4.9. The double peak is a feature arising from the ineffective feedback in high mass haloes, where the winds are not able to escape (Chapter 2). To illustrate this, Figure 4.9 also shows the distribution for a simulation in which star formation at densities above some threshold pressure happens with a top-heavy IMF. The extra available energy per unit stellar mass formed is used to increase the velocity of the wind from 600 to 1618 km s^{-1} . The second, high column density peak is absent, while the rest of the distribution is unaffected. In the model without any SN feedback and without metal-line cooling the very highest column densities reached are as high as the highest in the reference simulation. This (and the fact that the highest column densities in the simulation with a top heavy IMF at high pressure are lower) indicates that the highest (res-

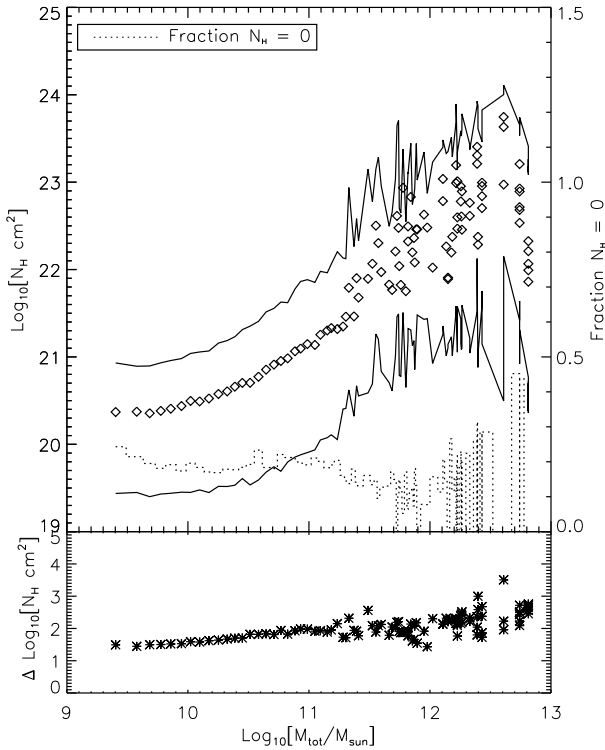


Figure 4.10: The relation between the hydrogen column densities along lines of sight to all star particles, binned according to the total mass of the halo they are in. In the upper panel, the diamonds are the medians in the bins on both axes (all bins contain equally many L.O.S.). The thin solid lines are the 16 and 84 percentile lines of the distribution in the bin. The dotted line (and right vertical axis) indicates the fraction of L.O.S. with zero column density. The lower panel indicates the range between the percentile lines in the upper plot.

olution dependent) column densities that can be reached are only reached when feedback is inefficient. The overall normalization of the model without SN feedback and without metal-line cooling is much higher, because many more stars have formed in that simulation. In the simulation with momentum driven winds and in the simulation with AGN feedback the distribution is very similar to the one in the simulation with the double IMF, with some small differences at the high column density end. The low column density end in all simulations with SN feedback is very similar, which is an illustration of the self-regulation of star formation by SN feedback.

Correlations between hydrogen column densities and halo properties

In order to investigate the dependence of the column densities along the line of sight to star particles on properties of the galaxies they are in, we use Friends-of-Friends haloes. For the star particles in haloes, which we will loosely call galaxies, we will correlate the median column densities in bins of physical properties like stellar mass, star formation rate or ISM mass of the same halo.

We bin the L.O.S. such that in every bin are equally many L.O.S., according to halo mass and star formation rate surface density ($\Sigma_{\text{SFR}} = \text{SFR}/R_{\text{vir}}^2$, where the total FoF group mass is used as the virial mass) for the reference simulation in Figures 4.10 and 4.11, respectively. The symbols plotted are the medians in both horizontal and vertical quantities. The thin lines are the 25th and 75th percentiles, while the thick straight solid line in Fig. 4.11 is a power-law fit to the medians. The dotted line indicates the fraction of L.O.S. that have zero column densities, as indicated on the right vertical axis (bins for which this fraction exceeds 0.5 are not used for the power law fits we discuss later on). The lower panel shows the difference between the two percentile lines as a function of the same halo quantity. In every case, the spread is about 2 orders of magnitude, with only a weak dependence on halo properties.

As can be seen from these plots, there is a tight correlation between the hydrogen column density and halo mass or star formation rate surface density. This also holds for the correlation between the hydrogen column density and stellar mass and between hydrogen column density and star formation rate (not shown). The spread in the data is about two orders of magnitude and increases slightly with halo mass, star formation rate and/or star formation rate surface density. The fraction of star particles that have zero column density is roughly constant at $\sim 15\%$. In high mass haloes this starts fluctuating more, because the fraction of star particles far away from the centre is higher, and also satellite galaxies contribute (centrals and satellites will be in the same FoF halo).

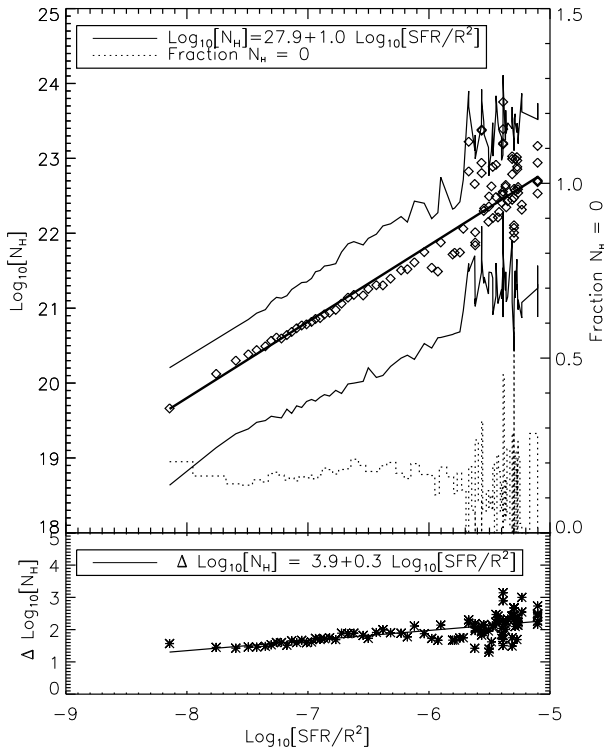


Figure 4.11: The relation between the hydrogen column densities along lines of sight to all star particles, binned according to the star formation rate surface density of the halo they are in for the reference simulation at redshift 2. Symbols are explained in Figure 4.10. The solid lines are power law fits to the medians, the relations for which are given in the legend.

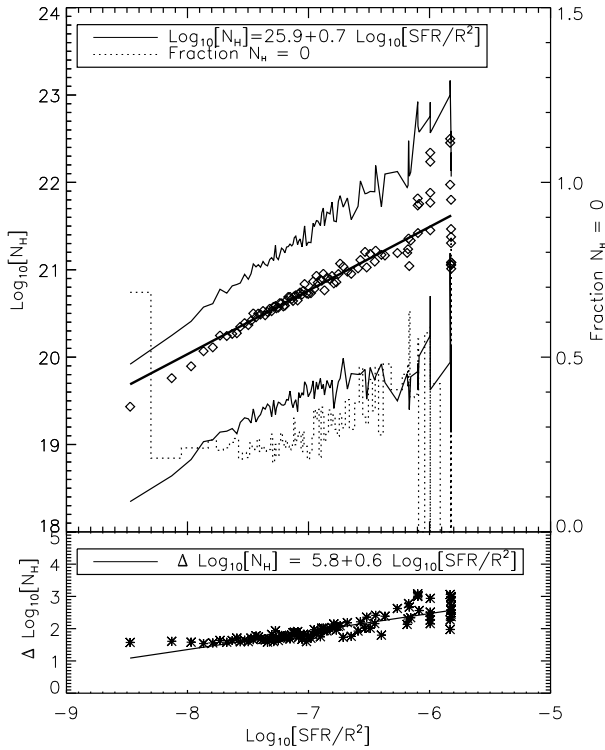


Figure 4.12: Same as Fig. 4.11, but now for the simulation with a top heavy IMF for star formation above a density threshold. The relation between median column density and star formation rate surface density is much flatter than in the reference simulation. Note that the extent of the vertical axis is different than in Fig. 4.11.

Effective feedback

In the DBLIMF, in which stellar feedback is efficient at all halo masses, winds escape more easily from high mass haloes. In these haloes, the gas density is expected to be lower, and the star formation rate also is. Therefore, this different implementation of star formation and feedback might result in different correlations between halo properties and column densities. We saw already before that the very high column density end was truncated for this simulation (c.f. Figure 4.9). In Figure 4.12 we show the correlation between the hydrogen column density and the star formation rate surface density as defined before. Indeed, the slope of the correlation is strongly different (~ 0.7 instead of ~ 1).

CHAPTER 4. SIMULATED GALAXY LUMINOSITY FUNCTIONS

Table 4.1: Correlations (Spearman rank correlation ρ) and power law exponents (n) from fits between the hydrogen column density and several halo properties in two of our simulations. The two not available power law indices represent simulations for which the correlation between that halo property and halo mass cannot be well described by a power law, as shown in Fig. 4.10 for the reference simulation.

Halo property	Reference		Top-heavy IMF	
	ρ	n	ρ	n
M_{halo}	0.54	n.a.	0.36	n.a.
M_*	0.55	0.76	0.37	0.36
SFR	0.55	0.60	0.41	0.33
$\text{SFR}/R_{\text{vir}}^2$	0.54	1.02	0.41	0.73

Correlation strengths

To discriminate between the different correlations found in the previous section, we calculate a Spearman rank correlation coefficient. The value of this coefficient will always be between -1 (perfect anti-correlation) and 1 (perfectly correlated), while a value close to 0 indicates a lack of correlation.

In Table 4.1 we compile the correlation coefficients ρ for correlations between the hydrogen column density and different halo properties. For the simulations for which the relation between the halo property and the column densities are well represented by a power-law, we also give the result for a fit of the form

$$N_H(X) \propto X^n \quad (4.6)$$

in which X are the halo properties, and n is the power law index quoted in the table. These are the fits shown in the figures of the correlations as well. We only fit on bins in column densities with non-zero medians, as otherwise the fit result depends on the value we assign to those. For the rank correlation coefficients we do include star particles with zero column density.

Correlation of residuals

If we correct all values for the column density for the value expected from one of the halo quantities (i.e. using the fit results quoted in Table 4.1, with the proper normalization), we remove the dependency on one of the relevant parameters. We can now investigate whether or not residuals correlate with other halo properties. So, we now do the same analysis, but between a corrected hydrogen column density ($\Delta \log(N_H) = \log(N_H) - \log(N_H)(X)$) and the other halo properties.

4.A. Column densities in SPH simulations

When doing so for every combination of parameters reported in Table 4.1, we find that all other correlations are insignificant and power law fits give slopes very close to zero (with normalization also close to zero), with the same spread of two orders of magnitude in the corrected hydrogen column density. The example of the `REF` simulation, with the L.O.S. corrected for the median value as a function of star formation rate surface density plotted against the stellar mass of their halo, is shown in Figure 4.13. There is no correlation left, the distribution is still two orders of magnitude wide and the median is very close to zero with a very weak dependence on the stellar mass. Without showing the results for other combinations of halo properties, we emphasize that this is true for all combinations of halo properties that correlate well with the halo mass (like, e.g. stellar mass, star formation rate and star formation rate surface density).

This means that the the median of column densities in a halo is uniquely determined by either one of the parameters, and that, after correcting for the correlation with that property, there are no correlations left in the data set between these halo parameters and residual column density. We are not able to determine the source of the scatter and do not identify what causes its extent.

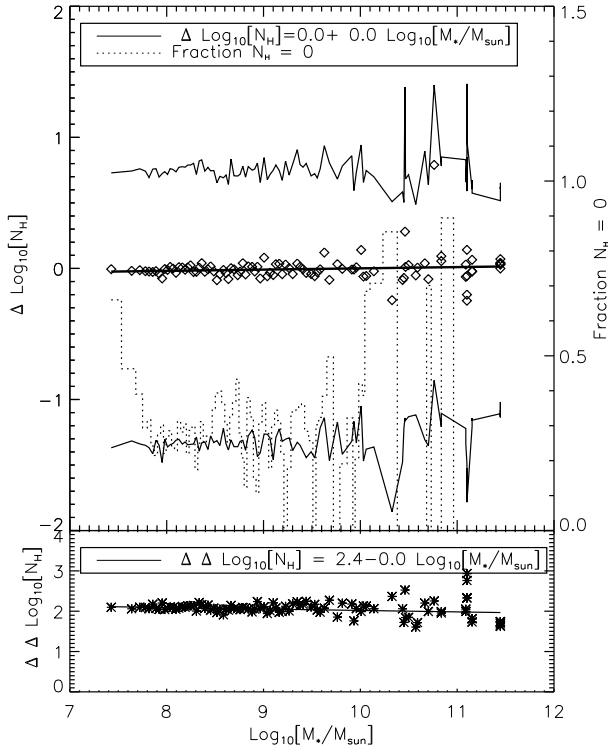


Figure 4.13: The relation between the column densities, corrected for the trend found with star formation rate surface density, and the stellar mass of the halo the corresponding star is in for the reference simulation at redshift 2. Symbols are explained in Figure 4.10. The lower panel shows the width of the distribution of residuals, similar to the lower panels of Figs. 4.10, 4.11 and 4.12. There is no relation between the residuals and any other halo property that correlates with halo mass.

5

Variations in Integrated Galactic Initial Mass Functions due to Sampling Method and Cluster Mass Function

Astronomy & Astrophysics, 2010, 512, 79
M.R. Haas & P. Anders

Abstract

Stars are thought to be formed predominantly in clusters. The star clusters are formed according to a cluster initial mass function (CMF) similar to the stellar initial mass function (IMF). Both the IMF and the CMF can be approximated by (broken) power-laws, which favour low-mass objects. The numerous low-mass clusters will lack high mass stars compared to the underlying IMF, since the most massive star cannot be more massive than its host cluster. If the integrated galactic initial mass function (IGIMF, i.e. the total stellar mass function of all stars in a galaxy) originates from stars formed in star clusters, the IGIMF could be steeper than the IMF in clusters. We investigate how well constrained this steepening is and how it depends on the choice of sampling method and CMF. We investigate the observability of the IGIMF effect in terms of galaxy photometry and metallicities. We study various ways to sample the stellar IMF within star clusters and build up the IGIMF from these clusters. We compare analytic sampling to several implementations of random sampling of the IMF and different CMFs. We implement different IGIMFs into the GALEV evolutionary synthesis package to obtain colours and metallicities for galaxies. Choosing different ways of sampling the IMF results in different IGIMFs. Depending on the lower cluster mass limit and the slope of the cluster mass function, the steepening varies between very strong and negligible. We find the size of the effect is continuous as a function of the power-law slope of the CMF if the CMF extends to masses smaller than the maximum stellar mass. The number of O-stars detected by GAIA will, if some uncertain factors are better understood, help to judge the importance of the IGIMF effect. The impact of different IGIMFs on integrated galaxy photometry is small, within the intrinsic scatter of observed galaxies. Observations of gas fractions and metallicities could rule out at least the most extreme sampling methods, if other sources of error are sufficiently understood. As we still do not understand the details of star formation and the sampling of the stellar IMF in clusters, one sampling method cannot be favoured over another. Also, the CMF

at very low cluster masses is not well constrained observationally. These uncertainties therefore need to be taken into account when using an IGIMF, with severe implications for galaxy evolution models and interpretations of galaxy observations.

5.1 Introduction

A series of papers (Kroupa & Weidner, 2003; Weidner & Kroupa, 2004, 2005, 2006, the latter WK06 from now on) pointed out that the distribution of initial stellar masses in a galaxy may significantly deviate from the initial mass function (IMF) the stars have when they are born, if the vast majority of stars is born in clusters. These clusters follow a power-law mass function (the cluster mass function, CMF), which means that most stars form in low-mass clusters. In low-mass clusters there is a deficiency of massive stars (as the most massive star cannot exceed the total cluster mass), resulting in an integrated galactic initial mass function (IGIMF) that is, at the high mass end, steeper than the IMF.

The universality of the IMF is still an often debated topic. It is as yet not clear whether the IMF in all Galactic star clusters is the same, whether or not the field stars in the Milky Way follow the same mass distribution as cluster stars, and whether the IMF in other galaxies is the same as here. The IMF is shaped by the very complicated processes which transform molecular cloud cores into stars, processes which would be expected to be environmental-dependent. Therefore, a non-universality of the IMF would intuitively be expected.

As the distribution of stellar masses has a profound impact on many aspects of the evolution of galaxies, it is important to know to what extent the IGIMF deviates from the underlying stellar IMF (which is often used as IGIMF in galaxy evolution studies) and how this affects galaxy properties. For example, the relation between star formation rate and $H\alpha$ luminosity is shown to be steeper in galaxies with a very low star formation rate (Skillman et al., 2003), which can be explained by having a steeper IGIMF for low SFR galaxies (Pflamm-Altenburg et al., 2007) due to the preferential formation of low-mass clusters. Also, the gradients in galactic disks of SFR and $H\alpha$ luminosity are different due to clustered star formation (Pflamm-Altenburg & Kroupa, 2008). The supernova rate per unit stellar mass formed and the chemical enrichment history of a galaxy are influenced by the IGIMF as shown by Goodwin & Pagel (2005). In a recent paper Hakobyan et al. (2009) study the difference in rates of supernovae of type Ib/c and type II and find that their results can be explained by having a steeper IMF in the outskirts of galaxies than in their centres, which can be explained by a different ‘IGIMF’ in the outskirts of the galaxy as compared to the inner regions due to a lower SFR in the outskirts.

Recently, Recchi et al. (2009) investigated the $[\alpha/\text{Fe}]$ versus velocity disper-

sion in early type galaxies and the rates of supernovae of both Type II and Ia in several galaxy types in the light of the IGIMF framework. They find that if one assumes a constant star formation rate over a Hubble time, then for all but the irregular galaxies these numbers agree well with the observed values. Recchi et al. (2009) explained this discrepancy by stating that for irregular galaxies a constant SFR over the age of the Universe is not likely to be a good approximation.

However, other studies (see e.g. Sandage (1986)) find approximately constant SFR for late-type spiral galaxies (Sd/Irr), and declining SFRs with time for earlier-type galaxies (where the decline time decreases while going from Sc to E galaxies). For Sa-Sc galaxies, the SFR is directly related to the available gas mass, resembling the Kennicutt-Schmidt law (Kennicutt 1998a). Starbursts, superimposed on any of the standard Hubble types, seem to be a common phenomenon. They have the strongest impact on photometry and chemical enrichment for late-type galaxies (which are typically of low mass) and major mergers (due to the triggered extremely high SFRs). Such starbursts might be interpreted as “recently rising SFR” as found by Recchi et al. (2009).

WK06 test three different scenarios for sampling stellar masses in a cluster. They conclude that ‘sorted sampling’ (see Sect. 5.3.3) best reproduces the observed relation between maximum stellar mass in a cluster and the cluster mass (but see Maschberger & Clarke (2008) for a critical re-evaluation of this relation). The amount of steepening of the IGIMF is found to depend on the sampling method and on the power-law index of the low-mass end of the CMF.

For galaxies as a whole, the low-mass end of the CMF is not well constrained. Even in the Milky Way we can only see low-mass star-forming regions (few to few tens of solar masses) nearby, while for distant galaxies such regions are too faint.

In this work we investigate the dependence of the IGIMF on the

1. *Sampling method*: stellar masses in clusters can be sampled in different ways from the stellar IMF. We will show that the specific sampling method is indeed important and that different sampling methods give different results, as was already shown by WK06. We will extend their set of sampling methods.
2. *Cluster mass function*: It is to be expected that the effects on the IGIMF depend on the CMF. Sampling issues become more important for low-mass clusters, and therefore a lower minimum cluster mass and/or a steeper CMF will result in a stronger steepening of the IGIMF. We take observed CMFs for high mass clusters and extrapolate them down to the masses of observed star forming regions in the solar neighbourhood. We investigate the impact of different lower mass limits and power-law indices.

In Sect. 5.6 we implement some IGIMFs into the GALEV galaxy evolution

models (Bicker et al., 2004; Kotulla et al., 2009), which follow the photometric and chemical history of idealized galaxy models self-consistently. We will investigate how properties like the integrated broadband photometry in several filters and total gas metallicity are influenced by taking into account sampling issues in the IMF, and discuss observational needs to quantify the importance of the IGIMF effects for galaxy evolution and observations of integrated galaxy properties.

We will start by presenting the mass distributions of stars and clusters that we use in Sect. 5.2 and discuss our sampling methods, including a consistency test of the sampling methods in Sect. 5.3. The results for the IGIMF are shown in Sect. 5.4 for several sampling methods with a constant cluster mass function and for one sampling method with a variety of cluster mass functions. In Sect. 5.5 we calculate the number of O-stars that will be observed by GAIA, under various assumptions, and we compare the results of our IGIMFs with the work on single O-stars by de Wit et al. (2004, 2005). Sect. 5.6 describes the galaxy evolution models and shows results on the integrated photometry and chemical enrichment of galaxies with various IGIMFs. The conclusions are presented in Sect. 5.7.

5.2 The underlying mass functions

Here we discuss our choices for the stellar IMF and the cluster mass function. The methods of sampling these distribution functions are the topic of the next section.

5.2.1 The stellar initial mass function

For stars we used the Salpeter (1955) IMF:

$$\xi(m) = \frac{dN}{dm} = A \cdot m^{-\alpha}, \quad (5.1)$$

with $-\alpha = -2.35$. The reason for this choice was computational simplicity. The steepening of the IGIMF as found by Kroupa & Weidner (2003); Weidner & Kroupa (2004) happens at relatively high stellar masses, for which other IMFs (e.g. Kroupa, 2001; Chabrier, 2003) have similar power-law indices. The differences are expected to be small between different IMFs. We will compare the Salpeter IMF to the Kroupa (2001) IMF in Sect. 5.4.1. The normalization constant (A) was calculated from the total number or mass of stars. The minimum and maximum stellar masses were taken to be 0.1 and 100 M_{\odot} , respectively. Although there are indications that there is a fundamental stellar upper mass limit of $\sim 150 M_{\odot}$ (Weidner & Kroupa, 2004, and references therein), the upper stellar mass limit has little influence on our results.

5.2.2 The cluster mass function

For the star clusters we assumed a power-law mass function similar to Eq. 5.1:

$$\frac{dN}{dM} = B \cdot M^{-\beta}. \quad (5.2)$$

There exists a debate between different groups who try to obtain the cluster initial mass function (CMF) in distant galaxies. In studies which try to constrain the power-law slope of the CMF from the relation between the SFR of a galaxy and the number of clusters in a galaxy (or, equivalently, the luminosity of the brightest cluster in a galaxy), many groups find values of $\beta \sim 2.3 - 2.4$ (e.g. Larsen, 2002; Whitmore, 2003; Weidner et al., 2004; Gieles et al., 2006a). More direct measurements of the masses of the clusters, however, tend to find values consistent with $\beta = 2.0$ (e.g. Zhang & Fall, 1999; de Grijs et al., 2003; McCrady & Graham, 2007; Larsen, 2008). Bastian (2008) notes that this discrepancy can be alleviated by assuming that the clusters really follow a Schechter-like mass distribution, which is a power-law at low masses, but turns over at a typical mass into an exponential fall-off of the number of clusters. The high mass of this turn-over (few $10^6 M_\odot$) makes it hard to infer directly from the masses. Their strong effect on the upper mass limit for the clusters in a galaxy makes it detectable from a statistical point of view, though. See below for a discussion on how Schechter-like CMFs might influence the IGIMF effect.

Here we took pure power-laws with a slope of $\beta = 2.2$ for consistency with the work of Weidner & Kroupa (2004), and to have a case that is in between the values found by the two competing camps. In Sect. 5.4.3 we discuss the specific case $\beta = 2.0$ as well as a continuum of slopes in the range $\beta = 1.8 - 2.4$, to cover the whole range of slopes found observationally.

Although the range of cluster masses probed is wide, the observationally accessible extragalactic star clusters have masses exceeding $1000 M_\odot$, except for clusters in the Magellanic Clouds. As minimum mass for star clusters we used a default value of $5 M_\odot$, as did Weidner & Kroupa (2004). As the value for a physical lower mass limit for clusters, if any, is unknown, this mass was taken because it is the lowest mass of groups of stars that is observed to be forming in the Taurus-Auriga region (Briceño et al., 2002). This lower limit is far below the range in which the power-law behaviour is observed. It is an extrapolation of more than two orders of magnitude. This extrapolation is assumed in other IGIMF studies as well and the best we can currently do. The upper mass limit for star clusters was set to infinity.

We varied both the lower and the upper mass limits to investigate how sensitive our results are to variations of these values. The minimum cluster mass is expected to be important, and $5 M_\odot$ is far below observational limits of any young star cluster

that is outside the solar neighbourhood. Observational indications for an upper cluster mass limit are found in e.g. the Antennae (Zhang & Fall, 1999) and M51 (Gieles et al., 2006b; Haas et al., 2008) and in general from the relation between the brightest cluster in a galaxy and its star formation rate by Weidner et al. (2004); Bastian (2008). These upper mass limits are found to be around $10^{5.5-6.5} M_{\odot}$. See Sect. 5.4.4 for an investigation of star formation rate dependent IGIMFs.

5.3 Sampling techniques

In this section we discuss several ways to sample the distribution functions described in the previous section.

5.3.1 Star formation scenarios and sampling of the IMF

Ideally, one would like to connect sampling methods in numerical experiments like the one conducted here in some way to the astrophysics going on in the studied system. Here this would mean that we construct a method of sampling stellar masses in a cluster, which is based on a scenario about how this cluster forms from its parent molecular cloud. It is expected that the IMF found in star forming regions harbours a wealth of information about the star formation process. A recent paper by Dib et al. (2010) indeed describes several ways of building up an IMF from star formation scenarios.

The problem with constructing sampling methods in this way is that it is not at all guaranteed that the mass function inside clusters follows the same functional form in all clusters. Besides, the mass function of cloud cores is an equally uncertain factor. Likewise, the large number of free parameters and inherent uncertainties of physical star formation scenarios would inhibit us in drawing any conclusions. The point of this paper is to show the effects of different sampling methods, given that the underlying IMF is the same. We chose therefore to use a single underlying IMF and constructed sampling methods that do not necessarily represent physical star formation scenarios.

5.3.2 Analytic sampling

The first method to sample a distribution function we discuss is analytic in nature. We use the fact that the total mass of stars inside a cluster (i.e. the cluster mass) is calculated from

$$M_{\text{cl}} = \int_{m_{\text{min}}}^{m_{\text{max}}} m \cdot \xi(m) dm, \quad (5.3)$$

where $m_{\min} = 0.1 M_{\odot}$ and $m_{\max} = \min(100M_{\odot}, M_{\text{cl}})$. Limiting the mass of the most massive star present in the cluster ensures that there are no stars more massive than their host cluster.

The normalisation of the IMF (A in Eq. 5.1) is defined by relation 5.3. Sampling the distribution function is done by using

$$N_i = \int_{m_i}^{m_{\max}} \xi(m) dm \quad (5.4)$$

with $N_i = N_1 = 1$ for the most massive star (this star has the mass m_1), 2 for the second most massive and so on. For any cluster mass the masses of all stars present in the sample are uniquely determined, see also Weidner & Kroupa (2004).

5.3.3 Random sampling

In order to introduce stochastic effects, we will mainly sample mass functions randomly, as it ensures that random fluctuations are present in the sample of masses. Whereas the analytic way of sampling will never produce a $80 M_{\odot}$ star in a $100 M_{\odot}$ cluster, this will happen (although rarely) when sampling randomly. There are nevertheless issues, as described below.

A random number from a distribution function was drawn using a random number, uniformly distributed between 0 and 1 as many numerical packages can provide you with, and the normalised cumulative probability function, which is the normalised cumulative probability density function, which (in this case) is itself an integral over the mass function :

$$\text{CPDF}(m) = \int_{m_{\min}}^m \text{CMF} dm, \quad (5.5)$$

normalised to $\text{CPDF}(m_{\max}) \equiv 1$. Inverting Eq. 5.5 and inserting uniformly distributed random numbers provided the desired randomly sampled masses.

For power-law distribution functions, the inversion can be done analytically, so that the necessity for time consuming numerical integration or the use of look-up tables (constraining the flexibility of our research) is prevented.

The total mass of the cluster

When sampling stars one by one, the chances of them adding up to exactly the cluster mass are marginal. Therefore one has to make a choice about which stars to include. One way is just sampling stellar masses until you first go over the predetermined total cluster mass. Four choices can be made:

1. Stop at that point. The cluster mass will always end up slightly higher than the predetermined value. We will indicate this method by ‘stop after’, as we always stop just after passing the cluster mass aimed for.
2. Remove the last star drawn. The cluster mass will now be systematically lower than the masses drawn from the CMF, we will therefore abbreviate it by ‘stop before’.
3. Only remove the last drawn star if then the total mass is closer to the desired value. The cluster masses are sometimes slightly lower, sometimes slightly higher than the predetermined value. This will be our default choice, indicated by ‘stop nearest’.
4. Like the previous option, but removing the star at 50% probability, regardless of whether it would bring the cluster mass closer to the predetermined mass or not. This will be called ‘stop 50/50’.

Sorted sampling à la Weidner & Kroupa (2006)

An alternative treatment was introduced and extensively tested by WK06, ‘sorted sampling’: Draw a number of stars ($N = M_{\text{cl}}/m_{\text{average}}$) in which M_{cl} is the cluster mass and m_{average} is the average stellar mass in the IMF under consideration. Then draw that many stellar masses from the IMF. Repeat this if the total mass is not yet the desired cluster mass by drawing an additional $(M_{\text{cl}} - \sum_i m_i)/m_{\text{average}}$ stars (where $\sum_i m_i$ is the sum of the masses already drawn). When the cluster mass is first surpassed, sort the masses ascendingly and remove the most massive star if that brings the total stellar mass closer to the desired cluster mass. Only the most massive star drawn can be removed. If the first sample of stars goes over the cluster mass by a large amount, still only one star can be removed, while the correction upwards in mass can be with any arbitrary number of stars.

Sampling to a total number of stars

Alternatively, one can once draw a predetermined number of stars for a given cluster from the IMF. The number of stars that is drawn is, as in ‘sorted sampling’, given by $N = M_{\text{cl}}/m_{\text{average}}$. In this case some clusters may become much more or much less massive than the mass that was sampled from the cluster mass function. We will indicate this method simply with ‘number’.

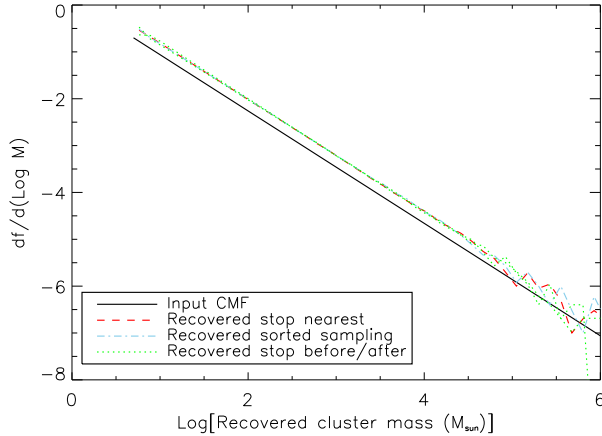


Figure 5.1: The fraction of clusters per unit $\log(M)$ as a function of cluster mass. The input CMF is shown as solid straight black line. The coloured, discontinuous lines are recovered CMFs after populating clusters with stars with the indicated sampling methods. The input CMF is plotted offset, to more easily distinguish the recovered CMFs.

Limiting the stellar masses to the cluster mass

By default we limited our maximum possible stellar mass to the mass of the cluster (so that e.g. a $M_{\text{cl}} = 10 M_{\odot}$ cluster can contain only stars at most as massive as $m_{\text{max}} = 10 M_{\odot}$). Otherwise, clusters of a predetermined mass may end up with a star that is more massive than the cluster itself. However, we also tried it without this constraint, in which case we add ‘unlimited’ to the name. Note that lowering the maximum possible stellar mass heightens the probability for drawing lower mass stars (per unit mass), as the integral of the probability density function of stellar masses should still be one.

5.3.4 The recovered cluster mass function

One consistency test for the sampling methods is to see whether or not the mass function of the clusters after populating them with stars from the IMF recovers the input CMF. For some of the methods mentioned it is obvious that the total mass will always be over- or underestimated (e.g. stopping the sampling always right after or right before you passed the cluster mass, where the mass will be over- or underestimated by on average half an average stellar mass for that IMF). For the high cluster mass end these differences are negligible, but that is not necessarily

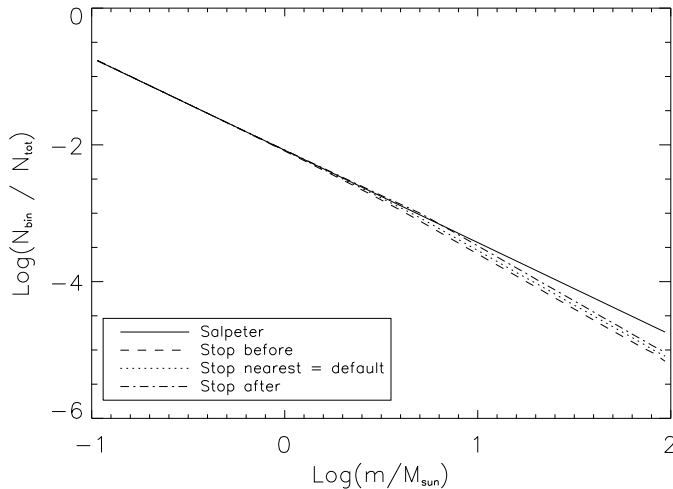


Figure 5.2: The IGIMF for randomly sampled stars in clusters until (1) the next star would overshoot the cluster mass (dashed), (2) a mass nearest to the cluster mass is reached (dotted), or (3) one star crosses the cluster mass (dot-dashed). The solid line is the input Salpeter IMF. The value on the vertical axis is the fraction of all the stars that are in that particular mass bin.

clear for very low cluster masses, where the recovered CMF could be steeper or shallower than the input CMF.

In Fig. 5.1 we compare the input CMF (solid black line, shifted by an arbitrary vertical offset), to several recovered CMFs after populating the clusters with stars. The default sampling method is shown in red (dashed), and the preferred method of WK06, sorted sampling, is shown in dash-dotted blue. The two models for which discrepancy is expected are shown in the dotted green lines. The expected under- or overestimate of the total mass is $\sim 0.3 M_{\odot}$, which is more than an order of magnitude less than the very lowest cluster mass. It turned out that even for these models the discrepancy is marginal. Therefore we cannot rule out one or another sampling methods based on the recovered CMF.

5.4 Integrated galactic initial mass functions

We drew samples of 10^7 clusters from a cluster mass function with $dN/dM \propto M^{-2.2}$. We tested several sample sizes and found 10^7 to be both computationally feasible and showing only tiny statistical fluctuations (using e.g. 10^6 clusters re-

sults in IGIMF scatter nearly as big as the difference between some models we tested). We constructed the IGIMF by sampling the stars in the clusters in different ways, as described in the previous section, and summed up all stars from the individual clusters. In Fig. 5.2 we show three IGIMFs from random sampling, together with the Salpeter IMF.

5.4.1 Sampling methods

Figure 5.2 clearly indicates that the IGIMF steepens for high stellar masses, due to the lack of high-mass stars in low-mass clusters. Also, the impact of using either of the three methods is comprehensible: stopping the sampling one star before the cluster mass filled up biases most against high stellar masses (as the chance of going over the cluster mass is higher for a higher-mass star) and going slightly over the cluster mass biases least against high mass stars. Because the differences are small, from now on we plot the fraction of all stars in a mass bin, divided by the fraction predicted from the input stellar IMF (i.e., Salpeter (1955)). The same data as in Fig. 5.2 are used for Fig. 5.3, where the differences become clearer.

In Fig. 5.3 we also compare the analytic method of sampling as explained in Sect. 5.3.2 to the random sampling methods. Both have the stellar masses limited to be at most the cluster mass, but in the random sampling technique sometimes a relatively high-mass star does occur in a low-mass cluster. This is not the case for the analytic sampling, which results in the sharp downturn at masses close to the upper limit. As noted by WK06, the ‘sorted sampling’ method resembles the shape of analytic sampling, although less severe. The relation is even steeper (approaching an IGIMF power-law index of -3) for $m > M_{\text{cl, min}}$.

Sampling a number of stars equal to the cluster mass divided by the average stellar mass for the IMF under consideration is also shown in Fig. 5.3. If the average mass is calculated with the upper mass limit in a cluster limited to the cluster mass, the method gives results rather similar to the default method. When the average mass is always calculated for a well sampled IMF between 0.1 and $100 M_{\odot}$, the resultant IGIMF is indistinguishable from the input IMF. Note that the cluster mass function is still intact.

Using a Kroupa (2001) IMF results in the green dot-dot-dot-dashed line in Fig. 5.3. The bend again is found at roughly the same stellar mass as for the Salpeter IMF. Deviations from this at lower mass are stronger, though, as the mean mass of a star in the Kroupa IMF is bigger than in a Salpeter IMF. Changing the upper stellar mass limit does not influence any of the results other than that the lines extend to higher stellar masses.

Comparing the calculations to the light grey dotted lines in Fig. 5.3 shows that all random sampling techniques give high-mass-end power-law indices of the

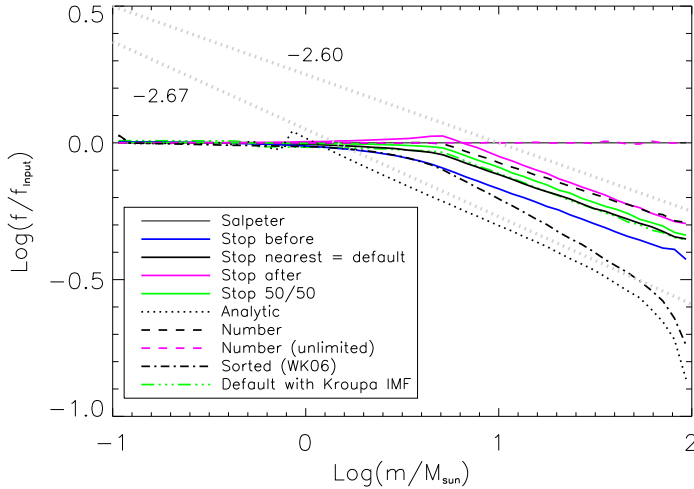


Figure 5.3: The same as Fig. 5.2, but for every mass bin divided by the expected value for the input IMF. The IGIMFs presented in Fig. 5.2 are represented by the solid lines in various colours. The ‘stop 50/50’ model is included as well. We also include the ‘analytic sampling’ case (dotted line), the sampling of a specific *number* of stars based on the expected mean mass, limited by the cluster mass (black dashed) and unlimited (magenta dashed, going around the Salpeter line). The black dot-dashed line is the ‘sorted sampling’ method of WK06. The realisation for a Kroupa (2001) IMF is shown in the green dot-dot-dot-dashed line (almost on top of the black solid (default) line). The light grey dotted lines with numbers are lines that would have the indicated power-law index in the IGIMF.

IGIMF very close to -2.60 , whereas the analytic sampling technique is slightly steeper, -2.67 and turns completely down close to the physical upper mass limit for stars (i.e. the mass of the cluster needs to become extremely high in order to sample a star with a mass very close to the upper mass limit).

5.4.2 The cluster mass function

In all randomly sampled realizations, the steepening becomes very prominent at $m = 10^{0.7} M_{\odot} = 5 M_{\odot}$, the lower mass limit for clusters. The analytically sampled case becomes steeper at lower masses, as there the most massive stars in these low-mass clusters are well below the cluster mass. We investigated how the steepening depends on the imposed lower cluster mass limit and the steepness of the cluster

5.4. INTEGRATED GALACTIC INITIAL MASS FUNCTIONS

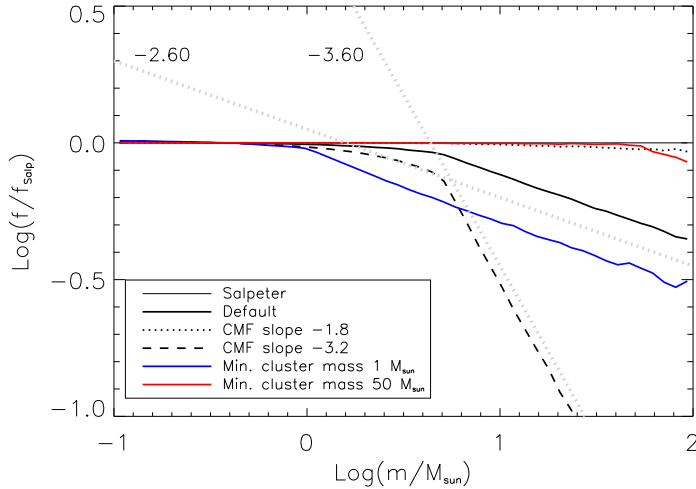


Figure 5.4: The same as Fig. 5.3, but now for variations of the cluster mass function. We show our default (minimum mass $5 M_{\odot}$, power-law index -2.2) model and four other models: slopes varied to -1.8 (dotted) and -3.2 (dashed) and the minimum cluster mass set to 1 (blue solid) and $50 M_{\odot}$ (red solid). The light grey dotted lines give an indication of the slope of the lines when plotted as an IGIMF with power-law indices as indicated.

mass function.

In Fig. 5.4 we show the IGIMFs, as obtained with our default random sampling model, for three different lower cluster mass limits (1 , 5 and $50 M_{\odot}$, for a CMF slope of -2.2) and three different cluster mass function slopes (-1.8 , -2.2 and -3.2 , for a lower cluster mass limit of $5 M_{\odot}$). The flattest CMF and highest minimum cluster mass use samples of 10^6 clusters instead of 10^7 clusters. The higher mass in clusters makes the IGIMF less sensitive to errors from sampling statistics in stars. It can be clearly seen that the deviations of the IGIMF from a standard Salpeter IMF start at the minimum cluster mass. Results therefore are sensitively dependent on the cluster mass functions at very low cluster masses. The steepness of the IGIMF depends on the power-law slope of the cluster mass function. Changing the cluster mass function power-law index from -2.2 into -3.2 (-4.2 , not shown in the figure) makes the IGIMF slope steepen from -2.6 to -3.6 (-4.8). The steepening still occurs at the minimum allowed cluster mass. A flatter CMF slope of -1.8 results in a much shallower IGIMF compared to our standard case, with little deviations from

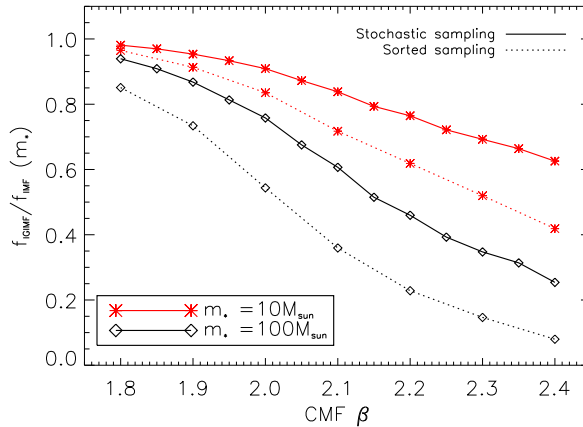


Figure 5.5: The deviation at 10 and $100M_{\odot}$ (stars and diamonds, respectively) of the value of the IGIMF as compared to the IMF as a function of the CMF slope β in the region around $\beta = 2$. For the ‘sorted sampling’ method (dotted lines) we performed the Monte Carlo simulations at intervals of $\Delta\beta = 0.1$ from 1.8 to 2.4 (including the entire range of observationally determined values) using one million clusters. The default, fully stochastic sampling (solid lines) simulations are performed using ten million clusters with β varying steps of 0.05.

the input Salpeter (1955) IMF. We can also conclude that as long as the *lower* mass limit of the CMF is higher than the *upper* mass limit of the IMF, IGIMF effects are negligible. We would like to emphasize that although we used a lower mass limit of the CMF of $5 M_{\odot}$ (i.e. considerably lower than the upper mass limit of the IMF), this value as well as the shape of the CMF at masses below a few hundreds solar masses is very uncertain due to a lack of observational data, even in the Milky Way.

5.4.3 The $\beta = 2$ CMF

In Elmegreen (2006) it was claimed that in the case where the CMF is described by a power-law of $\beta = 2$, IGIMF effects vanish, making this a singular case in between our $\beta = 1.8$ and $\beta = 2.2$ cases. In order to validate this result, we ran simulations with values for β close to and including 2. To address the behaviour of the deviation of the IGIMF from the IMF, we plotted the deviation of the IGIMF from the underlying IMF at two different stellar masses as a function of β in Fig. 5.5. We used a minimum mass of $5M_{\odot}$ for the cluster CMF, no upper mass limit and

5.4. INTEGRATED GALACTIC INITIAL MASS FUNCTIONS

plotted the results for $m_* = 10$ and $100 M_\odot$ in bins of width $\Delta \log(m_*) = 0.2$. We performed the exercise for our default sampling method at 13 different values of β (i.e., with $\Delta\beta = 0.05$), and for seven different values with the ‘sorted sampling’ technique from WK06 (i.e., with $\Delta\beta = 0.1$).

We found the results for $\beta = 2$ to be non-singular and to follow the expected behaviour from its surrounding points. The vanishing effects found by Elmegreen (2006) were not reproduced in our simulations. In the Monte Carlo simulations described in Elmegreen (2006) a small difference was already visible. In the intuitive analytic section it is explained why there should be no difference. This conclusion was based on the crucial statement that ‘the probability of forming a star of a particular mass is independent of cluster mass’. This is only true for stars in clusters with masses higher than the upper mass limit for stars. For clusters with lower total masses, the situation is more complex: stars with masses higher than the total cluster mass get assigned zero probability (unless one does not impose a limit to the stellar mass equal to the cluster mass), while stars with lower masses get higher probabilities to fulfil the IMF normalisation. For any value of β there is some number of clusters which will lack high mass stars, which makes $\beta = 2$ a normal case without singular features. The claim by Elmegreen (2006) is correct only if the lower limit of the CMF is higher than the maximum stellar mass, in agreement with our own findings.

We learn from Fig. 5.5 that choosing a value for the power-law index of the CMF of -2.2 instead of -2.0 produces a larger effect, as does the choice of sampling method made by WK06 compared to our default method. The observational support for $\beta = 2.4$ justifies the use of $\beta = 2.2$ in the rest of this work.

5.4.4 Star formation rate dependent upper cluster mass limit

On purely statistical grounds a relation between the star formation rate (SFR) and the mass of the most massive cluster in a galaxy is expected, as long as the timescale to form a complete population of clusters is fixed (see Maschberger & Kroupa, 2007, they find a timescale of 10 Myr). This relation is expected to be linear. However, Weidner et al. (2004) have found a relation between the SFR of a galaxy and the mass of its most massive cluster that is slightly shallower than linear:

$$\log(M_{cl,max}) = 0.75 \cdot \log(\text{SFR}) + 4.83. \quad (5.6)$$

In this section we will show Monte Carlo simulations with upper cluster mass limits which correspond to SFRs of 10^{-5} to $10^4 M_\odot \text{ yr}^{-1}$ in steps of half a dex in SFR.

As galaxies with a very low SFR in general also have very low masses (dwarf galaxies), we can expect to have more statistical (shot) noise in low SFR samplings. In order to get a handle on the median IGIMF and the 68% ($\sim 1\sigma$) confidence

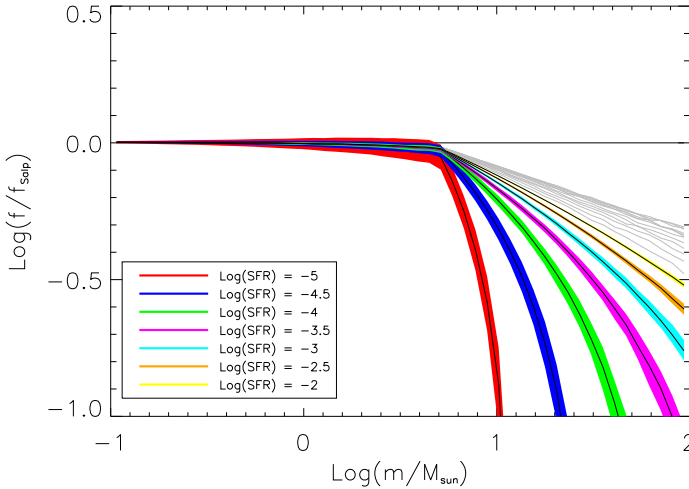


Figure 5.6: SFR dependent IGIMFs, in which the SFR sets an upper cluster mass limit, given by Eq. 5.6. We ran the lowest SFR models sufficiently long to get converged confidence intervals which are shown by the coloured regions around the solid line medians. For the higher SFR simulations, the results are very close and the confidence intervals extremely narrow. Therefore, we only plot the result of one simulation. The order is in a way that the higher the star formation rate (and hence the upper cluster mass limit), the shallower the IGIMF. Note that the highest SFR run is $10^4 M_{\odot} \text{ yr}^{-1}$.

intervals we assumed that the galaxies have formed stars for 10 Gyr, together with the SFR this gives a total stellar mass. The CMF (with a lower mass cut-off of $5M_{\odot}$ and a power-law index of -2.2) then sets the number of clusters drawn. For the very low SFR runs, there were not so many clusters to be drawn ($10^{-5} M_{\odot} \text{ yr}^{-1} \cdot 10 \text{ Gyr} = 10^5 M_{\odot}$ total stellar mass). We ran 500 realizations of the lowest SFRs, gradually reducing this number, as the 68% confidence intervals are very narrow already for relatively low SFRs. The corresponding upper cluster mass limits range from $10^{1.08} = 12 M_{\odot}$ to $10^{7.83} M_{\odot}$, so extending from extremely (maybe even unphysically) low star formation rates and corresponding upper cluster mass limits to extremely high SFR limits. Both limits are far beyond the range in which the relation between SFR and maximum cluster mass has been observed. We sampled the IMF with the method which samples up to a total mass and removes the last drawn star if that brings the total mass of stars closer to the predetermined cluster mass described before (i.e., “stop nearest”). In Fig. 5.6 we show the IGIMFs for the 19 different

5.4. INTEGRATED GALACTIC INITIAL MASS FUNCTIONS

SFRs (solid lines). For simulations with a series of runs we show medians (in black) and 68% confidence intervals in colour. It appears that for a given CMF and sampling method the statistical variation around the median IGIMF is very small. Also, the high mass end of the IGIMF is steeper for lower SFRs, due to the lower upper cluster mass limit. With a lower upper cluster mass limit relatively more clusters form with a low mass. As the upper cluster mass limit increases, the variation in the IGIMF becomes smaller. This indicates that our simulations, without an upper limit, are good representatives for high SFR objects (galaxies), whereas for galaxies with a low SFR the IGIMFs are steeper. So for galaxies with a low SFR *the effect will in reality be stronger than we indicate*.

In Bastian (2008) it was claimed that to reproduce the relation between SFR and the maximum cluster luminosity, it is preferred to have a Schechter-like CMF (i.e. a power-law with an exponential cut-off above some mass) instead of a pure power-law. The typical mass at which the CMF turns down exponential is a few times $10^6 M_{\odot}$. As this mass is much higher than the highest stellar mass, the precise shape of the cut-off is not expected to be important. An exponential turn-down at that mass has a similar effect on the IGIMF to truncating the CMF at that mass. For the lower limit to the cut-off mass found by Bastian (2008) the SFR corresponding to their cut-off mass, according to Eq. 5.6, would be $10^{1.6} M_{\odot} \text{ yr}^{-1}$. In Fig. 5.6 it can be seen that such IGIMFs are hardly distinguishable from CMFs without upper cluster mass limits.

5.4.5 Constructing IGIMFs from clustered and non-clustered star formation

The results described above are only valid if all stars are born in clusters. The fraction of stars formed in clusters is a strongly debated quantity nowadays. Different authors constrain the fraction of stars formed in clusters in different and not necessarily comparable ways. The main hindrance here is the definition of ‘a cluster’. Young clusters often get disrupted (sometimes called ‘infant mortality’) on time scales of about 10^7 yrs (Tutukov, 1978; Kroupa et al., 2001; Lamers et al., 2005). These young clusters may or may not have a stellar mass distribution similar to clusters which survive their childhood. Also, stars may form without ever being part of a ‘cluster’. Numbers for the estimate of the fraction of stars born in clusters vary from $\sim 5 - 10\%$ (Miller & Scalo, 1978; Bastian, 2008, and references therein) up to 40% or higher as found in the comparison of cluster mass production for a particular CMF power-law index by Piskunov et al. (2006). Different authors used different definitions of what a cluster/association is and found very different values for the fraction of stars that is a born in a cluster-like environment (see e.g. also Carpenter, 2000; Lada & Lada, 2003; Porras et al., 2003; Megeath et al., 2005;

Piskunov et al., 2008).

The ‘real IGIMF’ (i.e. the true distribution of stellar masses at birth for a whole galaxy) can be straightforwardly estimated from the IGIMF from clustered star formation (i.e. the results given above), and the IMF from stars born in isolation. If we denote the distribution of initial masses in the field as IMF_F , the IGIMF from clustered star formation (i.e. the results obtained above) as IGIMF_C and the total IGIMF (the pdf of initial masses of all stars in a galaxy) as IGIMF_T , we can simply write at any given stellar mass

$$\text{IGIMF}_T(m_*) = f \cdot \text{IGIMF}_C(m_*) + (1 - f) \cdot \text{IMF}_F(m_*), \quad (5.7)$$

where f is the fraction of the stellar mass that is born in clusters, assuming that this fraction f is independent of stellar mass and that the mass distributions in the right-hand side of the equation refer to distributions which are both well sampled. In practice, this means that the total IGIMFs will end up in between the IGIMFs described above and the underlying IMF, weighed by the fraction of clustered star formation (so lines in Figs. 5.3 and 5.4 will end up in between the horizontal line and the shown IGIMFs).

Note that if the second term in the right-hand side of Eq. 5.7 is large, IGIMF effects may well become negligible, or at least far less significant than indicated in the rest of this paper.

5.5 The number of O-stars in the Milky Way

One way to judge between the several IGIMFs (or judging on the importance of the IGIMF effect) would be high mass star counts by upcoming surveys like GAIA (e.g. Perryman et al., 2001).

In order to estimate how many O-stars will be observed by GAIA, we will here undertake the following exercise, in which we keep things as simple as possible. We assume that the IGIMFs described earlier are perfectly sampled (i.e. there are no sampling issues apart from those that make up the IGIMFs), that the SFR of the Milky Way has been constant for the last 10 Myr, which we will assume to be the lifetime of O-stars. Furthermore, we assume that the fraction of all O-stars in the Milky Way, observed by GAIA, is the same as the fraction of all stars together (i.e. $\sim 10\%$). This last number is very uncertain. O-stars are very bright and would therefore be visible to larger distances (the GAIA survey will be magnitude limited). If, however, all O-stars form in the disc, the extinction towards them will be typically higher than for stars above and below the disk. A fraction of the O-stars may be runaway stars, launched by multiple body interactions in young star clusters, which can bring them from the disk into less dusty regions (O-stars formed

5.5. THE NUMBER OF O-STARS IN THE MILKY WAY

Table 5.1: The factor A_{IGIMF} from Eq. 5.8 for Salpeter and all our IGIMFs.

IGIMF	$A_{\text{IGIMF, Salpeter}}$	$A_{\text{IGIMF, Kroupa}}$	ratio
Underlying IMF	2610	4090	1.9
Stop nearest	1650	2670	1.62
Stop before	1490		
Stop after	1830		
Stop 50/50	1710		
Analytic	1050		
Number	1810		
Number unlimited	2610		
Sorted sampling	1200	2050	1.71
CMF slope -1.8	2530		
CMF slope -3.2	280	450	1.61
CMF slope -4.2	60		
Min. cluster mass $1M_{\odot}$	1210		
Min. cluster mass $50M_{\odot}$	2570		

in isolation will typically not get far out of the disk, as with a random velocity of a few times 10 km/s, they will not get much further than a few parsecs away from the disc plane they were formed in). The observed number of O-stars is then given by

$$N_O = A_{\text{IGIMF}} \left(\frac{\text{SFR}}{1M_{\odot}/\text{yr}} \right) \left(\frac{\Delta t}{10\text{Myr}} \right) \left(\frac{f_{\text{obs}}}{0.1} \right), \quad (5.8)$$

in which the SFR is that of the Milky Way, averaged over Δt , which is the lifetime of O-stars, and f_{obs} is the fraction of O-stars in the Milky Way that will be observed. A_{IGIMF} is the number of O-stars under the given assumptions, calculated by dividing the total mass formed by the average stellar mass of the IGIMF, multiplied with the fraction of all stars that are more massive than $17 M_{\odot}$, in which all the IGIMF information is absorbed. In Table 5.1 we give the factor A_{IGIMF} for the Salpeter IMF and all our IGIMFs with underlying Salpeter IMF in the second column. We rounded the numbers off to multiples of ten.

It is now well established that the real IMF in star forming regions is not Salpeter-like, but bends over towards lower masses (e.g. Kroupa, 2001; Chabrier, 2003). The difference here mainly lies in the number of very low mass stars, for which our IGIMFs are all indistinguishable from the underlying IMF. The fraction of O-stars in IGIMFs with other underlying IMFs will be different though, as the fraction of very low mass stars is lower than in Salpeter, making the fraction of high mass stars higher. For example, the numbers in a Kroupa or Chabrier IMF will be about 1.6 times higher (the exact values of the ratio depends on the sampling methods and cluster mass functions, but do not vary much). To illustrate this, we ran a selection of our sampling methods also for an underlying Kroupa (2001) IMF, as displayed in the third column of Table 5.1. The last column gives the ratio

between the results for an underlying Kroupa IMF and an underlying Salpeter IMF. From the ratios (for rather ‘extreme’ sampling methods) it can be seen that they do not vary much from one sampling method to the other.

From the numbers in Table 5.1 it is clear that in principle several IGIMFs may be ruled out by the GAIA survey. The difficulty in judging between several IMFs will be in the other numbers quoted in Eq. 5.8. Some of the extreme IGIMFs can most probably be ruled out with less exact knowledge of the other important parameters. We stress here that the given numbers are only then the number of O-stars observed by GAIA, if the underlying IMF is Salpeter and if the cluster mass functions assumed are the true mass distributions of clumps of forming stars (as here they are heavily extrapolated from the observed mass ranges of young clusters).

5.5.1 Clusters consisting of one (O-) star

Using our sampling methods we could form clusters that consist of only one star. The question whether this is important or not was raised by de Wit et al. (2004, 2005). We track here a) the fraction of clusters that consist of a single star, b) the fraction of clusters that consist of a single O-star ($m > 17M_{\odot}$, see de Wit et al. (2005)) and c) the fraction of clusters for which the most massive star is an O-star, which contains more than half the total cluster mass (we call these “O-star dominated” clusters). The results are shown in Fig. 5.7. We plot probability distribution functions (PDFs) for the fraction of clusters that have the indicated properties in a cluster population. We ran ten thousand realisations of cluster populations and counted for example how many clusters were actually single O-stars and divide that number by the total number of clusters. The distribution of these fractions is what is plotted. So, the peak of blue dot-dashed line shows that out of all ten thousand cluster populations about 0.5-0.6% of their clusters are O-star dominated. PDFs that do not add up to 1, like the fraction of clusters that consist of exactly one O-star, indicate that the rest of the cluster populations had zero single O-stars in them.

For the default sampling method, there are very few clusters that consist of only one star, only one in $\sim 10^4$. The number of clusters in which this one single star is an O-star is again an order of magnitude smaller, with a median of $5.6 \cdot 10^{-3}$. This factor ten in between is less than the ratio of the number of O-stars to the number of all other stars, because it is more likely that one is close to the mass of the cluster if the star is an O-star than when it is less massive. The fraction of clusters that is dominated by an O-star (i.e. containing an O-star with at least half the cluster mass) shows a sharply peaked distribution function around 0.56%.

In the sorted sampling method of WK06, the fraction of clusters containing a

5.5. THE NUMBER OF O-STARS IN THE MILKY WAY

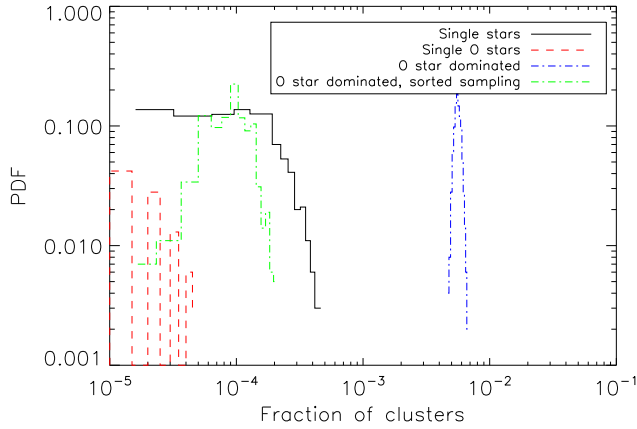


Figure 5.7: Distribution functions of clusters consisting of single stars (black solid line), single O-stars (red dashed line), and clusters dominated by O-stars (i.e. consisting of an O-star that has more than half of the cluster mass, blue dash-dotted line) in the default sampling method, in a cluster population with a power-law CMF with index -2.2 and a lower cluster mass limit of $5M_{\odot}$. In the sorted sampling method of WK06, the first two fractions are zero for all cluster samples. The O-star dominated fraction is ten times lower than in the default method, as shown by the green dash-dotted line.

single (O-) star is zero by construction: the first number of clusters to be drawn is calculated by dividing the total cluster mass aimed for, divided by the mean stellar mass in that cluster according to the appropriate IMF. This mean mass is more than one order of magnitude smaller than the assumed lower cluster mass limit. Therefore, of the order of ten stars or more are always drawn. If the cluster mass is exceeded already with the first drawing of stars (for instance, if there is a really massive O-star drawn, it has on its own as much mass as the rest of the stars or more), then at most one star is removed, resulting in a cluster with at least of the order of ten stars. The number of O-star dominated clusters is therefore also much lower: the chance of having an O-star with half the mass of the cluster or more while not going far over the cluster mass (far enough to let that O-star be removed) is small. Ten stars will mostly have an average mass that is close to the average mass of stars according to the IMF. The one dominating O-star then is several solar masses too massive, making it very likely to be removed. The median fraction of O-star dominated clusters is $9 \cdot 10^{-5}$.

5.5.2 The number of single O-stars

In their paper, de Wit et al. (2005) specifically looked at the fraction of all O-stars which are single, i.e. not part of a detected cluster. They claimed very low mass clusters can be detected, so that these are really O-stars without a surrounding cluster. Nevertheless they are only sensitive to very low mass clusters if these clusters are very concentrated (i.e. small). Clusters of very low mass are very easily disrupted, and extrapolating the results of Lamers & Gieles (2006) to lower mass clusters (by about an order of magnitude), the typical dissolution time of clusters is given by $t_d = 1.7 \cdot (M/10^4 M_\odot)^{0.67}$ Gyr, resulting in O-star lifetimes for $\sim 10 M_\odot$ clusters. Therefore it is very likely that if O-stars live in very low mass clusters, the clusters are in the process of being completely dissolved at the time of observation of the cluster. If not completely disrupted yet, the cluster will have dispersed already significantly, making it harder to detect the underlying cluster than assumed by de Wit et al. (2005).

We use this argument to claim that our “O-star dominated” clusters would also probably be observed as single O-stars. Together with the analysis of the previous section, we can now investigate which fraction of all O-stars would be observed to live outside star clusters (without taking runaway OB stars into account). For the default sampling mechanism 11% of the O-stars would be observed to live outside clusters (if all O-star dominated clusters are detected as single O-stars). For the sorted sampling method this is 0.24%. The difference of course is mainly caused by the different fraction of O-star dominated clusters.

de Wit et al. (2005) found that $4 \pm 2\%$ of the O-stars in the Galaxy cannot be traced back to a formation in a cluster or OB-association. Although this number is smaller than what we found, taking into consideration that we did include very low mass (and probably) dispersed clusters it is legitimate to correct our result by a factor of a few, bringing the results into nice agreement. Increasing the number of single O-stars in the “sorted sampling” method is much harder to justify, so we conclude that this method significantly underproduces single O-stars by a factor of 10-20.

5.6 Galaxy evolution models

The GALEV models (Bicker et al., 2004; Kotulla et al., 2009) are evolutionary synthesis models for galaxies and star clusters. Essentially, evolutionary synthesis models take a set of isochrones, assign a suitable stellar spectrum to each isochrone entry, weigh each entry according to a stellar mass function and a star formation history (SFH), and sum up all contributions for a given isochrone age. GALEV’s “chemically consistent” modelling follows the steady chemical enrichment of the interstellar

5.6. GALAXY EVOLUTION MODELS

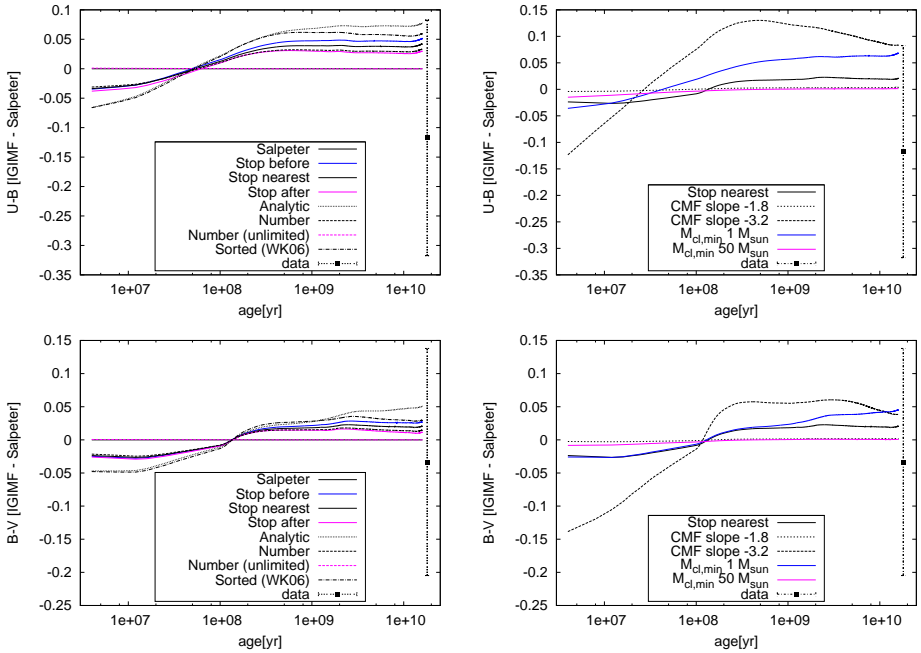


Figure 5.8: The impact of various IGIMFs on the time evolution of integrated Sd galaxy colours. Top row: U-B colour, bottom row: B-V colour. Left column: IGIMFs for various sampling methods, right column: IGIMFs for various CMF parameters. Shown are the differences between models with different IGIMFs and the corresponding model with a Salpeter (1955) IMF. At the highest ages, average colours (and their standard deviation) for Sd galaxies from the HyperLeda database are shown.

medium caused by stellar winds and supernovae, and forms stars at the metallicity available in the gas phase at this time. Nebular emission is taken into account for actively star-forming galaxies. We used models with the following input physics:

- isochrones: from the Padova group (Bertelli et al. (1994) with subsequent updates concerning the TP-AGB phase)
- spectral library: BaSeL 2.2 (Lejeune et al., 1997, 1998)
- SFH as a function of Hubble type: following Sandage (1986), with parameters adjusted to simultaneously reproduce a range of observations for galaxies of different Hubble types (for details see Kotulla et al. (2009))

– an Sd galaxy is modelled with a constant SFR

- an E galaxy with an exponentially declining SFR with a $1/e$ decline time of 1 Gyr
- Sa-Sc galaxies are modelled with SFRs depending on the available gas mass at a given time (similar to the Kennicutt-Schmidt law, see Kennicutt (1998b)), resulting in approximately exponentially declining SFR with $1/e$ decline times of 3.5 Gyr (Sa galaxy), 6 Gyr (Sb galaxy) and 10.5 Gyr (Sc galaxy)
- the gas mass-dependence of the Sa-Sc galaxies' SFR results in slight changes between models with Salpeter (1955) IMF and the various IGIMFs, with the IGIMF models having slightly lower SFRs by up to 5% for our standard IGIMF model (“stop nearest”) and up to 10% for extreme cases
- stellar yields: explosive nucleosynthesis yields are taken from Woosley & Weaver (1995) for high-mass stars ($M > 10 M_{\odot}$) and from van den Hoek & Groenewegen (1997) for stars with lower masses. In addition, SN Ia yields from Nomoto et al. (1997) are included (only total metallicity is traced, not individual elements)
- stellar MF: we use the various IGIMFs determined in this work.

Underlying assumptions for this approach include

- the IGIMF does not change with time or SFR (taking into account the SFR-dependent effects discussed in Sect. 5.4.4 would only strengthen the deviations, so our results are lower limits for the impact of the IGIMF effect)
- the IGIMF does not change with metallicity (no such dependence is known or expected for Population I or Population II stars and star clusters)
- no infall or outflow of material is used (but also not needed to reproduce a range of galaxy properties correctly, see Kotulla et al. (2009)), likewise we neglect galaxy interactions
- we assume instantaneous mixing and cooling of ejected material with the entire available gas reservoir (however, the SFH parameters are adjusted to reproduce available gas metallicities as a function of the galaxies' Hubble type at the present day)
- we aim at modelling L^* galaxies of the respective Hubble type, hence neglect any magnitude-metallicity relation.

For more details see Kotulla et al. (2009).

5.6.1 Integrated photometry of galaxies

In Fig. 5.8 we compare our Sd galaxy models using various IGIMFs with the standard model using the input Salpeter (1955) IMF (models for other Hubble types show very similar behaviour). On the right side (i.e. plotted at old ages) we show average colours and their standard deviation from data obtained from the HyperLeda¹ database (Paturel et al., 2003), subdivided according to their morphological type. In each of these plots, the intrinsic scatter within the morphological type class well exceeds the deviations introduced by the different IGIMFs. Therefore we do not expect that IGIMF variations can be constrained from integrated photometry of galaxies.

5.6.2 Chemical enrichment in galaxies from different IGIMFs

A more promising way might be the study of the gas properties in galaxies. In Fig. 5.9 we show the relation between gas fraction (i.e. the ratio between gas mass and gas + stellar mass) and gas metallicity (we give all metallicities as $[\text{Fe}/\text{H}]$, assuming solar abundance ratios and neglecting alpha-enhancement effects). Since the majority of chemical enrichment originates in massive stars, deficiencies of such stars due to IGIMF effects reflect directly in the gas metallicity. The red hashed area is the region covered using various individual metallicities instead of the “chemically consistent” modelling, and represents a worst-case uncertainty range. Consistent with this “uncertainty region” are four sets of models: the input Salpeter (1955) IMF models, the equivalent “Number (unlimited)” models, and the models “CMF slope = -1.8” and “ $M_{\text{cl,min}} = 50 M_{\odot}$ ”. This agrees with the little deviations between the input Salpeter (1955) IMF and the IGIMFs already seen in Sect. 5.4. The other models using different IGIMFs are clearly distinct from this “uncertainty region”, with differences in gas metallicity up to 1 dex, with various models offset by 0.2 – 0.4 dex (corresponding to factors 1.5 – 2.5).

To our best knowledge, there is no study which determines both gas fractions and gas metallicities for a large sample of galaxies in a consistent way. We therefore gathered data on galactic gas masses from Huchtmeier (1989) and Karachentsev et al. (1999), while for the gas metallicities we considered the catalogues by Kewley et al. (2005), Nagao et al. (2006), and Izotov et al. (2007). These catalogues were not only chosen for their (comparably) large sample sizes, but also for their diversity in the galaxy populations they address. Each of these samples has its own intrinsic biases and limitations. Huchtmeier (1989) and Nagao et al. (2006) are more literature compilation papers. The sample by Kewley et al. (2005) intentionally contains galaxies of all Hubble types with a wide range of proper-

¹<http://leda.univ-lyon1.fr/>

CHAPTER 5. VARIATIONS IN IGIMFS

Table 5.2: Average gas properties and integrated galaxy colours for various literature galaxy samples. The first three columns are: (1) Sample origin, (2) galaxy type, (3) number of galaxies in the sample, the others as indicated

(1)	(2)	(3)	gas fraction	error gas fraction		
Huchtmeier (1989)	E	46	0.36	0.16		
Huchtmeier (1989)	Sa	154	0.49	0.17		
Huchtmeier (1989)	Sb	635	0.53	0.16		
Huchtmeier (1989)	Sc	1284	0.59	0.18		
Huchtmeier (1989)	Sd	730	0.67	0.21		
Karachentsev et al. (1999)	E	7	0.007	0.008		
Karachentsev et al. (1999)	Sa	1	0.0003	-		
Karachentsev et al. (1999)	Sb	6	0.015	0.015		
Karachentsev et al. (1999)	Sc	21	0.078	0.092		
Karachentsev et al. (1999)	Sd	45	0.19	0.14		
combined	E	53	0.33	0.18		
combined	Sa	155	0.48	0.17		
combined	Sb	641	0.52	0.16		
combined	Sc	1305	0.59	0.18		
combined	Sd	775	0.67	0.26		
(1)	(2)	(3)	[Fe/H](gas)	error [Fe/H](gas)		
Kewley et al. (2005)	E	9	-0.09	0.18		
Kewley et al. (2005)	Sa	6	-0.08	0.27		
Kewley et al. (2005)	Sb	18	-0.09	0.27		
Kewley et al. (2005)	Sc	34	-0.13	0.16		
Kewley et al. (2005)	Sd	18	-0.42	0.32		
Nagao et al. (2006)	E	3	-0.74	0.22		
Nagao et al. (2006)	Sa	1	-1.05	-		
Nagao et al. (2006)	Sb	3	-0.71	0.19		
Nagao et al. (2006)	Sc	5	-1.07	0.34		
Nagao et al. (2006)	Sd	47	-0.92	0.24		
Izotov et al. (2007)	E	2	-0.85	0.1		
Izotov et al. (2007)	Sa	1	-1.04	-		
Izotov et al. (2007)	Sb	2	-0.66	0.24		
Izotov et al. (2007)	Sc	8	-0.84	0.30		
Izotov et al. (2007)	Sd	23	-0.95	0.31		
combined	E	14	-0.34	0.39		
combined	Sa	8	-0.32	0.50		
combined	Sb	23	-0.22	0.36		
combined	Sc	47	-0.35	0.42		
combined	Sd	88	-0.83	0.34		
(1)	(2)	(3)	U-B	error U-B	B-V	error B-V
HyperLeda database	E	547	0.36	0.21	0.83	0.13
HyperLeda database	Sa	166	0.14	0.23	0.68	0.17
HyperLeda database	Sb	329	0.02	0.19	0.61	0.16
HyperLeda database	Sc	397	-0.10	0.15	0.50	0.13
HyperLeda database	Sd	173	-0.23	0.20	0.39	0.17

ties, the Karachentsev et al. (1999) sample is volume-limited, and Izotov et al. (2007) considers specifically low-metallicity HII regions in nearby dwarf galaxies. We supplemented the catalogue information with data from the HyperLeda¹ database (Paturel et al., 2003), to have an as uniform as possible determination of Hubble type and absolute luminosity for the sample galaxies. From these data we estimate the average gas fractions and gas metallicities for the galaxy samples. Where multiple observations for a given galaxy were available, we included all of them individually, to access the uncertainties more realistically and to average out metallicity gradients in a single galaxy. In Table 5.2 we present the derived average values for the individual and the combined samples for five different galaxy types.

From Table 5.2 one can easily see the non-homogeneity of the samples. The multitude of biases and selection effects hampers a straightforward comparison of

these observational data with our models. A dedicated survey of a large number of L^* galaxies (GALEV attempts to model L^* galaxies, and therefore neglects galaxy mass-dependent effects!) for the different Hubble types, both in terms of gas fraction and in terms of gas metallicity, with a reliable estimate of the galaxies' Hubble types, will be needed to provide direct calibration values for our (and others) galaxy evolution models.

In Fig. 5.9 we present gas properties for GALEV models of Sd galaxies, based on the various IGIMFs (equivalent plots for galaxies of other Hubble types appear very similar). We included the data point corresponding to the combined data sets in Table 5.2. As uncertainties we plotted either the scatter for a given property within the combined sample of Sd galaxies, or the distance to the most deviating mean of any subsample, whichever was larger.

Based on the large spread in the observed gas fractions it is hard to constrain IGIMF models with these data. Future and more homogeneous samples will be helpful, as the spread in observed metallicities is smaller than or at most comparable to the difference arising from different IGIMFs.

5.7 Conclusions

We have conducted a suite of numerical experiments to investigate how the steepening of the IGIMF depends on the sampling method and the assumed cluster mass function. Hereby we extended the variations already studied by WK06. We found that, unless the maximum occurring stellar mass is not limited by the cluster mass, or the minimum cluster mass is higher than the maximum stellar mass, the IGIMF is always steeper at the high-mass end than the input IMF, assuming that stars all form in clusters and that these clusters follow a power-law CMF which extends down to masses well below the upper mass limit for stars. If there are many stars formed in a non-clustered environment (see Eq. 5.7) or the CMF does extend to these low masses (or turns over and peaks at higher masses), IGIMF effects are much smaller and possibly even become negligible. The amount of steepening and the mass where deviations set in depend on the sampling method and the adopted cluster mass function:

- The numerical method of sampling is important. While all random techniques result in the same high-mass slope (for constant CMF slope), the onset of deviations occurs at different stellar masses, showing a slight steepening already at stellar masses below the lower cluster mass limit.
- The slope of the cluster mass function as well as its lower limit are very important. The index of the cluster mass function sets the steepness of

CHAPTER 5. VARIATIONS IN IGIMFS

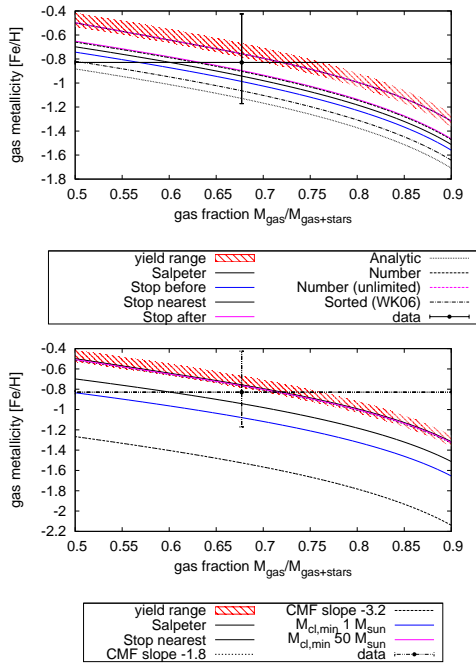


Figure 5.9: The impact of various IGIMFs on the relation between available gas mass and gas metallicity (e.g. chemical enrichment) for Sd galaxies. Top panel: IGIMFs for various sampling methods. Bottom panel: IGIMFs for various CMF parameters. The points mark estimates from observations, see text for details. The red hashed area is the region covered using various individual metallicities instead of the “chemically consistent” modelling and a Salpeter (1955) IMF. It represents a worst-case uncertainty range.

the IGIMF at the high mass end: a steeper cluster mass function results in a steeper IGIMF. Varying the CMF power-law index in the range $[-1.8, -2.2, -3.2]$ results in IGIMF slopes at the high mass end of approximately $[-2.4, -2.6, -3.6]$. The *observationally ill-constrained* lower cluster mass limit sets the mass at which the steepening sets in, i.e., the IGIMF becomes much steeper from $m = M_{\text{cl, min}}$. At slightly lower masses there is a very small deficiency of stars as compared to the input IMF. The magnitude of this discrepancy depends on the sampling method. Contrary to results by Elmegreen (2006), we do not find the $\beta = 2$ CMF to be singular.

All sampling methods reproduce the input cluster mass functions well. Even though some seem to steepen or shallow the CMF by construction, the effects are marginal and unobservable. The number of isolated stars that should be formed according to our method is very small (of the order of one out of 10,000 clusters in our sample consists of one star). The fraction of clusters consisting of only one O-star is even one order of magnitude smaller. We also tested the fraction of clusters which are O-star dominated (clusters which contain an O-star which represents at least half of the total cluster mass) to simulate observational incompleteness, since a small underlying cluster might stay unnoticed close to a bright O-star. This measure is rather sensitive to the sampling method. For our default method we found about 0.56% of such clusters, while for the “sorted sampling” by WK06 this fraction was more than one order of magnitude lower. For sufficiently large samples of O-stars the O-star count could be a suitable tracer of the IGIMF if the observed fraction of O-stars, delivered by surveys like GAIA, is well understood.

Our default sampling results indicate that $< 11\%$ of the O-stars in the Galaxy will be observed to be separate from any cluster environment, in nice agreement with results of de Wit et al. (2005). The sorted sampling method of WK06 strongly underproduces this number.

However, current knowledge, both observationally and theoretically, of the very formation processes of (especially massive) stars in star clusters (see e.g. high-mass star formation from high-mass cloud cores (Krumholz et al., 2005) vs competitive accretion (Bonnell et al., 2004)) prevents us from the conclusion as to which sampling method is favoured by nature.

We conducted numerical experiments using the GALEV evolutionary synthesis package, which self-consistently follows the photometric and chemical history of various idealised isolated galaxy models. The conclusions we draw on photometry and chemical enrichment resulting from our IGIMFs as compared to the standard IMFs can be summarised as follows:

1. Integrated photometry is likely not a good tracer of IGIMF variations, since

differences are smaller than the intrinsic galaxy-to-galaxy scatter for a given morphological type.

2. Chemical enrichment is a better tracer, as it is directly linked to the number of massive stars, however, observations are rare and cover only small sample sizes. Once the (systematic and random) uncertainties in determining gas mass fractions and metallicities are well understood, these quantities may be able to be the deciding factor between several sampling methods (at least the ones with the most extreme deviations from the underlying IMF).

Future studies of galaxy evolution and chemical enrichment have to take into account that the IGIMF is steeper than the normal IMF, as well as the amount of uncertainty in the amount of steepening, as the details of the sampling method nature chooses are poorly understood. Additional uncertainties are introduced as the shape of the cluster mass function is not well constrained at very low masses (i.e. cluster masses comparable to individual stellar masses), whereas the low mass end of the CMF is the most important quantity in shaping the IGIMF. These differences between the IMF and the IGIMF have pronounced implications for modelling galaxy properties.

Acknowledgements

It is a pleasure to thank the referee, John Scalo, for a very helpful and thorough report that greatly improved the paper. We kindly thank Nate Bastian, Pavel Kroupa, Carsten Weidner and Simon Goodwin for helpful comments on an early version of the manuscript, as well as Ralf Kotulla for reading and discussing details of the GALEV models. We acknowledge the usage of the HyperLeda database (<http://leda.univ-lyon1.fr>).

6

Nederlandstalige samenvatting

Wanneer we naar de nachtelijke sterrenhemel kijken is deze bezaaid met sterren. Kijken we nog beter dan zien we structuur aan de hemel: een band met meer sterren dan de rest van de hemel, met donkerdere gebieden en wazige vlekjes. Kijken we met verrekijkers of telescopen, dan zien we nog veel meer wazige vlekjes. Die vlekjes blijken niet allemaal hetzelfde te zijn. Sommige zijn gaswolken vlakbij die verhit worden door de sterren die er kort geleden in geboren zijn. Andere zijn het resultaat van zware sterren die ontploft zijn. Weer andere blijken volledige sterrenstelsels ver weg van de onze (zie Figuur 6.1). Ons eigen sterrenstelsel (het Melkwegstelsel) is ook precies datgene wat we zien als die band met meer sterren aan de hemel. Hoe komt de sterrenhemel aan deze rijke structuur en hoe hangen alle verschillende objecten en de processen die ze veroorzaken met elkaar samen?



Figure 6.1: M101 is een typisch spiraalvormig sterrenstelsel, dat erg lijkt op ons Melkwegstelsel. Van de zijkant zou je kunnen zien dat de schijf waar de spiraalarmen inzitten erg plat is. Duidelijk zichtbaar zijn het licht van de sterren in verschillende kleuren, en het effect van stof, wat een deel van dit licht, vooral in de spiraalarmen, tegenhoudt.

Structuur in het heelal

We weten dat het heelal in het begin (slechts 380.000 jaar na de Oerknal) bijzonder homogeen was. De temperatuur van de zogenaamde ‘kosmische achtergrondstraling’ vertoont slechts verbazingwekkend kleine fluctuaties en dit kan worden vertaald in een variatie in de dichtheid van het gas in het vroege heelal, die eveneens bijzonder klein is. In het huidige heelal zijn de dichtheidscontrasten enorm. Vele ordes van grootte verschil zit er tussen de allerdichtste en allerijlste stukken van het heelal.

De groei van structuur

De kleine variaties in de dichtheid in het heel vroege heelal zullen groeien: als er ergens net iets meer massa zit dan gemiddeld, dan trekt de zwaartekracht daarvan net iets harder dan gemiddeld omliggende materie die kant op. Hierdoor wordt het dichtheidscontrast groter, wat datzelfde effect versterkt, zodat er uiteindelijk steeds meer materie komt te zitten precies daar waar oorspronkelijk de dichtheid net een heel klein beetje hoger was. Laten we dit proces ‘uit de hand lopen’, dan ontstaan er

na verloop van tijd dus enorme concentraties materie (we noemen deze “halo’s”), met daar tussenin grote lege gebieden. Dit hele proces is volledig gedomineerd door de zwaartekracht. Aangezien we de zwaartekracht redelijk goed begrijpen zijn we al vrij lange tijd in staat nauwkeurig uit te rekenen hoeveel van die halo’s er zijn, hoe zwaar ze zijn, en waar ze zich bevinden.

De groteschaalstructuur van het heelal

De verdeling (in massa en in de ruimte) van deze halo’s noemen we de groteschaalstructuur van het heelal. In Figuur 6.2 zien we de vergelijking van een computersimulatie van die groteschaalstructuur met waarnemingen van hetzelfde. Elk puntje in dat plaatje is zo’n halo. De simulatie is simpelweg een simulatie van een heel groot stuk van het heelal, dat in de computer nageemaakt is vanaf toen het heelal bijzonder jong was, tot aan nu. Het enige wat in de simulatie is meegenomen is de zwaartekracht (dit is dus een sterke vereenvoudiging van alle processen die zich in het heelal afspelen!) en toch komt de structuur in het simpele computermodel erg goed overeen met de waarnemingen. In de waarnemingen zijn alle puntjes in Figuur 6.2 sterrenstelsels, waarvan een voorbeeld te zien in Figuur 6.1. Het feit dat gesimuleerde halo’s en waargenomen sterrenstelsels dezelfde verdeling in het heelal hebben geeft al aan dat de sterrenstelsels zich vormen in de halo’s, de verdichtingen die ontstaan uit de kleine verdichtingen uit het vroege heelal die we in de kosmische achtergrondstraling zien.

De vorming van sterrenstelsels

Binnen deze verdichtingen zullen zich de sterrenstelsels gaan vormen. Voor het maken van sterrenstelsels moeten we meer processen in ogenschouw nemen dan alleen zwaartekracht. Zo ligt het voor de hand dat we stervorming niet kunnen verwaarlozen. Sterren ontstaan uit gas, maar stoten ook weer gas uit, door ‘sterwinden’ en (in het geval van zware sterren) de zogenaamde supernova explosies. Ook bevatten sommige (of misschien zelfs alle) sterrenstelsels een enorm zwart gat in hun centrum, welke ook een grote invloed kan hebben op het gas en de vorming van sterren binnen het stelsel. In dit hoofdstuk zal ik op de belangrijkste processen kort ingaan om daarna in het volgende hoofdstuk te laten zien hoe we deze simuleren.

‘Normale’ materie

Het heelal bestaat voor een zeer groot deel (96%) uit dingen waarvan we weinig idee hebben wat het is. De termen ‘donkere energie’ (ongeveer 76% van de in-

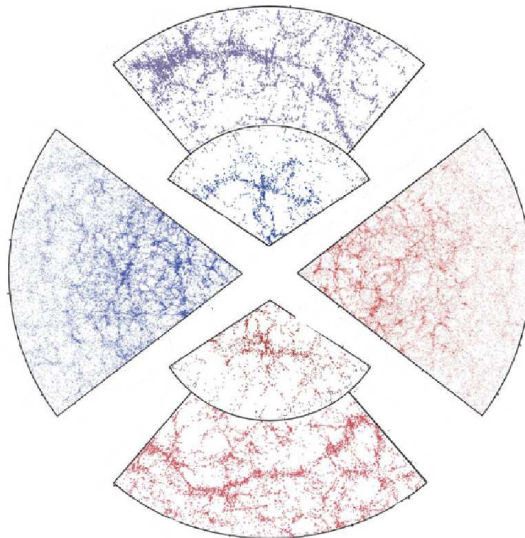


Figure 6.2: Een gesimuleerde (rood, rechts en onder) en waargenomen ‘taartpunt’ uit het heelal, waarop de groteschaalstructuur van het heelal goed te zien is wordt hier vergeleken met de waargenomen groteschaalstructuur (blauw, links en boven), waarin elk puntje een sterrenstelsel voorstelt waarvan de positie en de afstand zijn gemeten. De aarde staat in de punten van de taart, en naar de rand toe staan de stelsels steeds verder weg. Een goede overeenkomst tussen de simulatie en de waarnemingen is wat hier het meest opvalt. *Credit: V. Springel*

houd van het heelal) en ‘donkere materie’ (ongeveer 20%) worden gebruikt voor de twee verschijningsvormen die zich fundamenteel anders gedragen. Grofweg: donkere energie versnelt de uitdijning van het heelal, terwijl donkere materie, door de zwaartekracht, juist een rem zet op die uitdijning. De laatste 4% bestaat uit wat we ‘baryonen’ noemen en dit is het materiaal waarvan gas, sterren, planeten, mensen, tafels, etcetera zijn gemaakt. Op grote schaal (zoals hierboven beschreven) bepalen de donkere materie en donkere energie wat er gebeurt, maar op de kleine schaal (binnen sterrenstelsels) worden baryonen belangrijk. Bovendien zijn het de baryonen die kunnen worden waargenomen met telescopen en van de donkere componenten kunnen alleen indirect eigenschappen worden afgeleid uit waarnemingen. Hieronder ga ik kort in op sommige van de belangrijke processen in de vorming van sterrenstelsels.

Gasdynamica

Anders dan de donkere materie, werken er op gas meer krachten dan alleen de zwaartekracht, zoals bijvoorbeeld gasdruk (twee gaswolken vliegen niet zomaar door elkaar heen, maar zullen 'botsen' en kunnen daarbij opwarmen of afkoelen). Het simuleren van gas is alleen daarom al moeilijker dan donkere materie (zoals de simulaties hierboven beschreven, waar het slechts om de groteschaalstructuur van het heelal ging). Wanneer gas gesimuleerd moet worden moet dus bijgehouden worden of het gas opwarmt en afkoelt, processen die afhankelijk zijn van de dichtheid, temperatuur en samenstelling van het gas.

De vorming, evolutie en dood van sterren

Uit gas van hele hoge dichtheid kunnen sterren gevormd worden. Een gaswolk kan instorten onder zijn eigen zwaartekracht en in de allerdichtste gebieden zullen bollen van gas ontstaan die waterstof fuseren tot helium in hun kern: sterren (waarvan onze Zon er één is). Sterren zijn in feite hun eigen brandstof voorraad, het gas waar ze uit bestaan kan dienen als brandstof voor de kernfusie in hun binnenste. Na verloop van tijd is deze voorraad uitgeput en zullen de sterren 'overlijden'. Hoe snel dit gebeurt is voornamelijk afhankelijk van de massa van de ster: een zware ster leeft veel korter dan een lichte (hij heeft weliswaar meer brandstof, maar verbrandt deze ook heel veel sneller).

Aan het einde van hun leven stoten sterren hun buitenlagen van gas af (die verrijkt zijn door de kernfusie met zwaardere elementen). Zware sterren doen dat gewelddadiger dan lichte, in zogenaamde supernova explosies. In zo'n supernova explosie komt in een heel korte tijd bijzonder veel energie vrij, ongeveer net zo veel als in de rest van het hele sterrenstelsel (het equivalent van ongeveer een miljard sterren)! Deze energie wordt deels 'gedumpt' in het gas rondom de ontploffende ster. Dit verhit dat gas en duwt het ook weg.

Sterren vormen meestal in flinke groepen, waarin na ongeveer 10 miljoen jaar een aantal van dat soort explosies afgaat. De optelsom van deze supernovae is belangrijk voor hoe het gas in een sterrenstelsel zich gedraagt. Als er genoeg sterren gevormd worden, en dus genoeg van dergelijke explosies plaatsvinden, kan er zelfs op grote schaal gas het sterrenstelsel uitstromen (we noemen dat een galactische wind en zien dat ook gebeuren in waarnemingen). Ook zijn ze belangrijk in het verrijken van het gas met zware elementen (zwaarder dan waterstof en helium), wat heel belangrijk is voor het afkoelen van heet gas.

Simulaties

Dit proefschrift is grotendeels gebaseerd op gedetailleerde simulaties van een representatief volume in het heelal, waarin veel processen gevolgd worden die belangrijk zijn voor het vormen van sterrenstelsels. In dit hoofdstuk licht ik in het kort toe hoe dergelijke simulaties in elkaar zitten en wat het bijzondere is aan de set van simulaties die gebruikt wordt in de Hoofdstukken 2 en 4.

De groteschaalstructuur van het heelal

Voor het simuleren van de groteschaalstructuur van het heelal is alleen de kosmologie (om precies te zijn, de uitdijingsnelheid van het heelal als functie van de tijd en de samenstelling van het heelal) en zwaartekracht belangrijk. Het is dus afdoende om alle materie te beschouwen als donkere materie en alleen zwaartekracht uit te rekenen. Dit is lange tijd de belangrijkste manier geweest om kosmologische simulaties te doen. De Millennium Simulatie door Volker Springel en collega's is de grootste en meest gebruikte simulatie van deze soort.

Om de vorming van sterrenstelsels te volgen in simulaties met alleen maar donkere materie zijn de zogenaamde 'semi-analytische modellen' ontwikkeld. Dit zijn 'recepten' voor het gedrag van de baryonische materie in de gevormde donkere materie structuren. Om de vorming van sterrenstelsels consistent te volgen moeten echter alle baryonische processen worden meegenomen.

Fysica van baryonen in simulaties

Veel van de baryonische processen die van groot belang zijn voor het vormen van sterrenstelsels vinden plaats op heel kleine schaal. Door de limitatie van computers kunnen we, als we een realistische populatie sterrenstelsels willen simuleren, de resolutie (kleinste details die we kunnen nabootsen) van de simulatie niet hoog genoeg maken om dergelijke processen in detail te volgen. De simulaties die in dit proefschrift zijn beschreven bevatten baryonische 'deeltjes' met een massa die bijna een miljoen keer zo hoog is als de massa van een gemiddelde ster (zoals onze Zon). Om een systeem fatsoenlijk te kunnen simuleren moet het toch zeker uit zo'n honderd deeltjes bestaan. Sterren worden weliswaar meestal in groepen geboren, maar we hebben het dan over 'clusters' van ongeveer duizend tot een miljoen keer de massa van de Zon (en meer lichte systemen dan zware). Binnen die groepen van sterren ontploft ongeveer 1% van de sterren als een supernova, een van de heel belangrijke processen in de evolutie van sterrenstelsels. Het is dus duidelijk dat de belangrijke processen binnen een sterrenstelsel (stervorming, supernova explosies, maar ook de vorming van stervormingsgebieden en de groei van een superzwaar

zwart gat in het centrum) plaatsvinden op schalen beneden de resolutielimiet van de simulaties.

Om die baryonische processen toch hun welverdiende plaats in het verhaal te geven worden zogenaamde ‘sub-grid modellen’ ontwikkeld (wat letterlijk betekent dat ze gaan over schalen die fijner zijn dan de resolutielimiet van de simulatie). Deze modellen zijn simpele ‘recepten’ die aangeven hoe dergelijke kleine schaal processen invloed uitoefenen op de schalen die wél door de simulatie worden gevolgd. Hieronder worden kort enkele voorbeelden samengevat:

1. *Stervorming* Sterren moeten in de simulatie met ongeveer een miljoen stuks tegelijk gevormd worden. Omdat dit meer is dan wat onder de meeste omstandigheden in een sterrenstelsel gebeurt wordt een sub-grid model gebruikt, dat aangeeft wat de kans is dat een gasdeeltje (van dezelfde massa) wordt omgevormd in een sterdeeltje. Zo zorgen we ervoor dat gemiddeld genomen genoeg sterren worden gevormd door het hele heelal heen.
2. *Evolutie van sterren* We weten uit waarnemingen hoe, wanneer een groep sterren gevormd wordt, de verdeling van de sterren over de verschillende stermassa’s is. Met behulp van modellen voor de evolutie van sterren kunnen we dan bepalen hoeveel gas deze sterren weer uitblazen het heelal in, en wanneer en met welke samenstelling. Ook weten we hoeveel energie er in totaal in supernovae vrijkomt.
3. *Supernovae* Wanneer de supernovae ontploffen weten we dus de totale beschikbare energie, maar hoe we deze moeten terugvoeren in het gas is niet a priori duidelijk. Er bestaan verschillende manieren om energie in een gas te stoppen, bijvoorbeeld door het te verwarmen of door het snelheid te geven. Er zijn dan verschillende keuzes die je kunt maken: warm je een klein beetje gas heel veel op, of veel gas een klein beetje, en geef je een heel harde duw tegen weinig massa, of maar een klein duwtje tegen heel veel massa? Niemand die het goed weet en de verschillende mogelijkheden moeten worden nagegaan.
4. *Superzware zwarte gaten* In het centrum van veel (of alle) sterrenstelsels huizen de zogenaamde superzware zwarte gaten. Deze groeien door botsingen met andere superzware zwarte gaten (wanneer hun sterrenstelsels botsen en samensmelten) en door het ‘opeten’ van gas wat zich daarvoor in een hete schijf om het zwarte gat heen bevond. Wanneer dit gas wordt opgegeten komt er ook energie vrij, en die energie die wordt gebruikt om het gas in en om het sterrenstelsel heet te maken. Van heet gas is het moeilijker sterren vormen, dus de aanwezigheid van dit zwarte gat is een rem op het stervormingsproces.

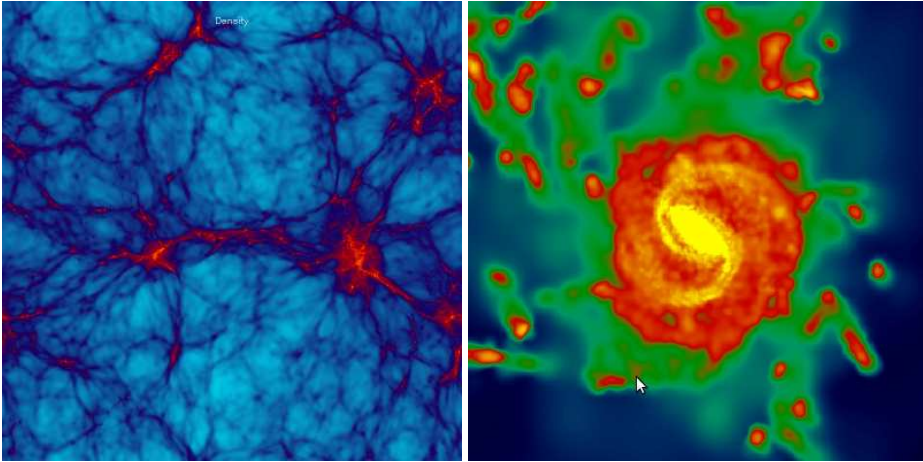


Figure 6.3: Twee plaatjes van de dichtheid van het gas in één van de OWLS model-heelallenen. Links is een plaatje van ongeveer 10 miljoen lichtjaar bij 10 miljoen lichtjaar, terwijl voor het plaatje rechts is ingezoomd op een sterrenstelsel. Het oppervlak wat is afgebeeld in het rechter plaatje is 62500 keer zo klein als in het linker plaatje.

Voor de laatste twee processen worden vaak samengevat onder de noemer ‘feedback’. Voor alle bovengenoemde processen zijn tot op zekere hoogte, uit waarnemingen of theoretische overwegingen, goed gemotiveerde modellen en parameters te gebruiken. Toch is het niet geheel duidelijk wat de juiste methode is om zulke processen te simuleren, en wat daarvoor de juiste parameters (zoals bijvoorbeeld de hoeveelheid massa die wordt uitgestoten door supernova explosies) zijn.

De ‘Overwhelmingly Large Simulations’

Precies die onzekerheid in modellen voor de zojuist genoemde processen is waar gebruik van gemaakt is in het project dat de ‘Overwhelmingly Large Simulations’ (OWLS) wordt genoemd, en waar twee van de hoofdstukken uit dit proefschrift gebruik van maken. Juist omdat er meerdere modellen voor stervorming (bijvoorbeeld meer of minder efficiënt), supernovae (bijvoorbeeld heel veel gas wegsturen met lage snelheid of vice versa), superzware zwarte gaten (hoeveel wordt het gas om het zwarte gat heen opgewarmt als het zwarte gat groeit?) etc. mogelijk zijn, kunnen we onderzoeken hoe verschillende eigenschappen van sterrenstelsels afhangen van deze modellen.

In OWLS is ervoor gekozen om op hoge resolutie veel verschillende modellen

te vergelijken, waarin we telkens maar 1 van de modellen tegelijk veranderen, zodat we direct kunnen zien wat het effect is van precies die verandering. Een voorbeeld van de gasdichtheid in een heel groot gebied (ongeveer 10 miljoen bij 10 miljoen lichtjaar) in het vroege heelal, en een sterrenstelsel die zich in datzelfde heelal bevindt is afgebeeld in Figuur 6.3. In Hoofdstuk 2, Figuur 2.2.2 staat hetzelfde sterrenstelsel, maar dan met allerlei variaties op de sub-grid modellen.

Dit proefschrift

In dit proefschrift is gekeken naar verschillende aspecten van (de vorming van) sterrenstelsels.

De invloed van kleine schaal processen op sterrenstelsels

De enorme variatie van sub-grid modellen in de OWLS database wordt in Hoofdstuk 2 onderzocht in termen van de fysische eigenschappen van sterrenstelsels (massa in sterren, stervormingssnelheid, hoeveelheid stervormend gas, etcetera). We vergelijken systematisch verschillende simulaties met elkaar om zo te identificeren welke modellen belangrijk zijn voor welke eigenschappen van sterrenstelsels.

Een interessante conclusie die kon worden getrokken is dat de hoeveelheid sterren niet wordt beïnvloed door de efficiëntie van stervorming, maar dat de stellaire massa van een sterrenstelsel voornamelijk wordt gedictieerd door de hoeveelheid beschikbaar gas (afhankelijk van het kosmologische model en de afkoeling van gas) en de hoeveelheid energie die weer terug wordt gevoerd in het gas door supernova explosies en superzware zwarte gaten. De sterrenstelsels passen hun voorraad gas zodanig aan dat er, als stervorming efficiënter is, altijd minder gas beschikbaar is om sterren van te maken, zodanig dat de totale hoeveelheid gevormde sterren en de totale hoeveelheid energie die door supernovae in het gas wordt geïnjecteerd hetzelfde blijven. We zeggen wel, dat de stervorming in sterrenstelsels ‘zelfregulerend’ is.

De ‘omgeving’ van sterrenstelsels

Omdat één van de grote vragen in het onderzoek naar de evolutie van sterrenstelsels is in hoeverre de eigenschappen van sterrenstelsels worden bepaald door interne processen en in hoeverre door hun omgeving, kijken we in Hoofdstuk 3 naar verschillende definities van de omgeving van sterrenstelsels. We gebruiken in dit hoofdstuk de Millennium Simulatie (die alleen donkere materie bevat), met

daarbovenop een model voor de vorming van sterrenstelsels. De baryonische fysica van deze sterrenstelsels werd dus niet expliciet gesimuleerd. De modellen zijn echter zo geconstrueerd, dat het goed mogelijk is een hele realistische populatie sterrenstelsels te vormen, veel realistischer dan bijvoorbeeld in OWLS. We laten zien welke definitie een goede maat is voor de massa van de halo waarin het stelsel zich bevindt (we hebben immers al deze gegevens ook, iets wat voor waarnemende sterrenkundigen zelden tot nooit geldt). Ook laten we zien hoe je een omgevingsparameter kunt construeren die onafhankelijk is van de halo massa. Dit is nog nooit gebruikt en is potentieel heel nuttig: we weten al dat veel eigenschappen van sterrenstelsels sterk afhangen van de halo massa. Wil je dus weten wat de invloed is van de omgeving, zonder daarmee halo massa te bedoelen, dan is het belangrijk een omgevingsparameter te hebben die onafhankelijk is van halo massa.

Gesimuleerde sterrenstelsels waarnemen

Om te zien hoe goed modellen en simulaties, zoals eerder beschreven, het waargenomen heelal beschrijven (en dus: hoe goed we begrijpen welke processen belangrijk zijn en hoe ze bijdragen aan de totstandkoming van sterrenstelsels) worden uiteraard de simulaties vergeleken met waarnemingen. Dit is echter nog niet zo eenvoudig als het lijkt. Waarnemingen geven ons alleen een bepaalde hoeveelheid waargenomen licht bij een bepaalde golflengte. Weten we de afstand van het sterrenstelsel nauwkeurig, dan komt dat overeen met een hoeveelheid licht die het stelsel uitstraalt, eventueel bij kortere golflengten (blauwer licht), als het stelsel ver weg staat. Dit laatste komt omdat het heelal uitdijt, dus als het licht lang onderweg is, dan heeft het een langere golflengte dan wanneer het werd uitgezonden. Deze hoeveelheid licht is niet per sé al het licht dat de sterren die in een stelsel zitten uitstralen, want onderweg komt het licht gas en stof tegen, waar het (gedeeltelijk) door geabsorbeerd kan worden. Bovendien vangen we dit licht op met grote telescopen en hun ‘camera’s’, en die laten de straling ook niet ongemoeid en veranderen het beeld van het sterrenstelsel een klein beetje (in het dagelijks leven is dit effect met digitale camera’s nauwelijks merkbaar, maar aanwezig).

In Hoofdstuk 4 kijken we naar de hoeveelheid licht die de sterrenstelsels in OWLS uitstralen. Om preciezer te zijn kijken we naar de verdelingsfunctie van de hoeveelheid licht (het aantal sterrenstelsels van iedere helderheid). Die functie noemen we de lichtkrachtverdeling. We kijken naar verschillende aspecten die op de lichtkrachtverdeling van invloed zijn, zoals:

1. *sub-grid fysica* De verschillende modellen die in OWLS zijn gebruikt, en met name de modellen met verschillende beschrijvingen van wat supernovae met hun omringende gas doen, resulteren in sterk variërende lichtkrachtverdelingen.

-
2. *absorptie van licht door stof* Stof houdt een deel van het licht dat er doorheen schijnt tegen, en het houdt meer blauw dan rood licht tegen. Lichtkrachtverdelingen in verschillende kleuren licht worden dan ook anders beïnvloed door het stof. Sterrenstelsels met meer ‘koud’ gas, en sterrenstelsels met meer zware elementen worden sterker beïnvloed door stof. In simulaties zoals OWLS is het echter erg moeilijk om een goede schatting te maken van de hoeveelheid absorptie door stof, omdat in werkelijke sterrenstelsels het grootste deel van de absorptie plaatsvindt in structuren die niet door onze simulaties worden opgelost (en de simulaties missen voor stof belangrijke fysica).
 3. *selectiemethode* Simulatoren noemen een door zwaartekracht bij elkaar gehouden ‘blob’ materie, die eventueel sterren bevat, een sterrenstelsel. De definitie van waarnemers is zoiets als: een ‘vlek’ licht op een plaatje, die duidelijk boven de achtergrond uitsteekt. Deze definities zijn nogal verschillend van elkaar en leveren alleen al daarom misschien een andere lichtkrachtverdeling op. Om dit te testen hebben we van onze simulaties plaatjes gemaakt, en daarna de lichtkrachtverdeling geprobeerd terug te vinden met de methoden die waarnemers zouden gebruiken. Over het algemeen vinden we dat deze behoorlijk gelijk zijn aan de lichtkrachtverdelingen die direct uit de simulatie volgen. Eén interessant verschil is dat als het beeld van een klein (of heel ver weg staand) sterrenstelsel meer door de telescoop wordt ‘uitgesmeerd’, dan lijkt de verdeling over lichtkrachten vlakker (dat wil zeggen: terwijl er in het algemeen veel meer zwakke stelsels bestaan dan heldere lijkt het er dan op dat het verschil in aantal tussen heldere en zwakke sterrenstelsels kleiner wordt).

De verdeling van stermassa’s binnen een sterrenstelsel

De verdeling van de massa’s van de sterren die in een sterrenstelsel geboren worden heeft zijn invloed op verschillende aspecten van de evolutie van sterrenstelsels. Zo worden verschillende elementen door verschillende typen sterren gemaakt, en hebben de verschillende sterren een verschillend spectrum (verdeling van hun lichtintensiteit over golflengten, oftewel kleuren). Variatie van deze verdeling over de massa geeft dus zowel een andere ontwikkeling van de samenstelling van gas en sterren in een sterrenstelsel als een andere kleur van het sterrenstelsel, terwijl massa en leeftijd hetzelfde zijn.

De verdeling van stermassa’s in stervormingsgebieden en sterrenhopen in ons Melkwegstelsel lijkt behoorlijk universeel. De simpelste aanname is dan ook dat dit geldt voor alle stervormingsgebieden, en voor elk willekeurig sample net gevorm-

nde sterren in het heelal. De verdeling van massa's is dus altijd hetzelfde, ongeacht waar of wanneer de groep sterren wordt geboren.

We weten echter ook dat de stervormingsgebieden en sterrenhopen zelf een massa-verdeling volgen, die zodanig is dat er meer lichte objecten bestaan dan zware. Als deze groepen té licht worden, dan zullen ze een systematisch gebrek aan zware sterren vertonen. Dit kan ertoe leiden dat de verdeling van stermassa's in een sterrenstelsel anders is dan die binnen afzonderlijke sterrenhopen. In Hoofdstuk 5 bekijken we de verdeling van stermassa's in een sterrenstelsel onder de aanname dat deze universeel is binnen de sterrenhopen (en stervormingsgebieden). We laten zien hoe de totale verdeling afhangt van de manier waarop we de sterren (willekeurig) uit de gegeven onderliggende verdeling trekken en van de massaverdeling van de jonge sterrenhopen. Ook bekijken we wat hiervan de invloed is op de helderheid van sterrenstelsels bij verschillende golflengten, de chemische samenstelling van het gas in sterrenstelsels en het aantal zware, jonge sterren dat kan worden waargenomen in ons eigen Melkwegstelsel.

Hoe nu verder?

Door het onderzoek dat is samengevat in de vorige paragraaf zijn we weer iets wijzer geworden over de totstandkoming van de populatie sterrenstelsels in ons heelal. Het eind van het verhaal is dit echter niet. Er zijn nog veel open vragen, en voor veel aspecten van sterrenstelsels komen de simulaties nog helemaal niet overeen met de waarnemingen. Simulaties zoals die in het OWLS project leren ons veel over de natuurkundige processen die belangrijk zijn voor de evolutie van sterrenstelsels, maar veel van die ingrediënten zijn nog sterk vereenvoudigd en een volledig begrip van de levensloop van sterrenstelsels is nog ver buiten bereik.

In de nabije toekomst zullen zowel waarnemende als simulerende sterrenkundigen een hoop leren over vooral de vroege stadia van de vorming van sterrenstelsels. Door de immer toenemende computerkracht en technologie komen zowel waarneming als theorie steeds een beetje verder. Af en toe een goed idee van een sterrenkundige is echter minstens zo belangrijk: wetenschap blijft mensenwerk.

Bibliography

- Abbas, U. & Sheth, R. K. 2005, **MNRAS**, 364, 1327
- Allen, C. W. 1976, *Astrophysical Quantities*, ed. C. W. Allen
- Angulo, R. E., Baugh, C. M., & Lacey, C. G. 2008, **MNRAS**, 387, 921
- Baldry, I. K., Balogh, M. L., Bower, R. G., et al. 2006, **MNRAS**, 373, 469
- Baldry, I. K., Glazebrook, K., Brinkmann, J., et al. 2004, **ApJ**, 600, 681
- Balogh, M., Eke, V., Miller, C., et al. 2004a, **MNRAS**, 348, 1355
- Balogh, M. L., Baldry, I. K., Nichol, R., et al. 2004b, **ApJL**, 615, L101
- Bamford, S. P., Nichol, R. C., Baldry, I. K., et al. 2009, **MNRAS**, 393, 1324
- Bastian, N. 2008, **MNRAS**, 390, 759
- Beckwith, S. V. W., Stiavelli, M., Koekemoer, A. M., et al. 2006, **AJ**, 132, 1729
- Berlind, A. A. & Weinberg, D. H. 2002, **ApJ**, 575, 587
- Bertelli, G., Bressan, A., Chiosi, C., Fagotto, F., & Nasi, E. 1994, **A&AS**, 106, 275
- Bertin, E. & Arnouts, S. 1996, **A&AS**, 117, 393
- Bertschinger, E. 1998, **ARAA**, 36, 599
- Bett, P., Eke, V., Frenk, C. S., et al. 2007, **MNRAS**, 376, 215
- Bicker, J., Fritze-v. Alvensleben, U., Möller, C. S., & Fricke, K. J. 2004, **A&A**, 413, 37
- Blanc, G. A., Heiderman, A., Gebhardt, K., Evans, N. J., & Adams, J. 2009, **ApJ**, 704, 842
- Blanton, M. R. & Berlind, A. A. 2007, **ApJ**, 664, 791
- Blanton, M. R., Eisenstein, D., Hogg, D. W., Schlegel, D. J., & Brinkmann, J. 2005, **ApJ**, 629, 143
- Blanton, M. R., Eisenstein, D. J., Hogg, D. W., et al. 2003a, in *Bulletin of the American Astronomical Society*, Vol. 36, *Bulletin of the American Astronomical Society*, 589–+
- Blanton, M. R., Hogg, D. W., Bahcall, N. A., et al. 2003b, **ApJ**, 594, 186
- Bonnell, I. A., Vine, S. G., & Bate, M. R. 2004, **MNRAS**, 349, 735
- Booth, C. M. & Schaye, J. 2009, ArXiv e-prints
- Bouchet, P., Lequeux, J., Maurice, E., Prevot, L., & Prevot-Burnichon, M. L. 1985, **A&A**, 149, 330
- Bower, R. G., Benson, A. J., Malbon, R., et al. 2006, **MNRAS**, 370, 645
- Bower, R. G., McCarthy, I. G., & Benson, A. J. 2008, **MNRAS**, 390, 1399
- Boylan-Kolchin, M., Springel, V., White, S. D. M., Jenkins, A., & Lemson, G. 2009, **MNRAS**, 398, 1150

BIBLIOGRAPHY

- Briceño, C., Luhman, K. L., Hartmann, L., Stauffer, J. R., & Kirkpatrick, J. D. 2002, **ApJ**, 580, 317
- Brook, C. B., Kawata, D., Gibson, B. K., & Flynn, C. 2004, **MNRAS**, 349, 52
- Bruzual, G. & Charlot, S. 2003, **MNRAS**, 344, 1000 (BC03)
- Bryan, G. L. & Norman, M. L. 1998, **ApJ**, 495, 80
- Cabanac, R. A., Alard, C., Dantel-Fort, M., et al. 2007, **A&A**, 461, 813
- Calzetti, D., Armus, L., Bohlin, R. C., et al. 2000, **ApJ**, 533, 682
- Calzetti, D., Kinney, A. L., & Storchi-Bergmann, T. 1994, **ApJ**, 429, 582
- Carpenter, J. M. 2000, **AJ**, 120, 3139
- Cassata, P., Guzzo, L., Franceschini, A., et al. 2007, **ApJS**, 172, 270
- Cen, R. & Ostriker, J. 1992, **ApJ**, 393, 22
- Cen, R. Y., Ostriker, J. P., Jameson, A., & Liu, F. 1990, **ApJL**, 362, L41
- Chabrier, G. 2003, **PASP**, 115, 763
- Charlot, S. & Bruzual, G. 2009, **MNRAS**, in prep (CB07)
- Charlot, S. & Fall, S. M. 2000, **ApJ**, 539, 718
- Cole, S., Aragon-Salamanca, A., Frenk, C. S., Navarro, J. F., & Zepf, S. E. 1994, **MNRAS**, 271, 781
- Cole, S. & Kaiser, N. 1989, **MNRAS**, 237, 1127
- Cole, S., Lacey, C. G., Baugh, C. M., & Frenk, C. S. 2000, **MNRAS**, 319, 168
- Cooper, M. C., Newman, J. A., Croton, D. J., et al. 2006, **MNRAS**, 370, 198
- Cooper, M. C., Newman, J. A., Madgwick, D. S., et al. 2005, **ApJ**, 634, 833
- Cooper, M. C., Newman, J. A., Weiner, B. J., et al. 2008, **MNRAS**, 383, 1058
- Couchman, H. M. P., Thomas, P. A., & Pearce, F. R. 1995, **ApJ**, 452, 797
- Cox, D. P. & Tucker, W. H. 1969, **ApJ**, 157, 1157
- Crain, R. A., Eke, V. R., Frenk, C. S., et al. 2007, **MNRAS**, 377, 41
- Crain, R. A., Theuns, T., Dalla Vecchia, C., et al. 2009, **MNRAS**, 399, 1773
- Croton, D. J., Springel, V., White, S. D. M., et al. 2006, **MNRAS**, 365, 11
- Daddi, E., Cimatti, A., Renzini, A., et al. 2004, **ApJ**, 617, 746
- Daddi, E., Dickinson, M., Morrison, G., et al. 2007, **ApJ**, 670, 156
- Dalla Vecchia, C. & Schaye, J. 2008, ArXiv e-prints, 801
- Davé, R. 2008, **MNRAS**, 385, 147
- Dave, R., Dubinski, J., & Hernquist, L. 1997, *New Astronomy*, 2, 277

- Davé, R. & Oppenheimer, B. D. 2007, **MNRAS**, 374, 427
- de Grijs, R., Anders, P., Bastian, N., et al. 2003, **MNRAS**, 343, 1285
- De Lucia, G. & Blaizot, J. 2007, **MNRAS**, 375, 2
- De Lucia, G., Kauffmann, G., & White, S. D. M. 2004, **MNRAS**, 349, 1101
- De Lucia, G., Poggianti, B. M., Aragón-Salamanca, A., et al. 2007, **MNRAS**, 374, 809
- De Lucia, G., Springel, V., White, S. D. M., Croton, D., & Kauffmann, G. 2006, **MNRAS**, 366, 499
- de Wit, W. J., Testi, L., Palla, F., Vanzi, L., & Zinnecker, H. 2004, **A&A**, 425, 937
- de Wit, W. J., Testi, L., Palla, F., & Zinnecker, H. 2005, **A&A**, 437, 247
- Dekel, A. & Birnboim, Y. 2006, **MNRAS**, 368, 2
- Dekel, A., Birnboim, Y., Engel, G., et al. 2008, ArXiv e-prints
- Di Matteo, T., Springel, V., & Hernquist, L. 2005, **Nature**, 433, 604
- Dib, S., Shadmehri, M., Padoan, P., et al. 2010, **MNRAS**, 405, 401
- Dressler, A. 1980, **ApJ**, 236, 351
- Dressler, A., Oemler, Jr., A., Couch, W. J., et al. 1997, **ApJ**, 490, 577
- Edge, A. C. & Stewart, G. C. 1991, **MNRAS**, 252, 414
- Ellison, S. L., Patton, D. R., Simard, L., McConnachie, A. W., & Baldry, I. K. 2010, ArXiv e-prints
- Elmegreen, B. G. 2006, **ApJ**, 648, 572
- Espino-Briones, N., Plionis, M., & Ragone-Figueroa, C. 2007, **ApJL**, 666, L5
- Evrard, A. E. 1988, **MNRAS**, 235, 911
- Fakhouri, O. & Ma, C. 2009, **MNRAS**, 394, 1825
- Faltenbacher, A. 2009, ArXiv e-prints
- Faltenbacher, A. & White, S. D. M. 2010, **ApJ**, 708, 469
- Ferrarese, L. & Merritt, D. 2000, **ApJL**, 539, L9
- Finlator, K., Davé, R., & Oppenheimer, B. D. 2007, **MNRAS**, 376, 1861
- Fontanot, F., Monaco, P., Cristiani, S., & Tozzi, P. 2006, **MNRAS**, 373, 1173
- Fontanot, F., Monaco, P., Silva, L., & Grazian, A. 2007, **MNRAS**, 382, 903
- Gao, L., Springel, V., & White, S. D. M. 2005, **MNRAS**, 363, L66
- Gao, L. & White, S. D. M. 2007, **MNRAS**, 377, L5
- Gao, L., White, S. D. M., Jenkins, A., Stoehr, F., & Springel, V. 2004, **MNRAS**, 355, 819
- Gieles, M., Larsen, S. S., Bastian, N., & Stein, I. T. 2006a, **A&A**, 450, 129

BIBLIOGRAPHY

- Gieles, M., Larsen, S. S., Scheepmaker, R. A., et al. 2006b, **A&A**, 446, L9
- Gnedin, N. Y. 1995, **ApJS**, 97, 231
- Gómez, P. L., Nichol, R. C., Miller, C. J., et al. 2003, **ApJ**, 584, 210
- Goodwin, S. P. & Pagel, B. E. J. 2005, **MNRAS**, 359, 707
- Goto, T., Yamauchi, C., Fujita, Y., et al. 2003, **MNRAS**, 346, 601
- Gottlöber, S., Klypin, A., & Kravtsov, A. V. 2001, **ApJ**, 546, 223
- Gottlöber, S. & Yepes, G. 2007, **ApJ**, 664, 117
- Guo, Q., White, S., Li, C., & Boylan-Kolchin, M. 2010, **MNRAS**, 404, 1111
- Haardt, F. & Madau, P. 2001, in *Clusters of Galaxies and the High Redshift Universe Observed in X-rays*, ed. D. M. Neumann & J. T. V. Tran
- Haas, M. R., Gieles, M., Scheepmaker, R. A., Larsen, S. S., & Lamers, H. J. G. L. M. 2008, **A&A**, 487, 937
- Hahn, O., Porciani, C., Dekel, A., & Carollo, C. M. 2009, **MNRAS**, 398, 1742
- Hakobyan, A. A., Mamon, G. A., Petrosian, A. R., Kunth, D., & Turatto, M. 2009, ArXiv e-prints:0910.1801
- Harker, G., Cole, S., Helly, J., Frenk, C., & Jenkins, A. 2006, **MNRAS**, 367, 1039
- Hernquist, L. & Katz, N. 1989, **ApJS**, 70, 419
- Hester, J. A. & Tasitsiomi, A. 2010, **ApJ**, 715, 342
- Hogg, D. W., Blanton, M. R., Brinchmann, J., et al. 2004, **ApJL**, 601, L29
- Hogg, D. W., Blanton, M. R., Eisenstein, D. J., et al. 2003, **ApJL**, 585, L5
- Hopkins, A. M. & Beacom, J. F. 2006, **ApJ**, 651, 142
- Hu, W. & Dodelson, S. 2002, **ARAA**, 40, 171
- Huchtmeier, O.-G., R. W. K. 1989, *A General Catalog of HI Observations of Galaxies. The Reference Catalog.*, ed. O.-G. W. K. Huchtmeier, Richter
- Ishiyama, T., Fukushige, T., & Makino, J. 2008, **PASJ**, 60, L13+
- Izotov, Y. I., Thuan, T. X., & Stasińska, G. 2007, **ApJ**, 662, 15
- Jing, Y. P., Suto, Y., & Mo, H. J. 2007, **ApJ**, 657, 664
- Jonsson, P. 2006, **MNRAS**, 372, 2
- Jonsson, P., Groves, B. A., & Cox, T. J. 2010, **MNRAS**, 403, 17
- Kaiser, N. 1984, **ApJL**, 284, L9
- Karachentsev, I. D., Makarov, D. I., & Huchtmeier, W. K. 1999, **A&AS**, 139, 97
- Katz, N., Weinberg, D. H., & Hernquist, L. 1996, **ApJS**, 105, 19
- Kauffmann, G., Colberg, J. M., Diaferio, A., & White, S. D. M. 1999, **MNRAS**, 303, 188

- Kauffmann, G., Heckman, T. M., White, S. D. M., et al. 2003, **MNRAS**, 341, 54
- Kauffmann, G., White, S. D. M., Heckman, T. M., et al. 2004, **MNRAS**, 353, 713
- Kay, S. T., Pearce, F. R., Frenk, C. S., & Jenkins, A. 2002, **MNRAS**, 330, 113
- Kay, S. T., Thomas, P. A., & Theuns, T. 2003, **MNRAS**, 343, 608
- Kennicutt, Jr., R. C. 1998a, **ARAA**, 36, 189
- Kennicutt, Jr., R. C. 1998b, **ApJ**, 498, 541
- Kereš, D., Katz, N., Weinberg, D. H., & Davé, R. 2005, **MNRAS**, 363, 2
- Kewley, L. J., Jansen, R. A., & Geller, M. J. 2005, **PASP**, 117, 227
- Khalatyan, A., Cattaneo, A., Schramm, M., et al. 2008, **MNRAS**, 387, 13
- Kitzbichler, M. G. & White, S. D. M. 2007, **MNRAS**, 376, 2
- Komatsu, E., Dunkley, J., Nolta, M. R., et al. 2009, **ApJS**, 180, 330
- Komatsu, E., Smith, K. M., Dunkley, J., et al. 2010, ArXiv e-prints
- Kormendy, J. & Richstone, D. 1995, **ARAA**, 33, 581
- Kotulla, R., Fritze, U., Weilbacher, P., & Anders, P. 2009, **MNRAS**, 396, 462
- Kovač, K., Lilly, S. J., Cucciati, O., et al. 2010, **ApJ**, 708, 505
- Kroupa, P. 2001, **MNRAS**, 322, 231
- Kroupa, P., Aarseth, S., & Hurley, J. 2001, **MNRAS**, 321, 699
- Kroupa, P. & Weidner, C. 2003, **ApJ**, 598, 1076
- Krumholz, M. R., McKee, C. F., & Klein, R. I. 2005, **Nature**, 438, 332
- Lacey, C. & Cole, S. 1994, **MNRAS**, 271, 676
- Lada, C. J. & Lada, E. A. 2003, **ARAA**, 41, 57
- Lamers, H. J. G. L. M. & Gieles, M. 2006, **A&A**, 455, L17
- Lamers, H. J. G. L. M., Gieles, M., Bastian, N., et al. 2005, **A&A**, 441, 117
- Larsen, S. S. 2002, **AJ**, 124, 1393
- Larsen, S. S. 2008, ArXiv e-prints, 0812.1400
- Larson, K. A., Wolff, M. J., Roberge, W. G., Whittet, D. C. B., & He, L. 2000, **ApJ**, 532, 1021
- Le Fèvre, O., Vettolani, G., Paltani, S., et al. 2004, **A&A**, 428, 1043
- Lejeune, T., Cuisinier, F., & Buser, R. 1997, **A&AS**, 125, 229
- Lejeune, T., Cuisinier, F., & Buser, R. 1998, **A&AS**, 130, 65
- Lemson, G. & Kauffmann, G. 1999, **MNRAS**, 302, 111

BIBLIOGRAPHY

- Lewis, I., Balogh, M., De Propriis, R., et al. 2002, **MNRAS**, 334, 673
- Li, C. & White, S. D. M. 2009, **MNRAS**, 398, 2177
- Lilly, S. J., Le Fèvre, O., Renzini, A., et al. 2007, **ApJS**, 172, 70
- Macciò, A. V., Dutton, A. A., van den Bosch, F. C., et al. 2007, **MNRAS**, 378, 55
- Maness, H., Martins, F., Trippe, S., et al. 2007, **ApJ**, 669, 1024
- Maraston, C. 2005, **MNRAS**, 362, 799
- Marchesini, D., van Dokkum, P. G., Förster Schreiber, N. M., et al. 2009, **ApJ**, 701, 1765
- Markevitch, M. 1998, **ApJ**, 504, 27
- Maschberger, T. & Clarke, C. J. 2008, **MNRAS**, 391, 711
- Maschberger, T. & Kroupa, P. 2007, **MNRAS**, 379, 34
- Maulbetsch, C., Avila-Reese, V., Colín, P., et al. 2007, **ApJ**, 654, 53
- McCarthy, I. G. & Others, S. 2009, **MNRAS**, in prep.
- McCraday, N., Gilbert, A. M., & Graham, J. R. 2003, **ApJ**, 596, 240
- McCraday, N. & Graham, J. R. 2007, **ApJ**, 663, 844
- Megeath, S. T., Flaherty, K. M., Hora, J., et al. 2005, in IAU Symposium, Vol. 227, Massive Star Birth: A Crossroads of Astrophysics, ed. R. Cesaroni, M. Felli, E. Churchwell, & M. Walmsley, 383–388
- Miller, G. E. & Scalo, J. M. 1978, **PASP**, 90, 506
- Mo, H. J. & White, S. D. M. 1996, **MNRAS**, 282, 347
- Monaco, P., Fontanot, F., & Taffoni, G. 2007, **MNRAS**, 375, 1189
- Monaghan, J. J. 1992, **ARAA**, 30, 543
- Mori, M., Yoshii, Y., Tsujimoto, T., & Nomoto, K. 1997, **ApJL**, 478, L21+
- Murray, N., Quataert, E., & Thompson, T. A. 2005, **ApJ**, 618, 569
- Nagamine, K. 2002, **ApJ**, 564, 73
- Nagamine, K., Springel, V., Hernquist, L., & Machacek, M. 2004, **MNRAS**, 350, 385
- Nagao, T., Maiolino, R., & Marconi, A. 2006, **A&A**, 459, 85
- Night, C., Nagamine, K., Springel, V., & Hernquist, L. 2006, **MNRAS**, 366, 705
- Nomoto, K., Iwamoto, K., Nakasato, N., et al. 1997, Nuclear Physics A, 621, 467
- Ocvirk, P., Pichon, C., & Teyssier, R. 2008, **MNRAS**, 390, 1326
- Oppenheimer, B. D. & Davé, R. 2006, **MNRAS**, 373, 1265
- Oppenheimer, B. D. & Davé, R. 2008, **MNRAS**, 387, 577

- Oppenheimer, B. D., Davé, R., Kereš, D., et al. 2010, **MNRAS**, 406, 2325
- Paturel, G., Petit, C., Prugniel, P., et al. 2003, **A&A**, 412, 45
- Peebles, P. J. E. 1993, Principles of physical cosmology, ed. P. J. E. Peebles
- Perryman, M. A. C., de Boer, K. S., Gilmore, G., et al. 2001, **A&A**, 369, 339
- Pflamm-Altenburg, J. & Kroupa, P. 2008, **Nature**, 455, 641
- Pflamm-Altenburg, J., Weidner, C., & Kroupa, P. 2007, **ApJ**, 671, 1550
- Pimblet, K. A., Smail, I., Kodama, T., et al. 2002, **MNRAS**, 331, 333
- Piskunov, A. E., Kharchenko, N. V., Röser, S., Schilbach, E., & Scholz, R. 2006, **A&A**, 445, 545
- Piskunov, A. E., Kharchenko, N. V., Schilbach, E., et al. 2008, **A&A**, 487, 557
- Porras, A., Christopher, M., Allen, L., et al. 2003, **AJ**, 126, 1916
- Postman, M. & Geller, M. J. 1984, **ApJ**, 281, 95
- Prevot, M. L., Lequeux, J., Prevot, L., Maurice, E., & Rocca-Volmerange, B. 1984, **A&A**, 132, 389
- Recchi, S., Calura, F., & Kroupa, P. 2009, ArXiv e-prints 0903.2395
- Ryu, D., Vishniac, E. T., & Chiang, W.-H. 1990, **ApJ**, 354, 389
- Salpeter, E. E. 1955, **ApJ**, 121, 161
- Sandage, A. 1986, **A&A**, 161, 89
- Scannapieco, C., Gadotti, D. A., Jonsson, P., & White, S. D. M. 2010, **MNRAS**, 407, L41
- Schaye, J. 2004, **ApJ**, 609, 667
- Schaye, J. & Dalla Vecchia, C. 2008, **MNRAS**, 383, 1210
- Schaye, J., Dalla Vecchia, C., Booth, C. M., et al. 2010, **MNRAS**, 402, 1536
- Scoville, N., Aussel, H., Brusa, M., et al. 2007, **ApJS**, 172, 1
- Seljak, U. & Zaldarriaga, M. 1996, **ApJ**, 469, 437
- Serna, A., Alimi, J.-M., & Chieze, J.-P. 1996, **ApJ**, 461, 884
- Shao, Z., Xiao, Q., Shen, S., et al. 2007, **ApJ**, 659, 1159
- Shapiro, P. R., Martel, H., Villumsen, J. V., & Owen, J. M. 1996, **ApJS**, 103, 269
- Sheth, R. K. & Tormen, G. 2004, **MNRAS**, 350, 1385
- Sijacki, D. & Springel, V. 2006, **MNRAS**, 366, 397
- Sijacki, D., Springel, V., di Matteo, T., & Hernquist, L. 2007, **MNRAS**, 380, 877
- Skillman, E. D., Côté, S., & Miller, B. W. 2003, **AJ**, 125, 593
- Smith, R. J., Hudson, M. J., Lucey, J. R., Nelan, J. E., & Wegner, G. A. 2006, **MNRAS**, 369, 1419

BIBLIOGRAPHY

- Somerville, R. S., Hopkins, P. F., Cox, T. J., Robertson, B. E., & Hernquist, L. 2008, ArXiv e-prints
- Somerville, R. S. & Primack, J. R. 1999, **MNRAS**, 310, 1087
- Sommer-Larsen, J., Götz, M., & Portinari, L. 2003, **ApJ**, 596, 47
- Spergel, D. N., Bean, R., Doré, O., et al. 2007, **ApJS**, 170, 377
- Springel, V. 2005, **MNRAS**, 364, 1105
- Springel, V. & Hernquist, L. 2003a, **MNRAS**, 339, 289
- Springel, V. & Hernquist, L. 2003b, **MNRAS**, 339, 312
- Springel, V., White, S. D. M., Jenkins, A., et al. 2005, **Nature**, 435, 629
- Springel, V., White, S. D. M., Tormen, G., & Kauffmann, G. 2001, **MNRAS**, 328, 726
- Steinmetz, M. 1996, **MNRAS**, 278, 1005
- Steinmetz, M. & Mueller, E. 1993, **A&A**, 268, 391
- Stinson, G., Seth, A., Katz, N., et al. 2006, **MNRAS**, 373, 1074
- Stolte, A., Brandner, W., Grebel, E. K., Lenzen, R., & Lagrange, A.-M. 2005, **ApJL**, 628, L113
- Stoughton, C., Lupton, R. H., Bernardi, M., et al. 2002, **AJ**, 123, 485
- Stringer, M. J., Benson, A. J., Bundy, K., Ellis, R. S., & Quetin, E. L. 2009, **MNRAS**, 393, 1127
- Sutherland, R. S. & Dopita, M. A. 1993, **ApJS**, 88, 253
- Teyssier, R. 2002, **A&A**, 385, 337
- Thacker, R. J. & Couchman, H. M. P. 2000, **ApJ**, 545, 728
- Thomas, D., Maraston, C., Bender, R., & Mendes de Oliveira, C. 2005, **ApJ**, 621, 673
- Thomas, P. A. & Couchman, H. M. P. 1992, **MNRAS**, 257, 11
- Tissera, P. B., Lambas, D. G., & Abadi, M. G. 1997, **MNRAS**, 286, 384
- Tonini, C., Maraston, C., Thomas, D., Devriendt, J., & Silk, J. 2010, **MNRAS**, 403, 1749
- Tornatore, L., Borgani, S., Dolag, K., & Matteucci, F. 2007, **MNRAS**, 382, 1050
- Tutukov, A. V. 1978, **A&A**, 70, 57
- van den Bosch, F. C., Yang, X., & Mo, H. J. 2003, **MNRAS**, 340, 771
- van den Hoek, L. B. & Groenewegen, M. A. T. 1997, **A&AS**, 123, 305
- van Dokkum, P. G. 2008, **ApJ**, 674, 29
- Walcher, C. J., Groves, B., Budavari, T., & Dale, D. 2010, ArXiv e-prints
- Wang, H. Y., Mo, H. J., & Jing, Y. P. 2007, **MNRAS**, 375, 633
- Wechsler, R. H., Zentner, A. R., Bullock, J. S., Kravtsov, A. V., & Allgood, B. 2006, **ApJ**, 652, 71

- Weidner, C. & Kroupa, P. 2004, **MNRAS**, 348, 187
- Weidner, C. & Kroupa, P. 2005, **ApJ**, 625, 754
- Weidner, C. & Kroupa, P. 2006, **MNRAS**, 365, 1333 (WK06)
- Weidner, C., Kroupa, P., & Larsen, S. S. 2004, **MNRAS**, 350, 1503
- Weingartner, J. C. & Draine, B. T. 2001, **ApJ**, 548, 296
- Weinmann, S. M., van den Bosch, F. C., Yang, X., & Mo, H. J. 2006, **MNRAS**, 366, 2
- Wetzel, A. R., Cohn, J. D., White, M., Holz, D. E., & Warren, M. S. 2007, **ApJ**, 656, 139
- White, S. D. M. & Frenk, C. S. 1991, **ApJ**, 379, 52
- Whitmore, B. C. 2003, in *A Decade of Hubble Space Telescope Science*, 153–178
- Whitmore, B. C. & Gilmore, D. M. 1991, **ApJ**, 367, 64
- Whitmore, B. C., Gilmore, D. M., & Jones, C. 1993, **ApJ**, 407, 489
- Wiersma, R. P. C., Schaye, J., & Smith, B. D. 2009a, **MNRAS**, 393, 99
- Wiersma, R. P. C., Schaye, J., Theuns, T., Dalla Vecchia, C., & Tornatore, L. 2009b, ArXiv e-prints
- Wilkins, S. M., Hopkins, A. M., Trentham, N., & Tojeiro, R. 2008a, **MNRAS**, 391, 363
- Wilkins, S. M., Trentham, N., & Hopkins, A. M. 2008b, **MNRAS**, 385, 687
- Wilman, D., Zibetti, S., & Budavari, T. 2010, ArXiv e-prints
- Wilman, D. J., Oemler, A., Mulchaey, J. S., et al. 2009, **ApJ**, 692, 298
- Woosley, S. E. & Weaver, T. A. 1995, **ApJS**, 101, 181
- Wuyts, S., Franx, M., Cox, T. J., et al. 2009, **ApJ**, 696, 348
- Xu, C., Buat, V., Boselli, A., & Gavazzi, G. 1997, **A&A**, 324, 32
- Yang, X., Mo, H. J., & van den Bosch, F. C. 2003, **MNRAS**, 339, 1057
- Yang, X., Mo, H. J., van den Bosch, F. C., et al. 2007, **ApJ**, 671, 153
- Zel'Dovich, Y. B. 1970, **A&A**, 5, 84
- Zhang, Q. & Fall, S. M. 1999, **ApJL**, 527, L81

Refereed publications

1. **M.R. Haas**, P. Anders, 2010, A&A, 512, 79, “*Variations in integrated galactic initial mass functions due to sampling method and cluster mass function*”
2. Joop Schaye, Claudio Dalla Vecchia, C. M. Booth, Robert P. C. Wiersma, Tom Theuns, **Marcel R. Haas**, Serena Bertone, Alan R. Duffy, I. G. McCarthy, Luca Tornatore, Freeke van de Voort, 2009, MNRAS, 402, 1536, “*The physics driving the cosmic star formation history*”
3. Laura V. Sales, Julio F. Navarro, Joop Schaye, Claudio Dalla Vecchia, Volker Springel, **Marcel R. Haas**, Amina Helmi, 2009, MNRAS Letters, 399, L64, “*The origin of extended disk galaxies at $z=2$* ”
4. **M.R. Haas**, M. Gieles, R.A. Scheepmaker, S.S. Larsen, H.J.G.L.M. Lamers, 2008, A&A, 487, 937, “*ACS imaging of star clusters in M51. II. The luminosity function and mass function across the disk*”
5. R.A. Scheepmaker, **M.R. Haas**, M.Gieles, N.Bastian, S.S. Larsen, H.J.G.L.M. Lamers, 2007, A&A, 469, 925, “*ACS imaging of star clusters in M51. I. Identification and radius distribution*”
6. M. Gieles, S.S. Larsen, R.A. Scheepmaker, N. Bastian, **M.R. Haas**, H.J.G.L.M. Lamers, 2006, A&A, 446, L9, “*Observational evidence for a truncation of the star cluster initial mass function at the high mass end*”

Conference proceedings

1. **M.R. Haas**, P. Anders, 2009, “*Galactic consequences of clustered star formation*”, Star clusters: galactic building blocks throughout space and time (IAU S266)
2. **M.R. Haas**, P. Anders, 2009, “*Population synthesis from clustered star formation*”, Population synthesis, planning for the next decade (IAU S262)
3. **M.R. Haas**, M. Gieles, R.A. Scheepmaker, S.S. Larsen, H.J.G.L.M. Lamers, N. Bastian, 2008, “*Variation of the cluster luminosity function across the disk of M51*”, Mass loss from stars and the evolution of stellar clusters
4. R.A. Scheepmaker, M. Gieles, **M.R. Haas**, N. Bastian, H.J.G.L.M. Lamers, 2008, “*Thousands of Star Clusters in M51 with HST/ACS*”, Mass loss from stars and the evolution of stellar clusters

BIBLIOGRAPHY

5. R.A. Scheepmaker, M. Gieles, **M.R. Haas**, N. Bastian, S.S. Larsen, H.J.G.L.M. Lamers, 2006, “*The radii of thousands of star clusters in M51 with HST/ACS*”, Globular Clusters: Guides to Galaxies
6. M. Gieles, S.S. Larsen, **M.R. Haas**, R.A. Scheepmaker, N. Bastian, 2006, “*The Maximum Mass of Star Clusters*”, Globular Clusters Guides to Galaxies

Curriculum vitae

On March 26, 1983 I was born in Oosterhout, the Netherlands. Only eight years later my fascination for astronomy started after getting my first book on the stars. From then on I was determined to become an astronomer. In the few years that followed I gathered more and more books and 2 telescopes. Membership of astronomical clubs enriched my early astronomical life. I went to grammar school at the Alberdingk Thijm College in Hilversum. During high school I also ended up in the finals of the Physics Olympiad and I won two hours of single-dish VLT observing time, which was the (unnecessary) last trigger to start my studies in physics and astronomy.

As I thought stellar evolution would become the field of my main interest and expertise, I went to start my undergraduate studies at Utrecht University. In the third year of my studies at Utrecht I gained some (but little) experience in solar physics, after a two week ‘observing’ trip (it was very cloudy) to the Dutch Open Telescope on La Palma, under supervision of Professor Rob Rutten. As my interests moved from stellar scales to bigger, I obtained my Master of Science degree in Astrophysics (cum Laude) after finishing a study of extragalactic star clusters in the Whirlpool galaxy in the group of Professor Henny Lamers.

During my studies in Utrecht I also became more active in popularisation of astronomy, mainly through the JongerenWerkGroep voor sterrenkunde (JWG: Dutch youth association for astronomy). Few things are more rewarding than teaching others about the topics of your passion. Therefore I also took up several student assistencies at the university from my third year on and I taught physics at the NOVA College in Amstelveen (4th and 5th year of HAVO) during my last two years of study.

For my PhD I moved to Leiden Observatory in June 2006, to work on the subject described in this thesis under the supervision of Dr. Joop Schaye, with Professor Marijn Franx as promotor. Leiden brought me my first experience at the larger scales, both science- and institute-wise. During my PhD I have presented my work and participated in meetings (besides those in the Netherlands) in Garching (Germany), Zürich (Switzerland), Durham (UK), Rio de Janeiro (Brazil), Ghent (Belgium), Stockholm (Sweden) and Tucson, San Diego, Irvine, Cambridge, New York and Baltimore (USA). I will continue my work in the field of galaxy evolution at the Space Telescope Science Institute in Baltimore.

De laatste pagina's van dit proefschrift wil ik gebruiken om die personen te bedanken zonder wie dit proefschrift niet tot stand zou zijn gekomen. Henny, ook na mijn vetrek uit Utrecht kon ik altijd bij je terecht voor onmisbaar advies en hulp waar nodig; enorm bedankt daarvoor!

In everyday life, colleagues are probably the people you see most. Also, they are the only ones with whom you discuss work in some kind of detail. Claudio, where would I have started, and where would I have ended up, without you? Thanks for a lot of help and advice. Rob, thanks for bringing in some 'normal life' (and sports) at the Sterrewacht. I hope we can stay in touch. Andreas, your German habits were some welcome diversifications. I am glad we are still in contact and hope to see you more when I am in the States too! When the three of you left the Sterrewacht, my life at work changed significantly. Olivera, for me you were until the end one of the 'original members of the group': thanks for the possibilities to share some human traits. When I was asked if I was willing to join in a project for a Master's student I was enthusiastic from the beginning. That enthusiasm lasted and I have enjoyed the many hours of working together with you, Freeke. You did an awesome job as the postdoc replacement, Craig, thanks for helping me out during numerous moments of ignorance, for being a fun guy and for your interesting contributions to the group meetings! I was happy when you arrived, Ben, as I was in serious need of someone else who knew how to party and sometimes cared just that little bit less about work. Besides the own group, there are many, many others you encounter every day again. Ann-Marie (almost part of our group I would say), thanks for being around and high five for awesome-ph! Ryan, I always enjoy discussing science and related issues with you. For all of those not mentioned yet: thanks to you too, really!

Een promotietraject is niet half zo leuk, en is ook moeilijk te doorstaan, zonder een leven naast de wetenschap. Vele uren heb ik besteed voor en met de Jongeren-WerkGroep voor Sterrenkunde. Behalve tijdverdrijf heeft dit ook vele vriendschappen opgeleverd en het zou te ver voeren al jullie namen hier afzonderlijk te noemen. Enorm bedankt voor vele uren gezelligheid, naast alle serieuzere zaken!

Pa, ma, zonder jullie was ik nooit terechtgekomen waar ik nu ben. Jullie steun, in wat voor vorm dan ook, is van onschatbare waarde. Enorm bedankt voor alles, ik houd van jullie. Fem, een betere zus had ik me niet kunnen wensen! Natuurlijk zijn de allerlaatste woorden hier voor jou, Joyce. Ik heb maar mazzel dat jij (en je ouders en zus!) zo'n groot deel van mijn leven zijn gaan vormen. Ik ben enorm gelukkig dat je bent meegegaan naar de andere kant van de grote plas en hoop dat we ook in de rest van ons leven elkaar overal zullen blijven volgen.